2000

METHOD FOR DETERMINATION OF THRESHOLD POWER OF AMPLIFICATION IN ERBIUM-DOPED FIBER, BY MEANS OF MEASUREMENTS OF ASE ON BOTH DIRECTIONS ON THE FIBER.

R.J. Selvas Aguilar.[b], E. Kuzin[a], J.J. Sánchez-Mondragón[a,b,] M.A. Basurto Pensado.[a,b],
L.C. Archundia Berra[b],

[a]Instituto Nacional de Astrofísica, Optica y Electrónica (INAOE)
Luis Enrique Erro #1, Apdo. 51 y216, C.P. 72000,Tonantzintla,Puebla,México.
[b]Centro de Investigaciones en Ingeniería y Ciencias Aplicadas (CIICAp),UAEM
Av.Universidad #1001,Col.Chamilpa,C.P. 62210,Cuernavaca,Morelos,México.

ABSTRACT

Recent developments in the construction of Erbium-doped fibers have seen parallel progress in the measurement techniques to characterise these fibers.
In this paper, we discuss a simple method of obtaining threshold power amplification of Erbium-doped fibers. The method can be used to measure the threshold power of this particular fiber. As a result, the predicted threshold power value is in very good agreement with the experimental results obtained. We have based our measurements of the amplified spontaneous emission on both the forward and the backward directions of the fiber axis.
We also report on other parameters such as Erbium doping concentration, the spectrum of absorption, and cross sections, with the objective of obtaining data for comparison of predicted threshold amplification with actual threshold amplification, when the Erbium-doped fibers are used in laser systems[1].

Index Terms:
Erbium Doped Fiber, Threshold Power P_{th}, Amplified Spontaneous Emission

1.Introduction:

Many methods of characterisation in optical fibers have been proposed [2]. However, in the rare-earth-doped fiber conventional methods, with certain modifications, are used with newly developed methods to obtain particular parameters in this kind of fiber. In the literature, we find that this kind of fiber is found to have the characteristics of propagation shown in Figure 1.

The behaviour and the parameters of the optical fibers are needed to build new systems and devices. Such as active fibre devices among which fibre lasers are one of the fast developing examples [3].

Moreover these parameters can reveal the type of fiber that we are working with.

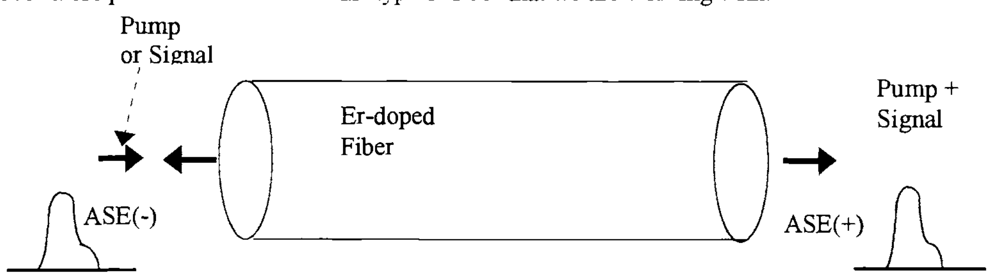

Figure 1. The basic parameters of propagation

Theoretically, a rare-earth ion has a lifetime t during which, by means of a spontaneous process, it returns to its ground state and emits a photon, which has no coherent properties. The process repeats by itself so the photons in the active medium are multiplied. This process is known as *Amplified Spontaneous Emission* or *ASE*.

SPIE Vol. 3572 • 0277-786X/99/$10.00

The collection of photons eventually reaches a certain value where the special fiber begins to produce a *LASER* signal. This means that the pump signal has been absorbed and converted into a signal with coherent properties. Using an estimation of this process, we can obtain a value of threshold power of the fiber. In other words, the boundary between stimulated process and spontaneous process, called threshold power.

2. Background

To start with, we take the atomic rate equations corresponding to their populations for the three level laser system, due to that an Erbium-doped fiber amplifier operates as a three-level system at room temperature, the three level laser system approximation is justified for Er^{3+}-glass fibers, as shown by Desurvire et. al. [4] and we can also take a series of equations for a piece of fiber with length dZ. [4]. To avoid the trivial solution, we have ignored propagation loss.

The relationship between the respective densities of the signal beam intensity *Is*, the ion densities at those respective levels, and the cross sections in a fiber can be expressed through the following equation [5-7].

$$\frac{dI_s}{dz} = (\sigma_s N_2 - \sigma_a N_1) I_s \qquad (1)$$

Where σ_s and σ_a are the emission and absorption cross section coefficients, respectively. *Is,* it corresponds to intensity of photons per unit frequency.

Moreover, the dependence of the pump intensity on length is given by

$$\frac{dI_p}{dz} = -\sigma_p N_1 I_p \qquad (2)$$

Where σ_p is the pump absorption cross section. On the other hand, the dependence of the *ASE* signal intensity also is given by

$$\frac{dI_{ASE\pm}}{dz} = \pm[\sigma_s N_2 - \sigma_a N_2] I_{ASE\pm} + h\nu\sigma_s N_2 \Delta\upsilon \qquad (3)$$

In equations 1-3, we can observe that I_p is the pump intensity, I_{ASE} is the amplification spontaneous emission intensity, *h* is the Plank's constant and ν correspond to the wavelength at *ASE* signal, and *hvs* the energy of a *ASE* photon. As well the ± in equation 3 corresponds to the *ASE* direction of propagation, we must remember that the spontaneous emission is amplified in both directions of the fiber axis, where the sign (+) indicates that the *ASE* and the pump signal both travel in the same direction, whereas the sign (-) indicates that the *ASE* and the pump signal both travel in opposite direction. The constant $\Delta\nu$ corresponds to the bandwidth of spontaneous emission, σa, σb, and σs are the cross sections of the fiber, and finally, *Ni* is the population density for levels i=1,2,and 3.

Note that for the system. We simply assume *Is*=0, and then equation (2) is equal zero.

$$\frac{dI_s}{dZ} = 0, \qquad (4)$$

So, we also can write the equation which described the inversion population and it is very useful for describing of the proposed method.

$$N_2 - N_1 = \rho \frac{\frac{\sigma_p}{h\upsilon_p} I_p + (\frac{\sigma_a + \sigma_s}{h\upsilon_s}) I_s - \frac{1}{\tau}}{\frac{\sigma_p}{h\upsilon_p} I_p + (\frac{\sigma_S + \sigma_p}{h\upsilon_S}) I_S + \frac{1}{\tau}} \qquad (5)$$

3. Results

In general, the work consisted in both theoretical and experimental process. The set-up showed in the figure 2 can be explain as follows. A fiber of known length L was placed in the configuration, a pair of dichroic mirrors with *HT@1550nm* and *HR@980nm* were placed at each cleaved ends of the fiber. A *Ti-Sa* Tunable laser was used as the pump source, which operated at 980nm. In addition, a pair of Germanium photo-detectors were used for measuring the ASE signal.

The use of this equipment allows the measurement of the *ASE* signal in both directions. In the experiment the dichroic mirrors were used because we needed to remove the pump signal from the data. In that case, the photo-detectors only took the signal at around 1550nm, which corresponds to the wavelength of the *ASE*. The characterisation of the mirrors resulted that in the 1550 nm wavelength region is transmitted though them, while the 980nm pump wavelength is reflected into the common output fiber.

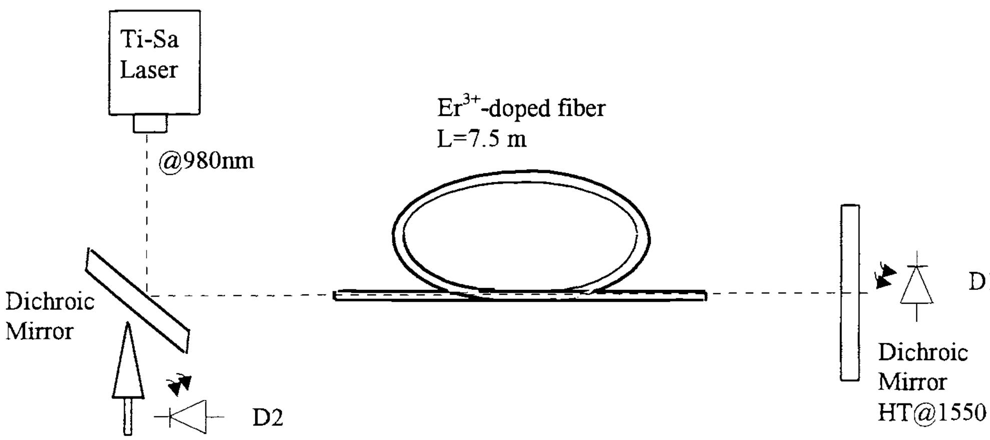

Figure 2. Experimental configuration for the measurement of ASE.

Using a relation between the forward and backward direction at signals, we obtained our data. This is plotted against the pump signal in the figure 4(a). As can be seen, we can calculate the threshold power, for $I_{(+)ASE}/I_{(-)ASE}=1$. These results are relevant when the Er-doped fibers are used in laser systems.

During the experimental part we have also built a code using MatLAB software which is enable us to calculate the threshold power. However, with this software we need other parameters such as $\sigma_p,\sigma_a,\sigma_s$ (cross sections) ι (lifetime) and ρ (concentration of ions), which prior to that were characterised.

The atomic rate equation and equations 1,2, and 3 of system were used in the programme to resolve the behaviour of pump signal and generation of spontaneous emission.

The description of how the code works is as follows. Without pump power the fiber presents high attenuation for signal with a wavelength of 1,55um. When the pump power is increased, the attenuation decreases which means that the pump power decays in an exponential way, hence the case is that the pump power reaches 0 at the end of the fiber. This pump power is referred to as the threshold power. For a long span of fiber, the pump power decreases along the fiber. So, as the pump power increases, the threshold conditions will be firstly provided at the initial part of the fiber. The *ASE* signal propagating in a forward direction will be initially amplified, but then it will be attenuated. The backward *ASE* signal is amplified by the closest part of the fiber to the input and immediately exits the fiber without attenuation.

It can easily be seen that the power of the backward ASE must be higher than that of the forward *ASE*. When the pump power reaches the threshold level at the output end of the fiber, neither forward nor backward *ASE* suffers attenuation. In this case, equal power on both outputs is expected. So, the pump power at the fiber output end corresponds to the point when the ratio between backward and forward *ASE* reaches the value 1and its corresponding value of power is equal to the threshold power. In our calculation, we obtained a value for the threshold power of 120μW. This behaviour is illustrated in Figure 3.

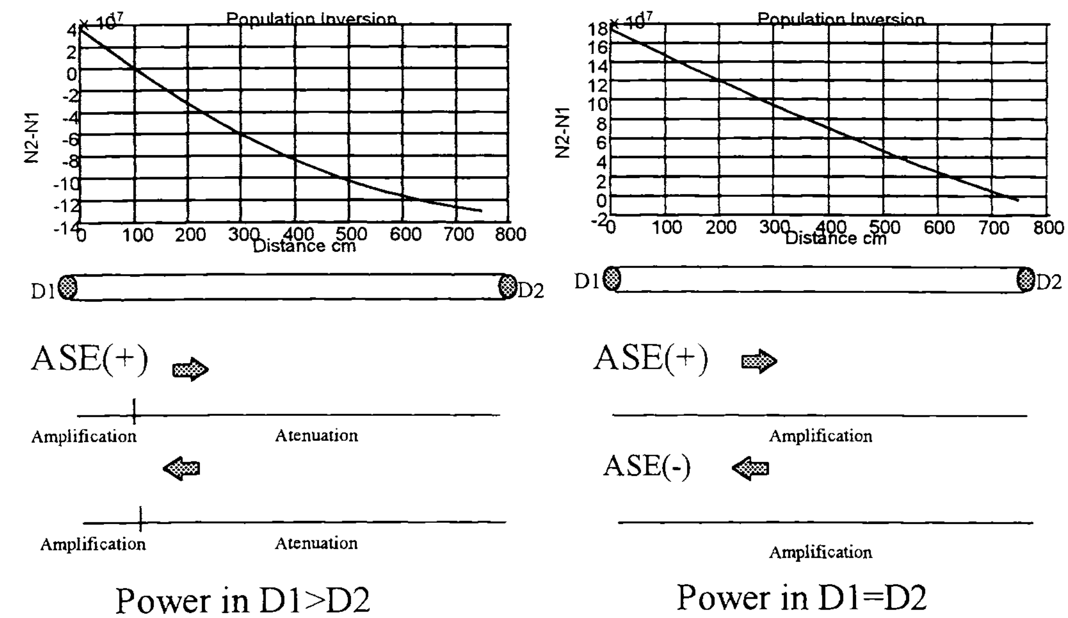

Figure 3 Method for characterisation of the threshold pump power.

The procedures of the code can be reviewed as follow, first of all we calculate the *ASE(+)* signal in one direction. That value is introduced in the second part of the program for calculating of opposite *ASE* signal. Also we needed to find a relation between the forward and backward signal value, and the data were plotted in Figure 4b., and the pump power corresponding to the power in the input or launched pump power into the fiber to obtain the pump in the output and with the help of the figure 5 which shows the pump in the output of the fiber in relation to the pump in the input and the latter value corresponds to the threshold power.

In addition to this procedures we measurement other parameters. The cross sections were calculated by means of the pump power which was later applied to rate equation. Also the absorption coefficient in the fiber was measured using the cut-back method.

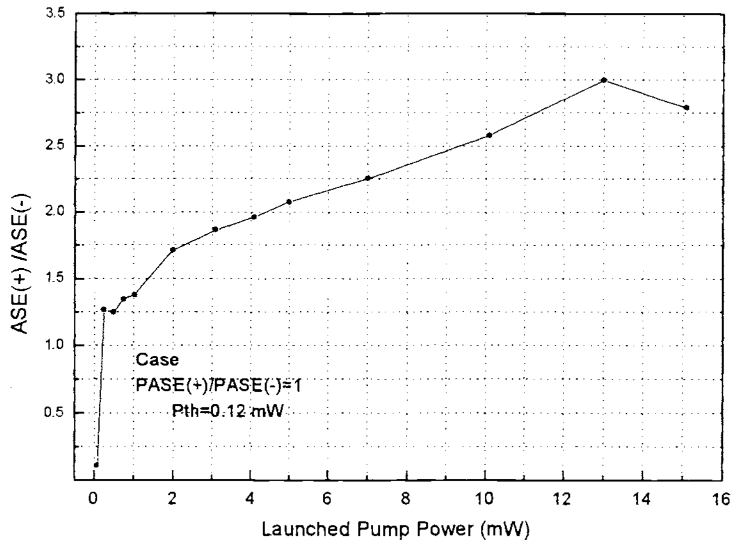

(4a)

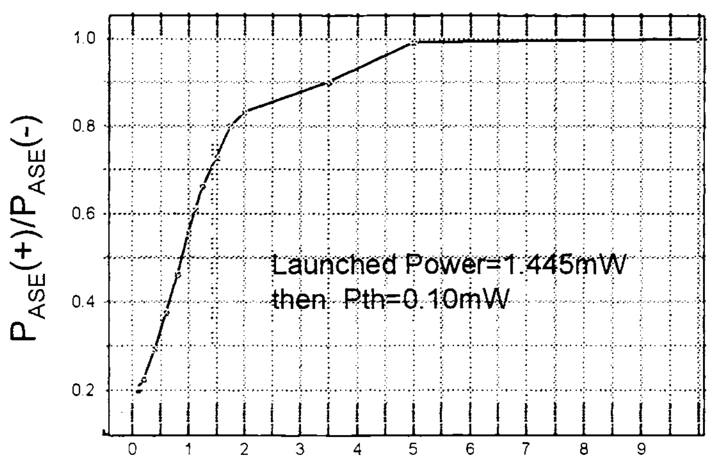

Launched power (mW)
As initial condition

(4b)

Figure 4. Determination of Pth value for amplification by experimental (4a), and by theoretical calculation (4b).

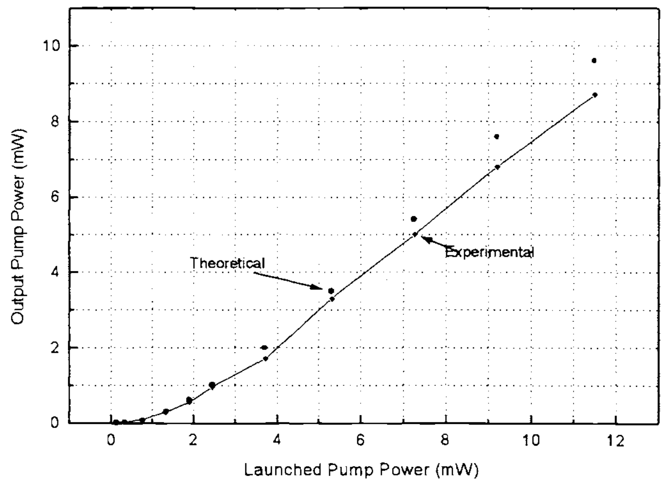

Figure 5. Comparison between theoretical data and experimental data of the pump signal.

4. Discussion and Conclusion:

There are many methods of characterisation of special parameters. However, most of them are very complex which makes the development of simple methods very relevant. Here we have described one method of measuring threshold power. This method provides a simple way of obtaining the threshold power in any doped fiber. The fiber to be tested, a pump laser, a pair of detectors and a pair of dichroic mirrors are only needed in this layout. As our results have shown, there is high agreement between calculated and experimental threshold power value.

In summary, we obtained the following parameters:
The threshold power is P_{th}=100μW in experimental study and P_{th}=120μW in computer simulation. In general the predicted value is in very good agreement with the experimental result.

The attenuation at 980 nm for the fiber was measured to be 2.14 dB/m. In that case we used the cut-back method. Data such as $\sigma_s=5\times10^{-25}$ cm^2, $\sigma_p=1.9\times10^{-25}$ cm^2, and ρ=98ppm were obtained by means of measurement of the pump power.

5. Acknowledgements

The authors are grateful to CONACYT-Mexico for its support which made this work possible and to MSc. Jose Alfredo Alvarez-Chavez for his valuable discussions and comments on the work.

6. References:

1. C. J. Koester and E. A. Snitzer, *Amplification in a fiber laser*, **Applied Optics**, Vol. 128 no. 10, 1182 (1964)
2. Simon B. Poole, David N. Payne, *Fabrication and Characterization of Low-Loss Optical Fiber Containing Rare-Earth Ions*, **Journal of Lightwave Technology**, Vol 4(7), pp 870-876 (July 1986)
3. Nayar, B. K., Alvarez-Chavez J.A. ,Grudinin, A.B, Mnelly, J.D., High Power 1540nm Fibre laser for Surgical applications, To be Published
4. Emmanuel Desurvire, 1994 , *Erbium-Doped Fiber Amplifier, Principles and Applications*, John Wiley&Sons , USA.
5. S. Shimada, H. Ishio, 1992, ***Optical Amplifiers and their Applications***, John Wiley&Sons, USA
6. Alvarez-Chavez, J.A. Minelly, J.D., Grudinin, A.B., E. Desurvire, *Characterization and Modeling of Amplified Spontaneous Emission in unsaturated Erbium-Doped Fiber Amplifier*, **Photonics Technology Letter**, Vol. 3, no.2, (Febraury 1991)
7. Desurvire E., and J.R. Simpson, 1988, Amplification of spontaneous emission in erbium-doped single-mode fiber, **IEEE J. Lightwave Technology**, Vol. 7, no. 5, 835.

2001

pressed as each emitter got feedback from adjacent microcores but no feedback of its own emission. The second feature was the beam shaping caused by diffraction of the output radiation at the edges of the central circle. The diffraction led to a well shaped beam with a central peak, which width corresponded to $\theta = 1.22\lambda/D$. The far-field cross-section for $z_M = 470$ µm is shown in Fig. 3. We obtained an output power of 5.5 W at a slope efficiency of 16%. The energy contained in the central far-field lobe was 10%. This is about 6 times higher than expected for a completely coupled MCF without beam shaping elements. In conclusion we have demonstrated that the novel mirror design increases not only the intermodal discrimination and the phase-locking but also combines a lot of energy in the central lobe and generates a well shaped far-field distribution.

4. References

1. V.V. Antyukhov, A.F. Glova, O.R. Kachurin, F.V. Lebedev, V.V. Likhanskii, A.P. Napartovich, and V.D. Pismennyi, JETP Lett., 44, 78(1986).
2. Wrage, P. Glas, D. Fischer, M. Leitner, D.V. Vysotsky, and A.P. Napartovich, Opt. Lett. 25, 1436 (2000).

CWM4 **6:15 pm**

Tuning characteristics of cladding-pumped neodymium-doped fiber laser

R. Selvas, J. Nilsson, *Optoelectronics Research Centre, University of Southampton, Southampton SO17 1BJ, England; email: rs@orc.soton.ac.uk*

Neodymium-doped glasses and crystals make excellent laser materials, and have been in the forefront of laser technology for the last three decades. This includes fiber lasers [Snitzer, Mears, Polaroid, Zellmer]. In the current drive for high-power cladding-pumped fiber lasers, however, neodymium has been overtaken by ytterbium as the dopant of choice for sources around 1 µm, because of the superior efficiency of ytterbium. Still, the four-level Nd^{3+} -ion is preferable to the two-level Yb^{3+} -ion when reabsorption would be a problem.

Here, we investigate the spectral characteristics of a cladding-pumped neodymium-doped fiber laser (NDFL) in a tunable configuration. The experimental set-up is shown in Fig. 1. Pump light from a fiber-coupled diode bar at 808 nm (Thomson-CSF) was launched into a 5 m long double-clad Nd-doped fiber (NDF) fabricated in house. The NDF had a 10 µm, 0.12 NA

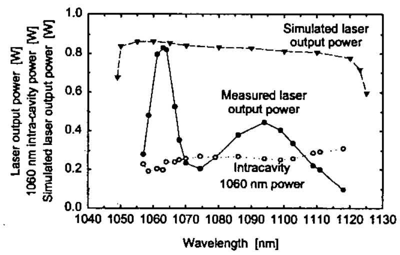

CWM4 Fig. 2. Simulated and experimental laser output power, and 1060 nm intra-cavity power measured at grating end.

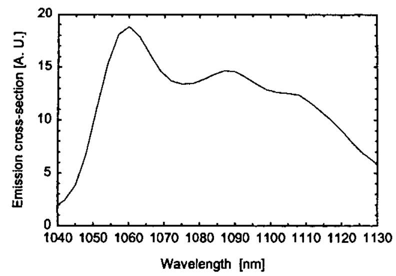

CWM4 Fig. 3. Emission cross-section spectrum as determined from fluorescence measurement.

core centered in a 220 µm diameter non-circular inner cladding. The fiber was coated with a polymer outer cladding for a nominal inner-cladding NA of 0.48. The pump absorption was 0.6 dB/m. The pump launch end of the fiber was perpendicularly cleaved, providing a 4% reflecting output coupler. The incident pump power was 15 W, of which 7 W could be launched into the NDF. In a free-running configuration with a perpendicularly cleaved facet also in the far end of the fiber, the NDFL produced up to 1.4 W of output power at 1062 nm, with a slope efficiency of up to 36% with respect to absorbed pump power. For wavelength-tuning, the far end of the fiber was instead angle-cleaved to suppress reflections and an external diffraction grating provided a wavelength selective tunable feedback. We estimate the fiber-to-grating-to-fiber reflectivity to ~20%. Because of the short fiber length and weak pump absorption, we double-passed the pump. However, we had previously tried longer fibers, and found that the fiber length did not significantly alter the emission spectrum.

Figure 2 illustrates the tuning characteristics of the laser. A maximum output power of 0.83 W is reached at a wavelength of 1063 nm. This wavelength corresponds to the peak of the emission cross-section spectrum determined from a fluorescence spectrum and shown in Fig. 3. Away from the peak, the power drops off rapidly, with a spectral shape correlated to the emission cross-section spectrum. This behavior is unusual for strongly saturated rare-earth doped fiber lasers. Similar behavior has been reported before from tunable NDFLs,[5] but with output powers of a few milliwatts. Figure 2 includes a simulated curve for our strongly saturated NDFL, which shows an almost constant output power over the tuning range of the laser. The difference between calculated and actual behavior may be caused by inhomogeneous broadening of the transition: The model calculations assumed a purely homogeneously broadened transition, but with inhomogeneous broadening, a lasing field at, say, 1100 nm would be unable to compress the gain at 1060 nm. Then, significant power is generated around 1060 nm and is lost from the cavity at the grating end when the laser is tuned away from 1060 nm. We measured this power, and it is also plotted in Fig. 2. In order to improve the efficiency for wavelengths away from 1060 nm, we modified the laser cavity by angle-cleaving also the pump launch end of the fiber and using a diffraction grating for feedback also there. At a tuning wavelength of 1100 nm, for example, the power from the laser (determined from the zero-order reflection power from the grating) at 1060 nm was small. Thus, we believe that with more careful cavity designs, an NDFL can operate efficiently also at wavelengths away from the 1060 nm emission peak.

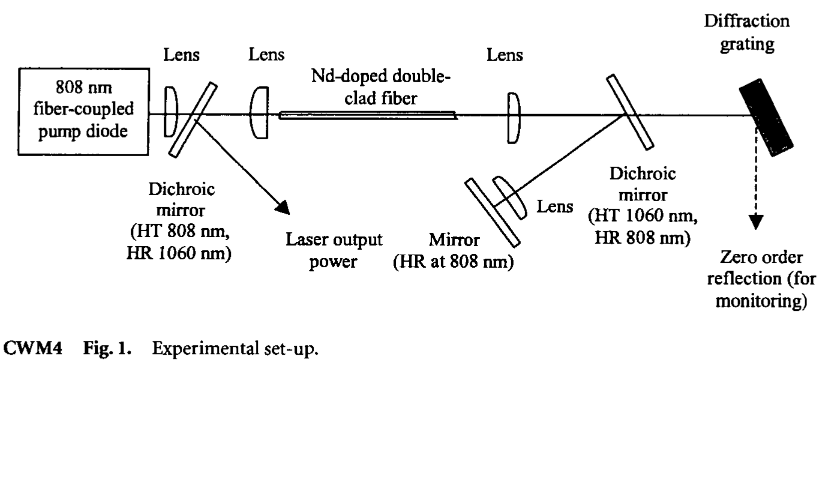

CWM4 Fig. 1. Experimental set-up.

References

1. E. Snitzer, "Neodymium glass laser", in *Third International Conference on Quantum Electronics*, v. 1, P. Grivet and N. Bloembergen, eds., (Columbia University Press, New York, 1963), pp. 999–1019.
2. R.J. Mears, L. Reekie, S.B. Poole, and D.N. Payne, "Neodymium-doped silica single-mode fibre laser", Electron. Lett. 21, 738–740 (1985).
3. E. Snitzer, H. Po, F. Hakimi, R. Tumminelli, and B.C. McCollum, "Double-clad, offset core Nd fiber laser", in *Proc. Opt. Fiber Sensors*, New Orleans, post-deadline paper PD5 (1988).
4. H. Zellmer, A. Tünnermann, H. Welling, and V. Reichel, "Double-clad fiber laser with 30 W output power", in Optical Amplifiers and Their Applications, OSA Trends in Optics and Photonics, vol. 16, Mikhail N. Zervas, Alan E. Willner, and Shinya Sasaki, eds., (Optical Society of America, Washington, D.C., 1997), pp. 137–140.
5. I.P. Alcock, A.I. Ferguson, D.C. Hanna, and A.C. Tropper, "Tunable, continuous-wave neodymium-doped monomode fiber laser operating at 0.900–0.94 and 1.070–1.135 µm", Opt. Lett. 11, 709–711 (1986).

2002

Raman amplification and pulsed lasing in cladding-pumped germanosilicate fiber

J. N. Jang, J. K. Sahu, R. Selvas, J. Nilsson, D. C. Hanna
Optoelectronics Research Centre, University of Southampton, Southampton SO17 1BJ, England
Phone: +44 23 8059 3143, fax: +44 23 8059 3142,

email: jnj@orc.soton.ac.uk

A. B. Grudinin
Southampton Photonics, Phi House, Enterprise Road, Chilworth Science Park, Southampton SO16 7NS, England

Abstract: We report for the first time Raman amplification in a cladding-pumped fiber. The double-clad germanosilicate fiber was pumped by a Q-switched Er-Yb co-doped fiber laser at 1570 nm. The power conversion efficiency was up to 36%, with a slope of 64%.

OCIS codes: (060.2320) Fiber optics amplifiers and oscillators, (140.3550) Lasers, Raman, (140.3510) Lasers, fiber

Introduction: Cladding-pumped rare-earth-doped fibers and Raman fiber devices have been two of the most compelling advances in the area of fiber amplifiers and lasers in recent years. Both cladding-pumped fibers and Raman fiber devices are primarily high-power devices. Cladding-pumping enables pumping with multi-mode pump sources that deliver high-power at a low cost. The core of the double-clad fiber can still be single-moded, so that robust single-mode amplification or lasing can be realized. Cladding-pumped silica fiber lasers and amplifiers have been demonstrated at 980 nm [1, 2, 3] and 1020 – 1150 nm [4] with Yb-doping, 1050 – 1120 nm with Nd-doping [5], 1530 – 1620 nm with Er-doping (normally with, but also without, Yb co-doping) [6], and 2000 – 2200 nm with Tm-doping [7]. These rare earths can be pumped by widely available high-power diode sources at around 800 nm or 910 – 980 nm.

Raman gain requires high pump powers. Raman fiber lasers are therefore only efficient at high power levels. On the other hand, Raman devices are very flexible in that gain is available at arbitrary wavelengths with the right pump source. Thus, a popular configuration for distributed Raman amplification at 1550 nm is to use a cascaded Raman laser as a pump source at 1450 nm (where rare-earth doped lasers are not available), which is in turn pumped by a high-power cladding-pumped Yb-doped fiber laser at 1060 nm. Besides this example, cladding-pumped fiber devices have many other real and potential applications in telecom and other areas, such as high-power fiber amplifiers, and sources for remote sensing (e.g., lidar). Raman amplification can be used for distributed or lumped amplification in telecom systems, but also more generally as a means for wavelength conversion (notably in cascaded Raman lasers).

Cladding-pumped Raman fiber devices, an exciting combination of multi-mode pumping and Raman amplification, have recently been proposed [8]. With such devices, single-mode gain can be created at arbitrary wavelengths with multi-mode pump sources (at the right wavelength). Conversely, any multimode source with sufficiently high power can be Raman-converted to a single-mode beam in a double-clad fiber configured as an amplifier or as a laser. One is no longer restricted to the absorption and emission bands of rare earths. While cladding-pumped Raman fiber devices require pump powers of, say, 100 W, such powers are available from fiber sources as well as traditional bulk sources. For example, a multimode Nd-doped fiber laser with 1 kW of output power was recently reported [9]. With pulsed sources, the required peak powers can be achieved with relatively modest average powers.

Here, we report for the first time Raman amplification in a cladding-pumped fiber, without any rare-earth doping. We believe that this is an important step towards a whole class of new optical amplifier devices based on brightness-enhancing nonlinear conversion of multimode pumps, including not only Raman converters but also Brillouin and optical parametric converters [10, 11].

Set-up: Our experimental set-up is shown in Fig. 1. We used a Q-switched Er-Yb co-doped fiber laser in a multi-fiber (GT-wave) arrangement [12]. See inset in Fig. 1. It was pumped by a pig-tailed multi-mode laser diode with 2.4 W of fiber-coupled output power at 910 nm. It generated up to 320 mW of average output power at high repetition rates (e.g., 70 kHz). In our experiment, we used the laser at low repetition rate, where it generated pulses with energies up to 40 μJ with pulse durations down to 200 ns and with a time jitter of ~5 ns. The lasing wavelength was 1565 – 1570 nm. The output from the fiber laser was free-space coupled into the double-clad Raman fiber (DCRF) via a dichroic mirror. Though the Q-switched fiber laser produced a single-moded output, we took great care to ensure that the pump beam was launched into the inner cladding, rather than the core, of the DCRF. Following all measurements presented here, we cut the DCRF a small distance from the pump launch end, and evaluated total launched pump power as well as pump power launched into the core by splicing the DCRF to a piece of standard single-mode fiber. We could launch up to 88% of the output power from the Q-switched fiber laser into DCRF. Of this power, typically 10 – 15% was in the core. We varied the launched pump power, without changing the pulse shape, repetition rate, or fraction of power in the core of the DCRF by inducing a bend-loss on the output fiber of the Q-switched fiber laser.

In the DCRF, the pump source generates Raman gain with a peak wavelength of 1680 – 1690 nm. Unfortunately, we did not have a signal seed source at that wavelength, and we therefore had to resort to the rather complicated set-up of Fig. 1, which effectively generates its own signal seed. However, we emphasize that the Raman converter itself is very simple, consisting only of the DCRF. The pump-to-signal conversion takes place in a single amplification pass. Thus, we consider the boxed portion of the set-up to be a cladding-pumped Raman fiber amplifier with input and output ends according to the figure. Besides being simple, the DCRF is also quite versatile in that it can be used with any pump source emitting within the wide transparency window of the fiber.

Alternatively, the set-up in Fig. 1 can be viewed as a synchronously pumped pulsed Raman laser.

The DCRF had a pure silica outer cladding and germanosilicate inner cladding and core, with different germanium contents. The inner cladding had a diameter of 21.6 μm and an NA of 0.22 with respect to the outer cladding. The core had a diameter of 9 μm and an NA of 0.14 with respect to the inner cladding, leading to an estimated cut-off wavelength of 1630 nm. The core propagation loss was 3.1 dB/km at 1550 nm. The loss for light in the inner cladding was 2.3 dB/km at 1550 nm. The fiber was 1.4 km long. Since Raman gain is essentially instantaneous and since the pump pulse is much shorter than the DCRF, the pump pulse creates Raman gain that travels with it through the fiber. Therefore, the Raman gain is much higher for signal light traveling with the pump than it is in the counter-propagating direction. Consequently, the signal at the output end of the DCRF will also be pulsed, and temporally coincident with the pump pulse.

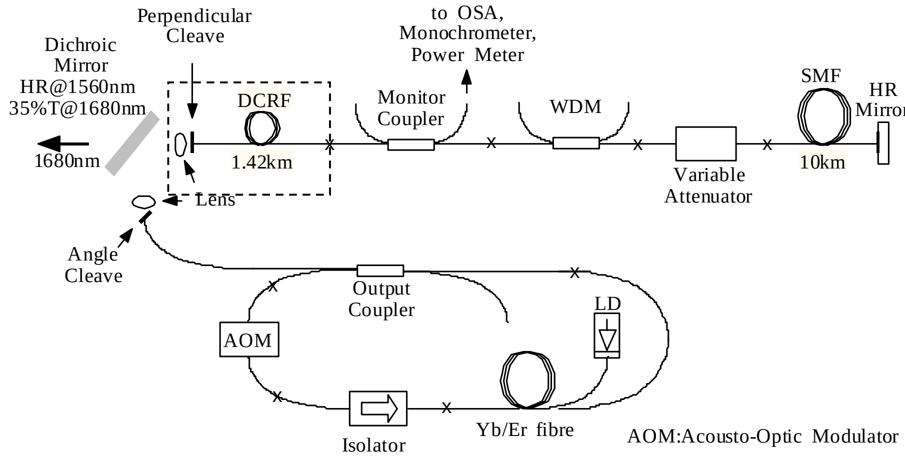

Fig. 1. Experimental setup for cladding pumped Raman fiber amplifier.

The signal pulse emitted from the DCRF continues on through the other components in the cavity. At its output end, the DCRF is spliced to a fused fiber coupler fabricated with standard single-mode fiber (NA 0.12, core diameter 8 μm). The splice loss between standard single-mode fiber (SSMF) and the DCRF was ~0.5 dB for the core mode. By contrast, since the cladding SSMF does not guide light, all pump light except the small fraction in the core is lost here. The coupler had a nearly flat wavelength response, and coupled out 40% of the incident power at ~1680 nm. The loss for the through-path was 4.3 dB at 1690 nm. This monitor coupler was then spliced to another, wavelength-selective, coupler. It had a low transmission loss (~2 dB) at the first stokes wavelength (~1680 nm) but a high loss at the second stokes wavelength as well as at the pump wavelength. Thus, it served as a filter that suppressed higher-order stokes generation. The couplers were followed by a variable optical attenuator (minimum insertion loss at 1550 nm 1.4 dB) that allowed us to change the cavity loss. Finally, there was ~10 km of standard single-mode fiber (loss at 1690 nm 5 dB). A high-reflecting mirror was butted to the fiber in the far end. We estimate the reflection loss to 2 dB.

The signal pulse is reflected back through the cavity all the way to the pump launch end of the DCRF. There, 4% is reflected again from the perpendicularly cleaved fiber end. At the same time, a new pump pulse is launched into the DCRF. The reflected signal light acts as a seed for the conversion in the cladding-pumped Raman fiber amplifier. Because the mode-selection that occurs in the SSMF and the low mode-coupling at splice and reflection points, the reflected signal is almost exclusively coupled to the core mode. The roundtrip cavity loss was ~55 dB. The roundtrip time was 115.27 μs, so the Q-switched fiber laser had to be carefully adjusted to a repetition rate of 8.6754 kHz for synchronous pumping. We used this repetition rate throughout. The pulse energy became 30 μJ and the pulse duration was 210 ns. Thus, the maximum peak power became 140 W, or 540 times the average power. This ratio remained constant also with an attenuated pump beam.

In an alternative configuration, a section of the DCRF was moved from its original location to a position between the VOA and the 10 km SSMF. At this point, the DCRF is un-pumped, so this way we could change the effective length of the DCRF without changing the total length or loss of the cavity.

Unfortunately, this set-up does not allow us to monitor the pump power remaining at the end of the DCRF. We cannot measure the pump power without breaking the DCRF. But if we do that, the cavity is destroyed and there is no longer any input signal seed. Nevertheless, we did measure transmitted pump power with the cavity opened at the end of the DCRF (1.4 km) , and found it to be ~68 mW for 100 mW launched.

Results: Figure 2 shows the DCRF gain vs. pump power for 1420 and 940 m long DCRFs. The gain was determined by varying the total cavity loss via the VOA, and adjusting the pump power until threshold for lasing was reached. The gain slopes are 1.5 dB/mW and 1.0 dB/mW, respectively. The effective lengths become 1000 m and 740 m. These numbers are in good agreement with theory, given the uncertainty in evolution of polarization and modal power distribution, and that the high Ge-content increases the Raman cross-section. Beyond the plotted range, laser threshold could not be reached because of the onset of strong ASE. Still, because of the high pump power, a gain of almost 70 dB could be reached. Figure 3 shows the output power from the DCRF vs. pump power for 1420 and 940 m long DCRFs. For these measurements, the VOA was set to its minimum loss value. The output power was evaluated by measuring the power exiting the coupler monitor port with a thermal power meter and recalculating it to the power coming out from the DCRF. The thresholds are 37 mW and 61 mW, and the slope efficiencies are 60% and 64% for the longer and shorter fiber, respectively. For both fiber lengths, the power in the core at the output end becomes significantly higher than in the input end: The highest pump power launched into the core was 10 – 20 mW. This demonstrates brightness enhancement via Raman amplification of a signal in the core with a pump beam substantially launched into the inner cladding.

At high pump power, higher-order Raman generation can occur. In Fig. 3, we restricted the pump power to values for which this was negligible. Thus, since higher-order generation occurs more readily in longer fibers, the maximum pump power for the 1420 m fiber is lower than that of the 940 m fiber.

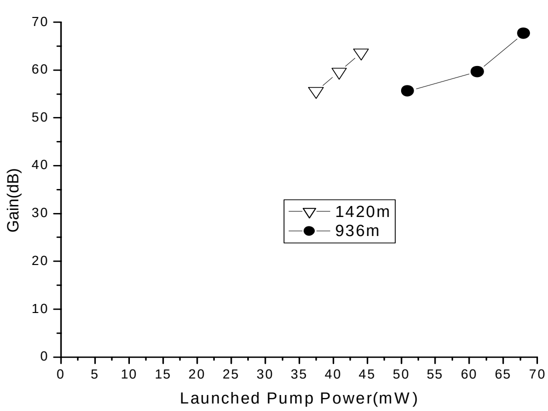

Fig. 2: Gain vs. pump power.

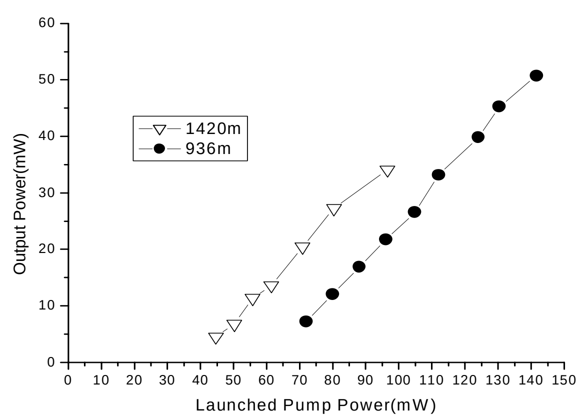

Fig. 3: Output power vs. pump power.

To study this further, we simulated our device in the cw regime, using simple, well-known equations for stimulated Raman scattering [13]. Since higher-order Raman conversion is very important in limiting the efficiency of these devices, this was also included in our simulations. The interactions of the pump and 1st and 2nd Stokes waves are given by the following equations:

$$\frac{dP_P}{dz} = -\alpha_P p_P - \frac{\lambda_P}{\lambda_{S1}} \frac{g_1}{A_{eff.S1}} P_P P_{S1} - \frac{\lambda_P}{\lambda_{S2}} \frac{g_2}{A_{eff.S2}} P_P P_{S2} \tag{1}$$

$$\frac{dP_{S1}}{dz} = -\alpha_{S1} p_{S1} + \frac{g_1}{A_{eff.P}} P_P P_{S1} - \frac{\lambda_{S1}}{\lambda_{S2}} \frac{g_1}{A_{eff.S2}} P_{S1} P_{S2} \tag{2}$$

$$\frac{dP_{S2}}{dz} = -\alpha_{S2} p_{S2} + \frac{g_1}{A_{eff.S1}} P_{S1} P_{S2} + \frac{g_2}{A_{eff.P}} P_P P_{S2} \tag{3}$$

where P_p, P_{S1}, and P_{S2} are pump, 1st Stokes, and 2nd Stokes powers. α and λ are corresponding absorption coefficients and wavelengths. g_1 and g_2 are Raman gain coefficients for 12 THz and 26 THz frequency shift, respectively, corresponding to the experimentally obtained shifts. Pump wavelength is 1564 nm and 1st, 2nd Stokes wavelengths are 1690 nm and 1810 nm. A_{eff} is the effective area of the fiber mode. The 3rd term in Eq. 1. represents the interaction between the pump and 2nd Stokes directly. We consider only 1st and 2nd Raman shifts because the 3rd Raman is very small and can be neglected. Signal seed source powers from the synchronously pumping scheme were calculated from the measured power and the total cavity loss. 1st Stokes powers are 2.3x10^{-4} mW for 90 mW pumping power and 8.43x10^{-4} mW for 140 mW pumping, respectively. We used the experimentally obtained Raman gain coefficient of g_1=0.233 Np/km/mW for the Raman gain peak. For the Raman gain between the pump and 2nd Stokes, we used the Raman gain spectra in Ref. 13. The absorption coefficients are 0.53 km^{-1} for α_p, 0.714 km^{-1} for α_{S1}, and 0.9 km^{-1} for α_{S2}. We used the laser repetition rate of 8.6754 kHz for synchronous pumping and the pulse duration time was 210 ns, which means the maximum peak power is 540 times higher than the average power.

Figure 4 shows simulation results of pump, 1st and 2nd Raman power evolution along the fiber for 90 mW and 140 mW pump power using the Eq. 1 to Eq. 3.

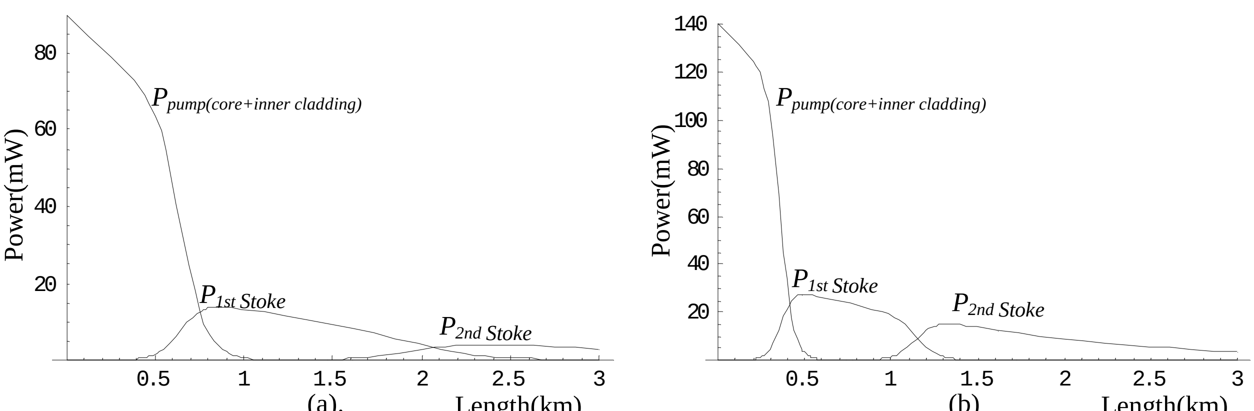

Fig. 4. Simulation result of pump, 1st and 2nd Raman power evolution along the fiber (a); 90 mW pump power, (b);140 mW pump power

As we can see in Fig. 4(a), there is no 2nd Raman conversion with 90 mW of pump power within 1.42 km of fiber, but with 140 mW of pump power in Fig. 4(b), higher-order Raman starts to appear after ~1 km of fiber. At 1.4 km, practically all 1st order Raman power has been converted to 2nd order Raman. These characteristics are in agreement with the experimentally observed behaviour.

Figure 5 shows experimentally obtained output spectrum, measured with an optical spectrum analyzer on the monitor output port for a fiber length of 940 m and a pump power of 140 mW. Unfortunately, the spectrum analyzer was limited to wavelengths up to 1750 nm, whereas the second stokes occurred at ~1810 nm. However, we also used a monochromator to resolve higher-order stokes radiation and for temporal measurements. Figure 6 shows output pulse shapes at the wavelengths of the pump and first and second stokes beams, measured with the monochromator and a germanium detector. We see that the signal at the second stokes wavelength is much weaker than that at the first stokes wavelength.

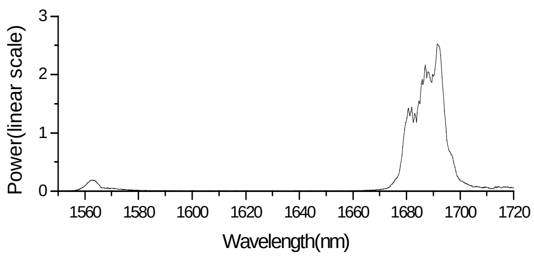

Fig. 5: Output spectrum after 940 m of DCRF.

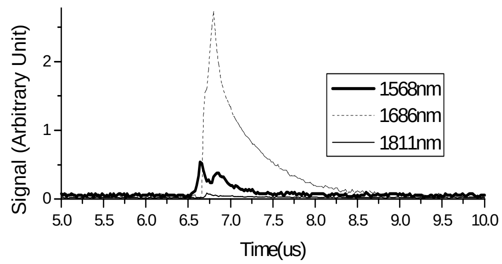

Fig. 6: Output pulse shapes

Discussion: Compared to rare-earth doped fibers, the Raman gain efficiency is quite low, especially in large structures. It is still relatively straightforward to reach high gain with pulsed pump sources. Even cw pump lasers (fiber and non-fiber ones) of sufficiently high powers are becoming increasingly available. In a laser configuration, the cavity losses can be sufficiently low for thresholds of a few watts, given a gain efficiency of the order of 1 dB/W (cw). Still, cladding-pumped Raman fibers only seem realistic with inner-cladding diameters of a few tens of microns, rather than with hundreds of microns as is common with rare-earth doped cladding-pumped fibers. This limits the scope for brightness enhancement and the high pump intensities required (pulsed or cw) presently preclude direct diode pumping. On the other hand, when suitable high-power pump sources are available, there are several advantages of Raman devices over rare-earth ones. Besides the flexibility in wavelength, the low loss of germanosilicate fibers allows the use of much longer devices, so that the heating per unit length can be small. At higher powers, however, the Raman conversion can occur in fibers as short as a few meters. Then, the small quantum defect of Raman scattering in silica simplifies the thermal management.

The length of the Raman fiber converter is important. A longer fiber leads to a higher gain efficiency in the small-signal regime. Therefore, it will be easier to reach threshold with a longer fiber. However, for higher powers, secondary Raman scattering occurs, this too with lower threshold for longer fibers. If this is to be avoided, there will be an upper limit on the pump power for a given fiber length. A shorter fiber has a higher upper limit. In Fig. 3, for pump powers up to 100 mW, the 1420 m fiber is better than the 940 m one. For higher pump powers, second-order Raman scattering occurs in the 1420 m fiber. Consequently, one can reach higher output powers with 940 m of fiber than with 1420 m, if sufficiently high pump power is available. Though a wavelength-suppressing filter could be used to suppress higher-order Raman scattering, this may be difficult to realize in practice.

Besides higher order Raman scattering, Raman scattering in the cladding should also be avoided. Since the core and cladding compositions are quite similar, and since the pump intensity is essentially similar in the core and inner cladding, the Raman gain will be similar in the core and inner cladding. If a single-moded output is required, one must then seed the core-mode (or provide mode-selective feedback in a laser).

The measured slope efficiency of up to 64% is as high as it reasonably can be with the loss in our fiber, given that all light quanta have t propagate through the whole length of fiber, as signal or pump photons. A lower-loss fiber or a shorter fiber (as appropriate for higher pump powers) would reduce total loss and thus improve slope efficiency. It is interesting to note that because of the nonlinear pump absorption, Raman devices can actually have quantum slope conversion efficiencies exceeding unity over a limited power range. Our fiber was indeed operating in that power range.

Conclusions: In conclusion, we report for the first time results on amplification in a cladding-pumped Raman fiber. We used a Q-witched Er-Yb co-doped fiber laser operating at 1565 – 1570 nm as a pump source. The power conversion efficiency was up to 36%, with a slope of 64%. We believe that cladding-pumped fiber devices present a very exciting alternative for amplification and brightness conversion at high powers.

References

1. L. A. Zenteno, J. D. Minelly, A. Liu, J. G. Ellison, S. G. Crigler, D. T. Walton, D.V. Kuksenkov, M. J. Dejneka, "1 W single-transverse-mode Yb-doped double clad fiber laser at 978nm", Electron. Lett, Vol. 37, pp 819-820, 2001.
2. L. B. Fu, R. Selvas, M. Ibsen, J.K. Sahu, S.A. Alam, J. Nilsson, D.J. Richardson, D.N. Payne, C. Codemard, S. Goncharov, I. Zalevsky, and A B. Grudinin, “An 8-channel fiber-DFB laser WDM transmitter pumped with a single 1.2W Yb-fiber laser operated at 977nm”, Technical digest 28th European Conference on Optical Communication ECOC-2002, Copenhagen, September, 2002. 08.3.5
3. R. Selvas, J. K. Sahu, J. Nilsson, S. A. Alam, and A.B. Grudinin, “Q-Switched 980nm Yb-doped fiber laser”, Technical digest Conference of Lasers and Electro-optics CLEO-2002, Long Beach, 2002, ThR6.
4. J.K. Sahu, C.C. Renaud, K. Furusawa, R. Selvas, D. J. Richardson, and J. Nilsson, “Jacketed air-clad cladding pumped Yb-doped fiber laser with wide tuning range”, Electronics Letter, Vol 37 (18), August 2001.
5. R. Selvas, J. Nilsson, “Tuning characteristics of cladding-pumped Neodymium-doped fiber laser”, Technical digest Conference on Laser Electro-optics CLEO- 2001, Baltimore, 2001. CWM4.
6. S.U. Alam, J. Nilsson, P.W. Turner, W.A. Clarkson, A.B. Grudinin, “Erbium-ytterbium co-doped cladding-pumped fiber laser tunable from 1533 to 1600 nm with up to 6.7W of output power, In proc. ASSL, Washington, 28-31, January 2001, TuA5.
7. R Hayward,, W. A. Clarkson, P.W. Turner, J. Nilsson, A. B. Grudini, D. C. Hanna, “High-power and tunable operation of a diode-bar-pumped double-clad Tm-doped silica fiber laser at 2 μm”, In proc. CLEO/Europe 2000, Nice 10-15, Sep 2000, CWA1
8. R. R. Rice, “Multimode Raman fiber amplifier and method”, US patent no. 6,353,087 (2002)
9. K.-I. Ueda, H. Sekiguchi, and H. Kan, “1 kW cw output from fiber embedded lasers”, in Proc. Conference on Lasers and Electro-Optics, Long Beach, USA, 2002, post-deadline paper CPDC4
10. B. C. Rodgers, T. H. Russell, and W. B. Rob, “Laser beam combining and cleanup by stimulated Brillouin scattering in a multimode optical fiber”, Opt. Lett. 24**,** 1124-1126 (1999)
11. A. Piskarskas, V. Smilgevicius, and A. Stabinis, “Optical parametric oscillation excited by an incoherent conical beam”, Opt. Comm. 143, 72-74 (1997)
12. S. U. Alam, J. Nilsson, P. W. Turner, M. Ibsen, A. B. Grudinin, A. Chin, “Low cost multi-port reconfigurable erbium doped cladding pumped fiber amplifier”, European Conference on Optical Communication 2000, München, Germany, paper 5.4.3.
13. G. P. Agrawal, Nonlinear Fiber Optics, 2nd Edition, (Academic press, 1995), pp. 316-361

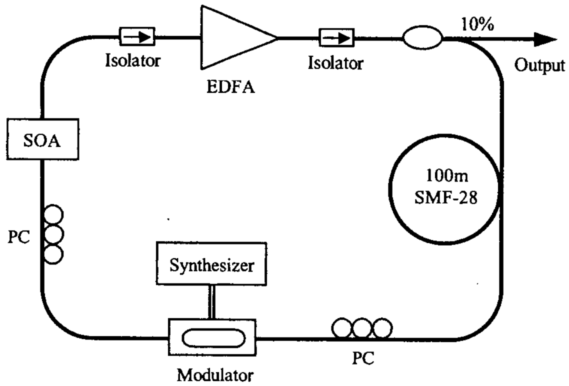

CThR5 Fig. 1. Experimental Setup.

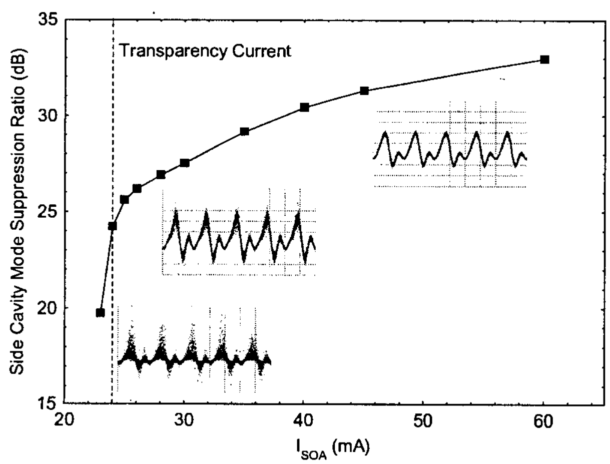

CThR5 Fig. 2. Side cavity mode suppression ratio increases with the driving current of the SOA.

Moreover, SMN is significantly suppressed when the SOA switches from absorption to gain. These results provide information about the mechanism of SMN suppression by SOAs, which is under further investigation.

The width of the uncompressed output pulses was also measured at different I_{SOA}. As shown in Fig. 3, the pulse width increases with I_{SOA}. This behavior was studied with a simple numerical model, which followed the Kuizenga-Siegman approach.[8] The pulse duration was assumed

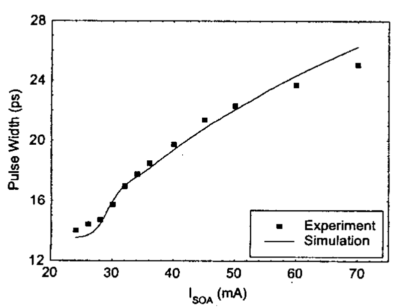

CThR5 Fig. 3. The uncompressed output pulse width varies with the driving current of the SOA.

much shorter than the carrier lifetime in the SOA so that the time-dependent gain can be expressed analytically.[9] The small signal gain was determined by experiment and the saturation energy was considered proportional to I_{SOA}. The linewidth enhancement factor was assumed to be 3.5. Other parameters were the same as in the experiment. The gain of the EDFA was adjusted to keep the average power a constant. The agreement between the simulation result and the experimental data demonstrates the validity of the model. Work is in progress to establish a more complete model to study the effects of the SOA on both SMN and pulse properties.

References

1. K. Tamura and M. Nakazawa, "Dispersion-tuned harmonically mode-locked fiber ring laser for self-synchronization to an external clock," *Opt. Lett.*, vol. 21, pp. 1984–1986, 1996.
2. C. Shu and Y. Zhao, "Characteristics of dispersion-tuning in harmonically mode-locked fiber laser," *IEEE Photon. Technol. Lett.*, vol. 10, pp. 1106–1108, 1998.
3. G.T. Harvey and L.F. Mollenauer, "Harmonically mode-locked fiber ring laser with an internal Fabry-Perot stabilizer for soliton transmission," *Opt. Lett.*, vol. 18, pp. 107–109, 1993.
4. M. Nakazawa, K. Tamura, and E. Yoshida, "Supermode noise suppression in a harmonically modelocked fibre laser by selfphase modulation and spectral filtering," *Electron. Lett.*, vol. 32, pp. 461–463, 1995.
5. N. Onodera, "Supermode beat suppression in harmonically mode-locked erbium-doped fibre ring lasers with composite cavity structure," *Electron. Lett.*, vol. 33, pp. 962–963, 1997.
6. J.S. Wey, J. Goldhar, and G.L. Burdge, "Active harmonic modelocking of an erbium fiber laser with intracavity Fabry-Perot filters," *J. Lightwave Technol.*, vol. 15, pp. 1171–1180, 1997.
7. Lingze Duan, Christopher J.K. Richardson, Zhaoyang Hu, Mario Dagenais and Julius Goldhar, "A stable, dispersion-tuned harmonically mode-locked fiber ring laser using a SOA," submitted to *IEEE Photon. Technol. Lett.*.
8. D.J. Kuizenga and A.E. Siegman, "FM and AM mode locking of the homogeneous laser—part I: theory," *IEEE J. Quantum Electron.*, vol. QE-6, pp. 694–708, 1970.
9. Govind P. Agrawal and Niloy K. Dutta, *Semiconductor lasers, 2nd* edition (Van Nortrand Reinhold, 1993), Chap. 11.

CThR6 **3:45 pm**

Q-switched 980 nm Yb-doped Fiber Laser

R. Selvas, J.K. Sahu, and J. Nilsson, Optoelectronics Research Centre, University of Southampton, Southampton SO17 1BJ, England, Email: rs@orc.soton.ac.uk

S.A. Alam, and A.B. Grudinin, Southampton Photonics, Phi House, Enterprise Road, Chilworth Science Park, Southampton SO16 7NS, England

Double-clad rare-earth doped fiber lasers pumped by high brightness laser diodes are very efficient and compact sources of cw and pulsed radiation. Ytterbium-doped fiber lasers (YDFLs) have been demonstrated at around 1100 nm in cw configurations with output powers of 110 W[1] and in Q-switched operation with pulse energies approaching 10 mJ.[2] Ytterbium can also emit at around 980 nm, with output power of around 1 W demonstrated in cw operation.[3] Here, we present a Q-switched 980 nm cladding-pumped YDFL with 1.2 μJ of energy and 60 W of peak power in pulses shorter than 20 ns at repetition rates of up to ~0.2 MHz and 250 mW of average output power for repetition rates between 0.2 and 0.65 MHz. A pulsed 980 nm source with high peak power and good beam quality is attractive for frequency conversion, e.g., frequency quadrupling to 245 nm.

A Q-switched cladding-pumped 980 nm YDFL presents two challenges: Its pronounced three-level nature leads to a high threshold and potential problems with strong amplified spontaneous emission (ASE) at 1030 nm.[4] Because of this, a high pump intensity and low cladding-to-core area ratio is needed for efficient operation. We used a jacketed air-clad fiber[5] that provided a tight pump confinement in a 28 μm diameter inner cladding with a high NA (up to 0.5)[5]). See inset in Fig. 1. Furthermore, the small inner cladding results in a high pump absorption and thus short device lengths, which promotes high

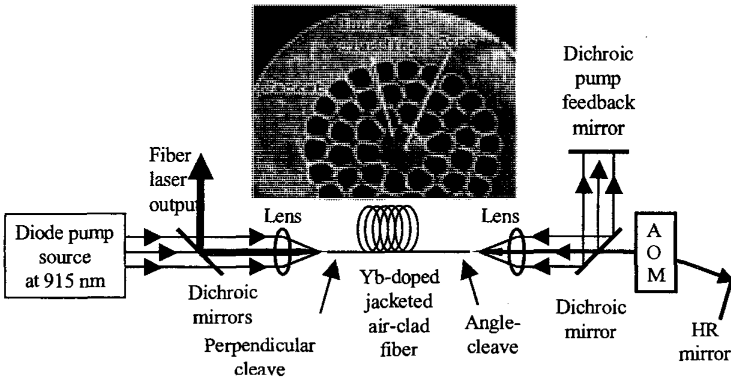

CThR6 Fig. 1. Experimental set-up. Inset: Yb-doped jacketed air-clad fiber.

peak powers with Q-switching. The second challenge is the large absorption and emission cross-sections of Yb at ~980 nm. This leads to a low saturation energy, which limits the energy storage and pulse energy. Our fiber had a core NA of ~0.11, a diameter of 6.5 μm, and a measured cut-off wavelength of ~900 nm. The robust single-mode character of the core ensures a diffraction-limited output beam. However, in such a core a saturation energy of 1–2 μJ can be expected.

Our experimental set-up is shown in Fig. 1. We could launch up to 2.6 W of pump power into the Yb-doped fiber from a 915 nm diode source. The single-pass pump operating absorption was 3 dB. An AOM was used for Q-switching. With the AOM in a blocking state, the fiber generated 260 mW of ASE in the forward direction (towards the AOM end) and 120 mW in the backward direction.

We Q-switched the laser by on-off modulating the AOM. The pulse energy and average output powers with and without ASE are shown in Fig. 2. The ASE build-up time was 5–6 μs. Increasing the pulse separation beyond this value did not increase the output pulse energy, but merely led to more ASE being generated between pulses.

The AOM provided some wavelength selection and it was in fact possible to tune the laser to 1030 nm. We did not determine the linewidth of our laser, except that it was below the 2 nm resolution of our spectrum analyzer.

With a saturation energy of ~2 μJ it should be possible to obtain pulse energies of at least 10 μJ with good on-off modulation of the AOM. However, the deflection efficiency of our AOM was only 20–30%. Since the AOM was double-passed, the feedback in the AOM end was not much more than 1%, i.e., comparable to the 3.5% feedback of the cleaved front-end of the fiber. Thus, we believe we lost more than half of the output energy in the AOM end. Rough measurements confirmed a similar power output from the two ends of the fiber. Furthermore, we measured the switching time of our AOM to 100 ns. In a short high-gain fiber cavity the pulse build-up time is quite short. We believe that the switching time of our AOM may have been large enough to induce excess losses.

The pulse duration is shown in Fig. 3. Because of the short fiber length we had clean single pulses of durations down to 20 ns. The peak power was ~100 W.

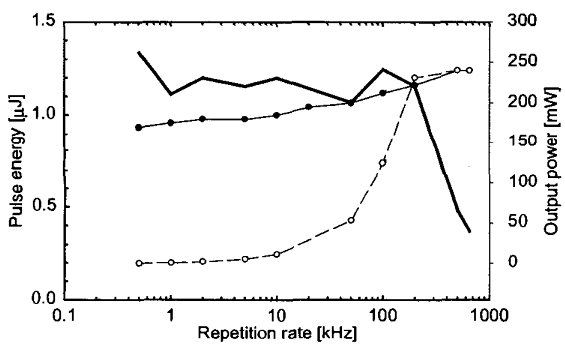

CThR6 Fig. 2. Extracted energy (black) and average power (white) against the repetition rate.

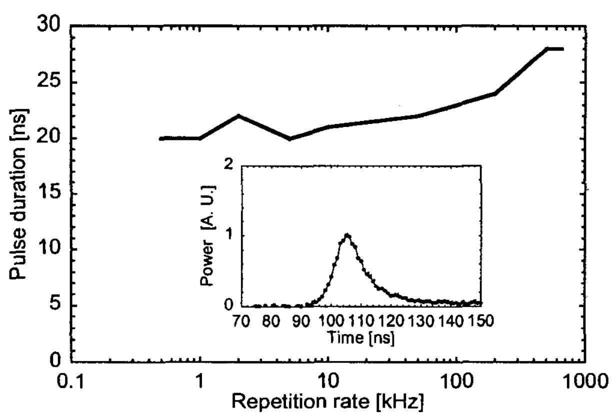

CThR6 Fig. 3. Pulse duration vs. repetition rate. Inset: pulse shape.

References

1. V. Dominic, S. MacCormack, R. Waarts, S. Sanders, S. Bicknese, R. Dohle, E. Wolak, P.S. Yeh, E. Zucker, "110 W fiber laser," Postdeadline paper, CPD 11, CLEO '99, Baltimore (1999).
2. C.C. Renaud, H.L. Offerhaus, J.A. Alvarez-Chavez, J. Nilsson, W.A. Clarkson, P.W. Turner, D.J. Richardson, and A.B. Grudinin "Characteristics of Q-switched cladding-pumped ytterbium-doped fiber lasers with different high-energy fiber designs", IEEE J. Quantum Electron. 37, 199–206 (2001).
3. L.A. Zenteno, J.D. Minelly, A. Liu, A.J.G. Ellison, S.G. Crigler, D.T. Walton, D.V. Kuksenkov, and M.J. Dejneka, "1 W single-transverse-mode Yb-doped double-clad fibre laser at 978 nm", Electron. Lett. 37, 819–820 (2001).
4. J. Nilsson, J.D. Minelly, R. Paschotta, D.C. Hanna, and A.C. Tropper, "Ring-doped cladding-pumped single-mode three-level fiber laser", Opt. Lett. 23, 355–357 (1998).
5. J.K. Sahu, C.C. Renaud, K. Furusawa, R. Selvas, J.A. Alvarez-Chavez, D.J. Richardson, and J. Nilsson, "Jacketed air clad cladding pumped ytterbium doped fibre laser with wide tuning range", Electron. Lett. 38, 1116–1117 (2001).

CThR7 **4:00 pm**

260-GHz Soliton Train Modulational Instability Laser in Highly Nonlinear Fiber

C.J.S. de Matos, D.A. Chestnut and J.R. Taylor, Femtosecond Optics Group, Imperial College of Science, Prince Consort Road, London SW7 2BW, U.K., Email: c.de-matos@ic.ac.uk

1. Introduction

Modulational instability (MI) in optical fibers can be used to obtain high-repetition-rate pulse trains for potential research-and-development applications in telecommunications. MI yields short pulses from continuous-wave (CW) light when amplitude fluctuations are amplified and compressed due to self-phase modulation (SPM) and anomalous dispersion in a fiber.[1] Efficient

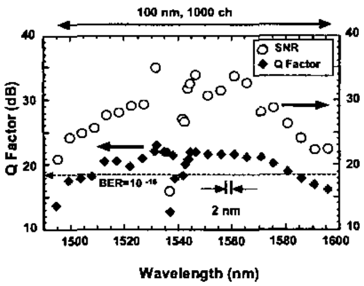

WR5 Fig. 2. Measured optical SNRs and Q factors of optical carriers

100 nm) and is realized when nonlinear materials, such as optical fibers, are pumped by picosecond optical pulses. It occurs due to the combined effects of self-phase modulation, cross-phase modulation, and parametric four-wave mixing. It is noteworthy that the generated SC light has high coherence and high SNR. Optical carriers are obtained by spectrally slicing individual longitudinal modes from the SC spectrum. Therefore, multiple carriers (multi-wavelength CW lights) can be generated by utilizing a wavelength demultiplexer whose channel spacing equals the repetition rate of the pump pulses. In Fig. 1, the source laser was a 1538 nm mode-locked laser diode (ML-LD), generating a 4.3 ps, 12.5 GHz pulse train.[8] It was then amplified with an EDFA and coupled into a polarization-maintaining (PM) SC fiber.[3] The output spectrum exhibited more than 100 nm spectrum broadening. The figure shows that over 1000-channel, 12.5 GHz-spaced optical carriers are generated. The spectrum around 1560 nm, which is more than 20 nm (200 ch) from the pump laser wavelength, exhibits equally-spaced optical carriers.

Noise characteristics (RIN and Q-factor) of each optical frequency were measured after one frequency was extracted with a 12.5-GHz-spaced AWG DEMUX.[9] The channel crosstalk of the adjacent optical frequencies was greater than −21 dB. The SNRs were calculated by integrating the RIN measured from 100 MHz to 2.5 GHz, and the Q-factors were measured after externally modulating each channel in a $LiNbO_3$ modulator at 2.5 Gbit/s ($2^{31}-1$ PRBS). Figure 2 shows the wavelength dependencies of the SNR and the Q-factor. The SNR ranged from 21 dB to 35 dB for 100 nm range. The Q-factor exceeded 18.3 dB (BER $\leq 10^{-16}$) for the wavelength range of 1512–1580 nm, which is sufficient for multispan transmission.

3. DWDM transmission experiment:

Figure 3 shows the experimental configuration for 10-Gbit/s DWDM transmission employing a single SC-MCS. More than 100 channels (1535–1555 nm) with equal spacing of 25 GHz on the ITU grid were generated from the SC-MCS. In this experiment, a normal dispersion and dispersion flat fiber was utilized as the SC fiber.[10] The optical power of each channel at the SC fiber output ranged from 8 dBm to 13 dBm. Two sets of odd and even channels were divided by two 50-GHz-spaced AWG-demultiplexer/multiplexers (DEMUX/MUXs). The odd and even channels were modulated independently with a 10-Gbit/s NRZ format ($2^{31}-1$ PRBS), and then combined with orthogonal polarization to yield a 106-channel, 25-GHz-spaced 10-Gbit/s DWDM signal. The inset in Fig. 3 shows the spectrum of the DWDM signal. The DWDM signal was injected into a recirculating loop. A 60 km A_{eff}-enlarged single mode fiber (SMF) and a 20 km reverse dispersion fiber (RDF) were employed as the transmission fibers in order to achieve, simultaneously, chromatic dispersion compensation and reduce optical nonlinearity.[11] The fiber input power of each channel ranged from −9 dBm to −6 dBm. The Q-factors after transmission exceeded 15.6 dB, which is equivalent to a BER of 10^{-9} in 106 channels (1535.82–1556.76 nm).

4. Conclusion

The paper reported the multiple optical carrier generation (over 1000 channels with 12.5-GHz spacing) from a single supercontinuum source. It was confirmed that these carriers have sufficient SNR to achieve Q-factors above 18.3 dB. The channel spacing is strictly determined by the microwave mode-locking frequency of the source laser and so Hz-level accuracy is possible. A transmission experiment utilizing the SC source was also presented. A 106-channel, 25-GHz-spaced, 10-Gbit/s transmission over 640 km with Q-factors of greater than 15.6 dB was achieved. The results show that the SC-MCS can be applied to over 100-channel DWDM systems. By improving the flatness of the SC spectrum, over 1000-km transmission is achievable. It is expected that SC-MCS will be a key technology in realizing WDM networks that offer hundreds of wavelengths. A part of this work was supported by Telecommunications Advancement Organization of Japan (TAO).

References

1. M. Koga, "Toward realizing a tera-bit per second throughput photonic transport system for bandwidth abundant multimedia communication", *OFC '99*, WI2 (1999).
2. T. Morioka, "Supercontinuum lightwave optical sources for large capacity transmission", *ECOC '95*, Th.A.1.2 (1995).
3. K. Mori, H. Takara, S. Kawanishi, M. Saruwatari, and T. Morioka, "Flatly broadened supercontinuum spectrum generated in a dispersion decreasing fibre with convex dispersion profile", *Electron. Lett.*, 33, 1806–1808 (1997).
4. Y. Takushima, and K. Kikuchi, "10-GHz, over 20-channel multiwavelength pulse source by slicing super-continuum spectrum generated in normal-dispersion fiber", *IEEE Photon. Tech. Lett.*, 11, 322–324 (1999).
5. K. Imai, M. Kourogi, and M. Ohtsu, "30-THz span optical comb generation by self-phase modulation in an optical fiber", *IEEE J. Quantum Electron.*, 34, 54–60 (1998).
6. J. Kim, Ö. Boyraz, and M. N. Islam, "150+ channel ultra-DWDM source with N × 10 GHz spacing utilizing longitudinal mode slicing of supercontinuum", *OFC 2000*, ThA2 (2000).
7. H. Takara, T. Ohara, K. Mori, K. Sato, E. Yamada, Y. Inoue, T. Shibata, M. Abe, T. Morioka and K-I. Sato, "More than 1000 channel optical frequency chain generation from single supercontinuum source with 12.5 GHz channel spacing", *Electron. Lett.*, 36, 2089–2090 (2000).
8. K. Sato, A. Hirano, and H. Ishii, "Chirp-compensated 40-GHz mode-locked lasers integrated with electroabsorption modulators and chirped gratings", *IEEE J. Selected Topics in Quantum Electron.*, 5, 590–595 (1999).
9. K. Takada, M. Abe, T. Shibata, M. Ishii, T. Inoue, H. Yamada, Y. Hibino, and K. Okamoto, "10 GHz-spaced 1010-channel AWG filter achieved by tandem connection of primary and secondary AWGs", *ECOC 2000*, PD 3.8 (2000).
10. E. Yamada, H. Takara, T. Ohara, K. Sato, T. Morioka, K. Jinguji, M. Itoh, and M. Ishii, "150 channel supercontinuum CW optical source with high SNR and precise 25 GHz spacing for 10 Gbit/s DWDM systems", *Electron. Lett.*, 37, 304–306 (2001).
11. H. Kawakami, Y. Miyamoto, K. Yonenaga, and H. Toba, "Highly efficient distributed Raman amplification system in a zero-dispersion-flattened transmission line", OAA '99, ThB5 (1999).

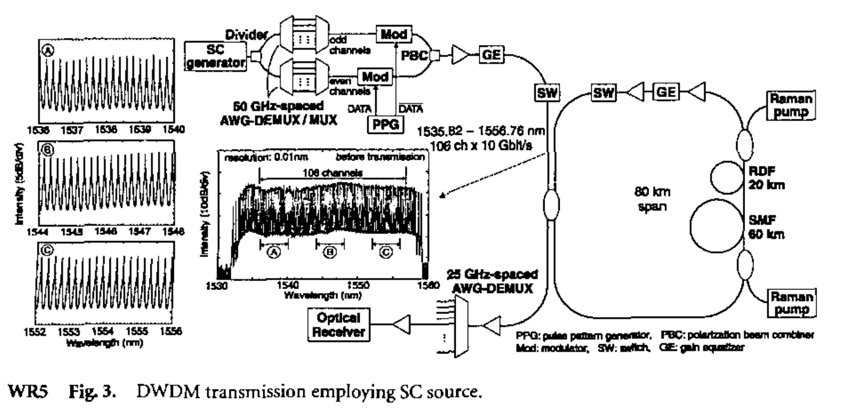

WR5 Fig. 3. DWDM transmission employing SC source.

WR6 **5:30 pm**

Continuous-wave pumped holey fiber Raman laser

J. Nilsson, R. Selvas, W. Belardi, J.H. Lee, Z. Yusoff, T.M. Monro, D.J. Richardson, *Optoelectronics Research Centre, University of Southampton, Southampton SO17 1BJ, England, Email jn@orc.soton.ac.uk*

K.D. Park, P.H. Kim, N. Park, *Optical Communication Systems Laboratory, National Research Lab for Next Generation Optical Amplifiers, Seoul National University, Seoul, Korea 151-742*

Introduction

Stimulated Raman scattering in optical fibers find many important applications in telecommunications, in particular in Raman amplifiers and lasers. Although stimulated Raman scattering is intrinsically a quite weak process, the tight confinement and low loss of optical fibers allow for quantum conversion efficiencies approaching unity in fiber Raman devices, with threshold pump powers as low as a watt or so.[1] However, in order to realize efficient devices with conventional fibers with a raised-index core, fiber lengths of several hundred meters or even several kilometers are often used. This is often a drawback. On the other hand, holey fibers can be fabricated with an order of magnitude smaller core areas, with a corresponding increase in the Raman interaction and reduction in device length. Recently, holey fibers with effective areas as small as a few square microns have been used for Raman amplification as well as all-optical Raman modulation.[2] Still, these devices were operated with pulsed pump sources, to overcome the limitation of the relatively low average pump power that was available.

Many Raman devices need to operate in a steady state rather than pulsed mode. Here we report on a holey fiber Raman laser (HFRL) pumped by a continuous-wave (cw) ytterbium-doped fiber laser operating at 1060 nm. The HFRL emitted up to ~0.7 W at a wavelength of 1110–1120 nm. To our knowledge, a holey fiber Raman device with cw pumping has not been reported before. Though the output from the HFRL in this instance exhibited strong relaxation oscillations and was thus temporally noisy, we believe that with better cavity designs stable cw operation will be possible.

Experimental set-up and results

Figure 1 depicts our holey fiber Raman laser set-up. The inset of Fig. 1 shows a scanning electron micrograph of the fiber we used in our experiments. The single material silica fiber had a core diameter of ~1.9 μm and an outer glass diameter of 125 μm. The relatively large hole sizes result in a tight mode confinement and thereby in a high optical nonlinearity. The effective nonlinear mode area was measured to be 2.9 μm^2 at 1550 nm. At 1060 nm, it was calculated to be 2.7 μm^2 for the fundamental mode (the fiber was slightly multi-moded there). At the pump (1060 nm) and Stokes (~1115 nm) wavelengths, the propagation losses were ~55 dB/km.

For pumping the holey fiber, we used a randomly polarized ytterbium-doped fiber laser that provided up to 9 W of fiber-coupled output power in a continuous wave at 1060 nm (Fig. 1). This power was launched into a pig-tailed polarization-insensitive isolator. Despite its high insertion loss of 2.1 dB, we were forced to use this isolator to prevent unpredictable interactions between the HFRL and the Yb-doped fiber laser. The isolator was then spliced to a 1060/1240 nm WDM coupler. The backward port of the coupler was terminated with a feedback-free arrangement, and was used for characterizing the output from the HFRL. After passing through the WDM coupler, the pump power was launched into free space via a perpendicularly cleaved fiber end. The output beam was collimated with a ~3 mm focal length aspheric lens and then focused into the holey fiber via another, ~1.1 mm focal length aspheric lens. The holey fiber had simple perpendicular cleaves in both ends. It was 40 m long, which lead to a single-pass transmission loss of 2.2 dB (40%) for pump and Stokes waves. The path-averaged single-pass power was thus 78% of the launched power. However, the pump was actually double-passed via a high-reflecting mirror that was butted to the far end of the fiber. We evaluated the resulting feedback to practically 100% (at the pump wavelength). Thus, total pump absorption was 4.4 dB or 64%, in the absence of any nonlinear pump depletion. A detector was placed behind the mirror to measure pump leakage, and to enable us to evaluate single-pass pump transmission. In the pump launch end, the cavity was closed by the 4% Fresnel reflection from the fiber facet(s).

At low powers, we evaluated the launch efficiency into the holey fiber to 65% (relative to the incident power between the two lenses). We also evaluated the back-coupling efficiency from the holey fiber into the WDM coupler fiber to be ~40% at 1060 nm (relative to the returning power between the two lenses). This value is lower than the forward-coupling value because of the bi-moded nature of the holey fiber (while it was single-moded at 1550 nm).

It was possible to maintain a high launch efficiency also at high powers. For example, in one experiment in which the isolator was removed we were able to transmit 3.2 W of 8.9 W incident to the holey fiber, indicating a launched pump power of 5.5 W. The cw power density at the holey fiber was thus 0.2 GW/cm^2, which demonstrates the excellent power handling capability of silica holey fibers. Still, in this case there was no high-reflecting mirror butted to the fiber, and laser threshold could not be reached.

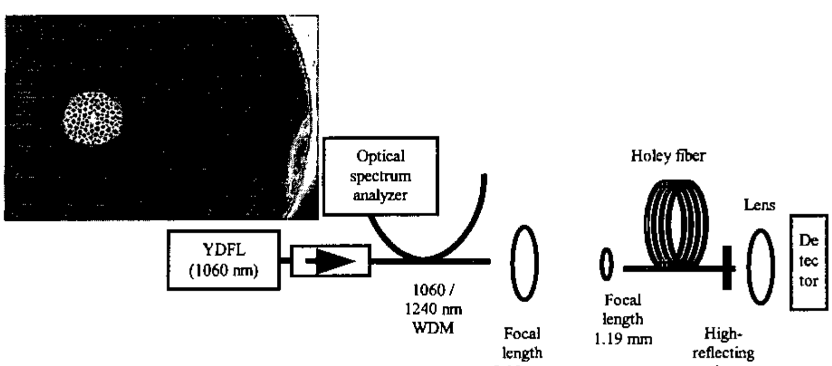

WR6 Fig. 1. Experimental set-up with scanning electron micrograph of holey fiber cross-section.

Figure 2 shows the laser characteristics of the HFRL of Fig. 1. Figure 2a shows the laser output power vs. incident power. The laser output power was measured with an optical spectrum analyzer at the return port of the 1060/1240 nm WDM coupler, but we compensated for the characteristics of the coupler as well as for the back-coupling efficiency. Thus, the quoted output power refers to a point between the lenses in Fig. 1. We assumed the back-coupling efficiency to be 40%, which is the value measured at low powers. However, at higher powers, the back-coupling efficiency may well have been somewhat smaller since it was difficult to keep the launch stable then. Figure 2b further illustrates this point, showing single-pass transmitted pump power measured after the mirror but recalculated to a point inside the fiber, just before the mirror, relative to incident power. The transmission decreases for higher incident powers, even before there is any significant pump depletion via stimulated Raman scattering. Figure 2c shows the laser output power vs. launched pump power, as determined from a measurement of transmitted pump power. In this case, pump depletion could be significant for the highest power, so there is no linear relation between launched and transmitted pump power. Nevertheless, we have made simple estimates for the nonlinear scattering to enable us to assess the launched pump power also in this case. The maximum output power was 0.75 W for a launched pump power of 3.9 W and the slope efficiency was around 70%. The threshold of the laser was ~2.9 W with respect to launched power. This should result in a round-trip Raman gain of around 12 dB. Taking background losses and reflection from external fiber facets into account, we estimate that the round-trip loss of our cavity may be around 16 dB, which is in fair agreement with our estimated Raman gain.

Figure 2d, finally, shows an output spectrum measured with the OSA off the WDM port. The spectral characteristics of the coupler have been compensated for, but not the back-coupling loss from free-space into the coupler fiber.

We also investigated the temporal characteristics of the Yb-doped fiber laser as well as of the HFRL. The Yb-doped fiber laser was quite stable, without any power fluctuations detectable at a 100 MHz measurement bandwidth. By contrast, the output from the HFRL appeared chaotic in nature, with large modulation of the output power with no evident pattern and with moderate peak powers. While a pulsed output is often undesirable, it does not necessarily affect slope efficiency or threshold. Thus, we believe we could obtain similar power characteristics in a cw output, with a better cavity design. Several effects may lead to an unstable output, e.g., the presence of higher-order modes, polarization effects (and we did not investigate temporal polarization characteristics of the Yb-doped fiber laser), as well as coupled cavity effects, given that a butted mirror as well as multiple perpendicularly cleaved fiber ends were present. On the other hand, a pulsed pump source would have resulted in other power characteristics.

In conclusion, we have presented a holey fiber Raman laser pumped by a continuous wave Yb-doped fiber laser. We believe this to be the first such device presented the literature. In one configuration we were able to launch up to 5.5 W of pump power into the holey fiber, with a cw power density of 0.2 GW/cm^2. In another configuration,

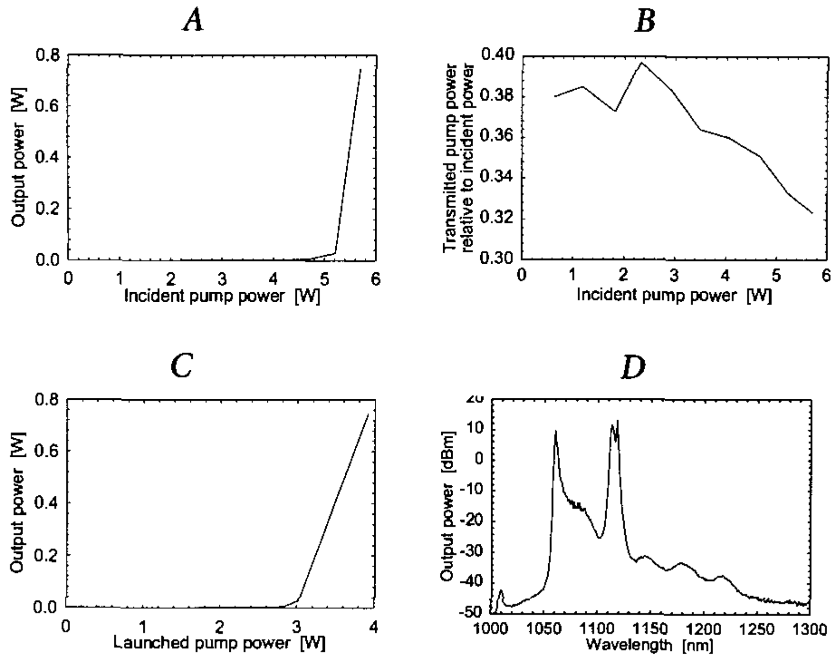

WR6 Fig. 2. a: Output laser power *vs.* incident pump power. b: Relative single-pass pump transmission *vs.* incident pump power, c: Output laser power *vs.* launched pump power., d: Output spectrum for 3.9 W of launched pump power

we obtained ~0.7 W of laser output for a launched pump power of 3.9 W and a slope efficiency of 70%.

References

1. G.P. Agrawal, *Nonlinear fiber optics*, 3rd edition (Academic Press: 2001)
2. J.H. Lee, Z. Yusoff, W. Belardi, T.M. Monro, P.C. The, and D.J. Richardson, "A holey fibre Raman amplifier and all-optical modulator", European Conference on Optical Communication, Amsteradam, Holland, 2001, post-deeadline paper.

WR7 5:45 pm

Modulational instability laser in highly nonlinear fiber yielding continuous-wave 260-GHz pulse train

C.J.S. de Matos, D.A. Chestnut and J.R. Taylor, *Femtosecond Optics Group, Imperial College of Science, Prince Consort Road, London SW7 2BW, U.K., Email: c.de-matos@ic.ac.uk*

1. Introduction

Recently there has been great interest in pulse sources with high repetition rates to satisfy the large demand for information capacity and to develop fast logic devices in optical communication systems. Electronics-based and direct modulation technologies have been widely investigated but are generally limited to repetition rates of around 40 GHz, although some exceptions have been demonstrated. Passive optical modulation techniques have, however, proven successful in obtaining repetition rates of up to a few terahertz. For example, rational mode-locking of fiber lasers, split semi-conductor laser cavities and various laser beating techniques have all demonstrated high-quality ultra-short pulse trains. Another powerful passive technique, modulational instability (MI), can be used to obtain high-quality pulses with repetition rates in excess of 100 GHz in optical fiber devices. MI refers to the transition from continuous-wave (CW) light to short pulses when amplitude fluctuations on the CW light level are amplified and compressed due to the interplay between self-phase modulation (SPM) and anomalous dispersion in an optical fiber. Pulses from MI have been generated in both single-pass[1] and ring cavity laser[2] configurations, with the latter demonstrating lower CW backgrounds. Furthermore, more efficient self-induced ring cavity configurations have been presented which use an intracavity erbium-doped fiber amplifier (EDFA) as a complementary gain mechanism.[3]

Current systems have the drawback of requiring high pump intensities to exceed the threshold for MI due to the low nonlinearity in most fibers. This pump requirement can be decreased through the use of highly nonlinear dispersion-shifted fibers (HNL-DSF) with nonlinear coefficients typically ten times that of standard fiber. Recently HNL-DSF has been employed in a variety of nonlinear effect-based devices such as fiber Raman amplifiers[4] and broadband wavelength converters.[5]

In this paper we present a self-induced MI ring laser based on HNL-DSF and an EDFA that produces a CW train of soliton pulses at a repetition rate of 260 GHz. Pulses exist in the average soliton regime and are shown to separately experience anomalous dispersion and SPM around the cavity.

2. Experiment

The experimental set-up for the modulational instability fiber ring laser is shown in Fig. 1. The

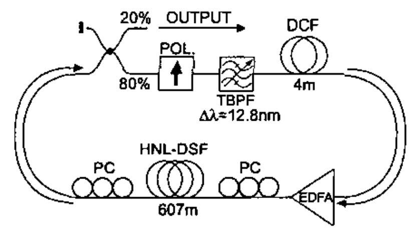

WR7 Fig. 1. Experimental configuration of the modulational instability ring laser

intra-cavity EDFA provided up to 600 mW of optical power and initiated the lasing process through amplified spontaneous emission (ASE) build-up in the ring. SPM occurred in 607 m of HNL-DSF that was kindly provided by Sumitomo Electric Industries, Ltd. The HNL-DSF had a low dispersion slope around 1.55 μm with a zero-dispersion wavelength at 1552 nm and a nonlinear coefficient of 21 $W^{-1}km^{-1}$. A tunable bandpass filter (TBPF) with a bandpass of 12.8 nm was included to optimize the modulational instability process by encouraging lasing around the zero-dispersion wavelength of the cavity. A polarizer (POL.) and two polarization controllers (PC) were also used to stabilize and optimize the system due to the high polarization-dependence of modulational instability. It was found that the cavity had a high dispersion that discouraged efficient MI. To compensate for the high dispersion, 4 m of dispersion-compensating fiber (DCF) was added to the configuration. 20% of the laser power was extracted via an optical coupler.

The MI laser was simultaneously analyzed in an optical spectrum analyzer (OSA) and a second harmonic generation autocorrelator (SHG-AC) at a ratio of 1:99 by using a tap coupler. Another piece of DCF was included after the ring output coupler to compensate for the dispersion introduced by the external measurement fibers.

3. Results and Discussion

The spectrum and autocorrelation of the optimized modulational instability laser output are shown in Fig. 2 and 3, respectively, for an EDFA output power of 280 mW. As can be seen in Fig. 2, the laser output centered around 1540 nm demonstrates a lobe structure that is characteristic of modulational instability. The overall spectrum had an approximate 3-dB bandwidth of 8.5

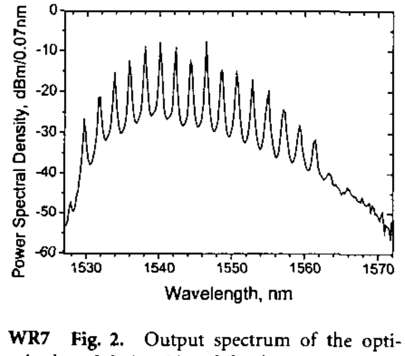

WR7 Fig. 2. Output spectrum of the optimized modulational instability laser

Cladding-pumped Raman fiber amplifier

J. Nilsson, J. K. Sahu, J. N. Jang, R. Selvas, D. C. Hanna
Optoelectronics Research Centre, University of Southampton, Southampton SO17 1BJ, England
phone: +44 23 8059 3101, fax: +44 23 8059 3142, email: jn@orc.soton.ac.uk
A. B. Grudinin
Southampton Photonics, Phi House, Enterprise Road, Chilworth Science Park, Southampton SO16 7NS, England

Introduction: Cladding-pumped rare-earth-doped fibers and Raman fiber devices have been two of the most compelling advances in the area of high-power fiber amplifiers and lasers in recent years. Cladding-pumping enables pumping with multi-mode pump sources that deliver high-power at a low cost. The core of the double-clad fiber can still be single-moded, so that single-mode amplification or lasing can be realized. Raman gain requires high pump powers and Raman conversion is therefore only efficient at high power levels. On the other hand, Raman devices are very flexible as gain is available at arbitrary wavelengths with the right pump source. Cladding-pumped Raman fiber devices represent a natural progression to multi-mode pumping and Raman fiber devices [1]. While cladding-pumped Raman fiber devices require pump powers of, say, 100 W, such powers are available from fiber sources as well as from traditional bulk sources. For example, a multimode Nd-doped fiber laser with 1 kW of output power was recently reported [2]. With pulsed sources, however, the required peak powers can be achieved with relatively modest average powers. Here, we report for the first time Raman amplification in a cladding-pumped fiber, without any rare-earth doping. We believe that this is an important step towards a whole class of new optical amplifier devices based on brightness-enhancing nonlinear conversion of multimode pumps, including not only Raman converters but also Brillouin and optical parametric converters. [3, 4]

Set-up: Our experimental set-up is shown in Fig. 1. We used a Q-switched Er-Yb co-doped fiber laser in a multi-fiber (GT-wave) arrangement. Here, we used the laser 8.7 kHz repetition rate, where it generated pulses at 1565 – 1570 nm with energies of 30 μJ and durations of 210 ns. Thus, the peak power became 140 W, or 540 times the average power. The time jitter was ~5 ns. The output from the fiber laser was free-space coupled into the double-clad Raman fiber (DCRF) via a dichroic mirror. Though the Q-switched fiber laser produced a single-moded output, we took great care to ensure that the pump beam was launched into the inner cladding, rather than the core, of the DCRF. Following all measurements presented here, we cut the DCRF a small distance from the pump launch end, and evaluated first total launched pump power and then power in the core by splicing the DCRF to a piece of standard single-mode fiber. We could launch up to 88% of the output power from the Q-switched fiber laser into DCRF, 10 – 15% of which was in the core. We varied the launched pump power by inducing a bend-loss on the output fiber of the Q-switched fiber laser, without changing the pulse shape, repetition rate, relation between peak and average power, or fraction of power in the core of the DCRF.

In the DCRF, the pump source generates Raman gain with a peak wavelength of 1680 – 1690 nm. We did not have a signal seed source at that wavelength, and therefore had to resort to the rather complicated set-up of Fig. 1, which effectively generates its own signal seed. However, the Raman converter itself is very simple, consisting only of the DCRF. The pump-to-signal conversion takes place in a single amplification pass. Thus, we consider the device under test to be the cladding-pumped Raman fiber, with signal and pump beams launched into its left end in Fig. 1. Alternatively, the set-up can be viewed as a synchronously pumped pulsed Raman laser.

The DCRF had a pure silica outer cladding and germanosilicate inner cladding and core. The inner cladding had a diameter of 21.6 μm and an NA of 0.22 with respect to the outer cladding. The core had a diameter of 9 μm and an NA of 0.14 with respect to the inner cladding (estimated cut-off wavelength 1630 nm). The core loss was 3.1 dB/km and the inner cladding was 2.3 dB/km, both at 1550 nm. We used different fiber lengths of around 1 km. Since Raman gain is essentially instantaneous and since the pump pulse is much shorter than the DCRF, the pump pulse creates Raman gain that travels with it through the fiber. This makes the Raman gain essentially uni-directional, and the signal at the output end of the DCRF will also be pulsed, temporally coincident with the pump pulse.

At its output end, the DCRF is spliced to a fused fiber coupler fabricated with standard single-mode fiber (NA 0.12, core diameter 8 μm). The splice loss between standard single-mode fiber (SSMF) and the DCRF is ~0.5 dB for the signal traveling in the core mode. By contrast, since the cladding in the SSMF does not guide light, essentially all pump light is lost here. The coupler had a nearly flat wavelength response, and coupled out 25% of the incident power at ~1680 nm. This monitor coupler was then spliced to another, wavelength-selective, coupler. It had a low transmission loss (~2 dB) at the first stokes wavelength (~1680 nm) but a high loss at the second stokes wavelength as well as at the pump wavelength. Thus, it suppressed higher-order stokes generation. The couplers were followed by a variable optical attenuator that allowed us to change the cavity loss. Finally, there was ~10 km of SSMF (loss at 1690 nm 5 dB). A high-reflecting mirror was butted to the fiber in the far end with an estimated reflection loss of 2 dB. The long SSMF delayed the signal feedback to match the low repetition rate of the pump.

The signal pulse is reflected back through the cavity all the way to the pump launch end of the DCRF. There, 4% is reflected again from the perpendicularly cleaved fiber end. At the same time, a new pump pulse is launched into the DCRF. The reflected signal light acts as a seed for the conversion in the cladding-pumped Raman fiber amplifier. Because the mode-selection that occurs in the SSMF and the low mode-coupling at splice and reflection points, the reflected signal is almost exclusively coupled to the core mode. The roundtrip cavity loss was ~55 dB. The roundtrip time was 115.27 μs. The Q-switched fiber laser was carefully adjusted to this for synchronous pumping. We varied the effective length of the DCRF without changing cavity length by moving a section of it from the location shown in Fig. 1 to a position between the VOA and the 10 km SSMF, where the DCRF is un-pumped.

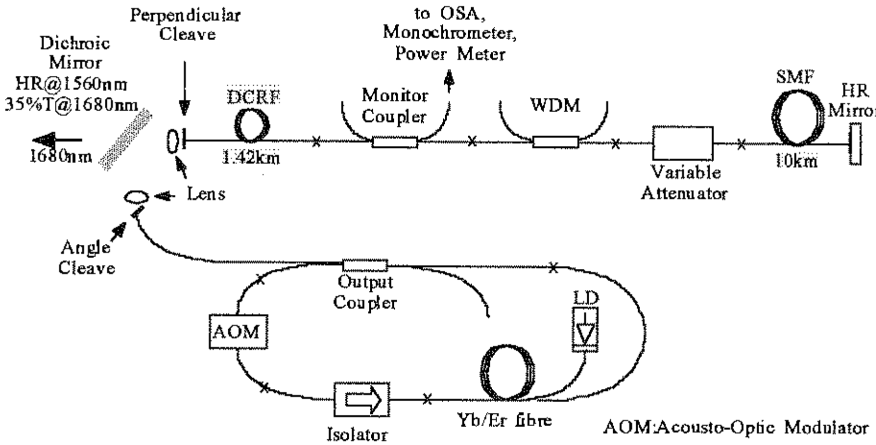

Fig. 1: Experimental set-up.

Results: Figure 2 shows the DCRF gain vs. pump power for 1420 and 940 m long DCRFs. The gain was determined by varying the total cavity loss via the VOA, and adjusting the pump power until threshold for lasing was reached. The gain slopes are 1.5 dB/mW and 1.0 dB/mW, respectively, or 2.8 dB/W and 1.9 dB/W with respect to peak power. The effective lengths become 1000 m and 740 m. These numbers are in good agreement with theory, given the uncertainty in evolution of polarization and modal power distribution, and that the high Ge-content increases the Raman cross-section.

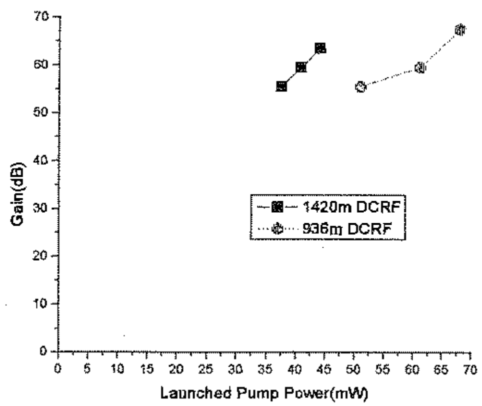

Fig. 2: Gain vs. pump power.

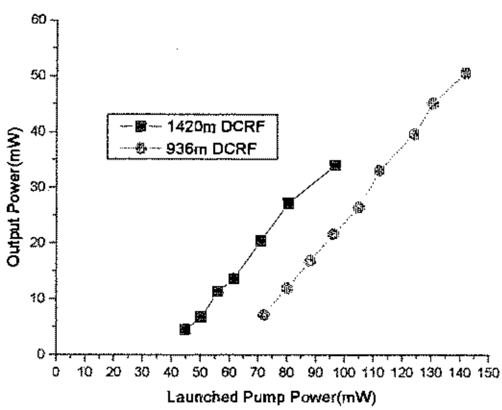

Fig. 3: Output power vs. pump power.

Figure 3 shows the output power from the DCRF vs. pump power for 1420 and 940 m long DCRFs, with the VOA at its minimum loss value. The output power was evaluated by measuring the power exiting the coupler monitor port and recalculating it to the power coming out from the DCRF. The thresholds are 37 mW and 61 mW, and the slope efficiencies are 60% and 64% for the longer and shorter fiber, respectively. For both fiber lengths, the power in the core at the output end becomes significantly higher than in the input end: The highest pump power launched into the core was 10 – 20 mW. This demonstrates brightness enhancement via Raman amplification of a signal in the core with a pump beam substantially launched into the inner cladding.

At high pump power, higher-order Raman generation can occur. In Fig 3, we restricted the pump power to values for which this was negligible. Thus, since higher-order generation occurs more readily in longer fibers, the maximum pump power (and ouptut power) is lower for 1420 m than for 940 m fiber length. Figure 4 shows the output spectrum for a fiber length of 940 m and a pump power of 140 mW. Unfortunately, the spectrum analyzer was limited to wavelengths up to 1750 nm, whereas the second stokes occurred at ~1810 nm. However, we also used a monochromator to resolve higher-order stokes radiation and for temporal measurements. Figure 5 shows output pulse shapes at the wavelengths of the pump and first and second stokes beams, measured with the monochromator and a germanium detector. The second stokes signal is much weaker than the first stokes signal.

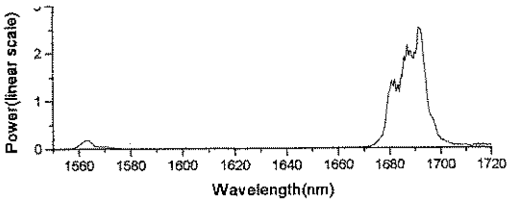

Fig. 4: Output spectrum after 940 m of DCRF.

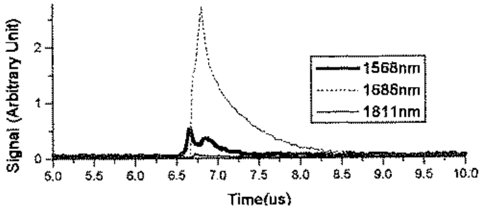

Fig. 5: Output pulse shapes

Discussion: Despite the low Raman gain efficiency, it is relatively straightforward to reach high gain with pulsed pump sources. Even cw pump lasers (fiber and non-fiber ones) of sufficiently high powers are becoming increasingly available. In a laser configuration, the cavity losses can be sufficiently low for thresholds of a few watts, given a gain efficiency of the order of 1 dB/W. Still, cladding-pumped Raman fibers require inner-cladding diameters of a few tens of microns rather than hundreds of microns as is common with rare-earth doped cladding-pumped fibers. This limits the scope for brightness enhancement and the high pump intensities required presently preclude direct diode pumping. On the other hand, there are several advantages of Raman devices over rare-earth ones. Besides the flexibility in wavlength, the low loss of germanosilicate fibers allows the use of much longer devices, so that the heating per unit length can be small. The small quantum defect of Raman scattering in silica further simplifies thermal management.

The length of the Raman fiber converter is important. A longer fiber leads to a higher gain efficiency in the small-signal regime, making it easier to reach threshold with a longer fiber. However, for higher powers, secondary Raman scattering occurs, this too with lower threshold for longer fibers. To avoid this, the pump power used with a given fiber length must be limited. A shorter fiber has a higher limit. In Fig. 3, for pump powers up to 100 mW, the 1420 m fiber is better than the 940 m one. For higher pump powers, second-order Raman scattering occurs in the 1420 m fiber. One can then reach higher output powers with 940 m of fiber than with 1420 m, with appropriate pump power. (Though a wavelength-suppressing filter could be used to suppress higher-order Raman scattering, this may be difficult in practice.) Raman scattering in the cladding should also be avoided. Since the core and cladding compositions are quite similar, and since the pump intensity is essentially similar in the core and inner cladding, the Raman gain will be similar in the core and inner cladding. If a single-moded output is required, one must then seed the core-mode (or provide mode-selective feedback in a laser)

Conclusions: In conclusion, we report for the first time results on amplification in a cladding-pumped Raman fiber. We used a Q-witched Er-Yb co-doped fiber laser operating at 1565 – 1570 nm as a pump source. The power conversion efficiency was up to 36%, with a slope of 64%. We believe that cladding-pumped fiber devices present a very exciting alternative for amplification and brightness conversion at high powers.

1. R. R. Rice, "Multimode Raman fiber amplifier and method", US patent no. 6,353,087 (2002)
2. K.-I. Ueda, H. Sekiguchi, and H. Kan, "1 kW cw output from fiber embedded lasers", in Proc. Conference on Lasers and Electro-Optics, Long Beach, USA, 2002, post-deadline paper CPDC4
3. B. C. Rodgers, T. H. Russell, and W. B. Rob, "Laser beam combining and cleanup by stimulated Brillouin scattering in a multimode optical fiber", Opt. Lett. **24**, 1124-1126 (1999)
4. A Piskarskas, V Smilgevicius, A Stabinis, "Optical parametric oscillation excited by an incoherent conical beam", Opt Comm **143**, 72-74 (1997)

An 8-channel fibre-DFB laser WDM-transmitter pumped with a single 1.2W Yb-fibre laser operated at 977nm

L. B. Fu (1), R. Selvas (1), M. Ibsen (1,2), J. K. Sahu (1), S.-U. Alam (2), J. Nilsson (1,2), D. J. Richardson (1,2), D.N. Payne (1,2), C. Codemard (2), S. Goncharov (3), I. Zalevsky (3) and A.B. Grudinin (2)
1: ORC – University of Southampton, Southampton SO17 1BJ, UK, lbf@orc.soton.ac.uk
2: Southampton Photonics Ltd., Southampton SO16 4NS, UK, anatoly.grudinin@southamptonphotonics.com
3: Milon Laser, Russia.

***Abstract** A 50GHz fibre-DFB laser transmitter source is demonstrated pumped by a CW fibre laser source at 977nm. Up to 9dBm of power is achieved per fibre DFB-laser with maintenance of all key operational parameters.*

Introduction

Fibre DFB-lasers have been demonstrated as a promising alternative source in WDM-transmission on a number of occasions [1,2,3]. It has previously been demonstrated how they can be designed to meet most requirements in dense WDM transmission, due to their many inherently attractive performance parameters. Powers in excess of 20mW with low insertion-loss, single polarisation operation with a keyed axis output [4] for easy connectivity to external polarisation sensitive components and very low relative intensity noise (RIN) at telecommunication transmission frequencies to mention just a few key points, are adding to their very attractive features. If a drawback indeed has existed it has been the requirement to operate the lasers with expensive semiconductor pump-diodes that typically have had the additional requirement to be Bragg grating stabilised to provide a constant pump-wavelength.

A number of WDM-DFB fibre laser configurations supported by a single pump-unit have been demonstrated in the past, these include a serial configuration where 5 DFB lasers were simultaneously pumped at 1480nm [2], and a superstructure approach where a DFB laser had its refractive index profile modulated with a superstructure function to produce 2 identical power channels with a separation determined by the superstructure period [3]. In this paper we demonstrate for the first time the pumping of fibre DFB-lasers with another fibre-laser source in a parallel configuration where 8 fibre DFB-lasers on an ITU-grid are simultaneously pumped by a single high-power (1.2W) fibre-laser operating at 977nm. Each laser produces ~9dBm of output power with a 50GHz frequency separation and we compare the performance of the DFB-fibre lasers when pumped by either a semiconductor LD or the 977nm fibre-laser source.

Experimental setup and transmitter lay-out

Fig. 1 shows the lay-out of our WDM-transmitter. A 977nm pump-signal of up to 1.2W of optical power from a cladding-pumped (@915nm) cw Yb-fibre laser coupled and split into 8 equal outputs through 7, 3dB 980nm couplers. The coupling-loss to the splitter is measured to be ~1.8dB due to a slight modal mismatch between the fibre-laser and the 980nm coupler-fibre. Furthermore the excess-loss in the splitter is measured to be 1dB giving a total of 11.8dB insertion-loss per channel from the pump-source. When operated at 1.2W this gives a total of ~70mW of pump-light at each output port of the splitting-tree.

8 asymmetric π phase-shifted fibre DFB-lasers [3] of length 5 cm and separated in frequency by 50GHz are written into a highly doped Er/Yb fibre with a photosensitive annular ring to the core [5]. The lasers are operated in a forward pumping configuration to eliminate the need for a pump/signal WDM and exhibit an forward output power-ratio of ~50:1. An isolator is employed at the output side of the lasers to prevent back-reflections that otherwise could cause the output to become unstable. They are written using our continuous grating writing technique operated with 244nm CW UV-light and a phase-mask assembly [3].

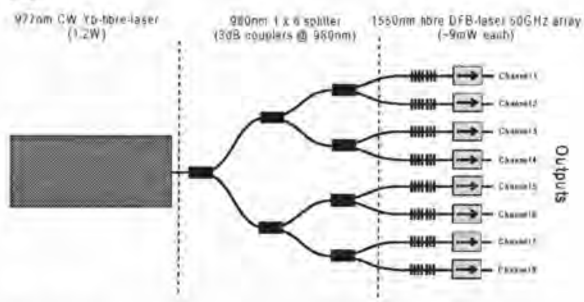

Fig. 1. Experimental set-up of the WDM-transmitter.

Experimental results and discussion

When operating the pump-fibre laser at maximum output the output comb of the array is shown in Fig.2a, this shows the 8 channels separated by 50GHz and demonstrates that an average power of 8-9mW per channel has been achieved when a total of ~800mW of power is incident in the 1x8 splitter. The slope efficiencies of the individual lasers are shown in Fig. 2b demonstrating that >10% slope-efficiency have been obtained for all the channels. When left "free-running" in time to monitor the power stability of the lasers less than 0.5dB variation was observed.

To investigate whether any performance penalties exist when operating the fibre DFB-lasers with a 977nm fibre-laser pump compared with a more traditional

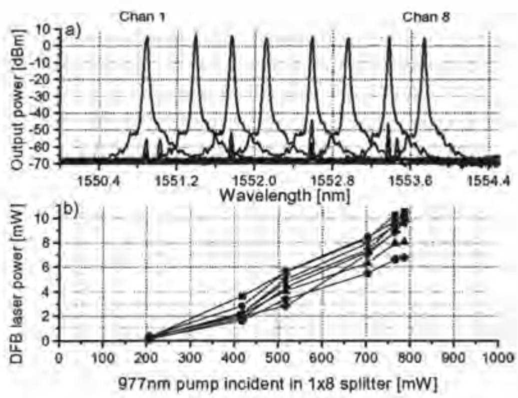

Fig. 2 Output characteristics of the fibre DFB-laser array a) channel wavelengths b) individual channel powers against total 977nm pump in the splitter.

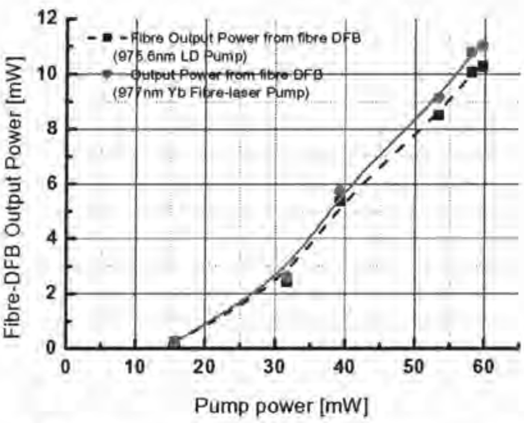

Fig. 3. Output powers against pump-power of the fibre DFB-laser when pumped by the semiconductor LD (square) and fibre-laser (circle).

semi-conductor laser-diode (LD), two comparing tests are set up. The first one is to measure the slope efficiency when pumped by either source. The most power efficient fibre DFB-laser is chosen for this exercise being channel no.5. The result of this is demonstrated in Fig. 3 and it shows that the output power performances are virtually identical in both configurations demonstrating that the power efficiencies are similar with no associated penalty. The second comparing test is related to the stability of output of the fibre DFB-laser. In this case the line-width of the fibre DFB is measured when operated in the two pump-configurations. Again the most efficient laser in terms of power is chosen for this. A delayed self-heterodyne technique is used with a resolution of 4.8kHz and a frequency-shift of 35MHz provided by an acousto-optic modulator is used. The line-width of the fibre DFB-laser when pumped with the LD is from a Lorenzian line fitting found to be ~29.3kHz where as its line-width has broadened to ~75.3kHz, additionally found from fitting a Lorenzian shape to the RF-power spectrum, when pumped with the fibre-laser (Fig. 4). This broadening we believe is due to the slightly broader pump-spectrum of the fibre-laser compared the LD together with a slight variation to the output power of this laser. Although this is quite a dramatic increase of the line-width it is not seen as an actual performance degradating factor in any way.

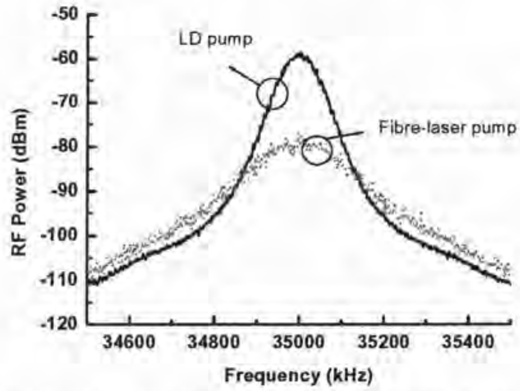

Fig. 4. Line-widths of fibre-DFB laser channel no.5 when pumped by either pump-source.

Conclusions

We have demonstrated how a recently developed 977nm high-power CW fibre-laser can provide a reliable and cheap pump-source alternative for an array-comb of 8 fibre-DFB lasers. We test the performance of the DFB-lasers when pumped with the fibre-laser source against a more standard laser diode pump-source and show that although there are some degradation to the line-width of the lasers they are by no means detrimental to their application as transmitter-sources in WDM transmission systems. We believe that this demonstration shows that an important parameter in employing fibre-DFB-lasers as transmitter sources in telecommunication-systems, namely the cost of the LD pump-sources, have been brought under control, mainly because the 977nm fibre-laser demonstrated here uses a relatively low-cost broad-stripe laser diode source at 915nm as its pump.

References

1 J.T. Kringlebotn et al., *Optics Lett.*, **19**, (1994), pp. 2101-2103.
2 J. Hübner et al., *Electron. Lett.*, **33**, (1997), pp. 139-140.
3 M. Ibsen et al., *Electron. Lett.*, **36**, (2000), pp. 143-144.
4 L.B. Fu et al., *OFC'02*, paper WJ5, 2002.
5 L. Dong et al., *Optics Lett.*, **22**, pp. 694-696, 1997.

2003

Cladding pumping technology for next generation fiber amplifiers and lasers

Kalle Yla-Jarkko, Shaif-ul Alam, Paul W. Turner, John Moore, Southampton Photonics Inc., Southampton, United Kingdom; Johan Nilsson, Romeo Selvas, Daniel B. Soh, Christophe Codemard, Jianto K. Sahu, Optoelectronics Research Centre, University of Southampton, Southampton, United Kingdom.

Abstract: We discuss recent advances in cladding-pumped fiber technology considering various applications of GTWave fiber amplifiers and 977 nm ytterbium-doped fiber devices based on jacketed-air clad fibers.

1. Introduction

Since the introduction of rare-earth doped double-clad fibers over a decade ago [1], cladding-pumping technology has broadened the application area of fiber lasers and fiber amplifiers. Output powers of hundreds of watts can be achieved from diode pumped single-mode fiber devices making fiber lasers serious contenders for lamp- and diode-pumped Nd:Glass lasers in material processing industry [2],[3]. In this paper we review recent developments of high power cladding pumped lasers and amplifiers based on both Er:Yb and Yb-doped fibers. We pay particular attention to the emerging cladding-pumping technology based on jacketed-air clad ytterbium-doped fibers operating in the region of 977 nm.

2. High Power Single Frequency MOPA

In a number of applications, such as spectroscopy and frequency doubling, a narrow linewidth and low relative intensity noise (RIN) performance is desired. For these purposes an all-fiber tandem comprising DFB fiber laser and a power-amplifier (so called MOPA configuration) looks to be the most viable solution. Major limiting factor of the all-fiber solution is stimulated Brillouin scattering (SBS). However, the detrimental effect of the SBS can be suppressed by choosing the gain medium of the power amplifier so that the SBS threshold is increased. This can be achieved by shortening the length of the amplifying media and/or by adjusting the diameter of the doped core. In our experiments the power amplifier was based on GTWave fiber.

A GTWave fiber assembly typically consists of one doped and two or more pump fibers, which are in optical contact and share a common external lower index coating. Thus pump light being launched into pump fiber propagates freely through all fibers in the assembly [4]. Depending on the application, the outer diameters of the signal and pump fibers can vary greatly whereas the core size is typically fixed for the 1.55 μm wavelength region by the requirement of single-moded output.

Most suitable medium for high power fiber lasers in the 1.55 μm region is double-clad Er:Yb co-doped fibers where Yb-ions absorb pump light and then non-radiatively transfer energy to Er-ions [5]. In the MOPA for power range from 1 W to 10 W, we use a DFB fiber laser with output power of 10 mW and a GTWave fiber assembly containing two pump fibers and one Er:Yb co-doped signal fiber (core diameter 8 μm, NA=0.12). The outer diameter of the fibers is 80 μm. The impact of SBS is minimized by having a high absorption coefficient of the doped core (~200 dB/m @915 nm) allowing the use of only 10 m long gain medium. An output power in excess of 5 W was achieved for a launched pump power of 25 W without any noticeable SBS. The power amplifier was pumped by two 915 nm multimode pump modules capable of delivering up to 15 W of optical power in 0.22 NA, 100 μm diameter, pump fiber. As shown in Fig. 1(a) fiber laser has a slope efficiency of about 30%. Inset of the figure illustrates the variation of SBS threshold as a function of SMF length added at the output of MOPA. This shows that by keeping the output pigtail of the fiber laser short, output powers in excess of 10 W can be achieved by scaling up the pump power. Further improvement can be achieved by shortening the length of the amplifying gain medium with 977 nm pumping or by increasing the diameter of the doped core.

Another application of cladding-pumping technology is low cost L-band (1570-1610 nm) amplifiers pumped by single 980 nm multimode diode. For this type of applications GTWave assembly can f. ex. consist of a pump fiber with 60 μm outer diameter and a pure Er-doped fiber with core diameter of 10 μm (NA 0.1). Depending on the output power requirements the number of pump fibers and pump modules can be increased. With one 977 nm pump module pigtailed to a fiber with a 50 µm core and capable of delivering up to 1.5 W of optical power, a L-band EDFA with a saturated output power of 21 dBm can be realized (see Fig. 1(b)). Amplifier exhibits 30 dB gain with gain flatness of ±1 dB over 1570-1607 nm spectral band and simultaneous noise reduction and transient suppression of the amplifier can be achieved by using a gain clamping seed signal (λ=1564 nm).

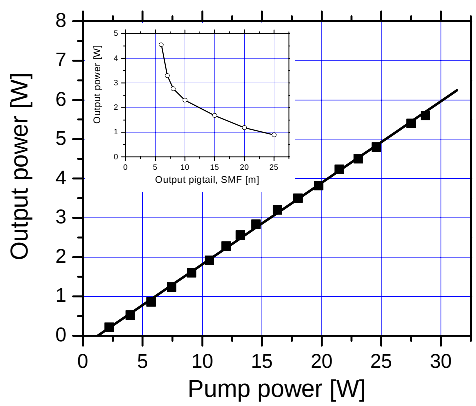

(a)

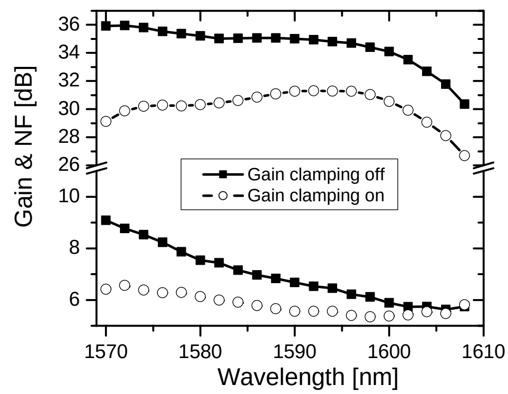

(b)

Fig 1. (a) Output power of the MOPA as a function of launched pump power. Inset shows the variation of SBS threshold as a function of SMF length added at the output of MOPA. (b) Gain and noise figure of the cladding-pumped EDFA as the gain-clamping laser is turned on/off. Input signal power is –20 dBm and the clamping power is –3 dBm.

3. Jacketed-air clad ytterbium-doped fibers

Recent advances in development of high power high brightness laser diodes and mature silica fiber fabrication technology [6], [7] have opened up new application areas for cladding pumping technology. One of the most spectacular examples of advanced cladding pumped devices is a 977 nm Yb-doped fiber laser based on jacketed air-clad fibers, see Fig. 2(a) The fiber consists of doped core, pump cladding and low index secondary cladding formed by a thin glass mesh with a wall thickness comparable to the wavelength. By introducing silica-air outer cladding in double-clad fibers the NA of the inner-cladding can be increased enabling the decrease of the inner-cladding diameter without sacrificing the efficiency of the pump coupling. This increases the overlap between the pump and signal fields and hence the output power from the diode-pumped fiber lasers can be raised without boosting the pump power [8].

There are two major difficulties in developing an efficient single-mode, cladding-pumped 980 nm ytterbium-doped fiber source: high threshold intensity of the two-level 980 nm transition and undesired lasing at 1030-1040 nm due to quasi-four level energy transition and weak re-absorption. These difficulties can be overcome by using high brightness pump source and fiber geometry with low inner-cladding-to-core ratio to reduce the lasing threshold. For a practical single-moded device having a threshold below 500 mW the inner-cladding diameter should be between 20-30 µm. At the same time the NA of the inner-cladding needs to be increased considerably compared to the NA of the conventional double-clad fiber (NA=0.35…0.47). In order to realize a high inner-cladding NA, we use a jacketed air-clad (JAC) geometry, which is based on robust reproducible conventional silica fiber technology [9]. With this technology an inner-cladding NA higher than 0.7 can be achieved.

Figure 2(a) shows a cross section of the Yb-doped JAC fiber, where the multimode inner cladding is formed from a thin mesh of silica glass. This resulted in very low pump leakage and hence high numerical aperture of the inner cladding. The core is single-moded with a cut-off of 950 nm (core diameter=9 µm, NA=0.1). The pump absorption at 915 nm is 6 dB/m. In order to suppress unwanted gain at 1040 nm we have utilized ring-doping of Yb-ions.

By using JAC fiber and a high brightness pump source a high power 977 nm Yb-doped fiber source can be achieved from simple ASE source or fiber laser using broadband feedback from a mirror or wavelength-selective narrowband reflectors such as fiber Bragg gratings. The output power from a fiber laser is shown in Fig. 2(b). The fiber laser has an output power of 3.5 W and slope efficiency of 65%. In this case the JAC fiber had a 10 µm, 0.1

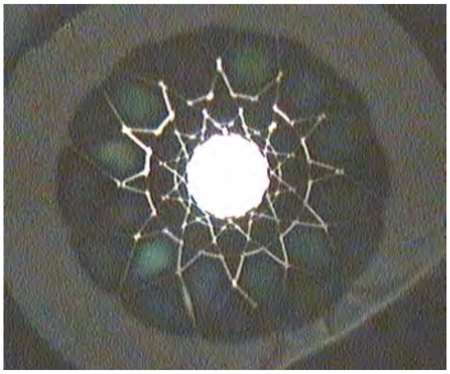

(a)

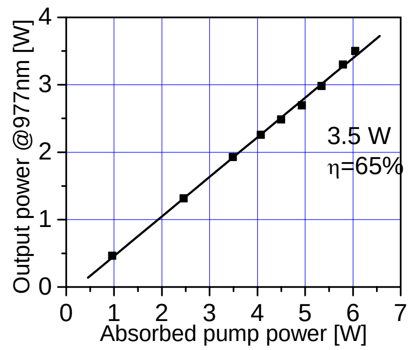

(b)

Fig. 2. (a) Cross-section of jacketed air-clad fiber. Inner cladding diameter 20 μm, NA 0.7. (b) Output power and slope efficiency of the JAC fiber laser as a function of absorbed pump power. Threshold and slope efficiency for the fiber laser are 260 mW and 65%.

NA core centered in a 28 μm diameter inner cladding with a high NA of up to 0.5 [10]. The benefits of the laser configuration compared to the ASE-source are that the output is less sensitive to back-reflection and the achievable output power is higher. The drawback of the laser is more complicated structure, as an external feedback is required to produce emission at 977 nm. For a practical device the reflectivity of the fiber Bragg grating needs to be ~10% with a FWHM of 0.2 nm [11].

4. Conclusions

We have reviewed the recent progress of cladding-pumped fiber lasers based on GTWave fiber assembly and Yb-doped-jacketed air-clad fiber. By using high brightness multi-emitter diode pumping and with suitable tailoring of GTWave fiber the output power from single frequency source can exceed 50 W. Mature fiber technology and high brightness pump sources have also promoted development of cost-effective high performance double-clad optical amplifiers and fiber lasers in the wavelength regions previously dominated by core-pumped devices (L-band amplifier) and semiconductor diodes (970-980 nm).

5. References

[1] H. Po, E. Snitzer, L. Tumminelli. F. Hakimi, N. M. Chu, and T. Haw, in Optical Fiber Communications Conf., Houston, TX, 1989, paper PD-7.

[2] J. Nilsson, J. K. Sahu, W. A. Clarkson, R. Selvas, A. B. Grudinn, S. Alam, “High-power fiber lasers: new developments,” in Photonics West Conf. San Jose, CA, 2003, paper 4974-11.

[3] . Limpert, A. Liem, T. Schreiber, H. Zellmer, A. Tuennermann, Friedrich Schiller, “Power and energy scaling of fiber laser systems based on ytterbium-doped large-mode-area fibers,” in Photonics West Conf. San Jose, CA, 2003, paper 4974-22.

[4] C. Codemard, K. Yla-Jarkko, J. Singleton, P.W. Turner, I. Godfrey, S.-U. Alam, J. Nilsson, J. Sahu and A. B. Grudinin, “Low noise, intelligent cladding pumped L-band EDFA”, in ECOC'02, Copenhagen, 8-12 Sept. 2002. PD 1.7., 2002.

[5] P. K. Cheo, and G. G. King, “Clad-pumped Yb:Er codoped fiber lasers,” IEEE Photonics Technol. Lett., vol 13, no. 3, pp. 188-190, 2001.

[6] J. C. Knight, T. A. Birks, P. St. J. Russel, and D. M. Atkin, “All-silica single-mode optical fiber with photonic crystal cladding”, Opt. Lett., vol. 21, no. 19, pp. 1547-1549, 1996.

[7] T. M. Monro, D. J. Richardson, and N. G. Broderick, “Efficient modeling of holey fibers, “in *Optical Fiber Communication Conf.*, San Diego, CA, Feb. 21-26, 1999, paper FG1.

[8] V. A. Kozlov, J. Hernandez-Cordero, R. L. Shubochkin, A. L. G. Carter, and T. F. Morse, “Silica-air double-clad optical fiber”, IEEE Photonics Technol. Lett., vol 12, no. 8, pp. 1007, 2000.

[9] J. K. Sahu, C. C. Renaud, K. Furusawa, R. Selvas, J. A. Alvarez-Chavez, D. J. Richardson, and J. Nilsson, “Jacketed air-clad cladding-pumped ytterbium doped fibre laser with a wide tuning range”, Electron. Lett. 37, 116-1117, 2001.

[10] K. H. Ylä-Jarkko, R. Selvas, D. B. S. Soh, J. K. Sahu, C. A. Codemard, J. Nilsson, S. A. Alam, and A. B. Grudinin, “A 3.5 W 977 nm cladding-pumped jacketed-air clad ytterbium-doped fiber laser”, in ASSP’03), San-Antonio, Texas, 2-5 Feb. 2003, PDP2.

[11] R. Selvas, K. Ylä-Jarkko, S.-U. Alam, J. Nilsson, P.W. Turner, J. Moore, J.K. Sahu, A.B. Grudinin, “High Power 977 nm Fibre Sources Based on Jacketed Air-Clad Fibres,” in *Optical Fiber communication conference 2003 (OFC’2003)*, Atlanta, 23-28 March, 2003, paper TuL4, 2003.

High Power Fiber Lasers: New Developments

Johan Nilsson [a, b, c], Jayanta K. Sahu [a, c], Yoonchan Jeong [a], W. Andy Clarkson [a], Romeo Selvas [a], Anatoly B. Grudinin, and Shaif-Ul Alam [c]

[a] Optoelectronics Research Centre, University of Southampton, Southampton SO17 1BJ, England
[b] Phone +44 23 8059 3101, Fax +44 23 8059 3142, Email jn@orc.soton.ac.uk
[c] Southampton Photonics, Inc., 3 Wellington Park, Hedge End, Southampton SO30 2QU, England

ABSTRACT

We assess different power limits of cladding-pumped fiber lasers. Despite recent advances in pump sources, these are still primarily limited by available pump power. We find that it should be possible to reach output powers beyond 1 kW in single-mode ytterbium doped fiber lasers. Experimentally, we have realized an ytterbium-doped fiber laser with 272 W of output power at 1080 nm, with an M^2-value of 3.2, as well as an erbium-ytterbium co-doped fiber laser with 103 W of output power at 1565 nm, with an M^2-value of 2.0. We believe these are the highest-power ytterbium and erbium-ytterbium fiber lasers ever reported.

Keywords: Fiber laser, power-scaling, diode-pumping, wavelength-tuning

1. INTRODUCTION

Cladding-pumped fiber technology has revolutionized fiber lasers over the last decade, increasing output power from less than 1 W with traditional core-pumping to well over 100 W [1], [2], [3]. Even 1 kW of power has been reached in multi-mode designs [4], when several devices have been arranged in series or in parallel. For output powers below 100 W, a few diode bars or multi-emitter laser diode assemblies are adequate pump sources. However, for powers beyond the 100 W level, diode stacks seem to be a better choice. The increasing availability of suitable diode stacks and the possibility of efficient fiber launch make them very attractive for pumping of high-power fiber lasers. At the same time, while fibers proved very reliable at powers up to ~100 W, it is clear that further power-scaling to the kW level with diode stack pumping requires significant fiber optimization in terms of fiber composition, pump coupling, and/or overall device layout. This is especially true when a single-mode output is required.

We will present recent work on high-power fiber lasers and amplifiers at University of Southampton and Southampton Photonics. We will cover work in the 1 and 1.5 μm spectral regimes with ytterbium-doped and erbium-ytterbium co-doped fibers, as well as power scaling via stack-pumping to several hundred watts of output power. We will also discuss relative advantages of fiber lasers compared to traditional bulk lasers, and highlight strengths of cladding-pumped fiber devices in areas such as broadband amplification, wavelength tuning, and operation at wavelengths where fiber lasers perform particularly well. We will also discuss narrow-linewidth devices, since nonlinear degradation arising from nonlinear effects such as stimulated Brillouin scattering is seen as a weakness of high-power, cladding-pumped, fiber sources.

2. THE CASE FOR HIGH-POWER CLADDING-PUMPED FIBERS AND STACK-PUMPING

Rare-earth (RE) doped fiber lasers were demonstrated as early as the 1960s [5], [6], [7]. Nevertheless, for many years they remained relatively obscure with performance far inferior to that offered by their “bulk” (i.e., non-waveguiding) counterparts like Nd:YAG lasers and gas lasers such as argon ion lasers. While bulk lasers can be lamp pumped or pumped by electrical discharges, it is essential to use laser sources for pumping of rare-earth doped fibers. However, at the time, laser pump sources were generally large, costly, and inefficient, and rare earth doped fiber devices offered no compelling benefits that outweighed the disadvantages of laser pumping. This changed in the mid 1980s, with the realization of rare-earth doped single-mode high silica fibers with low loss [8], [9], [10]. A single-mode core ensures robust single-mode operation, which is necessary for many applications. Furthermore, the tight beam confinement of a single-mode fiber leads to low laser thresholds, even though glass hosts (normally used for fibers) intrinsically have higher laser thresholds than crystal hosts (normally used for bulk lasers). RE-doped single-mode fibers constitute a glass gain medium with which low-threshold lasers, and high gain amplifiers (with a high gain efficiency) can be realized relatively easily. The transitions in glass are spectrally much broader than they are in crystals, which is important for broadband amplification, tunable lasers, and for short pulses. Crucially, high gain can be reached even in three-level systems with pump powers as low as a few milliwatts. A low propagation loss is important since it allows for devices many meters long, and thus for fibers doped sufficiently lightly for concentration quenching to be avoided.

These advantages of rare-earth doped fibers enabled the erbium-doped fiber amplifier (EDFA) [11], which can be used in optical communication systems. The EDFA has been a most compelling reason for the further development of rare earth doped fiber technology as well as of single-mode laser diodes at 980 and 1480 nm, for use as compact, low cost, and efficient laser pump sources.

While it is easy to reach, say, 40 dB of gain in an EDFA, bulk devices are not appropriate for high-gain broad-band amplifiers. Especially in case of a rare-earth doped glass amplifier, their large beam size leads to a low gain efficiency, and the short length essentially rules out a high gain. For example, in an erbium-doped glass it is difficult to reach more than 1 dB gain per centimeter. A crystalline amplifier is more efficient and allows for higher gain, but with a narrow bandwidth. In addition, in a bulk amplifier a large number of modes would see the high gain, leading to large amounts of undesired amplified spontaneous emission and making it difficult to ensure single-mode operation.

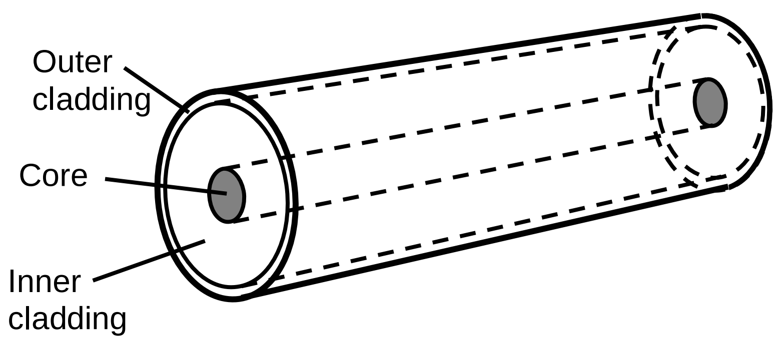

Figure 1. Schematic drawing of double-clad fiber.

The considerations for high-power devices are partly quite different from those for high gain and low power devices such as the EDFA. The very low threshold and high gain efficiency possible with a single-mode core are important features for low-power devices, but less important at higher powers. On the contrary, a small single-mode core is a serious obstacle to power-scaling of fiber lasers. Initially, fiber lasers as well as EDFAs were simple structures with a single core for guiding both the signal and the pump light, implying that single-mode pump diodes must be used. The limited power of single-mode diode pump sources has then limited the output powers to ~1 W. Consequently, cladding-pumping has been developed as a method to overcome this limitation [12]. Cladding-pumped fiber lasers do not require single-mode pump sources, but can still produce a single-moded laser output. In this case, a fiber that guides light in the inner cladding, typically a so-called double-clad fiber (DCF), must be used. See Fig. 1. A DCF has a primary waveguide (the core) for guiding the signal, surrounded by a lower-index inner cladding. Both of these are made from glass. The inner cladding also forms the core for a secondary waveguide that guides the pump light. The inner cladding is surrounded by an outer cladding of lower refractive index polymer or glass to facilitate waveguiding. In either case, the fiber may have a further layer of polymer for protection. Typically, the fiber is rare-earth doped throughout the core, while the inner cladding is undoped. The core is located within the inner cladding and forms a part of the pump waveguide, so pump light propagating in the pump waveguide reaches the core and excites the laser-active rare-earth ions. Since the gain medium is still a rare-earth doped glass, the gain remains spectrally broad, allowing for broadband amplification and wavelength tuning.

With a sufficiently thick inner cladding, it is at least in principle possible to launch arbitrarily large amounts of pump power into a double-clad fiber. This would mean that the usable pump power is only limited by the power delivered by the pump sources at hand. However there are many disadvantages with a thick inner cladding, and in practice a limited inner cladding diameter will restrict the amount of pump power that can be launched. The launched pump power obviously limits the output power from the fiber laser, and is therefore of principal importance for high-power operation. Power handling and power conversion efficiency are other important factors. By contrast, the threshold is quite low for high-power fiber lasers, and therefore normally insignificant. We will next discuss these limitations, in order to estimate the power limit of a cladding-pumped fiber laser.

We start with the pump power that can be launched into a fiber. We assume here a simple end-pumped configuration. Various alternatives for side-pumping exist, with the pump light propagating either along the core or perpendicular to it. These may allow for more pump power to be launched, but only insofar as thicker or longer fiber arrangements can be used.

To reach the power limit of doped fibers will require kilowatt class pump sources. Diode stacks seem most suitable at such power level. At Southampton we have state-of-the art diode stack sources capable of delivering approximately 0.4 kW of pump power into a 0.4 mm diameter inner cladding at an NA of ~0.3. With a thicker inner cladding and a higher NA, we will be able to launch more pump power (with a higher-power pump source). Inner cladding diameters of up to 1 mm may be feasible, but fibers thicker than that rapidly become difficult to manage. With a 2.5 times thicker inner cladding, we would be able to launch roughly 2.5 kW of pump power with an appropriate pump source of similar brightness. It may be possible to increase the NA somewhat, but on the other hand, higher-power pump sources are normally less bright than lower-power ones, offsetting the benefits of a higher NA. Thus, we take 2.5 kW as the maximum pump power that currently can be launched through the end of a double-clad fiber. Note though that this power will increase as brighter pump diodes become available in the future.

Once the pump power has been launched, the fiber has to efficiently convert it into usable laser output. Neodymium and ytterbium are the most efficient fiber dopants for which high-power diode stack pump sources are available, for Nd at ~808 nm and for Yb at 910 – 980 nm. High-power Nd-doped and Yb-doped fiber lasers both emit at around 1060 nm, with relatively large variations in wavelengths depending on device configuration and host composition. Neodymium's 1060 nm transition is a four-level system, which means that the threshold can be insignificant and that low-brightness pumping can be used. This is utilized in fiber embedded lasers, in which a large pump cavity allows for simple, high-power, but relatively low-brightness pumping. Three Nd-doped fiber embedded lasers were recently combined for a total output power of over 1 kW [4]. However, because the pump cavity is quite large, the doped volume must also be large in order to absorb the pump, especially since self-quenching limits the maximum allowable concentration of neodymium. Unfortunately it is difficult to achieve single-mode operation in a long, large-diameter, core. By contrast, ytterbium is a quasi-four level system at 1060 nm, with significant reabsorption. Therefore, a high pump intensity must be used to excite a sufficient fraction of the Yb-ions. This also means that it becomes easier to absorb the pump, allowing for a smaller core, especially since Yb can be used at higher concentrations than Nd. In addition, an ytterbium-doped fiber laser (YDFL) can be more efficient than a neodymium-doped fiber laser (NDFL). Thus, YDFLs look more attractive than NDFLs, at least when a high-brightness output is needed. Diffraction-limited or nearly diffraction-limited YDFLs with well over 100 W output power have been reported [1], [3]. We regularly attain 80% power conversion efficiencies in our Yb-doped fiber lasers, suggesting that 2 kW and 4 kW of output power would be possible with 2.5 kW of pump power launched in one or both ends of the fiber.

It is far from obvious that a fiber can handle such high power without failing. While powers of over a kilowatt have been reported, this was in heavily multimode designs with large cores. A single-mode realization is much more challenging, because of the higher power densities involved and the risk for optical damage. Certainly, one should not strive for a small core, but for a large core that can still operate on a single mode. We have demonstrated previously a Q-switched YDFL with 2.3 mJ pulses with 10 kW of peak power, corresponding to a power density of 6.5 W/μm^2 (650 MW/cm^2) [13], as well as a holey fiber Raman laser with a cw power density (of the pump) of 2 W/μm^2 [14] without reaching the damage threshold. These values can be compared to the damage threshold of bulk silica of ~20 W/μm^2. Though a cw YDFL is likely to have a damage threshold lower than the pure silica and pulsed peak power values, we estimate a cw damage threshold of ~1 W/μm^2 for our rare-earth doped fibers, or possibly a few times more. Special fiber terminations such as end-caps may have to be used to reach such damage threshold [15]. Still, a drawback of the end-pumping scheme is that the optical power densities and heat generation peak at the pump launch end. Schemes that use distributed injection of the pump power into the doped fiber, and leave the ends of the doped fiber free to be terminated in a damage resistant manner, are preferable from this point of view. The GTWave fiber is an example of such a scheme [16]. We also note that recently demonstrated cladding-pumped Raman fiber lasers [17] can be fabricated with a pure silica core, likely to have a higher damage threshold than an ytterbium-doped one.

With a cw damage threshold of ~1 W/μm^2, a kW class fiber laser will require a core area of ~1000 μm^2 or more. Such a core will not be intrinsically single-moded at ytterbium wavelengths. However, there are several ways of achieving single-mode operation of a multi-mode core, e.g., with a mode-selecting taper [18] or with selective excitation of the fundamental mode. For example, stable spatial fundamental mode operation has been demonstrated in a 50 μm core fiber amplifier [19], i.e., with a core area of 2000 μm^2. Thus, though these estimates are relatively uncertain, they do suggest that a multi-kW single-mode fiber laser is viable.

Besides optical damage, heat generation can also destroy an optical fiber, via thermal damage of the coating, fracture, or even melting of the core. However YDFLs are exceptionally good in terms of thermal management for two reasons: The high efficiency means that the fraction of absorbed pump power that is converted into heat can be less than 15%. Thus, the heat generation in the fiber will be approximately 150 W per kilowatt of output power. Furthermore, the fiber geometry means that heating can be distributed over a long length, and because of the proximity of the heat-generating core to the fiber surface, heat-sinking can be quite efficient. Brown and Hoffmann have evaluated fracture limits in optical fibers to over 0.1 kW/cm of generated heat [20], which is orders of magnitude larger than the heat that will be generated in kW-class fiber lasers. Thermal damage of the coating as well as melting of the core can occur at lower power levels, but can be mitigated by a suitable heat-sinking arrangement, as well as by using long fibers with low levels of power conversion per unit length. In practice, we have operated erbium-ytterbium co-doped fiber lasers that generated approximately 100 W of heat per meter [21].

The fiber geometry is then quite good from a thermal point of view. Furthermore, the ability to maintain a tight pump confinement, given by the spot size that the pump beam can be focused to at the relatively high inner-cladding NA, means that the threshold is relatively low, typically a few watts. Thus, the elongated geometry, as well as the benefits of pump and signal waveguiding, are key advantages of cladding-pumped fiber lasers for high power operation. The high pump intensity also enables operation of systems with high ground-state absorption, such as ytterbium's two-level transition at ~980 nm [22], albeit with significantly lower output power than at the quasi-four level transition at ~1060 nm. Besides, a glass host brings advantages in terms of wide wavelength tunability and access to different wavelengths in general. For example, for high-power operation in the "eyesafe" 1550 nm wavelength regime, erbium-ytterbium co-doping is often used, but this only work well in glasses.

There is a large variety of different high-power bulk lasers, with different gain media, cavity configurations, and pumping schemes. Ytterbium-doped crystal lasers [23] (e.g., Yb:YAG) are emerging as the preferred choice for high-power bulk solid state lasers. Thermal issues are critical for these lasers, and therefore, crystals, with superior thermal properties, are favored over glass hosts. Though Yb:YAG lasers with many kilowatts of output powers have been demonstrated, the non-waveguiding nature and large thermal gradients lead to aberrated thermal lensing and, therefore, a poor beam quality at high powers. Single-mode lasers operate at significantly lower powers. Compared to fiber lasers, the efficiency of Yb:YAG lasers is lower (but still quite good). Furthermore, the absence of tight waveguiding of the pump leads to a pump beam size that is significantly larger than in a fiber laser, and the larger signal beam implies that a larger number of ions need to be excited to reach sufficient gain than with a fiber laser. This leads to high thresholds that may well exceed 100 W even in quasi-four level systems such as Yb:YAG at ~1040 nm.

Because of the high efficiency and the beneficial effects of a waveguiding core on beam quality, high-power cladding-pumped fiber lasers seem likely to surpass bulk lasers in many areas, not least those for which a glass host brings particular advantages. However, the fiber geometry does have drawbacks: The tight signal confinement restricts energy storage to, say, values of the order of 10 mJ, while some pulsed laser applications require higher pulse energy than that. Furthermore, the tight signal beam confinement, together with the long length and high powers, means that well-known fiber nonlinearities such as stimulated Raman scattering, stimulated Brillouin scattering (for narrow-linewidth beams), and self-phase modulation (for pulsed light) occur quite readily in cladding-pumped fibers. For example, at a wavelength of 1 μm with an effective spot area of 100 μm^2, we get a Raman gain of 4×10^{-3} dB/m/W, a Brillouin gain of 2 dB/m/W, and a nonlinear phase shift of 2×10^{-3} rad/m/W. Nonlinear effects in fibers are further discussed in ref. [24]. Still, exciting results on the amplification of single-frequency beams in Yb-doped fiber amplifiers have recently been published [25]. An output power of 20 W has been achieved experimentally in a nearly diffraction-limited beam, from a 9 m fiber with a 30 μm diameter core [25]. This power was limited by available pump power, while the SBS limit was estimated to ~100 W. With shorter fibers, as should be possible with higher pump absorption (e.g., with 975 nm pumping instead of the 915 nm pumping used in ref. 25), the SBS limit would be several hundred watts, ultimately limited by attainable pump absorption, thermal limits, and the core size. In the past, we fabricated fibers with similar area ratios with peak absorption at ~975 nm of 12 dB/m, resulting in device lengths of 1.5 m [21]. This was an erbium-ytterbium co-doped fiber, but can equally well be realized without erbium, for operation at ~1060 nm. Thus, we believe that with appropriate fiber design, with a large, highly doped, core for a high pump absorption, SBS thresholds will be well above 100 W.

3. RESULTS

The case for cladding-pumped high-power fiber lasers is quite strong, made even stronger by recent results, enabled by developments in fiber and diode pump technology. We will next review some of our recent high-power results with ytterbium doped fibers operating at ~1060 nm [26] and erbium-ytterbium doped fibers operating at ~1550 nm [21], [27], as well as results on tunable fiber lasers [28].

Ytterbium-doped fiber laser

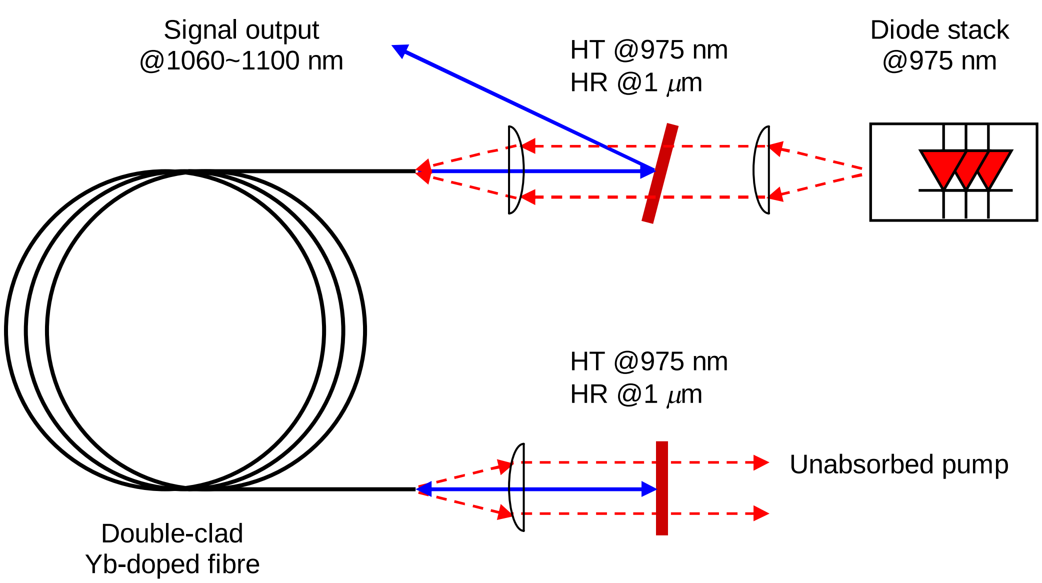

Figure 2. Yb-doped fiber laser arrangement comprising a diode-stack pump source. HR: high reflectivity, HT: high transmission.

Ytterbium-doping is attractive for high-power cladding-pumped fiber lasers because of the high efficiency and high pump absorption that are possible. Figure 2 shows our setup for high-power YDFLs. Our pump source is a beam-shaped diode-laser stack at 975 nm, coupled into the double-clad Yb-doped fiber through a combination of lenses. We set up an YDFL made with a fiber fabricated at the University of Southampton. The fiber was 5 m long and had 30 μm diameter Yb-doped core. The D-shaped inner cladding had a 375 μm diameter, and was coated with a low-refractive-index polymer outer cladding for a nominal inner-cladding NA of 0.48. The small-signal absorption at the pump wavelength was 3 – 4 dB in a 1 m long piece of fiber. The pump launch efficiency was more than 85%. A laser cavity was formed between a perpendicularly cleaved, 4% reflecting, facet in the pump launch end of the fiber and an external, high-reflecting mirror in the other end. The laser output was taken through the pump launch end. A dichroic mirror separated the output beam from the pump beam (Fig. 2).

The laser output power characteristics is shown in Fig. 3, together with an output spectrum [26]. The maximum laser output power was 272 W and the slope efficiency with respect to absorbed pump power was 85%. The laser spectrum was centered at ~1080 nm, and extended from 1070 nm to 1100 nm. The output power increased linearly with output power. There was no evidence of a power limit from nonlinear scattering or any other undesired effect. The fiber is multi-moded and no attempts were made to operate the laser on a single mode. We measured the beam quality factor (M^2) to 3.2.

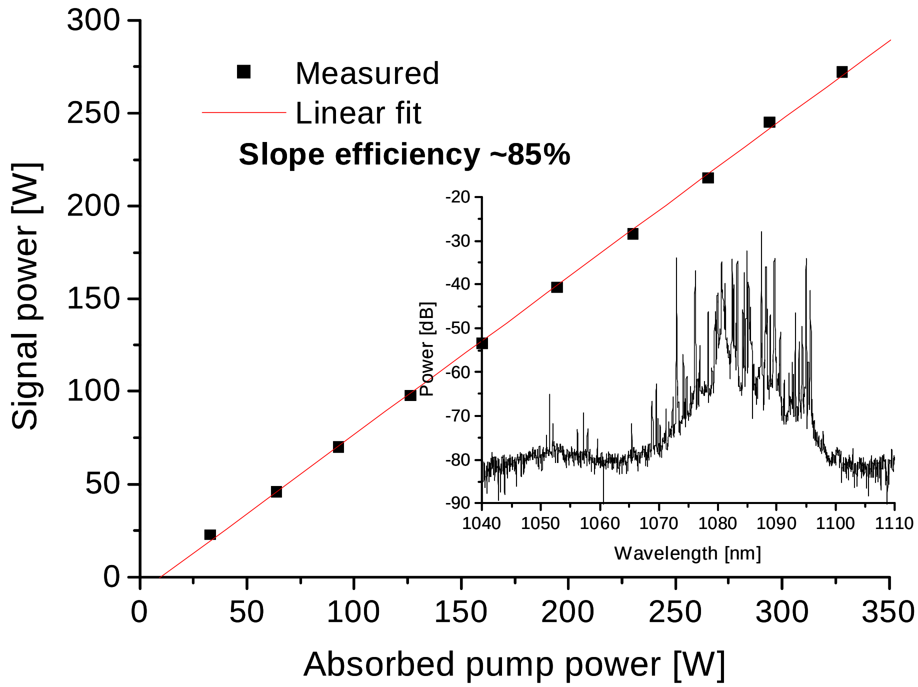

Figure 3. Output power characteristics of ytterbium-doped fiber laser. Inset: laser output spectrum.

Erbium-ytterbium co-doped fiber laser

The attraction of erbium-ytterbium co-doped fibers is their unsurpassed performance in the important, “eye-safe”, 1550 nm wavelength region. In an erbium-ytterbium co-doped fiber, pump photons are initially absorbed by Yb-ions. Then, the energy is transferred nonradiatively from excited Yb-ions to Er-ions, resulting in de-excitation of the Yb-ions and excitation of the Er-ions. Ytterbium has a larger absorption cross-section than erbium, as well as a much broader absorption band, from 910 to 980 nm. Furthermore, Yb can be incorporated in much higher concentrations than Er, thanks to its relative immunity to self-quenching. In total, this means that a fully adequate pump absorption of several dB/m can be reached, even in fibers with a large inner cladding-to-core area ratio.

We set up an erbium-ytterbium co-doped fiber laser (EYDFL), very similar to the YDFL in Fig. 2, based on a fiber fabricated in house. The fiber was 5 m long and had 25 μm diameter erbium-ytterbium co-doped core. The D-shaped inner cladding had a 400 μm diameter, and was coated with a low-refractive-index polymer outer cladding for a nominal inner-cladding NA of 0.48. We were able to launch up to 340 W of pump power into the fiber, of which 295 W was absorbed. Thus, the operating pump absorption was ~87% or 9 dB. Also for the EYDFL, a laser cavity was formed between a perpendicularly cleaved, 4% reflecting, facet in the pump launch end of the fiber and an external, high-reflecting mirror in the other end. The laser output was taken through the pump launch end, and a dichroic mirror separated the output beam from the pump beam.

The laser output power characteristics is shown in Fig. 4, together with an output spectrum [27]. The maximum laser output power was 103 W at 1565 nm, with an M^2-value of 2.0. The slope efficiency was ~40% for low powers, with respect to launched pump power, and close to 50% with respect to absorbed pump power. There is a roll-off at higher powers, caused by ytterbium-lasing at ~1060 nm, as the ytterbium-excitation increases at high pump levels. We estimate the heat generation to over 100 W/m near the pump launch end at maximum pump power.

We believe that the parasitic ytterbium-lasing can be suppressed, for an increased slope efficiency at ~1560 nm. In Fig. 4, the threshold for ytterbium lasing is approximately 70 W, at which point the 1565 nm power is ~25 W. However, we have operated EYDFLs that are similar except for having thinner core and inner cladding, at higher power densities without seeing parasitic Yb-lasing. A 4 m long fiber with a 12 μm diameter core and a 125 μm diameter inner cladding generated 17 W of output power at 1560 nm with a pump power of 44 W at 915 nm, without any Yb co-lasing, and without any roll-off of the 1560 nm power [21]. If these values are scaled to a larger core size, they suggest that 1560 nm output powers of 70 W should be possible with a 25 μm core without any Yb co-lasing or roll-off.

Our results underline the impressive power capacity of erbium-ytterbium co-doped fibers, and of doped fibers in general. Though the efficiency and output power are much lower than with an YDFL, there are few, if any, high-power lasers that can compete with an EYDFL in this spectral regime.

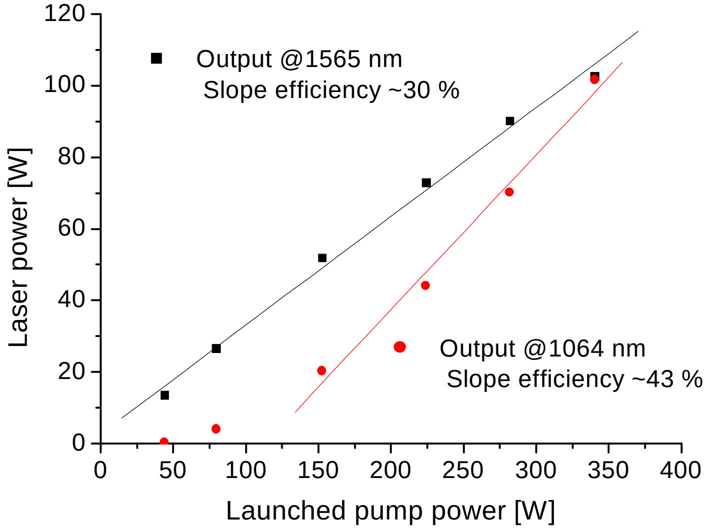

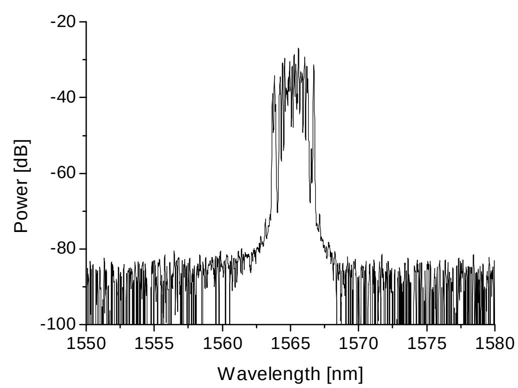

Figure 4. Output power characteristics of erbium-ytterbium co-doped fiber laser at ~1565 as well as ~1064 nm. Right: laser output spectrum at ~1565 nm.

Tunable fiber lasers

Wavelength-tunable rare-earth doped fiber lasers are attractive because of the high efficiency of rare-earth doped gain media and the broad emission linewidths in glass hosts. We have studied wavelength-tunable fiber lasers for several years. Figure 5 summarizes our results [28]. Though these investigations were performed with lower-power pumping, we expect that the benefits of new higher-power pump sources and improved fibers will have full impact on the performance of tunable fiber lasers, resulting in higher pump powers and also extended tuning ranges.

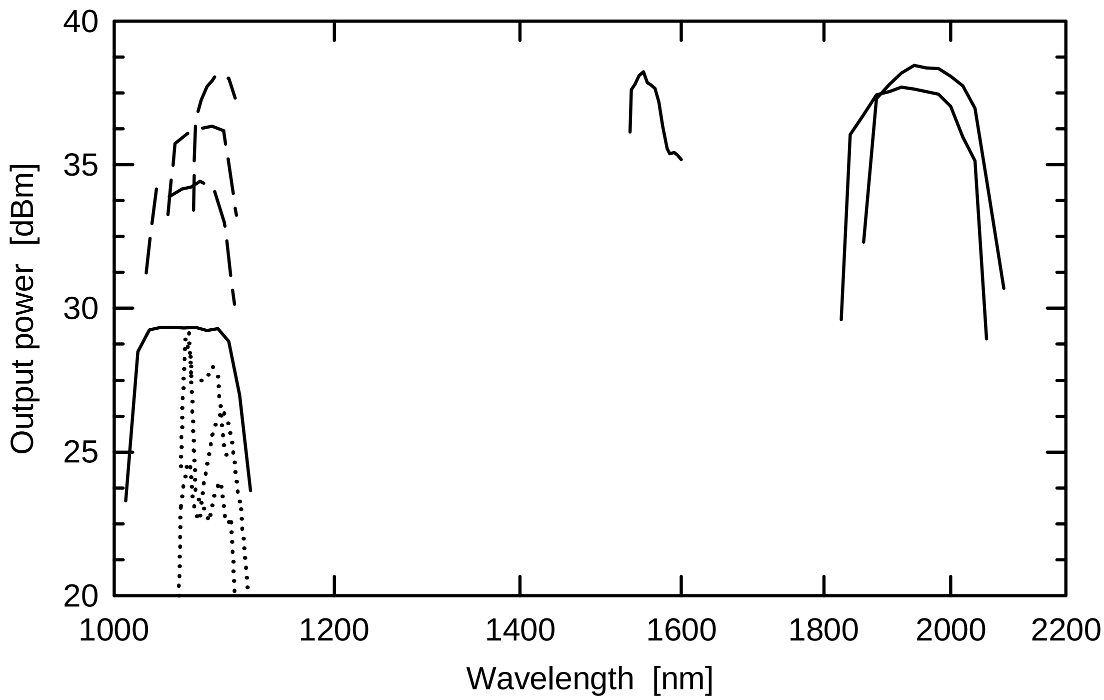

Figure 5. Tuning ranges of different cladding-pumped fiber lasers (logarithmic wavelength scale). The curves at ~2 μm are for a Tm-doped fiber of two different lengths, and the curve at ~1550 nm is for a Er-Yb co-doped fiber. At ~1 μm, the three dashed curves on top are for three different lengths of a Yb-doped fiber, the solid curve is for a Yb-doped fiber with a small inner cladding area, and the three dotted curves are for three different Nd-doped fibers.

4. CONCLUSIONS

We have analyzed the power-limit of end-pumped fiber lasers and estimate that it should be possible to reach output powers beyond 1 kW in single-mode ytterbium doped fiber lasers. Though nonlinear degradation may be a problem for some applications, the thermal properties of fibers and short fiber lengths possible with high concentration, large core, and high-brightness pumping suggest that the limits are quite high and have not been reached yet in general.

Experimentally, we have realized an ytterbium-doped fiber laser with 272 W of output power at 1080 nm, with an M^2-value of 3.2, as well as an erbium-ytterbium co-doped fiber laser with 103 W of output power at 1565 nm, with an M^2-value of 2.0. We believe these are the highest-power ytterbium and erbium-ytterbium fiber lasers ever reported. Ytterbium-doped fiber lasers are most efficient of all rare-earth doped fiber lasers, and erbium-ytterbium co-doped fiber lasers are the most efficient type of high-power laser of any kind operating in the in the “eye-safe” wavelength region at around 1550 nm.

Despite the rapid improvements of the output power of high-power fiber lasers, evidenced by these and other results, it is still limited by the available pump power. Single-mode fiber lasers with 1 kW of output power are not fundamentally beyond the fiber technology of today, and with appropriate fiber designs such lasers will be realized as soon as appropriate pump sources become available. We expect the rapid improvements to continue, and spread to more refined fiber lasers such as single-polarization, narrow-linewidth, wavelength-tunable, and pulsed sources. We believe that fiber lasers are leading candidates for various high-power applications, and will be chosen over bulk lasers, not least when the broad linewidths of glass hosts are advantageous.

5. ACKNOWLEDGEMENTS

This work is supported in part by DARPA under Contract MDA72-02-C-0049.

6. REFERENCES

1. V. Dominic, S. MacCormack, R. Waarts, S. Sanders, S. Bicknese, R. Dohle, E. Wolak, P. S. Yeh, and E. Zucker, “110 W fiber laser”, in Proc. Conference on Lasers and Electro-Optics, Baltimore, MD, USA 1999, post-deadline paper CPD26

2. J. Limpert, A. Liem, S. Höfer, H. Zellmer, and A. Tünnermann, “150 W Nd/Yb codoped fiber laser at 1.1 μm”, in OSA Trends in Optics and Photonics (TOPS) vol. 73, Conference on Lasers and Electro-Optics, OSA Technical Digest (Optical Society of America, Washington, DC, 2002), pp. 590 - 591.

3. N. S. Platonov, D. V. Gapontsev, V. P. Gapontsev, and V. Shumilin, “135 W cw fiber laser with perfect single mode output”, in Proc. Conference on Lasers and Electro-Optics, Long Beach, USA, 2002, post-deadline paper CPDC3

4. K.-I. Ueda, H. Sekiguchi, and H. Kan, “1 kW cw output from fiber embedded lasers”, in Proc. Conference on Lasers and Electro-Optics, Long Beach, USA, 2002, post-deadline paper CPDC4

5. E. Snitzer, “Optical maser action of Nd^{+3} in a barium crown glass”, Phys. Rev. Lett. **7**, 444 – 446 (1961)

6. E. Snitzer, “Neodymium glass laser”, in Proc. 3rd Int. Conf. Quantum Electronics, Paris, France, 1963, pp. 999-1019.

7. C. J. Koester and E. Snitzer, “Amplification in a fiber laser”, Appl. Opt. **3**, 1182-1186 (1964)

8. S. B. Poole, D. N. Payne, and M. E. Fermann, “Fabrication of low loss optical fibres containing rare-earth ions”, Electron. Lett. **21**, 737-738 (1985)

9. R. J. Mears, L. Reekie, S. B. Poole, and D. N. Payne, “Neodymium-doped silica single-mode fibre laser”, Electron. Lett. **21**, 738-740 (1985)

10. R. J. Mears, L. Reekie, S. B. Poole, and D. N. Payne, “Low-threshold tunable CW and Q-switched fibre laser operating at 1.55 μm”, Electron. Lett. **22**, 159-160 (1986)

11. R. .J. .Mears, L. Reekie, I. M. Jauncey, and D. N. Payne, “Low-noise erbium-doped fibre amplifier operating at 1.54 μm”, Electron. Lett. **23**, 1026-1028 (1987)

12. E. Snitzer, H. Po, F. Hakimi, R. Tumminelli, and B. C. McCollum, “Double-clad, offset core Nd fiber laser”, in *Proc. Opt. Fiber Sensors*, New Orleans, post-deadline paper PD5 (1988)

13. J. A. Alvarez-Chavez, H. L. Offerhaus, J. Nilsson, P. W. Turner, W. A. Clarkson, and D. J. Richardson, “High energy, high power ytterbium-doped Q-switched fiber laser”, Opt. Lett. **25**, 37-39 (2000)

14. J. Nilsson, R. Selvas, W. Belardi, J. H. Lee, Z. Yusoff, T. M. Monro, D. J. Richardson, K. D. Park, P. H. Kim, and N. Park “Holey fiber Raman laser”, in OSA Trends in Optics and Photonics (TOPS) Vol. 70, Optical Fiber Communication Conference, Technical Digest (Optical Society of America, Washington DC, 2002), pp. 315 – 317

15. C. C. Renaud, J. A. Alvarez-Chavez, J. K. Sahu, J. Nilsson, D. J. Richardson, and W. A. Clarkson, “7.7 mJ pulses from a large core Yb-doped cladding-pumped Q-switched fibre laser”, in Conference on Lasers and Electro-Optics (CLEO 2001) Technical Digest, (Optical Society of America, Washington, DC 2001), p. 219.

16. S. U. Alam, J. Nilsson, P. W. Turner, M. Ibsen, A. B. Grudinin, and A. Chin, “Low cost multi-port reconfigurable erbium doped cladding pumped fiber amplifier”, European Conference on Optical Communication 2000, München, Germany, paper 5.4.3.

17. J. Nilsson, J. K. Sahu, J. N. Jang, R. Selvas, D. C. Hanna, and A. B. Grudinin, “Cladding-pumped Raman amplifier”, in Proc. Topical Meeting on Optical Amplifiers and Their Applications, post-deadline paper PDP2, Vancouver, Canada, Jul. 14 – 17, 2002

18. J. A. Alvarez-Chavez, A. B. Grudinin, J. Nilsson, P. W. Turner, and W. A. Clarkson, “Mode selection in high power cladding pumped fibre lasers with tapered section”, in Conference on Lasers and Electro-Optics, OSA Technical Digest (Optical Society of America, Washington, DC 1999), pp. 247-248.

19. A. Galvanauskas, Z. Sartania, and M. Bischoff, “Millijoule femtosecond fiber CPA system”, in *Advanced Solid State Lasers*, Vol. 50 of OSA Trends in Optics and Photonics Series (Optical Society of America, Washington, D.C., 2001), postdeadline paper PD3.

20. D. C. Brown and H. J. Hoffmann, “Thermal, stress, and thermo-optic effects in high average power double-clad silica fiber lasers”, IEEE J. Quantum Electron. **37**, 207-217 (2001)
21. J. Nilsson, S. U. Alam, J. A. Alvarez-Chavez, P. W. Turner, W. A. Clarkson, and A. B. Grudinin, “High-power and tunable operation of erbium-ytterbium co-doped cladding-pumped fiber laser”, submitted.
22. L. A. Zenteno, J. D. Minelly, A. Liu, J. G. Ellison, S. G. Crigler, D. T. Walton, D. V. Kuksenkov, and M. J. Deineka, “1 W single-transverse-mode Yb-doped double-clad fiber laser at 978 nm”, Electron. Lett. **37**, 819-820 (2001)
23. W. F. Krupke, “Ytterbium solid-state lasers — the first decade”, IEEE J. Select. Topics Quantum Electron. **6**, 1287-1296 (2000)
24. G. P. Agrawal, *Nonlinear Fiber Optics*, 2nd Ed., San Diego, CA: Academic Press, Inc., 1995.
25. S. Höfer, A. Liem, J. Limpert, H. Zellmer, A. Tünnermann, S. Unger, S. Jetschke, H.-R. Müller, and I. Freitag, “Single-frequency master-oscillator fiber power amplifier system emitting 20 W of power”, Opt. Lett. **26**, 1326 - 1328 (2001)
26. Y. Jeong, J. K. Sahu, R. B. Williams, D. J. Richardson. K. Furusawa, J. Nilsson, “Ytterbium-doped large-core fibre laser with 272 W of output power”, submitted
27. J. K. Sahu, Y. Jeong, D. J. Richardson, and J. Nilsson., “A 103 W erbium/ytterbium co-doped large-core fiber laser”, submittted
28. J. Nilsson, W. A. Clarkson, and A. B. Grudinin, “High-power wavelength-tunable cladding-pumped rare-earth-doped silica fiber lasers”, accepted for publication in Opt. Fiber Technol.

ational wavelength of the laser can be set with high precision using our tuning-package. The laser also remained lasing in single mode operation across the large tuning range with side-mode extinction ratio >55dB.

The relative intensity noise (RIN) is also characterized @ 1553.45nm and 1535.5nm under the same pumping-conditions as described above. These results are summarised in Fig.4. The RIN floors at about -150 dB/Hz (>10MHz), which is only slightly higher than our normal fibre DFB noise level (typically less than -155dB/Hz >10MHz). This is believed to be due mainly to the beam material in which the DFB is mounted, due to its non-optimal heat conduction. By changing this to a more appropriate heat conducting material, we believe the noise level to reach the levels normally achieved from these lasers. The achieved level is suitable for most applications requiring a low-noise source.

4. Conclusion

We have analysed the performance of a single polarised all-fibre DFB laser when this is tuned over ~25nm using compression tuning. Single-mode and single polarisation operation is maintained over the entire tuning range as is the narrow line-width and low RIN characteristics.

5. References

[1] Mason, B., Barton, J., Fish, G.A., Coldren, L.A., Denbaars, S.P. ,"Design of sampled grating DBR lasers with integrated semiconductor optical amplifiers", IEEE Photonics Technology Letters, Vol.12,No.7, July 2000

[2] Jin Hong, Hyung Kim, and Toshi Makino, "Enhanced wavelength tuning range in two-section complex-coupled DFB lasers by alternating gain and loss coupling", Journal of Lightwave Technology , Vol. 16, No. 7, July 1998,1323-1328

[3] Timothy Day, "External-cavity tunable diode lasers for network deployment", paper TuJ4,OFC2001,

[4] D. Vakhshoori, P.D.Wang, M.Azimi, K.J.Knopp, M.Jiang, "MEMs-tunable vertical-cavity surface-emitting lasers", TuJ1, OFC2001

[5] G.A.Ball and W.W.Morey, "Continuously tunable single-mode erbium fiber laser ", Optical Letters.,Vol.17,No.6,pp.420-422,March15,1992

[6] G.A.Ball and W.W.Morey, "Compression-tuned single-frequency Bragg grating fiber laser", Vol.19,No.23,pp.1979-1981, Optics Letters, 1994

[7] M.Ibsen,S.Y.Set ,C.S.Goh, and K.Kikuchi, " Broad-band continuously tunable all-fiber DFB lasers",
IEEE Photonics Technology Letters, Vol.14, No.1, p21-23, Jan., 2002

[8] X.Z.Lin, Y.Zhang, H.L.An and H.D. Liu , "Electrically tunable single mode fibre Bragg reflective filter", Electronics Letters, May 1994, Vol.30, No.11, May, 1994

[9] A. Iocco, H.G. Limberger, R.P.Salathe, L.A.Everall, K.E.Chisholm, J.A.R.Williams, and I. Bennion,"Bragg grating fast tunable filter for wavelength division multiplexing", IEEE Journal Lightwave Technology,Vol.17, No.7, pp.1217-1221,July 1999

[10] C.S. Goh, M.R.Mokhtar, S.A.Butler, S.Y.Set, K.Kichuchi and M. Ibsen, "Over 70 nm wideband tuning of fiber Bragg gratings using a comprehensive bending technique", OECC'2002, postdeadline paper, Yokohama, Japan,2002

[11] M.Ibsen, E.Ronnekleiv, G.J.Cowle, M.O.Berendt, O.Hadeler, M.N.Zervas, R.I.Laming, "Robust high power (>20mW) all-fibre DFB lasers with unidirectional and truly single polarisation outputs ", CLEO '99 Baltimore 23-28 May 1999, paper CWE4.

[12] L.B. Fu, M.Ibsen, P.W. Turner, D.J.Richardson and D.N.Payne, "Single-polarization all-fiber DFB laser with keyed-axis output", paper WJ5,pp.248-249, Anaheim, OFC2002.

TuL4 **5:15 PM**

High Power 977 nm Fibre Sources Based on Jacketed Air-Clad Fibres

R. Selvas, J. Nilsson, J. Sahu, *Optoelectronics Research Centre, Southampton, United Kingdom;* K. Yla-Jarkko, S. Alam, J. Nilsson, P. Turner, J. Moore, J. Sahu, A. Grudinin, *Southampton Photonics Inc, Southampton, United Kingdom, Email: kalle.yla-jarkko@southamptonphotonics.com.*

Cladding-pumped single-mode Yb-doped fibre laser and ASE sources with over 1 W of output power at 977 nm are described. Their low RIN, high power, and high efficiency are attractive for a variety of applications.

1. Introduction

Cladding pumped Yb-doped fibre lasers operating at ~977 nm have been the subject of significant technical and experimental activity in recent years [1-4]. Despite obvious attractions of such sources – as pumps for EDFAs and as stand-alone lasers operating at the shortest wavelength available from cladding-pumped silica fibre lasers – there were no reports on practical, user-friendly, realizations. The principal requirement for practical implementations of high power 977 nm fibre lasers is to reach high enough population inversions, since otherwise emission occurs on the quasi-four level transition around 1040 nm, with large reabsorption at the two-level 977 nm transition. Additionally, Yb-doped fibre lasers are known as being notoriously noisy, with poor relative intensity noise (RIN) characteristics that significantly narrow their range of applications.

Here, we present detailed performance data on high-power cladding-pumped Yb-doped fibre laser and ASE sources at ~ 977 nm, made possible by recent advances in high power multimode pump diodes and fibre technology.

2. Fibre laser and ASE source

Cladding-pumping with high-power multimode diode pump sources is the preferred way to power-scale fibre lasers. In cladding-pumped devices the overlap of the pump field with the gain medium is small and therefore a large amount of dopant is required to absorb the pump. However before the pumping creates enough gain at 977 nm in a Yb-doped such laser, undesired gain at longer wavelengths (typically ~1040 nm) with weak re-absorption becomes so high that spurious oscillations cannot be suppressed. This unwanted gain restricts fibre length and thus pump absorption, resulting in low slope efficiency. To achieve lasing at 977 nm one has to ensure that the gain at 1040 nm is lower than the threshold for spurious lasing and that the pump intensity, and thus power, is high enough to invert more than 50% of the Yb-ions. Both pump threshold power and gain at ~1040 nm are proportional to the inner cladding area and for a practical device with, say, a threshold below 400 mW and a pump absorption of 6 dB, the inner cladding diameter should be below 25 μm [1]. For efficient pump launch into such a small inner cladding its numerical aperture should be as high as possible.

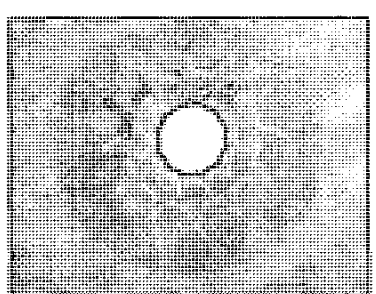

Fig.1. Cross section of jacketed air-clad fibre. Inner cladding diameter 20 μm, NA 0.7.

In our device we have chosen a jacketed air-clad (JAC) geometry, since it offers not only pump NA as high as 0.7 but also the robustness and reproducibility of conventional silica fibre technology [2]. Figure 1 shows a cross section of the Yb-doped JAC fibre, with white light launched into the inner cladding and emerging through the imaged end. The multimode inner cladding is supported by a thin glass mesh with a wall thickness comparable to the wavelength. This resulted in very low pump leakage and hence high numerical aperture. The core is single-moded with a cut-off of 950 nm. In order to suppress unwanted gain at 1040 nm we have utilized ring-doping of Yb ions [3]. The pump absorption is 6 dB/m.

The emission cross-section spectrum of Yb ions in silica glass has a relatively narrow (~ 4 nm wide) peak centred around 977 nm. Thus, high-power emission is possible at this wavelength both from a laser with either broadband feedback from a mirror or wavelength-selective feedback from a fibre Bragg grating, as well as from an ASE source. For the ASE source, the Yb-doped JAC-fibre was spliced to another fibre with an angled output facet that suppressed feedback. This makes the output nearly uni-directional even with a simple perpendicular cleave (4% reflecting) in the pump launch end of the fibre. For the laser configuration, a fibre Bragg grating with reflectivity ~10% was spliced to the output end of the JAC-fibre, while the laser was pumped through a broadband dichroic mirror that provided feedback in the other end of the cavity. Both sources used a 915 nm diode pump.

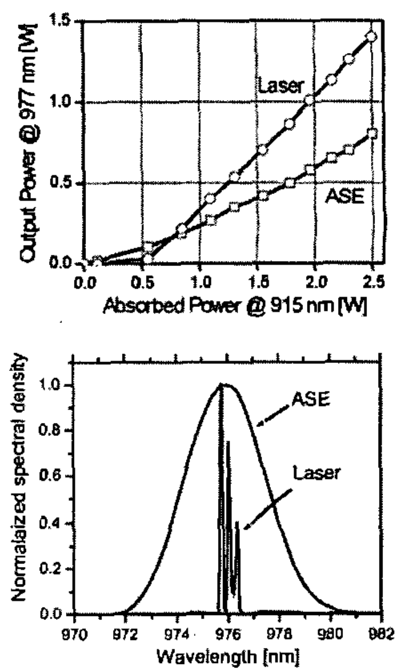

Fig. 2. Output power as a function of absorbed pump power (a) and output spectra (b) for laser and ASE source configurations

Both sources have benefits as well as some drawbacks. The structure of the ASE-source is simple as no external feedback is required to produce emission at 977 nm. Since the output is seeded by spontaneous emission, the RIN is essentially white, and the output essentially unpolarized even in the presence of weak polarizing effects. Drawbacks of the ASE-source are a lower efficiency and an inherent sensitivity to back-reflections. (Isolators for 980 nm do exist, but they are bulky, lossy, and expensive). On the contrary the fibre laser is less sensitive to back-reflections and has lower threshold and higher efficiency than the ASE-source. However, the structure is more complex and there are high RIN peaks at the relaxation oscillations frequency and at frequencies corresponding to the cavity round trip time.

The output power and slope efficiency of both sources are shown in Fig. 2, along with their output spectra. The suppression of emission at ~1040 nm is more than 20 dB for hoth sources. The spectral width of the ASE source is 3 nm and the centre wavelength is situated at 977 nm, which is practically at the peak of the 980 nm absorption band of erbium-ions in silica glass. The spectral width of the fibre laser was 0.5 nm, mainly determined by the characteristics of the reflective grating.

In some applications, such as pumping of DFB fibre lasers (DFB FLs) [5], the temporal stability of Yb-doped fibre-based pump source is as important as the wall-plug efficiency and output power. Figure 3 shows the relative intensity noise (RIN) spectrum of the 977 nm fibre laser and ASE sources.

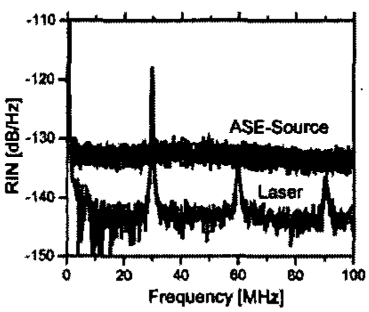

Fig.3 Relative intensity noise graphs of the fibre laser and ASE fibre source operating at~ 977 nm

The ASE-source has no cavity and hence its RIN is white, without any peaks arising, e.g., from relaxation oscillations or other cavity effects. The RIN of the ASE-source is below −130 dB/Hz and thus does not generate any extra contribution to RIN of the DFB FL as its RIN is integrated over all frequencies of the pump source. Hence, the ASE-source is an ideal pump source for DFB FLs in CATV and WDM systems. However, as the shot noise limit of the pump absorption is −153 dB/Hz the RIN below 1 kHz increases with RIN of the pump for all values above the shot noise limits. This may be a concern for some sensing applications for DFB FLs where the low-frequency range is of specific interest. As can be seen from Fig. 3 the fibre laser pump source has several RIN peaks. The relaxation oscillation peak occurs at 450 kHz at a RIN level of −100 dB/Hz. The RIN peak at 30 MHz is dependent on the cavity length and hence on the position of the grating output coupler. In our measurements the cavity length was 3.3 m. The additional peaks in the RIN spectrum are harmonics of the beat frequency of the longitudinal modes within the laser cavity. Outside the peaks the RIN of the fibre laser is very low and limited only by the sensitivity of the measurement device (~ −145 dB/Hz). Thus by optimising the device length of the fibre laser, it should be a suitable pump source for DFB FLs in both analogue CATV and digital WDM systems.

In addition to the flat RIN characteristics, the unpolarized output of the ASE source is also advantageous for pumping EDFA as it results to extremely low PDG [6].

3. Summary

We have presented data on high-power 977 nm fibre laser and ASE sources based on an Yb-doped jacketed air-clad fibre. With 2.5 W of absorbed pump power the laser source was capable of delivering up to 1.4 W of output power. To our knowledge, this is the bighest output power obtained from a single-mode fibre-coupled source at around 980 nm. Both sources exhibit RIN below −130 dB/Hz and are suitable for pumping of DFB fibre lasers and other applications that demand low noise and/or high-power.

4. References

[1] J. D. Minelly *et al., OFC'2000, Paper PD2,* Baltimore, USA (2000).

[2] J. K Sahu, *et al. Electron. Lett.* **37**, 1116 (2001).

[3] J. Nilsson *et al.*, Opt. Lett. **23**, 355-357 (1998).

[4] A. S. Kurkov *et al., OAA Technical Digest*, OMA4-1 (2001).

[5] L.B. Fu *et al., Technical digest 28th European Conference on Optical Communication ECOC-2002*, Copenhagen, paper 08.3.5 (2002).

[6] C. Codemard *et al*, "Fast transient control in EDFA pumped by 977 nm fibre pump source," submitted to *OFC'2003.*

TuL5 **5:30 PM**

An Optical Millimeter Wave Fiber Laser

Y. Lai, W. Zhang, J. A.R.Williams, I. Bennion,
Aston University, Birmingham, United Kingdom,
Email: laiy@aston.ac.uk.

Optical millimeter wave generation is realized using dual polarization modes operation from a co-located dual Distributed Feedback fiber laser configuration. A narrow linewidth optical millimeter wave signal at 32.5GHz is demonstrated without using complex control mechanism.

1. Introduction

The generation of microwave/millimeter waves using photonic technologies for various applications such as fiber-radio wireless access networks [1] and phase array antennas [2] has been focus of much research. Among various methods currently employed, an effective and favored technique is to use optical heterodyning between two lasers whose frequencies differ by the required millimeter wave frequency. It is particularly advantageous in fiber-radio applications since it reduces base station hardware complexity and overcomes limitations in transmission imposed by fiber chromatic dispersion. Optical heterodyning also has the advantage over other generation techniques of giving higher RF power, though extremely narrow linewidth optical sources or feedback loops are generally required during operation [3]. To date, the proposed techniques for achieving this include injection locking of laser diodes [4], dual-mode semiconductor laser sources [5] as well as using the optical phase locked loop (OPLL) configuration [6]. These demonstrations have relied on laser diodes or bulk solid-state lasers and the use of external high frequency synthesizers, high power RF amplifiers and injection/feedback controls are generally necessary to produce phase locked, narrow linewidth millimeter wave signals. Distributed Feedback (DFB) fiber lasers, with their intrinsic engineering simplicity and extremely narrow optical linewidth, offers a straightforward and promising alternative to optical generation of high frequency signals. Such devices have been demonstrated [7, 8] where a higb frequency polarization mode beating (PMB) signal is achieved by manipulating tbe birefringence of the laser cavity. In this paper, we describe an alternative fiber laser configuration based on a dual, co-located phase-shifted gratings structure for generating signals at millimetre wave regime and beyond. We emphasize the simplicity and flexibility of the fabrication process and more importantly, on contrary to previous reported schemes, the range of frequencies achievable is not determined by the characteristics of the fiber but by the fiber gratings parameters only. The all-fiber configuration generates stable dual polarization output and a narrow linewidth (< 1kHz, limited by measurement setup) millimetre wave signal at 32.5GHz is demonstrated without using a complex feedback mechanism or the need for an external high frequency synthesizer.

2. Background

Optical heterodyning of two modes from the same fiber laser cavity is an effective means to generate very narrow linewidth microwave beat signal without phase locking feedback control due to the common mode suppression of phase noise. Based on a similar context, by co-locating two DFB fiber laser cavities within the same fiber, a dual mode optical source can be realized to generate a narrow linewidth beat note at any frequency depending on the wavelength spacing between the two fiber laser grating structures (phase-shifted gratings) during fabrication. Furthermore, it has been demonstrated [9] that for a dual overwritten fiber Bragg grating (FBG), the spectrum of individual grating will be independent of each other under the condition $\Delta\Lambda \times L >> \Lambda^2/\pi$ where Λ is the grating period, $\Delta\Lambda$ is the period difference and L is the grating length. Evidently there is the natural tendency for each laser cavity to lase independently in both polarization modes, producing mode competition and mode hopping. However, by incorporating a uniform FBG fabricated in high birefringence (Hi-Bi) fiber, to the co-located dual DFB fiber laser structure, a polarization-discriminating self-injection locking mechanism can be realized. This mechanism then allows dual polarization modes operation by forcing each DFB laser cavity to operate in one, but mutually orthogonal, polarization mode only.

3. Experiment

A single phase-shifted FBG was first inscribed into a 40mm long Er/Yb codoped fiber by a focused UV beam through a phase mask with period Λ_{mask} = 1069nm. The Er/Yb codoped fiber has a small signal absorption ~230dB/m at 980nm and ~25dB/m at 1535nm. The fiber was adhered firmly on its ends to a translation stage to allow a strain to be applied to the fiber. By real time monitoring the spectrum of the first grating, the fiber was strained ~0.02% so that a wavelength shift of 0.26nm, corresponding to $\Delta\Lambda$ = 0.09nm, was observed on the Optical Spectrum Analyzer (OSA). A second phase-shifted FBG was then produced under the exact same conditions. The total fabrication time of the device was < 5min and the resultant profile of the laser cavity measured using a tunable laser (resolution 1pm) is as shown in Fig. 1 (solid trace). It is evident that the spectra profile of each phase-shifted FBG in the dual overwritten structure remains independent. The wavelength spacing between the transmission peaks from each grating measured 0.26nm and birefringence-induced polarization mode splitting ($\Delta\lambda_{bire}$ ~9pm i.e. birefringence ~ 8.5x10^{-6}) can be observed for both gratings.

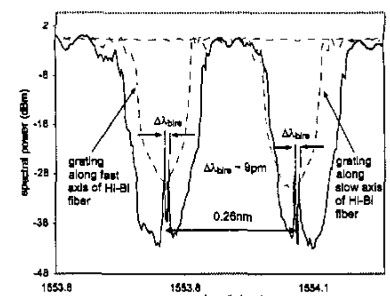

Fig. 1. Spectral profile of the co-located dual DFB fiber laser structure. Superimposed dotted traces show the spectral profiles of the Hi-Bi feedback grating along the fast and slow axes.

The experimental setup for the operation of the co-located dual DFB fiber laser is as shown in Fig. 2. A 980nm laser module was used as the pump source and isolators were used for both the pump laser and the output of the fiber laser structure. To reduce tbe effects of environmental temperature fluctuations, the fiber laser was placed in a temperature controller consisting of a Peltier device. A 15mm long Hi-Bi grating was spliced to tbe end of the fiber laser and a polarization controller (PC) was placed in the feedback path to align the polarization axes between the fiber laser and the grating. The desired Hi-Bi grating can be realized by a dual overwritten Hi-Bi uniform FBG. Each DFB fiber laser cavity will matcb to one reflection wavelength, along orthogonal axes, of the Hi-Bi grating. On the other hand, by using a

Cladding-pumped continuous-wave Raman fiber laser

J. N. Jang, Y. Jeong, J. K. Sahu, M. Ibsen, C. A. Codemard, R. Selvas, D. C. Hanna, and J. Nilsson

Optoelectronics Research Centre, University of Southampton, Southampton SO17 1BJ, England
Phone: +44 23 8059 3143, fax: +44 23 8059 3142,
email: jnj@orc.soton.ac.uk

Abstract: We report for the first time continuous-wave Raman lasing in a cladding-pumped fiber. The double-clad germanosilicate fiber was pumped by an Er/Yb co-doped fiber laser at 1545 nm. We obtained 3.4 W of output power at 1660 nm with a slope efficiency of 67%.

OCIS codes: (060.2320) Fiber optics amplifiers and oscillators, (140.3550) Lasers, Raman

Cladding-pumped Raman fiber devices have been recently proposed [1] and demonstrated in the pulsed regime [2]. Here, we believe for the first time, a cladding-pumped continuous-wave (cw) Raman fiber laser is reported.

Our experimental set-up is shown in Fig. 1. Our pump source was an Er/Yb co-doped fiber (EYDF) laser which in turn was cladding-pumped by multi-mode laser diode at 975 nm. The EYDF had a 25 μm diameter, 0.22 NA core, and a 400 μm diameter D-shaped inner cladding, surrounded by a polymer outer cladding of a low refractive index. The EYDF laser output power was up to 26 W at 1545 nm. The output was free-space coupled into a 1.42 km long double-clad Raman fiber (DCRF) via a dichroic mirror. The DCRF had a pure silica outer cladding and a germanosilicate inner cladding (diameter 21.6 μm, NA 0.22) and core (diameter 9 μm, NA 0.14, estimated cutoff wavelength 1630 nm). The inner cladding and core propagation losses at 1545 nm were 2.3 dB/km and 3.1 dB/km, respectively. Both the EYDF and the DCRF were fabricated by us.

A cutback measurement showed that we could launch up to 55% of the EYDF laser's output power into the DCRF. Of the launched power, around 6.8% was in the core mode. This was evaluated by splicing a standard single-mode fiber to a short piece of DCRF. In the DCRF, the 1545 nm pump beam generated Raman gain with a peak at ~1658 nm. The Raman laser cavity was formed by a perpendicularly cleaved, 4% reflecting, facet at the pump launch end, and a fiber grating, written directly in the DCRF, in the other end of the fiber. The reflectivity of the grating was > 99% at 1660 nm with a bandwidth less than 0.2 nm.

Figure 2 shows the launched pump power (at 1545 nm) vs. Raman laser output power. The laser threshold was 7.1 W, the slope efficiency was 67%, and the maximum output power was 3.4 W at 1660 nm for a 27% power conversion of launched pump power. Assuming a 22 dB round-trip loss, the gain coefficient becomes 0.525×10^{-13} m/W, in fair agreement with theory.

Unlike in a traditional rare-earth doped double-clad fiber, gain occurs both in the inner cladding and the core in our DCRF. Therefore, core-mode lasing must be promoted over cladding-mode lasing. In our case, the fiber Bragg grating selects the core mode. While also the inner cladding is photosensitive, and a grating is likely to have been formed in it, this grating may have a small overlap with cladding-modes and therefore a low modal reflectivity. In addition, the higher Ge-content in the core leads to higher Raman gain there. In any case, any grating in the inner cladding would reflect shorter wavelengths than that in the core (by ~10 nm or more), but lasing did occur on the wavelength of the fiber Bragg grating in the core. Figure 3 shows the output spectrum of the cladding-pumped cw Raman fiber lasers at maximum output power. Though we did not measure output beam quality, the clean spectrum is a clear signature of single-mode operation and thus brightness-enhancement in our cladding-pumped fiber laser.

Additional results will be presented at the conference.

References

1. R. R. Rice, "Multimode Raman fiber amplifier and method", US patent no. 6,353,087 (2002)
2. J. Nilsson, J. K. Sahu, J. N. Jang, R. Selvas, D. C. Hanna, and A. B. Grudinin, "Cladding-pumped Raman amplifier", in Proc. Topical Meeting on Optical Amplifiers and Their Applications, post-deadline paper PDP2, Vancouver, Canada, Jul. 14 – 17, 2002

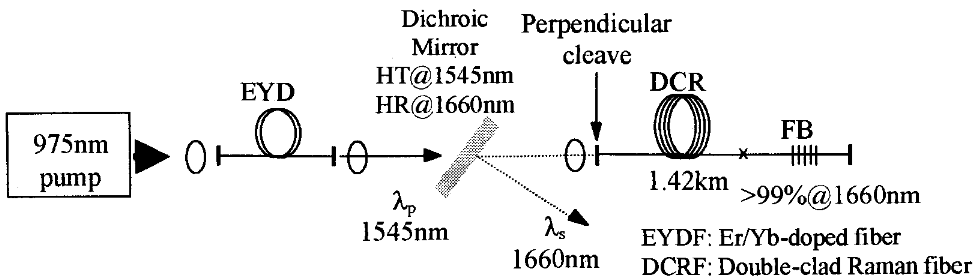

Fig. 1. Experimental set-up for cladding pumped Raman fiber laser.

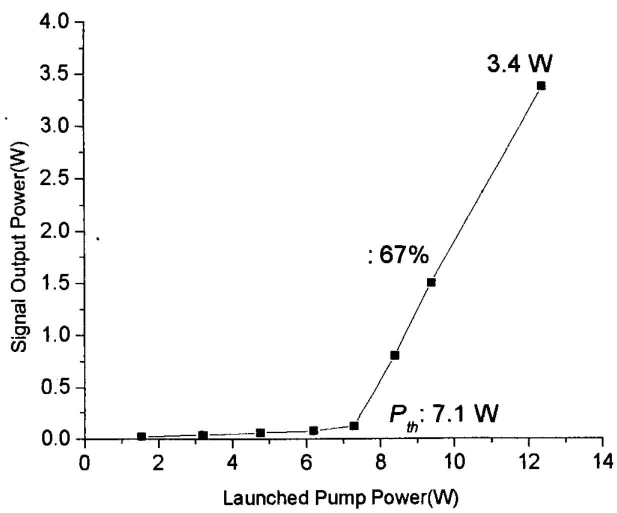

Fig. 2. Output power vs. launched pump power.

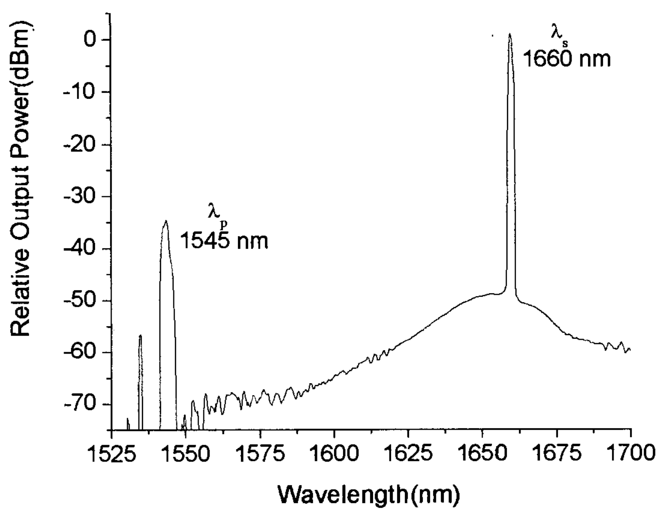

Fig. 3. Output spectrum of cladding-pumped CW Raman fiber laser at 3.4 W output power.

mounted p-side up on production aluminum nitride carriers. Chips were randomly sampled from a standard process wafer and an in-situ etched wafer. In-situ processed chips show on average a 20% decrease in threshold current from 9.3 mA to 7.6 mA at 25°C. Group means comparison of threshold current were done for 81 (standard) and 99 (in-situ) chips. The light-current characteristics of two standard chips show that the efficiency is similar using both processes: 0.23-0.24 mW/mA (Figure 2).

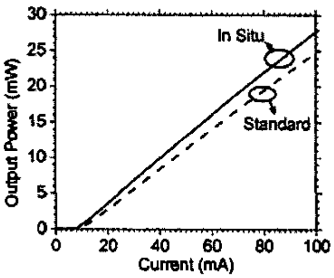

Figure 2: Light-current characteristics of BH devices.

The lasers were stressed by means of accelerated aging. All devices were aged at a constant current of 150 mA for 120 h at 100°C. Both standard (standard 1: 57 chips, standard 2: 54 chips) and in-situ etched (77 chips) devices showed a typical small increase in threshold current and decrease in efficiency in the first 12 h of burn-in. Figure 3A shows a 50-80% lower shift in threshold current for the in-situ etched devices compared with the standard devices in the group comparison. Figure 3B indicates that the standard devices show a mean change in efficiency of 1.5-2.5 times larger than the in-situ etched devices, cutting the efficiency degradation rate approximately in half. In figure 3, the center of the diamonds indicate the mean value for the chips tested and the vertical diameters of the diamonds span the 95% confidence interval for the mean value.

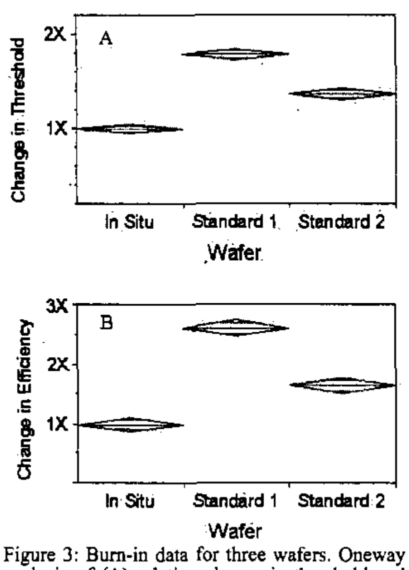

Figure 3: Burn-in data for three wafers. Oneway analysis of (A) relative change in threshold and (B) relative change in efficiency by wafer.

The in-situ etch and regrowth process is compatible with AlInGaAs materials. Figure 4 displays preliminarily results of in-situ etched mesas in AlInGaAs (12% Al, 73% In) and AlInAs (47% Al). The SEM displays mesas with smooth {111} planes with excellent surface morphology. The mesas are 7.5 μm wide at the top and 1.6 μm in height.

We have demonstrated that highly reliable buried heterostructure devices can be manufactured using in-situ etched and regrown mesas. This

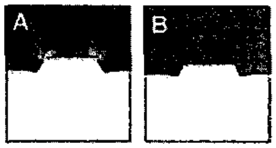

Figure 4: SEM of in-situ etched (A) AlInGaAs and (B) AlInAs mesas.

technique leads to significantly smaller degradation rates: in particular, up to 50% reduced burn-in threshold current degradation rates have been observed for in-situ processed wafers, compared with the degradation rates exhibited by standard processed devices. As well, a reduction of 20% is observed in the threshold current of the devices tested, due to reduced leakage current.

1. J. K. White, *et al.* Proc. European Conference on Optical Communication, Sept. 2002, Copenhagen, 5.3.3.
2. M. Meliga, Proc. European Conference on Optical Communication, Sept. 2002, Copenhagen, 5.3.1.
3. N. Chand, *et al*, Proc. European Conference on Optical Communication, Sept. 2002, Copenhagen, 5.3.2.
4. L. Nelson, I. Woods, and J. K. White, Proc. Optical Fiber Communication Conference, March 2002, Anaheim, ThF7.
5. S. N. G. Chu, S. Nakahara, M. E. Twigg, L. A. Koszi, E. J. Flynn, A. K. Chin, B. P. Segner, and W. D. Johnston, Jr. J. Appl. Phys. 63, 611 (1988).
6. N. Yamamoto, K. Kishi, S. Matsumoto, Y. Kadota, R. Iga, H. Okamoto, and H. Mawatari, J. Vac. Sci. Technol. B 15, 103 (1997).
7. T. Kallstenius, J. Backstrom, U. Smith, and B. Stoltz, J. Lightwave Tech. 17, 2584 (1999).
8. R. Gessner, A. Miler, J. Rieger, and E. Veuhoff, Proc. 11th International Conference on Metalorganic Vapour Phase Epitaxy, Berlin Germany, (2002), Wed-P20, p. 210.
9. T. Okuda, H. Ko, Y. Ohsawa, K. Tsuruoka, T. Terakado, K. Kurihara, A. Gomyo, T. Nakamura, and K. Kohayashi, Proc. Optical Fiher Communication Conference, Anaheim, March 2002, ThF5.
10. H. Sato, A. Taike, H. Uchiyama, T. Tsuchiya, K. Nakahara, and S. Tsuji, Proc. European Conference on Optical Communicatton, Sept. 2002, Copenhagen, 5.3.4.

FH 8:00 AM - 10:00 AM

Murphy l

High Power Effects and Fiber Nonlinearities

Raman Kashyap, *PhotoNova, Inc.,Canada, Presider*

FH1 (Invited) 8:00 AM

Beyond 1 kW with Fiber Lasers and Amplifiers

J. Nilsson, Y. Jeong, C. Alegria, R. Selvas, J. Sahu, R. Williams, K. Furusawa, W. Clarkson, D. Hanna, D. Richardson, T. Monro, D. Payne, *Univ. of Southampton, Southampton, United Kingdom;* K. Ylä-Jarkko, S. Alam, A. Grudinin, *Southampton Photonics, Inc., Southampton, United Kingdom, Email: dnp@orc.soton.ac.uk.*

We report recent progress and future prospects of high-power fiber sources in the 1 and 1.5 μm spectral ranges, with a 103 W, 1565 nm erbium-doped fiber laser as an example. Our emphasis is on diode stack pumping and short fibers with high Brillouin thresholds.

Cladding-pumped fiber technology has revolutionized fiber lasers over the last decade, increasing output power from less than 1 W with traditional core-pumping to well over 100 W from single-mode devices [1 – 3], and even over 1 kW in multi-mode designs [4]. For output powers below 100 W, a few diode bars or multi-emitter laser diode assemblies are adequate pump sources. However, for powers beyond the 100 W level, and certainly for kilowatt devices, the increasing availability and relatively low cost of suitable diode stacks and the possibility of efficient fiber launch suggests that stacks are a better choice. At the same time, while fibers have proven very reliable at powers up to ~100 W, further power-scaling to, and beyond, the kW level with diode stack pumping is likely to require radically new fiber designs in terms of materials, geometry, pump coupling arrangement, and heat-sinking. This is especially true when a single-mode, single-polarization, and/or narrow-linewidth output is required.

We will present recent results on high-power fiber lasers and amplifiers. We will cover work in the 1 and 1.5 μm spectral regimes with ytterbium-doped and erhium-ytterhium co-doped fibers, as well as power scaling via stack-pumping to several hundred watts of output power. We will discuss fundamental limits of high-power fiber sources, and the scope for devices beyond 1 kW. We are not only seeking high power but also high-brightness (preferably single mode) and narrow-linewidth output.

Short fibers have many advantages over longer fibers, including higher nonlinear thresholds, less mode-coupling (with multimode fibers), and lower total propagation losses. Another advantage is that of reduced fiber material usage. Stack-pumped fibers may require inner-cladding (in which the pump light is guided) diameters of 0.5 – 1 mm. This raises a cost issue: The diameter is almost an order of magnitude larger than the standard 125 μm diameter normally used for core-pumped fibers, so such cladding-pumped fibers consume up towards two orders of magnitude more preform per unit fiber length than core-pumped fibers. Furthermore, the large inner cladding-to-core area ratio means that the pump light propagates primarily outside the ytterbium-doped core. This reduces the pump absorption, typically by two orders of magnitude, so that longer fibers are required to absorb the pump. All told, without special measures, a high-power cladding-pumped fiber device can expend three or four orders of magnitude more preform than a core-pumped fiber device. Therefore, a reduction of the fiber device length, e.g., to below 10 m, becomes a very important cost issue.

The low pump absorption is one of two factors that set the lower limit on the fiber length. By employing high Yb-concentrations and relatively small area ratios, we regularly obtain pump absorptions of over 1 dB/m, so that fibers shorter than 10 m can be used. Heat generation is the other limiting factor. This must be low enough per unit length to prevent thermal damage of the coating, fracture, or even melting of the core. Brown and Hoffmann have evaluated fracture limits in optical fibers to over 0.1 kW/cm of generated heat [5], which is much larger than the heat that will be generated in kW-class fiber lasers. Thermal damage of the coating as well as melting of the core can occur at lower power levels, but can be mitigated by a suitable heat-sinking arrangement. We note that even with pump powers of the order of 1 kW, the heat deposition per unit length is still below 100 W/m in highly efficient Yb-doped fibers (slope efficiency > 80%) with a pump absorption of 2 dB/m.

In practice, we have recently realized an erbium-ytterbium co-doped fiber laser with a single-ended output power of 103 W at the eye-safe wavelength of 1565 nm with a slope efficiency of 40% for low powers [6]. See Fig. 1. There is a roll-off at higher powers, caused by ytterbium-lasing at ~1060 nm, as the ytterbium-excitation increases at high pump levels. We believe that this parasitic lasing can be suppressed, for an increased slope efficiency at 1565 nm. The fiber was 5 m long and generated over 100 W of heat per meter in the pump launch end. Our result highlights the impressive power capacity of erbium-ytterbium co-doped fibers, and of doped fibers in general.

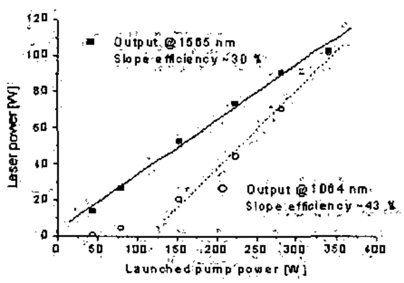

Fig. 1: Power characteristics of erbium-ytterbium co-doped fiber laser, emitting both at 1565 nm and 1064 nm.

Exciting results on the amplification of single-frequency beams in Yb-doped fiber amplifiers have recently been published [7]. High-power single-frequency amplification in cladding-pumped optical fibers is troublesome because the narrow linewidth, relatively long fibers, and tight confinement lead to a low threshold for stimulated Brillouin scattering (SBS), which is detrimental to performance. Nevertheless, 20 W of output power has been achieved experimentally in a nearly diffraction-limited beam, from a 9 m fiber with a 30 μm diameter core [7]. This power was limited by available pump power, and the authors estimated an SBS limit of ~100 W. With shorter fibers, as should be possible with higher pump absorption (e.g., with 975 nm pumping instead of the 915 nm pumping used in ref. 7), the SBS limit would be several hundred watts, ultimately limited by attainable pump absorption, thermal limits, and the core size. As long as single-mode operation can be maintained, a large core is preferable since it reduces the signal intensity for a given signal power. Thus, SBS can be avoided. Furthermore, the pump absorption increases with a larger core so that shorter fibers can be used (if thermal limits allow). Alternatively, with a larger core, a larger inner cladding can be used without compromising pump absorption, allowing larger, higher-power pump beams to be used. For example, stable spatial fundamental mode operation has been demonstrated in a 50 μm core fiber amplifier [8].

To conclude, we emphasize that despite the recent rapid increase of output power from different fiber sources, the power is still limited by available pump sources rather than by fiber properties. An optimized single-mode fiber can have an output in excess of a kilowatt with sufficient pump power. Up-to-date results on high-performing, high-power, fiber lasers and amplifiers will be presented at the conference.

References

[1] V. Dominic, S. MacCormack, R. Waarts, S. Sanders, S. Bicknese, R. Dohle, E. Wolak, P. S. Yeh, E. Zucker, "110 W fiber laser," Postdeadline paper, CPD 11, CLEO'99, Baltimore (1999).

[2] J. Limpert, A. Liem, S. Höfer, H. Zellmer, and A. Tünnermann, "150 W Nd/Yb codoped fiber laser at 1.1 μm", in *OSA Trends in Optics and Photonics (TOPS) vol. 73, Conference on Lasers and Electro-Optics*, OSA Technical Digest (Optical Society of America, Washington, DC, 2002), pp. 590 – 591.

[3] N. S. Platonov, D. V. Gapontsev, V. P. Gapontsev, and V. Shumilin, "135 W cw fiber laser with perfect single mode output," in *Proc. Conference on Lasers and Electro-Optics*, Long Beach, USA, 2002, post-deadline paper CPDC3.

[4] K. I. Ueda, H. Sekiguchi, and H. Kan, "1 kW cw output from fiber embedded lasers", in *Proc. Conference on Lasers and Electro-Optics*, Long Beach, USA, 2002, post-deadline paper CPDC4.

[5] D. C. Brown and H. J. Hoffmann, "Thermal, stress, and thermo-optic effects in high average power double-clad silica fiber lasers," IEEE J. Quantum Electron. 37, 207-217 (2001).

[6] Y. Jeong et al, to be submitted.

[7] S. Höfer, A. Liem, J. Limpert, H. Zellmer, A. Tünnermann, S. Unger, S. Jetschke, H.-R. Müller, and I. Freitag, "Single-frequency master-oscillator fiber power amplifier system emitting 20 W of power," Opt. Lett. 26, 1326 - 1328 (2001).

[8] A. Galvanauskas, Z. Sartania, and M. Bischoff, "Millijoule femtosecond fiber CPA system," in *Advanced Solid State Lasers*, Vol. 50 of OSA Trends in Optics and Photonics Series (Optical Society of America, Washington, D.C., 2001), postdeadline paper PD3.

FH2 **8:30 AM**

Fiber Fuse Effect in Microstuctured Fibers

E. Dianov, A. Frolov, I. Bufetov, *Fiber Optics Research Center at A.M. Prohorov General Physics Institute of RAS, Moscow, Russian Federation;* Y. Chamorovsky, G. Ivanov, I. Vorobjev, *Institute of Radio Engineering and Electronics of RAS, Moscow, Russian Federation, Email: dianov@fo.gpi.ru.*

The fiber fuse effect in microstructured silica fibers has been observed for the first time. The threshold intensity of laser radiation and some features of catastrophic damage differ strongly from those for conventional silica-based fibers.

The fiber fuse effect in silica-based fibers was observed for the first time in 1987 [1] and since that time it has been investigated in detail (see, e.g., [2-4]). The phenomenon represents the propagation of optical discharge along a fiber towards the source of laser radiation. The high mechanical strength of glasses provides the maintenance of high density plasma in optical discharge, which effectively absorbs the laser radiation. The propagating optical discharge destructs the core region, the residual damage consisting of a sequence of bullet-shaped bubbles. The fuse effect can be initiated by contacting the end of the fiber with a metal needle or by heating a section of the fiber with the help of electrical discharge. Quite low power densities of about 1÷5 MW/cm^2 (corresponding to optical power of ~1 W for telecommunication fibers) are enough to sustain the propagation of optical discharge in silica-based fibers [3].

Microstructured fibers differ from standard optical ones by their mechanical and thermophysical properties because of the presence of air holes in their structure. So one may expect some different features of the fiber fuse effect in these fibers.

In this paper we report the first observation of the fuse effect in a microstructured fiber. The fiber was fabricated by drilling holes in a silica rod and subsequent drawing of a fiber with output diameter of 125 μm. Fig.1 shows a scanning electron micrograph image of a cleaved end-face of the fiber. The diameter of holes was about 1 μm, the distance between hole centers was about 2 μm.

A 1.06 μm CW Nd:YAG laser (Antares, Coherent) and CW Ar laser (Beamlock, Spectra Physics) with output wavelength of 0.5 μm were used as sources of the laser radiation. The microstructured fiber was single-mode at 1.06 μm and few-moded at 0.5 μm. However, by input tuning it could be possible to get 80% of 0.5 μm optical power in the fundamental mode of the fiber. The value of the mode field diameter (MFD) was about 2 μm for both wavelengths, MFD for 1.06 μm being somewhat larger.

The laser radiation was launched into the cleaved fiber end using a microscope objective. The power at the output of 2 m long-fiber was up to 9 and 4 W at the wavelengths of 1.06 and 0.5 μm correspondingly.

To initiate the optical discharge a tungsten needle was brought to the core area of the output fiber end at the distance of several micrometers from the surface. After this the laser radiation was turned on.

In our experiments the optical discharge propagated in the microstructured fiber only under the argon laser radiation. The fuse effect was highly reproducible at the power of 4 W, and no plasma propagating was observed at the power of 3 W. In the last case only some damage took place in the vicinity of the output end at this power.

Threshold intensity of laser radiation in the core of the fiber was ~ 100 MW/cm^2. This value is about 10 times higher than it can be expected for the conventional silica-based fibers with the same MFD [3]. According to [4] the velocity of discharge propagation at the light intensity in the core ~ 100 MW/cm^2 can be expected to be ~ 10 m/s (in conventional fibers). But in our experiments with microstructured fibers the velocity of 2 m/s only was observed.

The passage of the optical discharge left behind the catastrophic damage of the core region as in case of a standard silica-based fibers. But the character of the damage was quite different. Fig.2 shows an electronic micrograph of the fiber cross-section after the passage of optical discharge. A continuous capillary was formed in the central part of the fiber, its cross-section having the shape of a six-pointed star (in accordance with the number of holes).

When the end of the damaged fiber is plunged into the glycerine all holes and the capillary were filled with it, leading to a completely transparent structure. This confirms the formation of the continuous capillary and proves the absence of coloured substances which could be formed during the propagation of the optical discharge along the silica fiber.

The propagation of the optical discharge has never been observed with the radiation of a Nd:YAG laser at the optical power up to 9 W. Physical mechanisms preventing the fuse effect in this case will be discussed at the Conference.

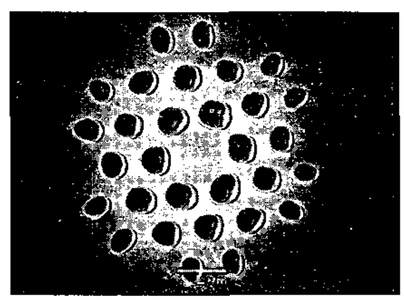

Fig. 1. The scanning electronic micrograph image of a cleaved end-face of the microstructured fiber. Scale: the length of white line is 2 μm.

Tunable Tm – doped silica fibre laser

J. K. Sahu, C.A. Codemard, R. Selvas, J. Nilsson, M. Laroche, W.A. Clarkson

Optoelectronics Research Centre, University of Southampton, Southampton SO17 1BJ, England
Phone: +44 23 8059 3143, fax: +44 23 8059 3142,
email: jks@orc.soton.ac.uk

Abstract: We report the continuous-wave operation of a Thulium-doped silica fibre laser, pumped at 1567 nm from an Erbium/Ytterbium-doped fibre laser. The quantum efficiency of 51% (with respect to absorbed pump power) is obtained at a wavelength of 1830 nm. The laser can be tuned continuously from 1750 to 1880 nm using an external grating.

OCIS codes: (060.2320) Fiber optics amplifiers and oscillators, (140.3550) Lasers, Raman

The broad emission spectra resulting from the $^3H_4$ • $^3H_6$ Y transition in Thulium –doped silica fibre attracted attention in fabrication of widely tunable fibre lasers, and hence finds applications in areas such as medicine, remote sensing and fibre optic sensors [1,2]. Here we report a tunable Tm-doped silica fibre laser, pumped by 700 mW Er/Yb doped fibre laser at 1567 nm, with up to 204 nm of output at 1825 nm, and with lasing wavelength tunable from 1755 to 1860 nm.

The Tm doped fibres used for this work is fabricated in house using MCVD technique. The fibre has a core diameter of 8 microns with NA ~ 0.18, and cut off around 1.55 microns, and is doped with ~ 500 ppm wt of Tm^{3+} ions. The laser set up is a standard end pumping scheme. A 1.5 m long Tm fibre is fusion spliced to a 1x2 WDM fibre coupler (1550 nm / 1750 nm). First, a simple laser cavity is constructed by 4% Fresnel reflections at the end face of Tm fibre and that of 1750 nm arm of WDM coupler. The other arm of the WDM is spliced to an Er-Yb fibre laser, which is operating at a wavelength of 1567 nm. Fibre lasing occurred at a wavelength of ~ 1825 nm (measured with a monochromator), and a total signal power of 230 mw is obtained for 750 mw of launched pump power of which 650mW is absorbed. The slope efficiency of 45% with respect to launched pump power is measured (Fig.1.).

In a second set-up, a wavelength tunable cavity is formed with an external diffraction grating in Littrow configuration (300 lines/mm, blaze wavelength 2 microns). The Tm fibre end is angle cleaved to suppress the wavelength independent feedback, while a lens was used to couple light from the fiber to the grating and back again. By adjusting the angle of the grating the lasing wavelength could be tuned from 1750 to 1860 nm (Fig.2.). We believe that the tuning range was restricted by the WDM coupler.

References

1. W.A. Clarkson, N.P. Barnes, P.W. Turner, J. Nilsson, and D.C. Hanna, "High-power cladding pumped Tm-doped silica fibre laser with wavelength tuning from 1860nm to 2090nm", Opt. Lett.,**27**, 2002
2. T.Yamamoto, Y. Miyajima and T. Komukai,"1.9um Tm-doped silica fibre laser pumped at 1.57um", Elec. Lett.,vol.30 ,1994

0-7803-7734-6/03/$20.00 2003 IEEE

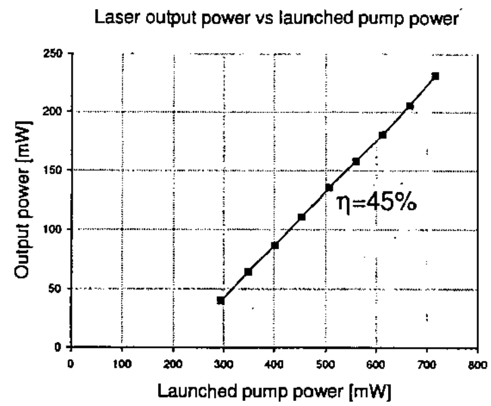

Figure 1: Laser output power versus launched *pump power*

Pump wavelength : 1567nm
Tm-doped fiber length = 1.5m

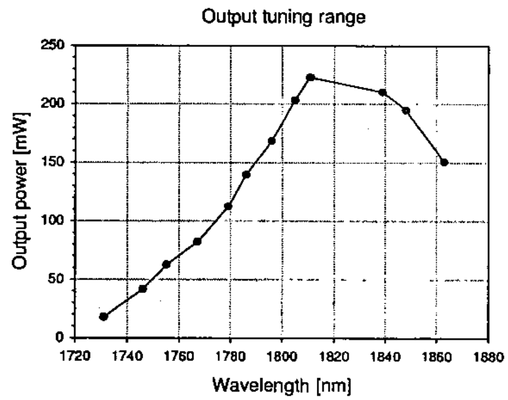

Figure 2:Laser tuning range

A 3.5 W 977 nm cladding-pumped jacketed-air clad ytterbium-doped fiber laser

K. H. Ylä-Jarkko [2], R. Selvas [1], D. B. S. Soh [1], J. K. Sahu [1,2],
C. A. Codemard[1], J. Nilsson [1,2] *, S. A. Alam[2], and A. B. Grudinin
1) Optoelectronics Research Centre, University of Southampton, Southampton SO17 1BJ, England
** Phone +44 23 80593101, Fax +44 23 80593142, Email jn@orc.soton.ac.uk*
2) Southampton Photonics, Inc. Phi House, Enterprise Road, Chilworth Science Park, Southampton SO16 7NS, England

Abstract: We present a cladding-pumped ytterbium-doped jacketed air clad fiber laser operating at 977 nm and generating a record-breaking 3.5 W of output power in a nearly diffraction-limited output beam, with a slope efficiency of 42% and a threshold of 410 mW with respect to launched power.

OCIS codes: (140.3510) Lasers, fiber; (140.3570) Lasers, single-mode

Introduction

High-power laser sources operating on a single transverse mode at 980 nm are important for pumping erbium-doped fiber amplifiers. This application is completely dominated by traditional laser diodes, which are limited in power to ~1 W or less [1]. Higher-power sources would be useful for higher-power erbium pumping as well as for many other applications such as pump sharing schemes [2] and frequency-doubling. Consequently, alternatives such as optically pumped, vertically emitting, semiconductor lasers as well as cladding-pumped ytterbium-doped fiber lasers (YDFLs) [2, 3] have been investigated for high-power 980 nm operation. So far, however, these too have been limited in output power to ~1 W. Thus, they have so far failed to decidedly improve on the continuous-wave (cw) power available from traditional diodes, though they may bring some particular advantages. For example, fiber lasers can be Q-switched to generate high pulse energies. Nevertheless, cladding-pumped YDFLs at 980 nm can be scaled to much higher power than that.

Here, we report a cladding-pumped Yb-doped jacketed-air-clad (JAC) fiber [4] laser generating 3.5 W of output power at 977 nm in a nearly diffraction-limited beam. To the best of our knowledge this result is the highest power, by far, achieved from any 980 nm source with nearly diffraction-limited output. It demonstrates the capability of YDFLs to generate the power needed for efficient frequency conversion at this wavelength. In our fiber laser, high power and high slope efficiency are achieved by using an intrinsically efficient, high numerical aperture JAC fiber, together with high-brightness pumping.

Fiber design and set-up

There are two important issues for an efficient cladding-pumped 980 nm YDFL. First of all, the pump must be able to reach the threshold intensity of the two-level 980 nm transition, meaning that a high-brightness pump source must be used. Secondly, even more importantly, the lasing at quasi-four level wavelengths around 1030 – 1040 nm needs to be avoided. This puts an upper limit on the inner-cladding to core area ratio that can be used [5], and since the core size is constrained by the requirement of single-mode operation at 980 nm, this effectively puts an upper limit of the inner-cladding, or pump waveguide, size. In practice we have found that an inner cladding diameter of ~30 μm works best. In order to launch as much pump power as possible into this relatively small inner cladding, it is important, again, to use a high-brightness pump source. Equally important is to use an inner cladding with a high numerical aperture.

Three features of our set-up allowed us meet these prerequisites: We used two high-brightness pump sources that were in addition polarization-multiplexed, and the pump beam was furthermore double-passed through the fiber. We used a jacketed air-clad fiber [4], which we developed to allow for cladding-pumping with small inner claddings and high numerical apertures. We used wavelength-selective feedback to promote 980 nm over 1030 nm.

Figure 1 shows our experimental set-up. Pump light at 915 nm from two multi-emitter broad-stripe diode sources (New Optics) were collimated and polarization-multiplexed with a halfwave-plate and a polarization beam-combiner. The polarization-combined pump beam was then passed through a dichroic mirror and a focusing lens before being launched into a jacketed-air clad Yb-doped fiber (YDF). Together, the two pump sources provided up to 18 W of power incident on the fiber, of which roughly 50% could be launched into the JAC fiber. The launch efficiency was relatively poor, since the focused pump spot size was too large for an efficient fiber launch – the pumps were general-purpose sources that had not been optimized for this particular application. The JAC YDF had a

10 μm, 0.1 NA core centered in a 28 μm diameter inner cladding with a high NA of up to 0.5, surrounded by a silica:air structure outer cladding. This in turn was jacketed by a solid silica cylindrical shell and a mode-stripping, high-index polymer, see Fig. 1. The pump launch end of the fiber had a perpendicularly cleaved flat facet providing around 4% broadband reflection. The other end of the fiber was angle-cleaved. There, a lens and a dichroic mirror were used to reflect pump and 977 nm signal light back into the fiber, while light at 1030 nm was rejected. Thus the pump and signal at 977 nm were double passed. The total single-pass pump absorption was 3 dB in a 40 cm long fiber. We estimate that in the double-passed configuration, 65% of the launched pump power was absorbed by the fiber, with the rest either being transmitted twice through the fiber or lost in the pump reflection arrangement.

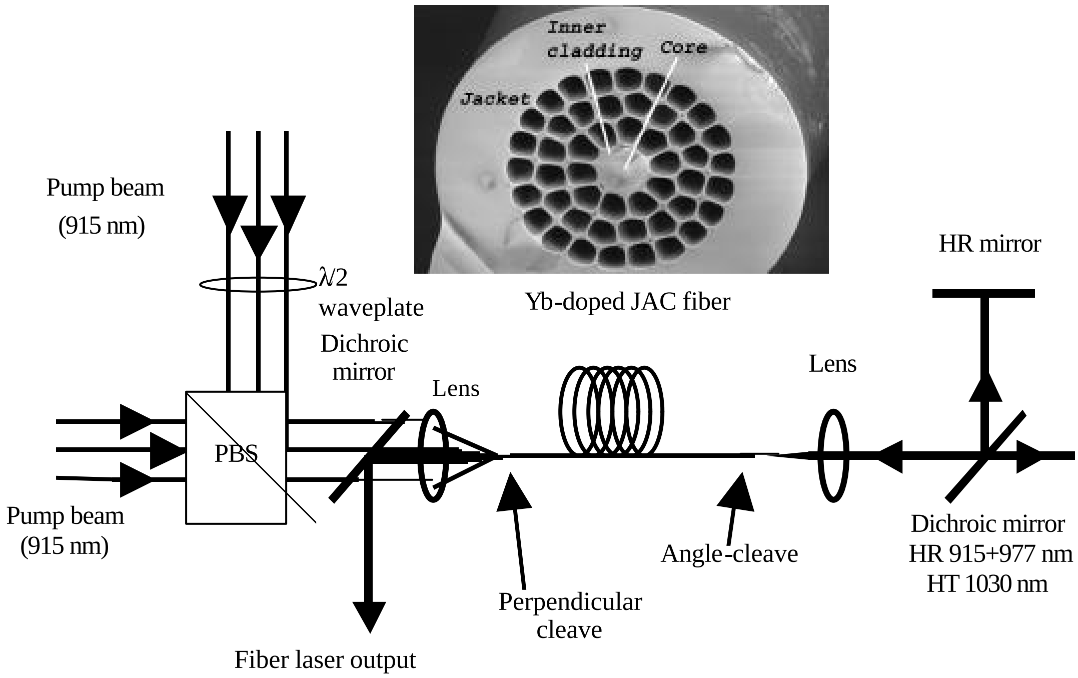

Fig. 1. Experimental set-up.

Results

Figure 2 shows the power characteristics of the YDFL. At the maximum pump power coupled into the fiber (9.4 W), the YDFL produced up to 3.5 W of output power at 977 nm, with a slope efficiency of up to 65% with respect to absorbed pump power, or 42% with respect to launched pump power. The threshold was 0.26 W with respect to absorbed pump power, and 0.41 W with respect to launched power. We also measured an M^2-value of 1.2 at ~1.0 W of output power.

Because of the short fiber with a relatively low total absorption, the pump leakage was considerable. The significant fraction of unabsorbed pump power (35%) reduced the overall efficiency and the maximum power that could be attained. In addition, we found severe thermal problems at high pump powers, in many cases limiting the output power of the laser. We attribute this to the large pump launch loss and concomitant large thermal load in the pump launch end. An improved launch efficiency, possible with a smaller pump spot size (with an optimized pump source or simply with an intermediate aperture), would reduce power loss and dissipation, and, we believe, largely mitigate this limitation. We note that the curve in Fig. 2 does not show any roll-off, indicating that the fiber could deliver still more power with a higher-power, optimized, pump source.

The dichroic mirrors used in the setup provided only coarse wavelength-selectivity. However, the emission spectrum of ytterbium-doped silica fibers has a quite sharp peak in the 975 – 980 nm wavelength range, with a linewidth of a few nanometers. We obtained, in fact, a surprisingly narrow linewidth of only 0.2 nm. This may be sufficiently narrow for efficient frequency-doubling in materials such as PPKTP. Nevertheless, for improved stability, and, if necessary, a narrower linewidth, a free-space diffraction grating or a fiber Bragg grating can be used instead of the broadband dichroic mirror feedback arrangement to provide a finer wavelength selection. We have investigated such configurations in the past with good results, albeit at lower power levels. Figure 3 depicts the output spectrum, on a high-resolution wavelength scale as well as on a broad scale that shows the high suppression of emission at 1030 nm.

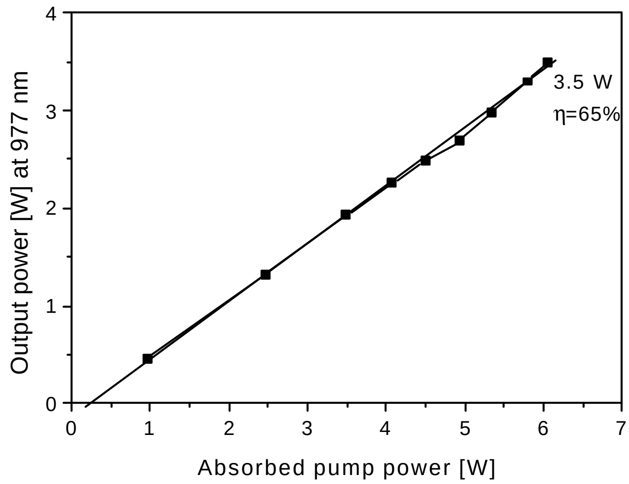

Fig. 2. Output power vs. absorbed pump power of 977 nm Yb-doped fiber laser.

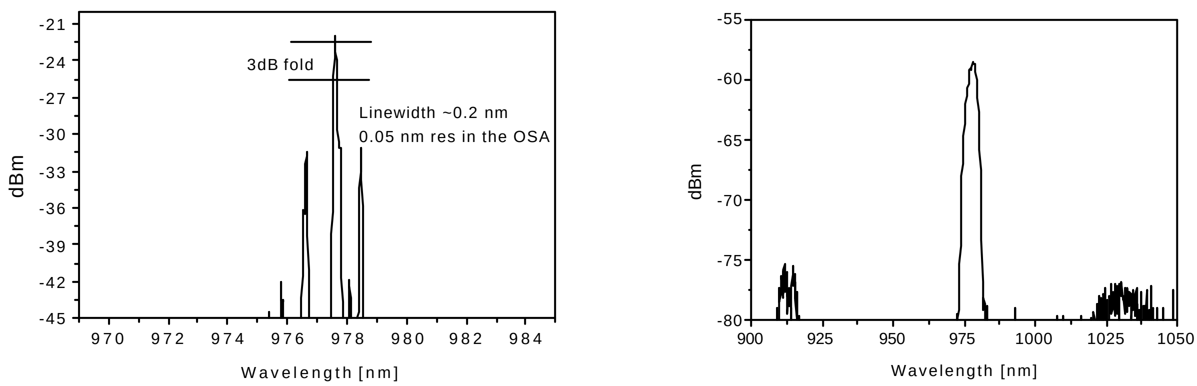

Fig. 3. High resolution and low resolution output spectra.

Conclusions

In conclusion, we have described a cladding-pumped ytterbium-doped jacketed air-clad fiber laser that produced a record-breaking 3.5 W of output power at 977 nm in a nearly diffraction-limited beam. We believe that this source is attractive for high-power pumping of erbium-doped fibers as well as in pump sharing schemes. Furthermore, it had a narrow linewidth as required in different wavelength conversion schemes. These applications often also require a single polarization, which can be implemented in the fiber laser in a relatively straightforward manner.

References

1. B. Sverdlov, B. Schmidt, S. Pawlik, B. Mayer, and C. Harder, "1 W 980 nm pump modules with very high efficiency", Proc. European Conference on Optical Communication, Vol. 3, Copenhagen, Denmark, Sept. 8 – 12, 2002 post-deadline paper 3.6

2. L. B. Fu, R. Selvas, M. Ibsen, J. K. Sahu, S.-U. Alam, J. Nilsson, D. J. Richardson, D. N. Payne, C. Codemard, S. Goncharev, I. Zalevsky, and A. B. Grudinin, "An-8-channel fiber DFB laser WDM transmitter pump with a single 1.2 W Yb-fibre laser operated at 977 nm", Technical digest 28th European Conference on Optical Communication ECOC-2002, Copenhagen, September 2002, 08.3-5

3. L. A. Zenteno, J. D. Minelly, A. Liu, A. J. G. Ellison, S. G. Crigler, D. T. Walton, D. V. Kuksenkov, and M. J. Dejneka, "1 W single transverse-mode Yb-doped double clad fiber laser at 978 nm," Electron. Lett. **37**, 819-820 (2001)

4. J. K. Sahu, C. C. Renaud, K. Furusawa, R. Selvas, J. A. Alvarez-Chavez, D. J. Richardson, and J. Nilsson, "Jacketed air-clad cladding pumped ytterbium doped fibre laser with a wide tuning range", Electron. Lett. **37**, 116-1117 (2001)

5. J. Nilsson, J. D. Minelly, R. Paschotta, D. C. Hanna, and A. C. Tropper, "Ring-doped cladding-pumped single-mode three-level fiber laser", Opt. Lett. **23**, 355-357 (1998)

An Associated Degree in Electronic Engineering with specialization in optics

J.J. Sánchez-Mondragón
Instituto Nacional de Astrofísica, Óptica y Electrónica
Luis Enrique Erro #1, Apdo. 51 y 216 CP 72000, Tonantzintla, Puebla, México
telephone: 52 2222 128583; fax: 52 2222 472231; e-mail: jsanchez@inaoep.mx

J. Escobedo-Alatorre, M. Tecpoyotl-Torres, and M.A. Basurto-Pensado
Centro de Investigación en Ingeniería y Ciencias Aplicadas
Av. Universidad 1001, Col. Chamilpa, Cuernavaca, Morelos, México

R. Rodríguez-Vera and R. Selvas
Centro de Investigación en Óptica
Lomas del Bosque 115, Colonia Lomas del Campestre, León, Guanajuato, México

Abstract: We have experienced an Associated Degree on Engineering and a subsequent Bs on Electronic Engineering that uses Optics as the essential introduction to Modern Ondulatory Physics. This first experience in Mexico is important because the popular origin of Mexican Engineering Students, that represents the 27% of the National enrollment [1].

OCIS codes: (000.2060) Education, (000,2170) Equipment and techniques

1. Introduction

An Associated Degree on Engineering (ADE) emerges from the necessities of a developing country. The current industry also requires personal with specialization in specific areas. In particular optics is growing within the context of other engineering such as electronics. In this context, it is required to provide opportunities to students who want to complete a studies program, which covers technical and engineering basis. An ADE and the subsequent Bs on Electronic Engineering have then been created for this necessity. Chronologically these are typically composed by a plan of 4 years degree divided in two parts, where students covering their first two years, they have the opportunity to explore all the technical issues of an Electronics degree. Subsequently, the experienced students are ready to incorporate straightforward to the demanding industry. On the other hand, while the student is deciding for incorporating to the industry, the plan gives the flexible option to continue and finish a Bs degree in the subsequence years.

The basic education in Mexico has typically a framework where optics raises from physicist and electronics from Engineering. However, a program with both specialties claims many challenges and benefits, such as, how to incorporate photonics, optical engineering, quantum mechanics and electronics in a unified program.

This vision was widely accepted at the UAEM. In 1998, a syllabus of the Electrical engineering was proposed, so that it fulfilled the requirements of an ADE in electronics engineering with specialization in optics, one of the first of its kind implemented in Mexico. This paper will be giving the experience concerning in the development of such a plan of ADE & Bs.Eng. With 5 years of experience in this program, many challenges have been treated and overcome.

2. Summary

With an invitation from the Morelos State University (UAEM), we started in the creation for a research centre in electrical engineering. The main objective was to support the engineering program already inscribed at the UAEM as well as to open the electronic and computer areas with a new scheme.

A survey data [1] by the Mexican ministry of education revealed that up to 80% of student leave the university system because social-economic problems. For that reason, a reorganization was claimed for solve all these problems, creating a challenging and interesting academic problem.

The ADE and the Bs en Electronic engineer were then created and this comprise of two stages schedule. The first step has a duration of 2 ½ years and has a design in such a way that enables students to focus on practical abilities and the required physics-mathematics background. The scheme allows to incorporate the students directly to the productive sectors at the end of this first step, and creates the economical conditions such that a larger population continue the second stage and to conclude with an engineering degree.

From a methodological point of view, the engineering degrees in Mexico did not have a strong emphasis on physics and mathematics. However, this new program shows the students the convenience of learning optics because of current availability of optoelectronic components, and by doing it, eases the understanding of quantum mechanics that has traditionally limited their perusing graduate studies.

It is important to point out that these programs were developed pursuing the ABET guidelines (Accreditation Board for Engineering and Technology), that almost simultaneously published the ADE guidelines. The program has received positive remarks from the department of Education and the General Direction of Technological Universities, responsible of the ADE programs in Mexico.

3. References

[1] “Programa Nacional de Educación Superior 2000’2006”, Reporte de la SEP, (2000).

Superfluorescence three-level neodymium doped fiber source

R. Selvas [a,c*], A. Martinez-Gamez [a*], A. Martinez-Rios [a*], X. Sanchez-Lozano [a*], M. A. Basurto-Pensado [b*] and J. Nilsson [c]
[a] Centro de Investigaciones en Optica, Lomas del Bosque 115, Leon, Gto., 37150, Mexico
[b] Centro de Investigaciones en Ingenieria y Ciencia Aplicadas, Cuernavaca, Morelos, 62210, Mexico
[c] Optoelectronics Research Centre, University of Southampton., Southampton, SO17 1BJ, United Kingdom, email: rselvas@cio.mx

ABSTRACT

We report on a new type of cladding-pumped neodymium-doped fiber which enables strong ASE emission at the wavelength region of 940 nm with a highly reduced emission in the four-level transition at 1060 nm when is pumped by a 806 nm source. This ASE source delivers a total emission power of 60 *mW* from 500 mW of absorbed pump power. The arrangement setup consisted in a pump diode emitting at 806 nm with a total output power of 1.5 W, a collimated and focused lenses and a dichroic mirror. The broadband of the neodymium source was measured to be 25 nm. Moreover, a numerical simulation for the ASE source is also discussed.

Keywords: Fiber laser, neodymium doped fibers, three-level transition

1. INTRODUCTION

Fiber lasers draw much attention since the first realization of the diode-pumped fiber laser in 1989 [1]. Currently, ytterbium doped fiber laser at 1.1 μm are the most studied rare-earth-doped devices and it is possible to generate output power beyond 100 W [2], similarly neodymium doped fiber laser at the emission region of 1.06 μm can generate output power as high as 30 W. However, these two important materials operate in a (or a quasi) four-level transition with the only exception of the erbium doped fiber laser, in which is achievable to generate less than 1W but with an specific composition arrangement like the one for the Er-Yb fiber laser (by help of the sensitized process in the erbium-ytterbium energy transfers), output power exceeding 100 W is now possible to demonstrate [3]. For the generation of laser in a pure three-level transition like to the neodymium-doped fiber, there is no much work developed. Although recently, a cladding-pumped 938 nm neodymium doped fiber laser was demonstrated but this fiber was at liquid nitrogen temperature [4]. This means that this operation was not realized in a room temperature. This is in fact make a pure three-level transition more difficult process since the thermal population of the upper Stark-levels of the ground state of the transition terminates on is higher at higher temperature. This therefore increases the ground state absorption. Consequently a cladding pumped laser at 0.9 μm at room temperature remained to be demonstrated.

In other words, neodymium doped fiber lasers (NDFLs) that operates in its four level transitions (1060 nm) are systems without any ground state absorption (GSA) while GSA is significant at the three-level transition at wavelength of 900 – 950 nm. NDFLs normally generate high gain at 1.1 μm already with a low fraction of the Nd-ions excited, which makes operation at other wavelengths particularly sensitive to GSA and create good competition to the others wavelengths too. Spectroscopy data from NDF with aluminum host composition indicated that the emission cross-section is larger at wavelength around 870 nm than at 900 – 950 nm, but the GSA increase even more, making an 870 nm double clad fiber laser even more difficult. Consequently, a CP NDFL at 0.9 μm remained to be demonstrated. In contrast, core-pumped fiber lasers are not much sensitive to GSA, and operation around 900 nm has been demonstrated with 3.2 mW of output power for 53 mW of absorbed pump power. In a more recent paper, it was demonstrated with 43 mW of output power for 85 mW of launched pump power at 800 nm and revealed a good performance of this 3-L NDFL in the core-pumping scheme [5], while efficiencies were lower in some older publications [6-8]. However, for high power operation, power scaling via cladding-pumping is required.

5th Iberoamerican Meeting on Optics and 8th Latin American Meeting on Optics, Lasers, and Their Applications, edited by A. Marcano O., J. L. Paz, Proc. of SPIE Vol. 5622 (SPIE, Bellingham, WA, 2004) · 0277-786X/04/$15 · doi: 10.1117/12.589256

Here, we investigated an efficient superfluorescent source (SFS) at 938 nm. One attraction for this source is that it can be used as a low-noise pump source for Er-Yb FA or for YDFL. From our point of view, a greater attraction is that an SFS allows for an alternative source configuration. SFS are based on the principle that if the gain of a medium is high enough, ASE can build up to a significant fraction of the saturation power in a single-pass through the gain medium. Typically, rare-earth doped fibers have shown to make good SFS as the differential gain efficiency can be as high as 1 dB per milliwatt of absorbed pump power, or even significantly more. With a gain requirement of typically 30-40 dB for a SFS (or 20 dB per pass for double-pass configuration), the pump power requirements become quite reasonable.

2. FIBER DESIGN

A double clad-germanosilicate NDF was fabricated with the following parameters: core NA 0.2, diameter 7.4 μm, Nd^{3+}-concentration 300 ppm (wt%), inner cladding NA 0.4, diameter 80 μm; low-index polymer outer cladding. The background loss was measured to be 0.09 dB/m. The fiber has an area ratio of 100. The chemical constitution of this fiber helps in that the branching ratios between the 1060 and the 900 nm emission were quite similar. By a simple angle-cleaved fiber facet end is possible to induce large propagation loss at 1060 nm and together with the characteristics of the feedback mirror, a dichroic mirror that has a high transmitivity at 1060 nm and a good reflectivity at 900 nm.

3. EXPERIMENT

The experimental configuration is shown in Fig. 1. The simplicity of the set up is very notable. The fiber had 0.2 NA, 7.4 μm diameter core, 0.4 NA, 80 μm diameter inner-cladding. This fiber with a perpendicularly cleaved facet in one end and an angle-cleaved facet in the other end, and it constitutes the heart of our SFS and it was as much 30 m long. The lack of feedback in one end makes the output nearly uni-directional even with a simple perpendicular cleaved in the pump launch end. Pump power from a laser diode was launched into the fiber through a collimating and a focusing lens. The power characteristics are shown in Fig. 2.

A maximum of 60 mW of output power was achieved. A slope efficiency of around 25% were achieved (with respect to absorbed pump power, and 12% wrt. launched power). The ratio between the ASE output powers in the two ends was measured to be 4:1.

The pump source was a diode laser emitting at 806 nm. The diode laser output power was 1.5 W, of which 0.9 W could be launched into the pump waveguide of the NDF. Figure 3 shows the output spectrum of our SFS CP NDF. Simple end pumping was used, with the pump being launched through a perpendicularly cleaved fiber facet. The other end of the NDF was angle-cleaved in order to suppress broadband feedback. The operating single-pass pump absorption was 3 dB. The NDF SFS delivered up to 60 mW of output power (with the transmitted pump and signal at 1060 nm removed from this measurement).

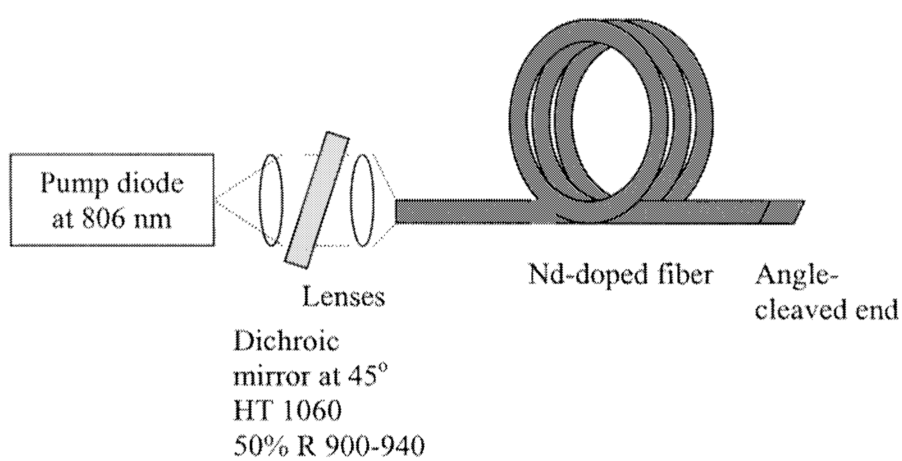

Figure 1: Experimental set-up

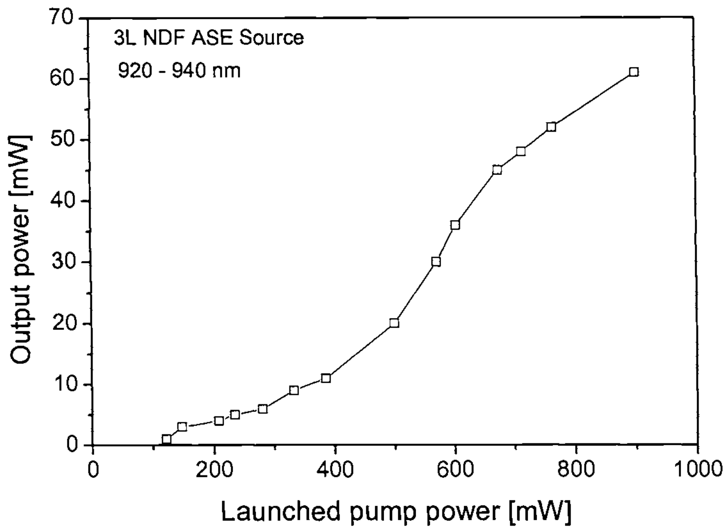

Figure 2: Output power of ASE as a function of launched pump power: Threshold and slope efficiency for ASE source are 400 mW and 12%

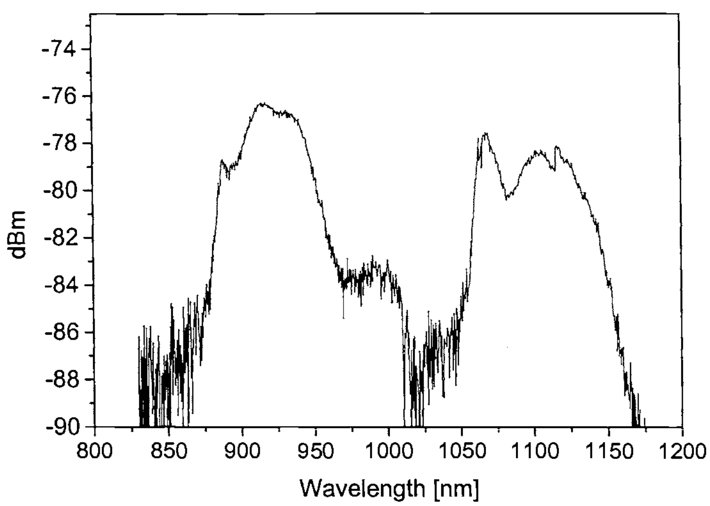

Figure 3: Output power spectrum from the SFS neodymium-doped fiber (at high input power, Res. 1 nm)

4. NUMERICAL VERIFICATION

We also verify the target designs with numerical simulations at the beginning. Special simulation software was used for numerical simulation of a 0.9 μm CP SFS NDF in a low-gain cavity configuration.

The simulated fiber had a core diameter of 8 μm and an inner cladding diameter of 80 μm (area ratio of 100). The fiber was neodymium-doped to the level of 13 dB/m small-signal core absorption at 806 nm. The maximum launched pump power was 1 W and the total pump absorption of 4 dB. We used dichroic mirror, a bare perpendicularly cleaved facet and an angle-cleaved faced end (with 0.1% reflectivity feedback). The emission band was around 938 nm due to the germanosilicate host characteristics with the 30 m long fiber. For longer fiber (>50 m), the ASE at 1080 nm increased and the strong 0.9 μm ASE emission was no longer possible. This simulation showed as an example an output power of 60 mW from a 1 W of incident pump power.

5. DISCUSSION

An alternative approach to improving the efficiency is to use distributed filtering, as this would remove many constraints that hamper a 0.9 μm NDFL. Still, in this simple demonstration, the efficiency with respect to absorbed power is poor, and this is not automatically addressed by a higher pump absorption. If the reason for the low efficiency is background loss, then a higher pump absorption via a smaller inner cladding does help. However, if there is some problem with the gain medium itself (e.g. OH-absorption or quenching) then this must be remedied in some other way.

6. CONCLUSIONS

A superfluorescent source was realized in a very simple configuration. The output power of over 60 mW was reached. We also consider the numerical simulation of a low-gain, 0.9 μm, germanosilicate CP NDF source, without any distributed suppression at 1080 nm. This first step is quite encouraging since we were only limited by pump power and it is highly acceptable that higher output power can be reached as well (simulations indicated more than 100 mW by doubling the input power would be possible) by increasing the pump modules. The broadband source was 25 nm in the 3dB bandwidth

7. ACKNOWLEDGEMENTS

We (*authors) thank for the support of CONACyT, Mexico. The authors also wish to thank to Dr Jayanta Sahu (Optoelectronics Research Center) for providing the neodymium-doped fiber.

REFERENCES

1. E Snitzer, Rare-earth fiber laser, *J. Less-Common Metals*, Vol. **148**, pp 45-58, 1989.
2. J Nilsson, Y Jeong, C Alegria, R Selvas, JK Sahu, RB Williams, K Furusawa, WA Clarkson, DC Hanna, DJ Richardson, TM Monro, DN Payne, Yla-Jarkko, SU Alam, AB Grudinin, Beyond 1 kW with fiber lasers and amplifiers, *in proc. Optical Fiber Communication Conference*, TOPs Vol. **86**, pp 685-6, 2003.
3. J Dawson, R Beach, A Drobshoff, Z Liao, D Pennington, and S A Payne, High power 938 nm cladding pumped fiber laser", *in Advanced in Fiber lasers, L N Durvasula, Ed.* Proc. SPIE Vol. **4974**, pp 75-82, 2003.
4. JK Sahu, Y Jeong, DJ Richardson, J Nilsson, 103 W Erbium/Ytterbium co-doped large core fiber laser, *Opt. Commun.*, Vol. **227**, pp. 159-63, 2003.
5. A Cook, and H Hendricks, *Appl. Optics*, **37**, pp 3276, 1998.
6. A Cook, H Hendricks, *in Proc. Conference on Laser and Electro-Optics*, pp 311, 1997.
7. L Reekie, IM Jauncey, SB Pooole, DN Payne, *Electron. Lett.*, **23**, pp 884-5, 1987.
8. IP Alcock, AI Ferguson, DC Hanna, AC Tropper, *Optics Communication*, **58**, pp 405-8, 1986.

2004

All-Fiber Tunable MMI Fiber Laser

J. E. Antonio-Lopez[1], A. Castillo-Guzman[2], D. A. May-Arrioja[1], R. Selvas-Aguilar[2], and P. LiKamWa[3,†]
[1] Photonics and Optical Physics Laboratory, Optics Department, INAOE
Apdo. Postal 51 y 216, Tonantzintla, Puebla 72000, México
[2] Facultad de Ciencias Físico Matemáticas, UANL
Cd. Universitaria, Nuevo León 66450, México
[3] CREOL & FPCE: The College of Optics and Photonics
University of Central Florida, Orlando, FL 32816, USA

ABSTRACT

We report on a novel tuning mechanism to fabricate an all-fiber tunable laser based on multimode interference (MMI) effects. It is well known that the wavelength response of MMI devices exhibits a linear dependence when the length of the multimode fiber (MMF) section. Therefore, tuning in the MMI filter is achieved using a ferrule (capillary tube of 127 μm diameter) filled with a liquid with a higher refractive index than that of the ferrule, which creates a variable liquid MMF. This liquid MMF is used to increase the effective length of the MMI filter and tuning takes place. Using this simple scheme, a tuning range of 30 nm was easily achieved, with very small insertion losses. The filter was tested within a typical Erbium doped fiber (EDF) ring laser cavity, and a tunable EDF laser covering the full C-band was demonstrated. The advantage of our laser is of course the simplicity of the tunable MMI filter, which results in an inexpensive tunable fiber laser.

Keywords: Multimode Interference, MMI, Tunable Laser, Fiber Laser, EDFL, Erbium Doped, Wavelength Tunable Laser, Widely Tunable Laser, Fiber Ring Laser.

1. INTRODUCTION

During the last two decades a vast variety of applications have been developed relying entirely on the properties of lasers. Several applications such as sensing, instrument testing, optical signal processing, optical communications, and photon analog-to-digital conversion (ADC) [1, 2] have benefited from laser developments. Among the different kind of lasers systems developed up to now, tunable lasers have been particularly important due to their applications related to spectroscopy, optical communications, and sensing. Absorption spectroscopy usually implies having a tunable frequency source and producing a plot of absorption as a function of frequency. Therefore, laser spectroscopy has led to advances in the precision with which spectral line frequencies can be measured, and this has fundamental significance for our understanding of basic atomic processes [3, 4]. In optical communications, the need for more bandwidth increases exponentially every year. Therefore, the development of wavelength division multiplexing (WDM) systems can be easily and inexpensively covered using a tunable laser. In the sensors arena, tunable laser allow for testing of wavelength multiplexed sensors.

Several materials and configurations have been used in order to develop a tunable laser. Among them, all-fiber systems are advantageous because they do not require free space optical components, and thus, are simple, flexible, and rather inexpensive. All-fiber tunable laser have been mostly developed using either variations of fiber Bragg gratings (FBGs) or long period gratings (LPGs) [5-8]. In both cases, a grating has to be inscribed on the fiber, which increases the cost of the tunable laser. Recently, we demonstrated the use of multimode interference (MMI) effect in multimode fibers (MMF) as a simple tunable mechanism [9, 10]. The advantage of such filters is that they only require splicing a section of MMF

*Email: dmay@inaoep.mx; Phone: +52 (222) 247-2011 Ext. 8115; Fax: +52 (222) 247-2940; www.inaoep.mx
† also with the Dept. of Electrical and Computer Engineering, University of Central Florida

Enabling Photonics Technologies for Defense, Security, and Aerospace Applications V,
edited by Michael J. Hayduk, Peter J. Delfyett Jr., Andrew R. Pirich, Eric J. Donkor, Proc. of SPIE Vol. 7339,
73390Q · © 2009 SPIE · CCC code: 0277-786X/09/$18 · doi: 10.1117/12.819078

between two single mode fibers. However, the maximum tuning wavelength range has been limited to only 12 nm. This limitation is not due to the MMI filter itself, but rather from other effects arising from the way the filter was implemented.

In this work we report on an all-fiber tunable MMI fiber laser. The tuning mechanism relies on a capillary tube filled with a high refractive index liquid to effectively increase the length of the multimode fiber (MMF). According to the MMI theory when the MMF length is modified its peak wavelength response is also modified, and thus wavelength tuning is achieved. The use of the liquid also removes some of the problems experienced before. Using this filter a ring-based tunable Erbium doped fiber laser (EDFL) is demonstrated with a tunability of 30 nm covering the full C-band.

2. TUNABLE MULTIMODE INTERFERENCE FILTER

The operation of the MMI filter is as follows. The key component is a multimode waveguide that supports several modes (≥ 3), which is spliced between two SMF. After the supported modes are excited by launching a field using the input SMF, the interference between the modes propagating along the MMF gives rise to the formation of self-images of the input field along the MMF. Therefore, the length of the MMF has to be precisely cleaved in order to have a self-image right at the facet of the output SMF. The MMI effect has been previously studied and the length of the MMF can be calculated using

$$L = p\left(\frac{3L_\pi}{4}\right) \qquad with\;\; p = 0,1,2,....., \tag{1}$$

where L_π is the beat length

$$L_\pi \cong \frac{4n_{MMF} D^2{}_{MMF}}{3\lambda_0}. \tag{2}$$

Here n_{MMF} and D_{MMF} correspond respectively to the refractive index and diameter of the MMF core, with λ_0 as the free-space wavelength. As shown in Eq. (1), in principle self-images should be periodically formed along the MMF. However, due to the nature of the MMI effect, the true images of the input field are given at every fourth image. The images formed at other locations are known as pseudo-images, and although they resemble the input field they exhibit higher losses. Therefore, we operate our MMI filters at the fourth image. Since the fibers are spliced the wavelength response is fixed. In order to make this a tunable filter, we have to look at the wavelength dependence of the filter. By combining the MMI governing equations (1) and (2), and expressing the peak wavelength in terms of all the other parameters we obtain,

$$\lambda_0 = p\left(\frac{n_{MMF} D^2{}_{MMF}}{L}\right) \qquad with\;\; p = 0,1,2,...... \tag{3}$$

It is clear from Eq. (3) that in order to tune the peak wavelength response, we need to modify either the refractive index, the length, or the diameter of the MMF. In our previous attempts to tune this filter, one of the SMF-MMF junctions is left un-spliced and the separation between the SMF and MMF facets is separated in order to increase the MMF length [9, 10]. However, due to the refractive index difference between air and fiber, Fabry-Perot (FP) resonances are observed and the tuning direction is reversed after 12 nm of tuning. Therefore a novel tuning mechanism is required in order to fully exploit the potential of MMI filters.

Our new tuning mechanism is shown in Fig. 1. The key component is a fused silica (n=1.444) ferrule with an inner diameter of 127 µm, and outer diameter of 5 mm that facilitates its handling. When the ferrule is filled with a high refractive index liquid with n=1.62 (Cargille Index Matching Liquid), a liquid multimode waveguide (MMW) is formed within the ferrule. The SMF and MMF can then be inserted in the ferrule, and when the separation between them is changed, the effective length of the MMF will be the sum of the real MMF length plus the liquid MMW segment. Therefore, if the effective length of the MMF is increased, according to Eq. (3), the wavelength response should be effectively tuned.

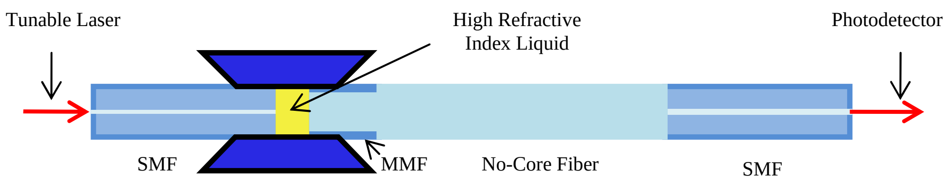

Fig. 1. Schematic of the tuning mechanism for the tunable MMI fiber filter.

As shown in Fig. 1, our MMF segment is made of two different MMF. It was recently shown that having a bigger refractive index difference between core and cladding provides a MMI filter with narrower linewidth and better contrast [11]. The fiber that fulfills this requirement is known as No-Core fiber, which is basically a 125 μm diameter MMF with air as the cladding. Since we are using a liquid with a high refractive index, inserting the No-Core fiber directly into the ferrule could result in losses since liquid accumulates in the end of the ferrule. Therefore, a section of No-Core fiber whose length is calculated to have the third image at its facet was spliced to a SMF. Another section of 105/125 MMF, having the length to form one image, is then spliced to the end of the No-Core fiber. The combined length of both MMF´s still forms the fourth image, but the 105/125 MMF has a cladding and thus should not be affected by the high refractive index liquid.

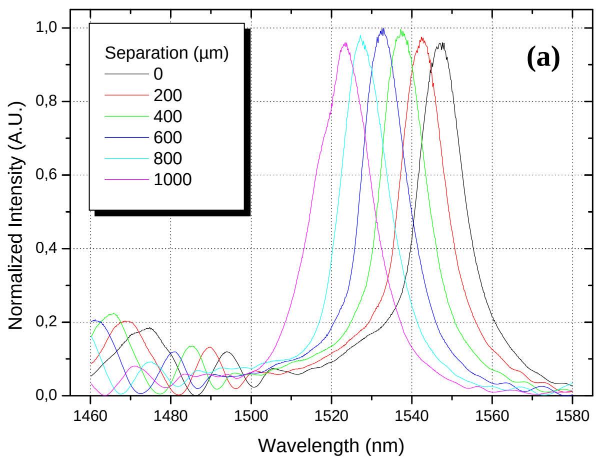

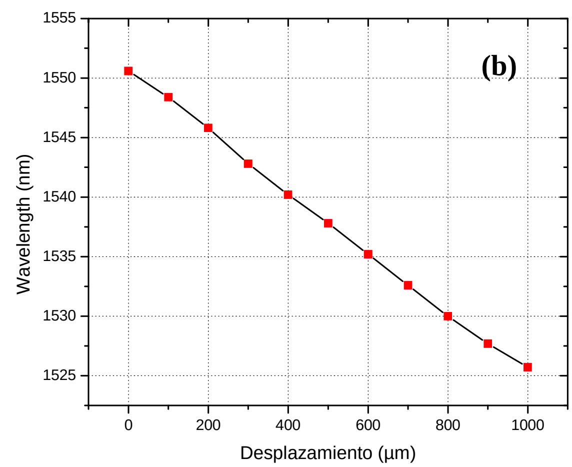

Fig. 2. (a) Tuning response of the tunable MMI filter, and (b) Peak wavelength against separation between SMF and 105/125 MMF.

The tunable MMI filter was characterized by coupling light to the input SMF from an Agilent tunable laser, with a range from 1460 to 1580 nm. After passing through the MMI filter, light is measured at the output SMF using a photodetector. The response of the tunable MMI filter is shown in Fig. 2 (a). Shown here is the response of the filter at every 200 μm separation between the SMF and 105/125 MMF. A tuning range of almost 30 nm was easily achieved with less than 0.4 dB insertion losses. We can also observe that as the filter is tuned there is an additional loss which is related to slight different diameter between the ferrule and MMF. Therefore, to minimize its effect, we maximize the filter transmission at the center of the tuning range and the loss is kept to less than 0.2 dB within the 30 nm tuning range. Beyond this range the filter response is quickly degraded, which we believe is related to the different diameter of the MMF´s used in the MMI filter. The peak wavelength response of the filter for every 100 μm separation is also shown in Fig. 3 (b). As shown here, the tuning range should be enough to easily cover the C-band.

3. TUNABLE MMI FIBER LASER

The all-fiber tunable laser was fabricated using a standard ring laser cavity, as shown in Fig. 3 (a). The ring was composed of 5 meters long Erbium Doped Fiber (EDF), a C-band optical isolator to keep the laser unidirectional, a 980/1550 nm WDM coupler to pump the EDF, a 10/90 coupler to monitor the tunability of the laser, and of course our tunable filter. The laser was pumped using a 980 nm wavelength laser diode with a power of 150 mW. At the 10% output coupler an optical spectrum analyzer (OSA) was used to monitor the spectral response of the tunable MMI laser.

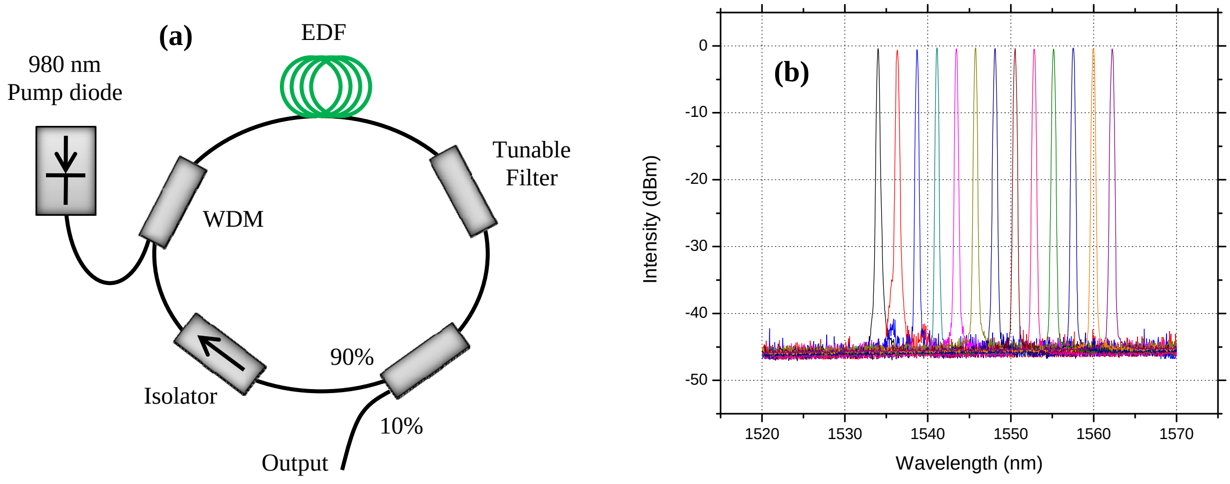

Fig. 3. (a) Experimental setup for the tunable MMI fiber laser, and (b) Superimposed spectral response of the tunable MMI fiber laser.

The tunability of the laser was characterized by first adjusting the filter to maximum transmission at the center of the tuning range, and then the SMF and 105/125 MMF were brought into contact. The EDF was pumped at maximum power, and laser spectral response was acquired using the OSA. Tuning was achieved by separating the fibers within the ferrule at small steps using a micrometer, and the spectrum is taken at every time. The superimposed spectrum of the tunable MMI laser is shown in Fig. 3 (b). A side mode suppression ratio (SMSR) of 45 dB was achieved, with a 3-dB bandwidth of 0.35 nm. Power variation is also minimum across the tuning range, which eliminates the need for a variable attenuator. Given the resolution of the micrometer, continuous tuning can be easily achieved. We should also point out that given the cost of the filter, expanding the tuning range is relatively simple and not expensive.

4. CONCLUSIONS

An all-fiber tunable MMI fiber laser was demonstrated. The tunable MMI filter was fabricated using a capillary tube filled with refractive index matching liquid to effectively increase the length of the multimode fiber (MMF). According to the MMI theory when the MMF length is modified its peak wavelength response is also modified, and thus wavelength tuning is achieved. Using this filter a ring-based tunable Erbium doped fiber laser (EDFL) is demonstrated with a tunability of 30 nm covering the full C-band. This scheme results in a very simple and cost-effective tunable laser that can find applications in sensing and optical communications.

REFERENCES

1. S.K. Liaw, H.Y. Tseng, and S. Chi, “Parallel pump-shared linear cavity laser array using 980-nm pump reflectors or N pieces of gain fibers as self-equalizers”, *IEEE Photon. Technol. Lett.*, 12(1), 19–21 (2000).
2. S.K. Liaw *et al.*, “Wavelength tuning and multiple-wavelength array-waveguide-grating lasers”, *Opt. Eng.*, 42, 2178–2179 (2003).
3. Kaveh Sahba, Sreten Askraba and Kamal E. Alameh, “ Non-contact laser spectroscopy for plant discrimination in terrestrial crop sparring”, Opt. Express, 14(25), 12485-12493 (2006).
4. H. Waechter1, J. Mohn, B. Tuzson, L. Emmenegger, and M.W. Sigrist1, “Determination of N2O isotopomers with quantum cascade laser based absorption spectroscopy”, Opt. Express, 16(12), 9239-9244 (2008).
5. L. Shien-Kuei, H. Kuan-Luen, L. Yi-Tseng, C. Chia-Chin, and S. Chow-Shing, “C-band continuously tunable lasers using tunable fiber Bragg gratings”, *Opt. and Laser Technol.*, 39, 1214-1217 (2007).
6. S. Y. Li, N. Q. Ngo, and Z. R. Zhang, “Tunable Fiber Laser With Ultra-Narrow Linewidth Using A Tunable Phase-Shifted Chirped Fiber Grating”, *IEEE Phot. Technol. Lett.*, 20(17), 1482-1484 (2008).

7. H. Sakata, H. Yoshimi, and Y. Otake, "Wavelength tunability of L-band fiber ring lasers using mechanically induced long-period fiber gratings", *Opt. Commun.*, 282, 1179-1182 (2009).
8. W. Shin, K. Oh, B.-A. Yu, Y. L. Lee, Y.-C. Noh, D.-K. Ko, and J. Lee, "All-Fiber Wavelength-Tunable and Mode Convertible Bandpass Filter for Optical Interconnections", *IEEE Phot. Technol. Lett.*, 20(6), 404-406 (2008).
9. R. Selvas, I. Torres-Gomez, A. Martinez-Rios, J. Alvarez-Chavez, D.A. May-Arrioja, P. LiKamWa, A. Mehta, and E. Johnson, "Wavelength tuning of fiber lasers using multimode interference effects", Opt. Express, 13(23), 9439-9445 (2005).
10. G. Anzueto-Sánchez, A. Martínez-Ríos, D. A. May-Arrioja, I. Torres-Gómez, R. Selvas-Aguilar and J. Alvárez-Chávez, "Enhanced tuning mechanism in fibre laser based on multimode interference effects", *Elect. Lett.*, 42(23), 1337-1339 (2006).
11. Waleed S. Mohammed and Peter W. E. Smith, Xijia Gu, "All-fiber multimode interference bandpass filter", *Opt. Lett.*, 31(17), 2547-2549 (2006).

Effects of out-coupling in fiber lasers

J. Escobedo-Alatorre [a], R. Selvas [b], A. Martinez-Rios[b], D. May Arrioja[c],
M.A. Basurto-Pensado[a] and J. Sanchez-Mondragon[a,d]
[a] Centro de Investigaciones en Ingenieria y Ciencia Aplicadas, Cuernavaca, Morelos, 62210, Mexico.
[b] Centro de Investigaciones en Optica, Lomas del Bosque 115, Leon, Gto., 37150, Mexico.
[c] School of Optics: CREOL & FPCE, University of Central Florida, Orlando, FL 32816-2700,
[d] Nacional Institute of Astrophysics Optics and Electronics, AP 51 y 216, Puebla, Puebla, Mexico,
email: rselvas@cio.mx

ABSTRACT

An analysis of out-coupling in a laser shows an optimum way of subtracting more output power by choosing an appropriate cavity arrangement from a high-power fiber laser. This investigation consisted in resolving analytically the effect of different cavities in our laser system and one thing that outcome was to know that a fiber laser can operate with high efficiency even with high losses in one end of the cavity (e.g. at an external diffraction grating), only if the feedback in the out-coupling end is low. Moreover, it was also found that is possible to improve the output power by reducing the feedback in the out-coupling end. Parameters considered in this resolved method are 0.1 NA, 10 μm diameter core, 200 μm inner-cladding diameter and 10 dB small-signal absorption. The fiber laser was doped with ytterbium and lases at 1080 nm, when pumped at 915 nm. The maximum pump power was set to 10 W.

Keywords: High power fiber laser, optical fibers

1. INTRODUCTION

Currently, the production of fiber lasers has demanded too much attention and it becomes an important topic for the realization of many milestones [1-3]. Important components in a fiber laser are the ultimate objective. These are ranging from the state of art of high power diode lasers, fiber design, to the fiberlised of prototypes. Notwithstanding, the cavity design is still one of the most important role in the construction of an efficient fiber device. Together with the way of pumping of a fiber laser, the cavity designs (formed by butted dichroic mirrors, thin films or by fiber Bragg gratings), are the essential part of a good design. Applications of these devices, in fact, demand five important requirements, wall-plugging conversion, all-fiber device design, beam quality, unidirectional output and good efficiency. The latter can be easily obtained by the trade-off in the transmitivities of the output ends of a rare-earth-doped fiber, by selecting the percentage of reflectivities and the strength of the in-fiber mirror [4]. Here, we made an extensive study of how the efficiency in terms of the output effective power can be obtained by varying the percentage of the reflectivity of our Fabry-Perot cavity.

2. ANALYSIS

By rule in a Fabry-Perot cavity, the out-coupling fraction is given by the mirror transmitivity. This term is important in the threshold and efficiency of a laser since both depend on the fraction of the power that is out-coupled from it. In fact, the out-coupled power is lost from the cavity and therefore such expression "out-coupling loss" is often used, although the out-coupled power is clearly not the lost here but is actually the useful output. As long in a laser is required either a low threshold or a high slope efficiency, it is found that the transmitivity must be chosen as a compromise between these two requirements. e.g. a high reflectivity (or low transmitivity) gives a low threshold but also a low slope efficiency, while a lower reflectivity improves the slope efficiency at the expense of a higher threshold power.

5th Iberoamerican Meeting on Optics and 8th Latin American Meeting on Optics, Lasers, and Their Applications, edited by A. Marcano O., J. L. Paz, Proc. of SPIE Vol. 5622
(SPIE, Bellingham, WA, 2004) · 0277-786X/04/$15 · doi: 10.1117/12.590743

On the other hand, it is well know that most fiber lasers benefit from be a high-differential gain devices and are operating with a deeply saturated gain. If is required, a high gain can be reached easily, where, the threshold is low and, in comparison with the laser output power, it only depends weakly on the output coupling. Moreover, a very low cavity feedback from a specific design can still work efficiently. Since losses such as background losses are typically large in a fiber laser compared to most other types of lasers, it is important to have a significant output coupling, since otherwise a large intra-cavity field leads to large intra-cavity losses. Therefore, it is suggested that a high output coupling, with low feedback, should be used in fiber lasers. Notwithstanding, a too low feedback in the out-coupling end can lead to undesirable effects such as instabilities and trimmed tuning range for tunable lasers. In the practice, the total output power can be nearly independent of the amount of feedback over a wide range of values.

Efficient single-ended output can be obtained for high gain lasers with high output coupling even if the feedback in the other end is relatively low. This is important because it simplifies the cavity design for high-gain systems. Normally, for a Fabry-Perot cavity, the ratio between the power P_1 and P_2 depends on the feedback R_1 and R_2 at the ends as $P_1 / P_2 = \left|(1-R_1)/(1-R_2)\cdot(R_2/R_1)^{1/2}\right|$. The amount of feedback is the fraction of a (guided) laser mode that is reflected at a fiber end and couples back to the guided mode. However, for the case of a multimode fiber, modal cross-coupling would complicate the picture, but for simplicity, we consider single-mode fibers. For example, in a fiber cavity with 20% feedback (for example, from the reflectivity of a bulk grating) at one end and 3.5% (–14 dB) at the other, out-coupling end, the fraction usefully coupled out from the fiber laser becomes 74% of the net power emitted from the fiber, with the other 26% lost in the grating end. Thus, even with a feedback as low as 20% in the grating end of a tunable fiber laser, a high efficiency is still possible.

Obviously, an improved grating end feedback, e.g., with an improved grating-to-fiber coupling efficiency, would improve the efficiency, but this may be difficult in practice. However, it is also likely to improve the output power by reducing the feedback in the out-coupling end. For instance, from the formula above, 92% of the power emitted from the fiber would emerge at the out-coupling end if the feedback is only 0.2% there and 20% at the grating end. Though the Fresnel reflectivity from a perpendicularly cleaved end of a silica fiber becomes ~3.5%, a feedback lower than this can be obtained by angle-cleaving the fiber ends. There are some other alternatives for smaller feedback including anti-reflection coatings. A smaller feedback necessitates a higher fiber gain, which can lead to a smaller output power and a reduced tuning range. However, the required single-pass gain is 17 dB with these cavity end-reflections. This is much smaller than the typical small signal gain of 30 – 40 dB or higher, readily obtained in many rare-earth doped fibers. Thus, the fiber would still be strongly saturated, which implies that the power conversion efficiency would remain almost intact (as would the tuning range).

The expression for the power distribution of two ends of a laser with a Fabry-Perot laser is exact insofar as there are no non-reciprocal elements in the cavity, and the power gain is the same in both directions. However, it does not reveal the actual output power. Therefore, the previously described simulation model was used to evaluate this, in an ytterbium-doped fiber laser. The parameters used in the simulation are: 0 dB propagation loss for an ytterbium-doped fiber with alumino-silicate core in cladding-pumped configuration, with a 200 μm diameter, 0.4 NA inner cladding. The length was adjusted for a 10 dB small-signal pump absorption. The pump was launched into the fiber through its out-coupling end, with 10 W of pump power incident on the fiber facet.

3. DISCUSSION

The results from the simulation are shown in Figure 1 [4]. For example, with 3.5% feedback in the out-coupling end, the output power decreases by a relatively modest 18% if the far-end feedback moves from 100% to 20%. With 40% feedback, the power penalty, relative to 100% feedback, becomes 9%. It would be nice to reduce the penalty further, by increasing the far-end feedback, but if we consider the external tuning configuration, larger feedback than ~40% may be difficult to achieve with an external diffraction grating. However, even with a 40% far-end feedback, the penalty can be reduced with a lower front-end feedback. According to Figure 1, with a front-end feedback of 1%, the power penalty is 5% with 40% far-end feedback relative to the laser output power obtained with 100% far-end feedback.

Note that the feedback of the output coupler was assumed to be controlled with an optical coating deposited directly on the fiber end. The feedback is then equal to the out-coupler reflectivity, and this was assumed to extend also to the pump wavelength. The signal and pump wavelengths are rather closely spaced in an YDFL, and with a relatively simple coating deposited on a fiber end, it would be difficult to provide wavelength discrimination between the two. Thus, the pump launch was directly affected by the near-end feedback in the simulations. It was 90% (9 W) with 10% near-end feedback, and 99% (9.9 W) with 1% near-end feedback. If instead the same pump launch is assumed for all values of near-end feedback, which is also reasonable, the differences between the maximum output powers achieved with different amounts of near-end feedback would be reduced or even disappear.

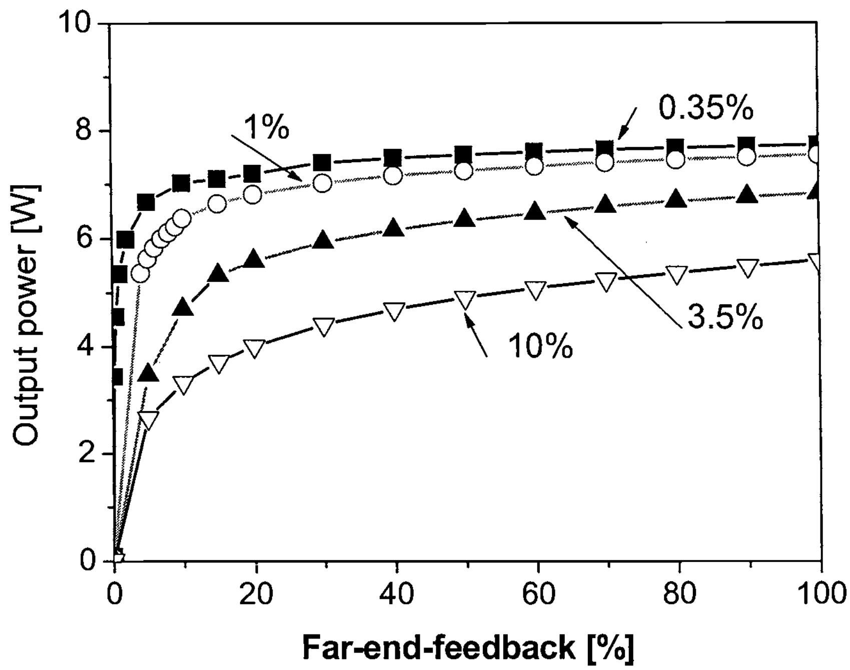

Figure 1. Laser output power vs. far-end feedback: simulations for various amounts of feedback (0.35 – 10%) at the out-coupling end of an YDFL.

4. CONCLUSIONS

Thus, the simulation results shown in Figure 1 confirmed that fiber lasers can operate with high efficiency even with high losses in one end of the cavity (e.g., at an external diffraction grating), if the feedback in the out-coupling end is low. The reason for this is the high gain that can be achieved in fiber lasers, even under saturated conditions. However, to repeat, a high operating gain can lead to problems such as instabilities.

5. ACKNOWLEDGEMENTS

We thank to the National Mexican Council for Science and Technology by supporting part of this research, project G-29141-A.

REFERENCES

1. K. –I. Ueda, H. Sekiguchi, and H. Kan, *in proc. Conference on Lasers and Electro-optic*, Long Beach, USA, 2002, post-deadline paper CPDC4
2. J Limbert, A. Liem, H. Zellmer, A Tünnermann, *Electron. Lett.*, **39**, pp 645-647, 2003
3. J K Sahu, Y Jeong, D.J. Richardson, and J Nilsson, *Opt. Lett.* **28**, pp 1537-1539, 2003
4. JA Alvarez-Chavez, J Nilsson, PW Turner, WA Clarkson, CC Reanud, R Selvas, DC Hanna, and AB Grudinin, *in proc. European Conference on Optical Fiber Communication*, Munchen, Germany, 1999, post-deadline paper LWA5-1.

2005

Novel Multimode Interference Modulator

D. A. May-Arrioja[a], R. J. Selvas-Aguilar[b], P. LiKamWa[a], and J. J. Sanchez-Mondragon[c]
[a] *College of Optics and Photonics: CREOL & FPCE, University of Central Florida, Orlando, FL 32816-2700 USA*
[b] *Centro de Investigaciones en Optica, Lomas del Bosque 115, León, Gto. 37150, México*
[c] *Instituto Nacional de Astrofísica, Optica y Electrónica, Apdo. Postal 51, Tonantzintla, Pue. 7200, México*
Email: may@creol.ucf.edu

Abstract: A new structure for an ultra-compact MMI-based modulator is proposed. Extinction ratios as low as -37 dB are demonstrated. This value is only increased to -35 dB when low electro-absorption effects are included.

OCIS codes: (230.3120) Integrated optics devices; (230.2090) Electro-optical devices; (230.5590) Quantum-well devices; (250.7360) Waveguide modulators.

We propose a new structure for an ultra-compact multimode interference (MMI) InGaAsP multiple quantum well modulator. A schematic of the proposed MMI modulator is shown in Fig. 1(a). The device consists of a 12 μm wide and 350 μm long MMI waveguide. Light is launched and extracted from the MMI region using 2 μm wide single mode waveguides. The dimensions of the MMI region are calculated such that the injected light will be coupled to the output waveguide. The shaded area, denoted by n_1 in Fig. 1(a), indicates the index modulated region.

The operating principle is similar to the Mach-Zehnder modulator, which restricts the coupling of the light into the output waveguide, but our device relies on a much simpler method. The MMI modulator operates under the condition of restricted symmetric interference. In this regime, only the even modes are excited within the MMI waveguide by center-feeding the MMI region with a symmetric mode. This is achieved by injecting the light into the MMI region using a single mode input waveguide. In addition, a shorter device is obtained since the distance at which the first image will be formed is reduced by a factor of four [1]. When the index modulated region is not perturbed, there is no mode conversion, and therefore an exact replica of the input beam is produced at the end of the MMI region, and subsequently coupled into the output waveguide as shown in Fig. 1(b). However, when a π phase shift is induced, as shown by the shaded region in Fig. 1(a), the phase of the propagating modes is asymmetrically modified such that all the even modes are converted to odd modes. Since the output is a single mode waveguide, neither an individual mode nor any combination of the modes will be coupled, this is shown in Fig. 1(c). This allows for modulation of the propagating beam by alternately introducing and removing the applied phase shift.

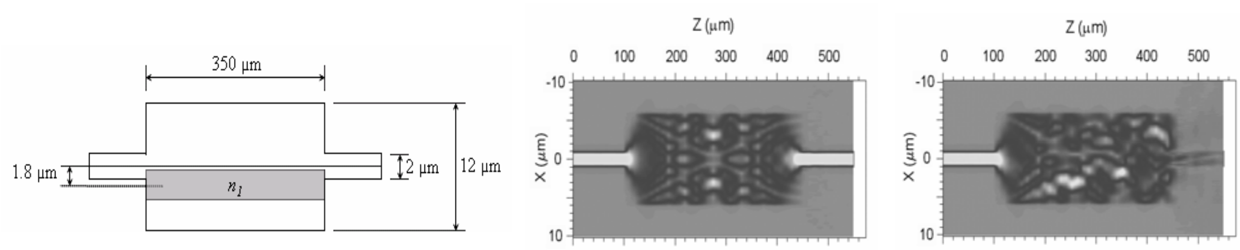

(a) (b) (c)

Fig. 1 (a) Schematic of the device, (b) Beam propagation without index modulation, and (c) Beam propagation with index modulation.

The modulation characteristics are analyzed using the finite-difference beam propagation method. In our simulations, a maximum refractive index change of $\Delta n = 1x10^{-2}$ is assumed in the MQW due to the quantum confined Stark effect (QCSE). An optimum width of 3.5 μm was calculated for the index modulated region which is shifted by a distance of 1.8 μm as measured from the center of symmetry of the device to the center of symmetry of the index modulated region. Extinction ratios as low as –37 dB are demonstrated without electro-absorption effects. For the case of low electro-absorption, which corresponds to a more realistic situation, this value is only increased to –35 dB.

[1] L.C. Soldano and E.C.M. Pennings, "Optical multi-mode interference devices based on self-imaging: principles and applications," *Journal of Lightwave Technol.* **13,** 615-627 (1995).

MMI-based 2x2 photonic switch

D. A. May-Arrioja*, N. Bickel, R. J. Selvas-Aguilar, and P. LiKamWa
College of Optics and Photonics: CREOL & FPCE
University of Central Florida, Orlando, FL 32816, USA.

ABSTRACT

We propose a robust, multi-mode interferometer-based, 2x2 photonic switch, which demonstrates high tolerance to typical fabrication errors and material non-uniformity. This tolerance margin is dependent upon the properties inherent to the MMI design and benefits from the high symmetry of the switch. The key design parameter of the device is to form a pair of well defined self-images from the injected light in the exact center of the switch. In allowing the index modulated regions to precisely overlap these positions, and by creating identical contact features there, any refractive index change induced in the material due to electrical isolation will be duplicated in both self-images. Since the phase relation will remain unchanged between the images, the off-state output will be unaltered. Similarly, offset and dimension errors are reflected symmetrically onto both self-images and, as a result, do not seriously impact the imaging. We investigate the characteristics of the switch under different scenarios using the finite difference beam propagation method. Crosstalk levels better than -20 dB are achievable over a wavelength range of 100 nm when utilizing this configuration. Polarization independence is maintained during device operation.

Keywords: Multimode interference, photonic switch, integrated optics, semiconductor, electrooptic, polarization independent.

1. INTRODUCTION

Multimode interference (MMI) effects are attracting a great deal of interest with respect to their application toward the development of passive integrated devices. Widely investigated, they offer several clear advantages over traditional waveguiding structures, such as very compact size, low polarization sensitivity, and relaxed fabrication tolerances.[1] Moreover, their use has recently been expanded from passive to active devices, and several photonic switches have been proposed that employ MMI effects.[2, 3, 4] The operation of the switching mechanism behind each of these MMI-based switches entails a modification of the refractive index at specific areas within the MMI waveguide. Collocated with the occurrence of multiple self-images, these areas of index modification change the phase relation between the self-images. As a result, the output image is altered, with the light being switched between the output waveguides.

Since, in principle, very efficient switching can be realized, these designs hold significant promise for use in optical networking applications. However, it is necessary to utilize the principle of carrier induced refractive index change in semiconductors to access the large refractive index change required for switching ($\Delta n = 3\times10^{-2}$). Electrical current injection is therefore needed to achieve device operation. This requirement imposes some limitations on the device configuration, due to the fact that the index change is assumed to occur at a very precise region within the MMI waveguide. Any excessive current spreading will seriously deteriorate the switching performance[4] and it then becomes necessary to electrically isolate the index modulated regions from the rest of the MMI waveguide. There are several techniques currently available to achieve electrical isolation, such as zinc in-diffusion and proton implantation.[5,6] The main disadvantage when using these approaches is that, even in the absence of an injected current, an effective refractive index difference exists between the active region and the rest of the waveguiding structure. In the case of proton implantation, this effect results from the difference in the built-in electric field between implanted and un-implanted regions.[6] When zinc in-diffusion is implemented, this occurs due to the presence of the zinc doping.[7] The presence of the built-in refractive index difference could modify the imaging conditions of the MMI waveguide, which would in turn deteriorate the device crosstalk. Ideally, the contacts used for current injection should have the same dimensions as the index modulated regions. In actuality though, a finite amount of current leakage can be anticipated regardless of the

*Email: may@creol.ucf.edu; Phone: (407) 823-6862; Fax: (407) 823-6880; www.creol.ucf.edu

Optoelectronic Devices: Physics, Fabrication, and Application II, edited by Joachim Piprek,
Proc. of SPIE Vol. 6013 (SPIE, Bellingham, WA, 2005) · 0277-786X/05/$15 · doi: 10.1117/12.630955

isolation technique. Therefore, the width of the index modulated region will always be wider than that of the contact.

Moving from simulation to the actual device fabrication often requires implementing changes to the optimum design parameters in order to account for physical realities and material limitations. In the case of an MMI switch, contact width reduction might be required in order to isolate adjacent contacts, and also to better define the refractive index modulated regions. This will, however, create finite sections within the MMI waveguide that possess an effective index change, which can lead to deterioration of the switch crosstalk. Moreover, during device fabrication, we often have to deal with offset errors resulting from the misalignment between different masking layers. Such a displacement of the index modulated regions, with respect to the optimum positioning, is potentially a very serious issue. This offset error may cause an imbalance in the phase of the adjacent self-images, thereby making it impossible to achieve the phase difference required for switching. An error of this type would manifest as an increase in the switching crosstalk. It is therefore very important to address these issues during the design of an MMI-based switch.

In this paper we propose a highly robust 2x2 MMI-based photonic switch and carry out a comprehensive analysis of the device performance as related to the deviation from the optimum dimensions of the index modulated regions. We also demonstrate that the device is extremely tolerant to material non-uniformities and typical fabrication errors. This is a consequence of the MMI design and the high symmetry of the switch. The switch characteristics, under different scenarios, are investigated using the finite difference beam propagation method (FD-BPM). In the device configuration presented in this paper, polarization independence is maintained, even as crosstalk and switching contrast levels better than -20 dB are projected over a wavelength range of 100 nm.

2. SWITCH DESIGN

Fig. 1 shows a schematic of the proposed switch. The device consists of a MMI waveguide with a width of W=18 µm and a length of L= 998 µm. Light is launched using 3 µm wide input and output waveguides that are separated by 3 µm. The shaded zones correspond to the index modulated regions. The dimensions of the MMI switch were calculated using the well known relations for restricted interference in MMI waveguides.[1] The length is set to correspond to the beat length, such that light coupled to the upper input waveguide will be imaged into the lower output waveguide during the off-state, as shown in figure 2(a). The device modeling incorporated a 1 µm thick InGaAsP guiding layer ($\lambda_g = 1.3\ \mu m$) and a 1.5 µm thick InP top cladding layer. The refractive indices of the layers are 3.41 and 3.17 respectively.

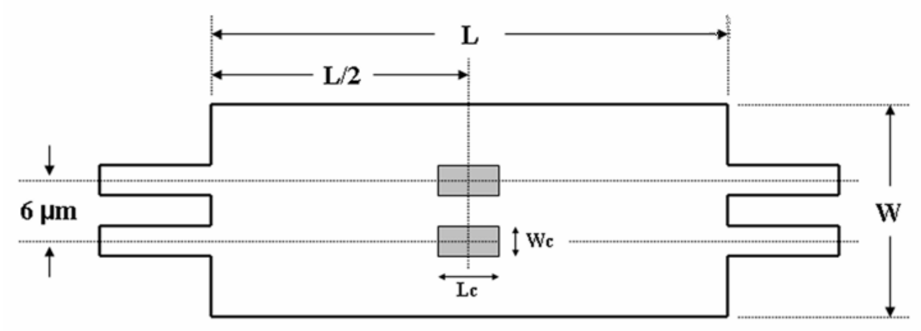

Fig. 1. Schematic of the 2x2 photonic switch and design parameters.

The most critical parameter for ensuring proper device operation is the requirement that the injected light create a pair of well defined self-images in the exact center of the switch, and that each self-image is bisected by the central axis of one of the two access waveguides, as shown in Fig. 2(a). The index modulated regions are located so that they precisely overlap the positions where these two self-images are formed. By creating identical features at these locations, the off-state output will remain unchanged since any variances induced in the material's refractive index due to electrical isolation will be duplicated in both self-images. Similarly, the final imaging properties of the device are not seriously affected by offset and dimension errors, which are highly symmetric with respect to the axis centered between these two images. It is important to note that, in the on-state, only one of the index modulated regions will be active.

The operation of the switch is as follows: In the absence of an applied current, light coupled to the upper input waveguide is emitted from the lower output waveguide, and vice-versa. However, when a π phase shift is applied to either one of the index modulated regions, light coupled to the upper input waveguide will be imaged onto the upper output waveguide, as shown in Fig. 2(b). A similar performance is achieved for light coupled to the lower input waveguide. Current injection was used to obtain the required phase shift, with a maximum refractive index change of 1%.[4] The dimensions of the index modulated regions were selected so as to obtain the lowest possible crosstalk for both TE and TM polarizations at a wavelength of 1.55 µm. In this case, an optimum width and length of Wc=3.5 and Lc=28 µm were calculated, respectively.

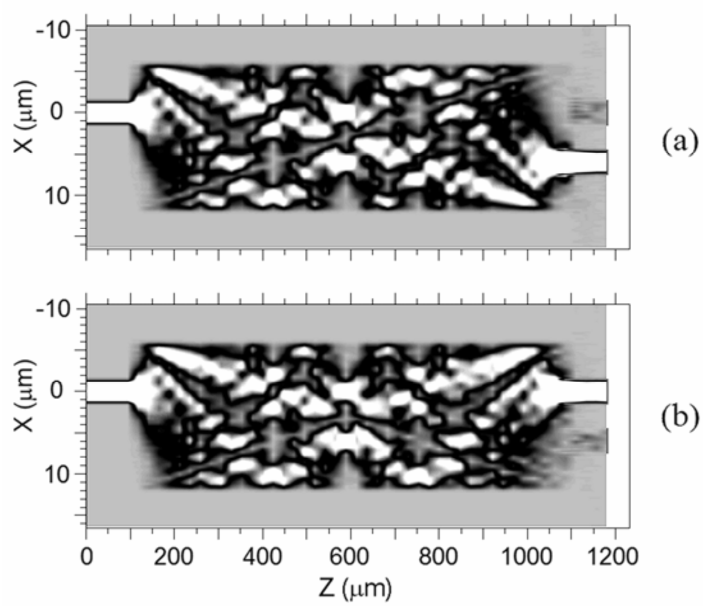

Fig. 2. Beam propagation characteristics (a) Without index modulation, and (b) With π phase shift applied to lower index modulated region.

3. ANALYSIS

The FD-BPM was used to investigate the switch performance. For both device contacts, an initial refractive index change of $\Delta n_1 = 1\times10^{-2}$ due to contact isolation[6,7] was assumed for all simulation runs. While this value is marginally higher than what could typically be expected, it helps to demonstrate the high tolerance of the device to such effects. Also included in the simulations is an intrinsic propagation loss of 5 cm^{-1}, as well as increased absorption losses for the index modulated areas as a result of carrier injection.[4]

For each switching state, the analysis considered a combination of effects that can result in a deterioration of the optimum crosstalk. During the off-state, we were mainly concerned about modifications to the imaging due to Δn_1 variance induced through contact isolation. Reducing the contact size, as previously mentioned, may be a necessary step to keep the injected current within the optimum value calculated for the refractive index modulated region. However, this also reduces the area that is affected by Δn_1, which could have a detrimental effect during the off-state operation. To determine the extent of the effect, the contact width (Wc) was modified from 3.5 to 1.5 µm, and the off-state crosstalk was calculated for each case. As shown in Fig. 3 the induced perturbation Δn_1 stays entirely within the image as the contact width is reduced, and has a negligible effect on the off-state crosstalk. Furthermore, lateral offset errors typically encountered during device fabrication are included in the simulation. With the current state of available technology, the offset can be easily controlled within +/- 0.5 µm. In Fig.4, we show the off-state crosstalk for different contact widths as a function of the offset error along both directions. As anticipated, there is an increase in the crosstalk as the contact is shifted away from its nominal position. However, even when the contact width is reduced to 1.5 µm, and shifted by +/- 0.5 µm, the calculated crosstalk is still better than -35 dB. Additionally, since a narrower contact will remain within the image, even with an offset applied, a reduced contact width results in a more symmetric response. Offsetting a wider contact, though, generates an asymmetric phase shift in the images, and therefore, the response becomes asymmetric with respect to the offset position. Unexpectedly, there is a position for *Wc* = 3.5 μm at which the crosstalk is slightly lower than that calculated for the nominal position. Nevertheless, the selected nominal position provides the best switching performance when wavelength and polarization dependence are considered.

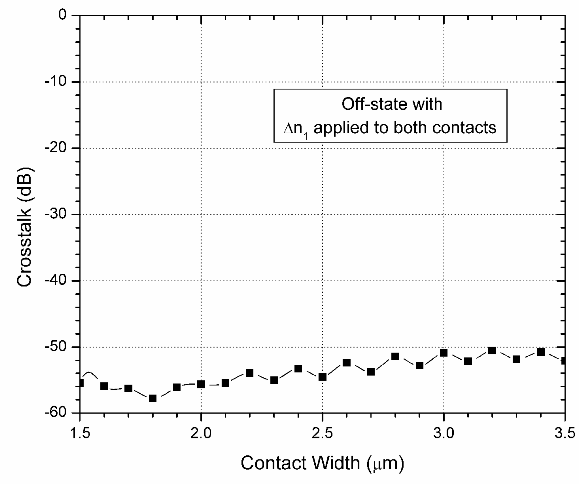

Fig. 3. Off-state crosstalk as a function of contact width.

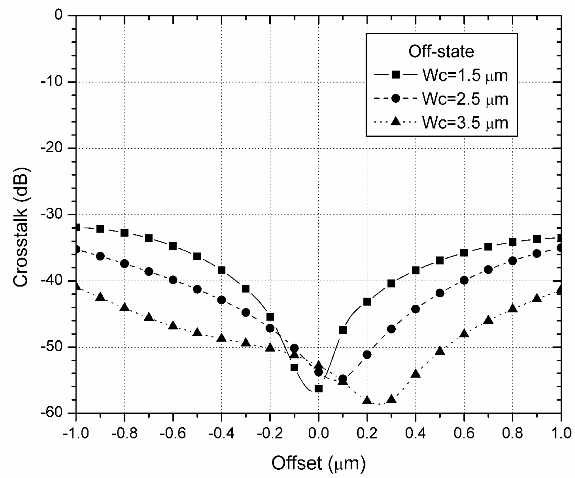

Fig. 4. Off-state crosstalk for different contact widths versus lateral offset.

During the on-state, the primary concern centers on whether the injected current will be confined within the optimum index modulated region. From the above it is found that reducing the contact width does not significantly influence the off-state crosstalk, consequently a contact width *Wc*=1.5 μm is selected for the following simulations. As previously mentioned, irrespective of the isolation technique, an effective increase in the contact width due to a slight current leakage can always be expected. Therefore, it is important to determine the effects of increasing the width of the index modulation region. We define an effective index modulated width as *Wi*=*Wc*+*C*, where *C* represents the total amount of current spreading namely 2 μm, 3 μm and 4 μm. As shown in Fig. 5, increasing this width has only a minimal effect on the on-state crosstalk, with the value maintained below -30 dB. To maintain completeness, the added effects of offset errors were considered, and the resulting crosstalk characteristics are presented in Fig. 6. For this situation, we can see that the device becomes less sensitive to offset errors as the width of the modulated regions is increased. This is expected since, despite increases in the width of the modulated region, the phase shift is still applied over the entire image. The presence of offsets or the lack thereof has no effect on the response in this case. This robustness directly results from the switch's high symmetry, and therefore, typical lateral offset errors can be considered negligible for the on-state operation.

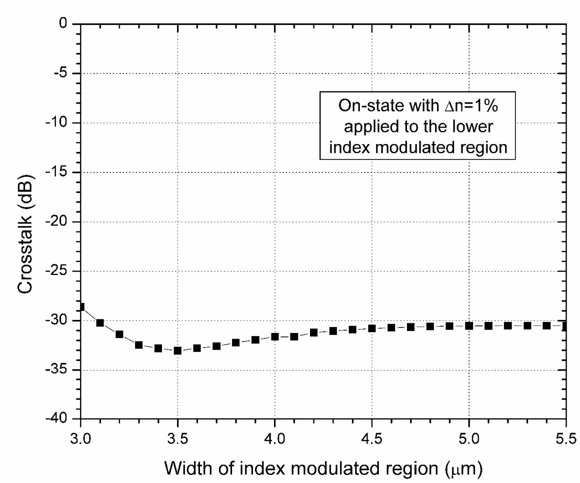

Fig. 5. On-state crosstalk versus modulated width.

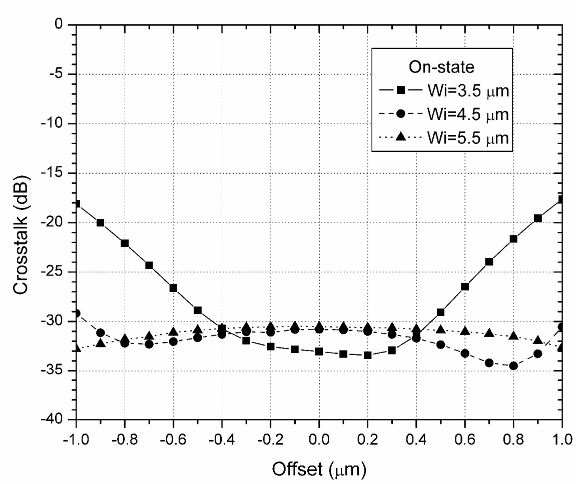

Fig. 6. On-state crosstalk for different index modulated widths versus lateral offset.

We also investigated the polarization and wavelength response of the switch. The wavelength was scanned from 1.45 to 1.65 µm for both TE and TM polarizations, and for both states of operation. As shown in Fig. 7, there is a 100 nm window within which the crosstalk can be maintained below -20 dB for both polarizations. Initially, the switching speed is limited by depletion of the injected carriers (typically within the nanosecond range). However, this restriction could be eliminated by taking advantage of the remarkable symmetry exhibited by the device. One way to overcome the carrier lifetime limitation is to sweep out the injected carriers from the active region. This has often been accomplished by reverse biasing the active region.[8,9] In our device, both contacts could be reverse biased during the off-state without a major change in the off-state crosstalk, and needing only very low power consumption. During the on-state, one of the contacts is forward biased so that the light is switched. When the switching is completed, the contact is reverse biased such that the carriers are swept out of the active region, allowing a faster transition between the on and off states.

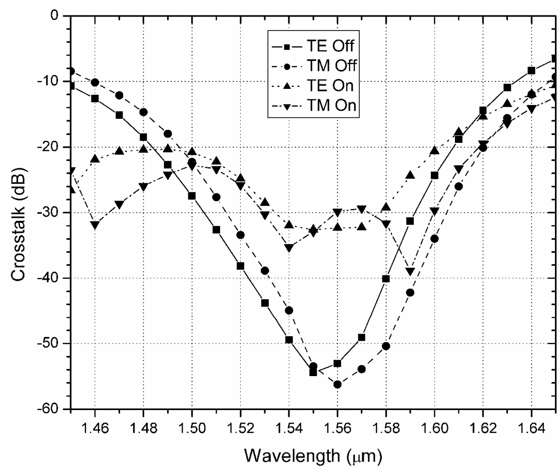

Fig. 7. Wavelength and polarization dependence of switch crosstalk for both operation states.

According to our results, it is evident that contact dimensions can be modified as required to achieve optimization of the index modulated region, without any significant deterioration of the switch performance. This demonstrates the feasibility of using very simple isolation techniques, such as zinc in-diffusion, in the fabrication of high performance photonic switches. Lastly, it should be mentioned that while the length of the switch can be reduced by decreasing the width of the MMI region, the switch becomes increasingly more sensitive to the issues that we have discussed above. These issues can lead to a deterioration of the crosstalk, and a narrowing of the operational window for both polarization and wavelength independence. The dimensions used in our calculations correspond to the best device performance that can be achieved given the expected tolerance limits of conventional device fabrication techniques.

4. CONCLUSIONS

A highly robust 2x2 MMI photonic switch has been proposed, and we have shown that the switch can be made extremely tolerant to perturbations resulting from material modifications and fabrication errors by appropriate selection of the MMI design. By utilizing this configuration, crosstalk levels better than -20 dB can be realized over a wavelength range of 100 nm. This switching performance makes the switch a perfect candidate for incorporation into future wavelength division multiplexing systems. Furthermore, the device has demonstrated polarization independence and has shown that limitations in switching speed resulting from the depletion of carriers could be significantly reduced by taking advantage of the high symmetry inherent to the MMI structure.

REFERENCES

1. L.B. Soldano and E.C.M. Pennings**,** **"**Optical multi-mode interference devices based on self-imaging: principles and applications**"**, *J. Lightwave Technol.,* **13,** 615-627, 1995.

2. C.H. Lien, H.H. Lin, S.W. Weng, H.J. Wang, and W.C Chang, "A compact photonic switch based on multimode interference with partial index-modulation regions", *Microwave Opt. Technol. Lett.*, **33,** 174-176, 2002.
3. M. Yagi, S. Nagai, H. Inayoshi, and K. Utaka, "Versatile multimode interference photonic switches with partial index-modulation regions", *Electron. Lett.*, **36,** 533-534, 2000.
4. S. Nagai, G. Morishima, H. Inayoshi, and K. Utaka, "Multimode interference photonic switches (MIPS)", *J. Lightwave Technol.*, **20,** 675-681, 2002.
5. I. Yun and K. Hyun, "Zinc diffusion process investigation of InP-based test structures for high-speed avalanche photodiode fabrication", *Microelectron. Journal*, **31,** 635-639, 2000.
6. T. Huang, Y. Chung, L.A. Coldren and N. Dagli, "Field-induced waveguides and their application to modulators", *IEEE J. Quantum Electron.*, **29,** 1131-1143, 1993.
7. F. Ito, M. Matsuura and T. Tanifuji, "A carrier injection type optical switch in GaAs using free carrier plasma dispersion with wavelength range from 1.06 to 1.55 μm", *IEEE J. Quantum. Electron.*, **25,** 1677-1681, 1989.
8. P.J. Duthie, N. Shaw, M.J. Wale and I. Bennion, "Guided wave switch array using electro-optic and carrier depletion effects in indium phosphide", *Electron. Lett.*, **27,** 1747-1748, 1991.
9. Barrios C. Angulo, V.R. Almeida, R. Panepucci and M. Lipson**, "**Electrooptic modulation of silicon-on-insulator submicrometer-size waveguide devices", *J. Lightwave Technol.*, **21,** 2332-2339, 2003.

Bistability, Chirping and Switching in a Nonlinear and Partially Nonlinear Cylindrical Photonics Crystal

J. Sanchez-Mondragon[1], J. Escobedo-Alatorre[2], M. Tecpoyotl-Torres[2],
M. Basurto-Pensado[2], R. Selvas-Aguilar[3] and M. Torres-Cisneros[4]
[1]National Institute for Astrophysics, Optics, and Electronics (INAOE), P.O. 51 & 216, Z.P. 72000, Puebla, Mexico
[2]Autonomous State University of Morelos (UAEM). Research Center of Engineering and Applied Sciences, CIICAp, Av. Universidad No. 1001, Z.P. 62210, Cuernavaca, Mor., Mexico.
[3]Research Center on Optics. Lomas del Bosque No. 115, Col. Lomas del Campestre. León, Guanajuato.
[4]Faculty of Mechanics, Electrical and Electronics Engineering (FIMEE).
Lascuráin de Retana No. 5, Centro, 36000, Guanajuato, Gto. México

ABSTRACT

The study of nonlinear photonics crystals is quite complex and cumbersome [1-5], because of their inherent architectural complexity and, in addition, because of the nonlinearity that couples propagating and counterpropagating waves. However, they are quite attractive because of their potential capabilities, and that has lead to use different approximated methods. In a one dimensional stack, it has been successfully demonstrated that they show switching, bistability and chirping as nonlinear characteristics. Band gap solitons are a well established feature of the coupled wave equations. We have extended a method that have previously shown its success for a stack with a Kerr nonlinearity, to a much more complex structure such as an omniguide fiber, as part of our suggestion that such method could be applied to numerical or analytical methods as long as the linear solution were available. Such a restriction, hinder our ability of getting analytical solution beyond their enabling approximations, however, it is completely adequate for the purpose of to develop devices.

A comparative numerical analysis of a one dimensional photonic crystal and an omniguide fiber, made of a dielectric and stratified linear and nonlinear media, has been carried out. They were considered as multilayer arrangements with a finite numbers of periods: linear-linear, nonlinear-linear and nonlinear- nonlinear in order to study and isolate those features. Finally, a comparison of multilayer systems with variations in the diffraction indexes profiles is presented.

Keywords: Photonic crystal, perturbative approach, Slowly Varying Envelope Approximation, bistability, chirping and switching.

I. INTRODUCTION

Photonic Crystals (PC) are already complex enough to, in addition, consider nonlinear features. However, their wide possibilities that go from switches, logic and all optical storage devices make worthwhile additional approaches. In fact, manufacturing of much more complex PC structures is not a deterrent, since we are confident on our mastering of the nanofabrication techniques that includes both linear and nonlinear materials. Nanofabrication has allowed creating almost any structure for a linear PC, and it is clear that such a capability will not be an essential restriction on a

Photonic Crystal Materials and Devices III, edited by Ali Adibi, Shawn-Yu Lin, Axel Scherer,
Proc. of SPIE Vol. 5733 (SPIE, Bellingham, WA, 2005) · 0277-786X/05/$15 · doi: 10.1117/12.591390

Nonlinear PC (NLPC). The complexity of a linear PC structure has been given enough support to produce generic codes, often available to the public and even commercial.

On the other hand the propagation in NLPC [6] is characterized for both, complex PC structures and a nonlinear dynamics, which prevents the linear PC handling of the now, strongly coupled counterpropagating waves. Propagation in a nonlinear homogeneous media describes precisely a media that is not further independent of the propagating radiation and where the propagating and counterpropagating waves are strongly coupled everywhere in the material. In addition, a linear PC is described by its material characteristics, resumed on the photonic band gap structure that is a quite convenient concept to understand a device. Such an expectation remains in a nonlinear PC, however, the modified band gap reflects the interaction with the field and that should reflect the observed phenomena. Nonlinear propagation in homogeneous media has introduced concepts such as solitons, nonlinear chirping and bistability in a media where the nonlinearity is at its core, or where the nonlinearity is at the substrate such as in resonant pulse propagation on the presence of nonlinearity. Therefore, we should expect that those features will also occur, somehow, in an inhomogeneous material such as a NLPC. There are two approaches that have significant contributions in this direction.

a) The solution in a stack in a Slowly Varying Envelope Approximation (SVEA) that has lead to the Coupled Mode Equations, and that assume that the solution is of the form $E_\omega = E_0\ \mathcal{E}(z)\ e^{ikz}\ e^{-i\omega t}$, where $\mathcal{E}(z)$ is the SVEA envelope and satisfies the Mode Coupled Equations, that among others produce a symmetric photonic bandgap and solitons.
b) Chen and Mills proposed that the solution in a Slab is of the form $E_\omega(z) = E_0 \varepsilon(z) e^{i\phi(z)}\ e^{-i\omega t}$, explicitly exhibiting the intensity dependence of the chirping $\Phi(z)$, in addition of a real envelope and two constant of each variable.

The SVEA approach requires of low contrast, and in fact of limiting the reflected signal [7]. On the other hand the effort of Chen and Mills to develop an M matrix nonlinear procedure did not find a way to overcome such a difficulty and this methodology had to resort to a reduced role for the reflected signal, and such a restriction was in its limit introduced by Winful et al. [8]. In either case, the geometry they have considered is one dimensional or Cartesian, but is already evident that both proposals should lead to some relation. There is enough evidence to guide an analysis of more complex structures. A one dimensional stack has been demonstrated to show switching, bistability and chirping. On the other hand, spatial solitons, in circular and in particular in an annular cross sections, have been demonstrated [9] using and one dimensional analytical analysis. The need to integrate, this disperse evidence is one of our objectives.

We will explore the most typical characteristics of a nonlinear PC on two simple examples, a stack and an omniguide fiber. Without restricting ourselves to a null reflective signal as was done by Winful et al. [8], in a series of papers that also emphasizes the device point of view, but that however pointed out the lead to a specific type of analytical solutions that explicitly exhibit chirping and is not in the frame of the SVEA. Null reflectivity is a very sensible assumption on specific cases [10], but we will focus on its explicit presence. A second, and closely related set of analytical solutions are those that lead to Gap solitons introduced as early as Chen and Mills [11], that are obtained by the SVEA, that requires that the difference between the refraction indexes is small, an undesirable condition for wide use of NLPC. Actual solutions were given by Aceves and Wabnitz [12] and Christodoulides and Joseph [13], and are widely reviewed [14], generalized [15] and experimentally demonstrated [16]. Disregarding the index restriction, does not rule out the existence of solitons solutions, however, those will be in addition those SVEA solitons, that at the core of the approximated methods developed by Goodman [17] and supported by experiments cited there.

We introduce an iterative method to buildup the nonlinear, Kerr type, solution, more along the lines of an effective dielectric constant. The numerical nonlinear method is based on the introduction of small intensity dependent perturbation on the lineal method by means of infinitesimal changes and corrections on the nonlinear refraction index, repeatedly, until converging to the conditions of the wanted nonlinearity. The internal field (that is the overlapping of the forward and backward incident waves within the material); it is infinitesimally modified in each iteration and reintroduced in the change of the refraction index for a new iteration. A series of iterations of the propagation are carried out, and each propagated anew. We keep adding and correcting small effects due to the non linear index of the material. Reintroducing the correction iteratively, the solution for the system converges. As a demonstration, we carry out this process in a system with a Kerr non linearity [18].

2. SINGLE SLAB: ANALYTICAL METHOD

In this section we discuss briefly the methodology used by Chen and Mills [4] to discuss a single nonlinear slab without using the SVEA. They consider that the polarization is customarily given by:

$$P = \int_{-\infty}^{t} \varepsilon(x, t-t')E(x,t')dt' \qquad \text{or} \quad P_\omega = \varepsilon_\omega(x)E_\omega(x) \tag{1}$$

with a frequency Kerr Nonlinearity term given by $P_{nl}(x,\omega) = \beta I_\omega$ where $I_\omega = |E_\omega(x)|^2$ is the spectral intensity. The resulting wave equation is given by:

$$\frac{\partial^2 E_\omega(x)}{\partial x^2} - \left(\frac{\omega}{c}\right)^2 \varepsilon_\omega(x)E_\omega(x) = 0 \text{, where} \quad \eta = \eta_0 + \beta I_\omega \tag{2}$$

The single lossless and nonlinear n_{th} slab is described, Chen [19], by:

$$\frac{d^2E_\omega}{dz^2} + (1 + \beta_n |E_\omega|^2)E_\omega = 0 \tag{3}$$

where β_n is the nonlinear coefficient of that layer and z = x k_n . There are several approaches to solve this equation; one of them is resorting to the SVEA, which corresponds to actually riding on the basic plane waves linear solutions. However, Chen focuses its solutions on the chirping on the slab, by proposing a solution of the form:

$$E_\omega(z) = E_0 \varepsilon(z) e^{i\phi(z)} \tag{4}$$

where $\varnothing$ is the chirping and ε is a real envelope. After substitution on the wave equation, Chen obtains an intensity dependent for the chirping and the real envelope given by:

$$\frac{d\phi}{dz} = \frac{w}{\varepsilon^2} \tag{5}$$

$$\int_{I_n(d)}^{I_n(x)} \frac{1}{\left(w^2 + aI - I^2 - \frac{1}{2}\widetilde{\beta_n} I^3\right)^{1/2}} dI = \pm 2k_n(x-d) \tag{6a}$$

$$\widetilde{\beta_n} = \beta |E_0|^2 \text{ and } \ I_n(z) = \varepsilon^2(z) \tag{6b}$$

where w and a are two integration constants, that were not further explored. The first one w is directly related to the chirping, and Matulic [20] in a similar problem of Self Induced transparency on Two Level Atoms in a nonlinear substrate identified a as the rate of flux along the propagation axis.

The envelope solutions as described by Eq. (6) are given by complex elliptic Jaccobi functions in terms of three parameters: w, a and $\widetilde{\beta_n}$. Its importance can be pointed out, if we rewrite this integral equation in a much more convenient and understandable form:

$$\int_{\alpha}^{\beta}\frac{1}{\left[1-i^2-\gamma i^3\right]^{1/2}}di=\pm 2k\mathrm{B}^{1/2}(x-d) \qquad (7)$$

by the change of variables:

γ = ½ β $A^{1/2}/B^{3/2}$ and $i = I/I_{th}$

Where: $I = I + ½ a - s$ with $s = 3 (a/2)^2 \widetilde{\beta_n} / (1+ 3/4\ \widetilde{\beta_n}\ a)$

and $I_{th} = [A/B]^{1/2}$

with: $A = w^2 + (½ a)^2 - s^2 - ½\ \widetilde{\beta_n}\ (½ a - s)^3$ and $B = 1+ 3/2\ \widetilde{\beta_n}\ (½ a - s)$

This threshold value I_{th} has a definite meaning, as such differentiating between oscillatory solutions ($I < I_{th}$) such as the plane wave like and other of the hyperbolic type ($I > I_{th}$). In particular, this value is expressed primarily by those integration constants ($\widetilde{\beta_n} \rightarrow 0$):

$$I_{th} \approx [w^2 + (½ a)^2]^{1/2} \qquad (8)$$

The integral is quite complex, however the first condition, describes oscillatory functions sine and cosine according to the sign selection, the second one describes hyperbolic functions that leads to the possibility of another class of pulse like solitons that will be discussed elsewhere. The type of solution was determined primarily by I_{th}, therefore, the oscillatory solutions can be explored for very small $\widetilde{\beta_n}$ (i.e. γ) to recognize its relation to plane wave solutions. The lowest approximation, choosing the negative sign, is given by:

$$I = I_0 + I_{th} \cos [2k\mathrm{B}^{1/2}(x-d) + q_0] \qquad (7)$$

A perturbative approach allows us to rewrite this equation as:

$$\int_{\alpha}^{\beta}\frac{1}{\left[1-i^2\right]^{1/2}}di+\gamma\int_{\alpha}^{\beta}\frac{i^3}{\left[1-i^2\right]^{3/2}}di \simeq \pm 2k\mathrm{B}^{1/2}(x-d)$$

And
$$\arccos(i) \simeq \pm 2k\mathrm{B}^{1/2}(x-d)-\frac{\gamma}{\left[1-i^2\right]^{1/2}}-\gamma\left[1-i^2\right]^{1/2}$$

Then the solution:

$$i = I_{th} \cos [\Theta - \gamma \csc \Theta - \gamma \sin \Theta] \quad \text{where} \quad \Theta = 2k\mathrm{B}^{1/2}(x-d) \qquad (8)$$

will have Kerr and constant of motion corrections trough γ corrections. The selection of opposite signs will produce and analog sine solution:

$$i = I_{th} \sin [\Theta - \gamma \sec \Theta - \gamma \cos \Theta] \tag{9}$$

Therefore, after substitution, we can rewrite our proposed solutions for a slab (Eq. (4) and (5)).

Chen and Mills disregarded the stack reflection on their solution, however, pointed out the intensity dependent chirping for a slab as one of the characteristics on the propagation in a nonlinear layer. We shall prove that this is a characteristic of the stack as a whole and more generally for a PC.

3. NUMERICAL METHOD

Currently, we own not only an advanced capability of manufacturing PC, but also a developed numerical and analytical technology that allows us to solve almost any of the linear PC that we may be interested, and that we may describe by solving the linear equation:

$$\Lambda(\eta_0)E_\omega = 0 \tag{12}$$

for every slab (in the case of a one dimensional stack) or layer (in an omniguide fiber). Where $\Lambda(\eta_0)$ in most cases is a differential operator, with a linear refraction index η_0 that characterizes that slab, and that leads to a solvable PC. For the sake of clarity, we will refer to a nonlinearity of the Kerr type; however, the method can be adequate to much other nonlinearity.

The solution of the nonlinear propagation in a NLPC, compared with the solution in a single nonlinear slab o layer, is by far much more cumbersome even for very regular arrays as the ones already mentioned. The nonlinear coupling of the forward and backward waves becomes an unmanageable problem, unless we can make an approximation such as minimizing the reflected wave. The first problem is to solve, slab by a slab of the stack or fiber layer, of a nonlinear equation of the form:

$$\mathrm{N}_L(\eta^2)E_\omega = 0 \tag{13}$$

where the nonlinear operator for a Kerr type nonlinearity can be described in the following form:

$$\mathrm{N}_L = \Lambda(\eta_0) + (\eta^2 - \eta_0^2\ ) \tag{14}$$

That has been already outlined in the previous section. However, an inhomogeneous media such as a PC is much more complex, and we need to develop reliable alternatives. Such is the case of the development of an iterative method that solves Eq. (15) as an approximation to the NLPC described by Eq. (13):

$$\Lambda(\Delta\eta_{N,i}^l)E_\omega = 0 \tag{15}$$

$$\eta_{N,i}^l = \eta_{0,i} + \Delta\eta_{N,i}^l \tag{16}$$

$$\Delta\eta_{N,i}^l = (1-\gamma)\ \Delta\eta_{N,i}^l + \gamma\beta_{N,i}I_{N,i} \quad \text{with} \qquad I_{N,i} = \left|E_\omega\right|^2 \tag{17}$$

where:
- $\Delta\eta$ Intensity dependent change of the refraction index each iteration
- γ Correction parameter
- l Iteration number
- η Nonlinear refraction index

i	Dielectric medium index in the layer, ($i=1,2$)
N	Period Number on the stack
$\eta_{0,i}$	Lineal refraction Index of each dielectric medium
β	Non lineal material coefficient
I	Electric field mean intensity at each step

We have developed this method for a one dimensional stack, already reported, for an omniguide fiber, whose linear solutions are also reported in this meeting (paper 5733-38). For a stack the nonlinear equation to solve are given by:

$$\mathrm{N}_L(\eta^2)E_\omega = \frac{d^2E_\omega}{dx^2} + \eta^2 E_\omega = 0 \quad \text{with} \quad \Lambda = \frac{d^2}{dx^2} + \eta_0^2$$

It is clear, that the plane wave method applies at every step of this procedure, according to Eq. (15). Also, in the case of an omniguide fiber, the transversal equation is described by the Bessel equations. This is indeed the limitation of the method, since we do not approximate the functional solution as the SVEA method does, but the system response as described by its nonlinear refraction index for arbitrary refraction index difference.

Figure 1 shows the typical convergence and its dependence on β. Also, the material characteristics (band gap) become field dependent trough the refraction index and the internal field, that describes the coupling of the forward and backward incident waves within the material.

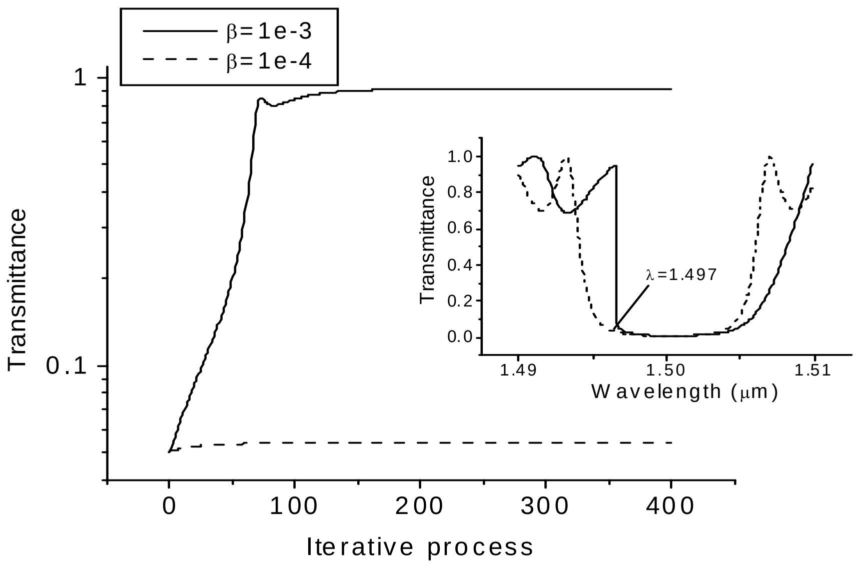

Figure 1: Convergence of the solution as a function of the wave vector.

In the following section, we will describe some of the most typical phenomena of this nonlinear systems, comparing a stack with the transversal section of an omniguide fiber, they are: switching, bistability and chirping.

4. NUMERICAL RESULTS

SWITCHING

A stack can be characterized by its forbidden photon gap, which shows an intensity shift due to the presence of high intensities as shown in the inset of Fig. 2. Under such conditions, for example, a narrow frequency (quasi monochromatic) pulse on the lower edge of the photonic gap, at low intensity is rejected, but at high intensities can be transmitted and therefore, we have switching (see Fig. 2).

Such a behavior will show in other PC structures as well. This is the case of an omniguide fiber by describing the changes of the radial photonic gap as a function of β, to describe a change of intensity according to Eq. (6a), when one of the layers is nonlinear or both of them are nonlinear.

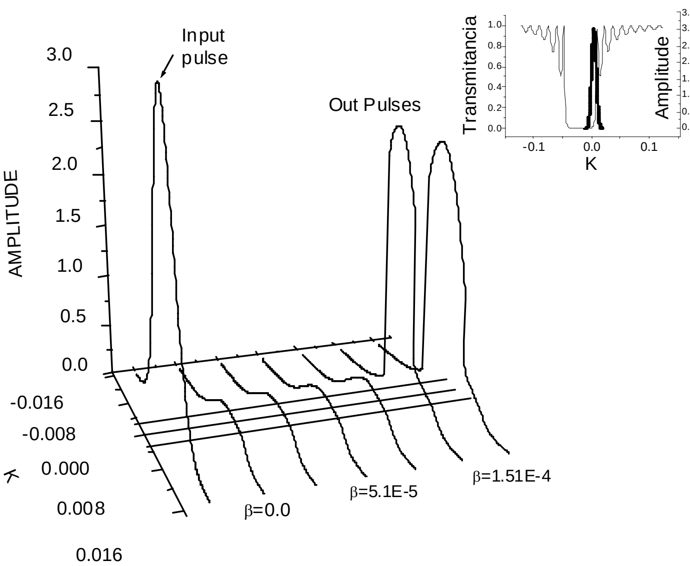

Figure 2: Switching. An originally rejected pulse, with the increasing of power can be transmitted.

For the case of a one-dimensional stack, we are going to carry the one-dimensional comparison of two different cases. In the first two cases we will consider the linear refraction index η_0. In the first case, only the second one is nonlinear $\beta \neq 0$ and in the second case, both of them are nonlinear and with the same β value. We have chosen the same η_0 for both cases, but in the first case, only the first one is nonlinear (Figure 3a). In the second one, both of them have the same nonlinearity (Figure 3b). In the background we can recognize the linear band gap as a reference, and the increasing nonlinearity produces a small shift of the center of the band gap, but quite a noticeable stepping or red shift of the blue band edge, with the consequent narrowing of the gap. When both of them have the same nonlinearity, it is evident that the width remains, however such a shift and stepping occurs.

On the other hand, *for the case of a cylindrical geometry (bidimensional)*, we analyze the same cases presented above. In Fig. 4a, we show the changes that occur on photon gap, as a consequence of nonlinearities (we consider nonlinear effects for both materials with refraction indexes η_1 and η_2, respectively).

We show the double effect in Figure 4b, where we consider as nonlinear only to the first material (η_1). This figure shows the shift of the band, as well as a narrowing of the band. This last effect is due to the increase on the first refraction index due to the nonlinearity, and the decrease of its difference with η_2.

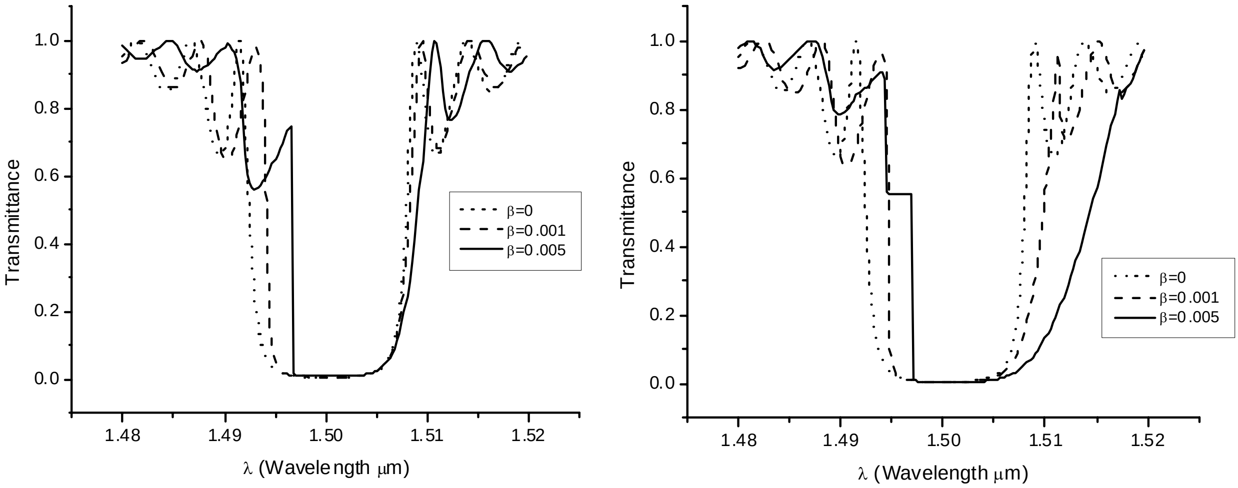

(a) (b)

Figure 3: a): An alternating linear and non linear stack is shown. The nonlinear layers are those of lower refraction, and because the nonlinearity, the refraction indexes difference decreases, and henceforth the width of the transmission band. However is quite noticeable a stepping of the low edge of the gap. b) The variations of the transmittance band due to the same nonlinearity in both media.

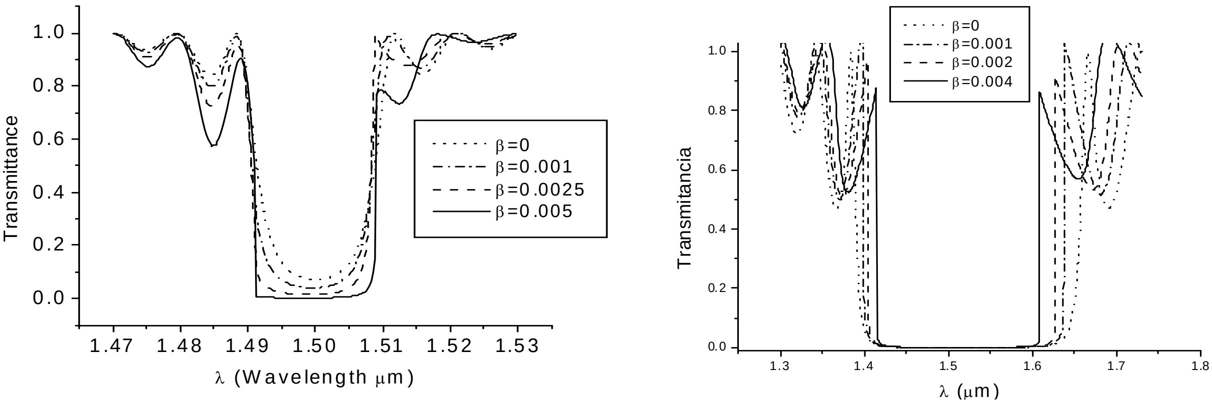

(a) (b)

Figure 4: a) Transversal propagation in a multilayer cylindrical system, where we show the nonlinear effect of $\beta_1 = \beta_2$. b) Transversal propagation in a cylindrical multilayer system, where we show a double effect due to the nonlinearity $\beta_1 \neq 0,\ \ \beta_2 = 0$.

Finally, *for the one dimensional case (stack)*, we analyze the formation and disappearance of the photonic gap (switching off and on) as a consequence of intensity if only one of the dielectrics is nonlinear. In a stack with the same linear η_0 for both dielectrics, a partial gap is formed at several values of β (see Figure 5a). A nonlinear stack switch is produced with slightly different refraction indexes of very close values. If the lower refraction index is nonlinear, and this nonlinearity increases, then the difference between indexes is reduced by an increasing intensity. Then, the photonic gap disappears (see Figure 5b).

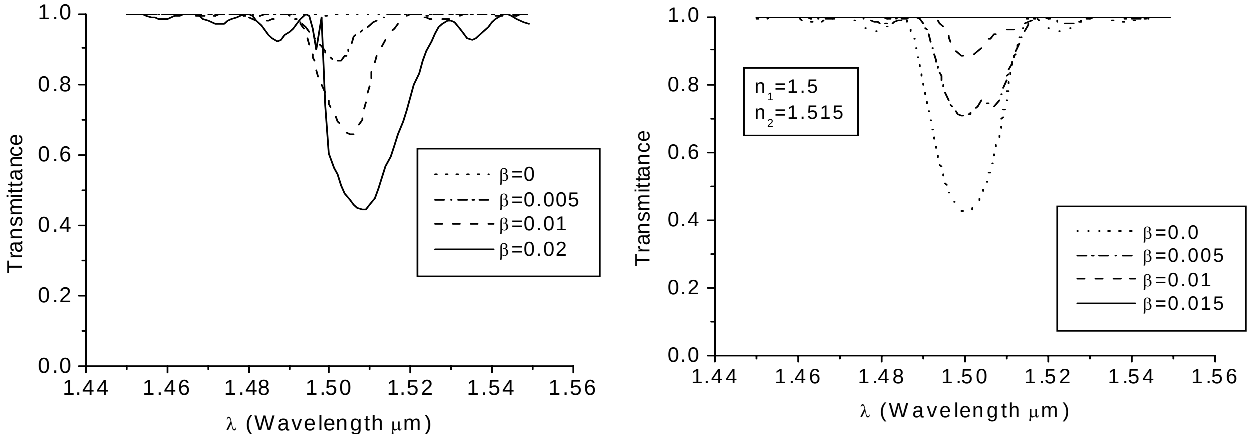

(a) (b)

Figure 5: a) Formation of the photonic gap. b) Disappearance of the photonic gap.

BISTABILITY

Another characteristic of the nonlinear systems is the presence of the bistability or multistability. This has been shown experimentally demonstrated *in the one dimensional case (stack) by* Christopher J. Herbert [21], for wave vectors with a modified input power, and reproduced in our numerical results with the same experimental data (see Figure 6).

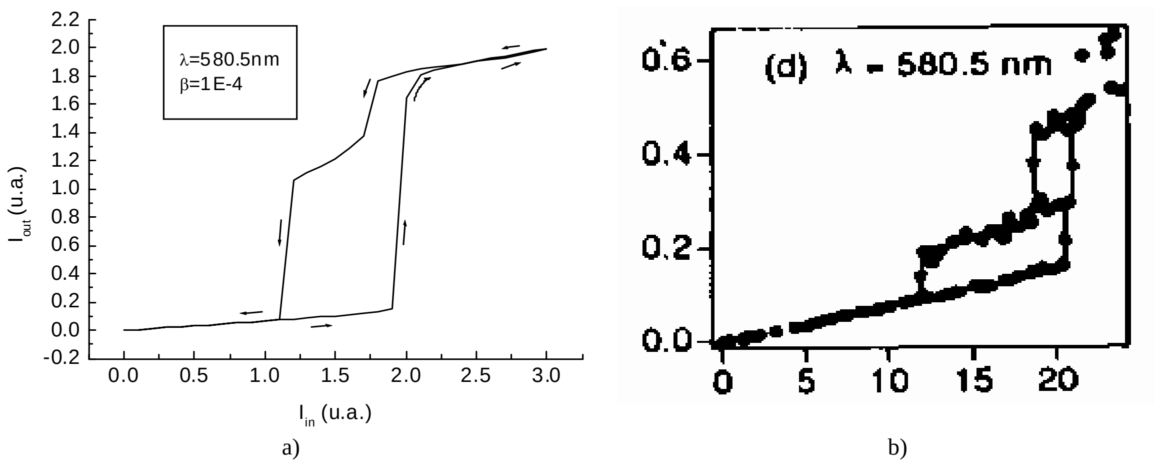

a) b)

Figure 6: Multistability a) Simulation results. b) Experimental data of Herbert.

Bistability in more than one dimension is a much more intriguing question [22]. In Figure 7, we show the radial bistability of an Omniguide fiber *(cylindrical geometry)*. It is important to notice the expected similarity with the stack, but also its slight differences. It will be rather interesting to analyze the angular distribution that leads to the creation of higher intensity point and much more complex dynamics.

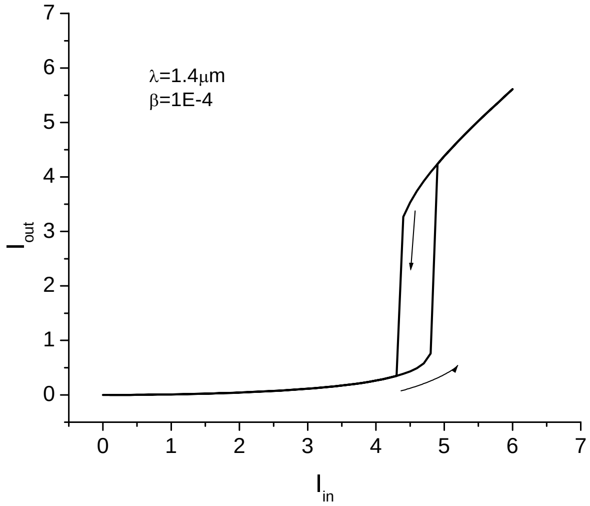

Figure 7. Bistability in an omniguide fiber.

CHIRPING

The nonlinear chirping of a stack, a feature suspected but not commonly predicted, is displayed in Figure 8. There, we display the phase and its inverse, as well as the transmitted and incident wave as a function of *k*. It is rather evident that the inverse of the phase is strongly related to the intensity pulse of the mentioned pulses, and strongly modified by the band gap and its phase changes (notice the sharp turns).

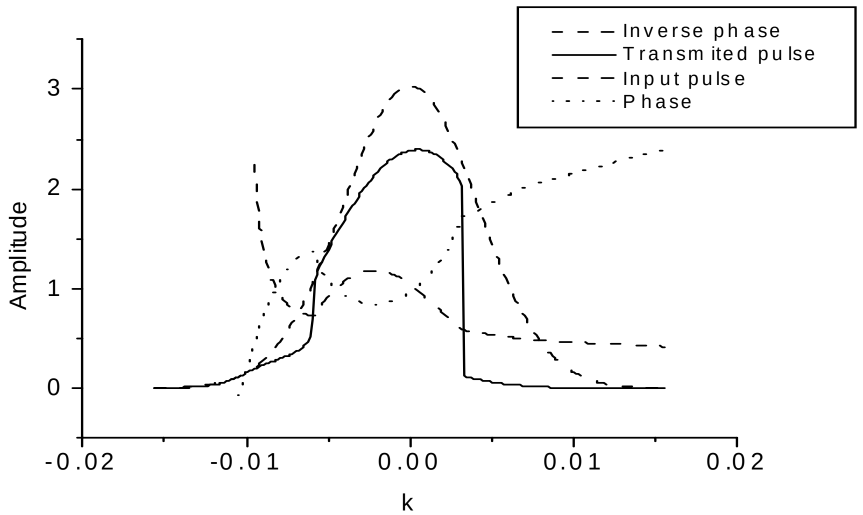

Figure 8: The phase and its inverse; and the transmitted and the incident pulses are shown as a function the of the wave number k.

4. CONCLUSIONS

An interest on a functional behavior of a device based on a NLPC may be well served by an iterative numerical method based on the linear PC solutions, where dimensional analogies provide a solid support as shown by the stack and the Omniguide array. However, in order to go beyond to the one dimensional NLPC, it is required a further improvement that takes into account spatial distributions. From the analytical point of view, there is already enough evidence to expect that additional analytical solutions for NLPC may be found beyond SVEA or a combination of both methods, since that each shows specific strengths.

ACKNOWLEDGMENTS

The authors would like to thanks the support of the National Council and Technology (CONACyT) of Mexico trough grant 45667-F and JJEA also thanks the support of CONACyT during his PhD studies, without such support, this research could not have been undertaken.

REFERENCES

1. H. G. Winful et al.: Appl. Phys. Lett. **35**, 379 (1979)
2. H. G. Winful and C. D. Cooperman: Appl. Phys. Lett. **40**, 298 (1982)
3. H. G. Winful and G. I. Stegerman.: Proc. SPIE, **517**, 214 (1894)
4. W. Chen and D. L. Mills: Phys. Rev. Letter. **58**, 160 (1987)
5. D. L. Mills and S. E. Trullinger: Ohys. Rev. Lett. B. **36**, 947 (1987)
6. Sergei F. Mingaleev and Y. Kivshar, Post conference Digest. Tops V80. Pag. NLMD1-1 to NLMD1-2. Sergei F. Mingaleev and Y. Kivshar, J. Opt. Soc. Am. B (Sep 2002 Focus Issue); Reprint: ArXiv:cond-mat/0201266.
7. Nonlinear Photonic Crystals. R. E. Slusher, B. J. Eggleton EDS. Springer Series in photonics V10, Sprinegr Verlag 2002.
8. H. G. Winful and G. D. Cooperman, Appl. Phys. Lett. 40 (1982), 298–300.
   H. G. Winful, J. H. Marburger, and E. Garmire, Appl. Phys. Lett. 35 (1979), 379–381
9. Scheuer J., D Arbel and M. Orentein. Formation and switching of multilobed patterns in ring shaped complex Nonlinear Media. NLGW 99', Dijon, France, paper WD42 pp. 180 of the proceedings.
10. J.E. Heebner, R.W.Boyd, Physical Review E, Vol. 65, 036619 (2002).
11. W. Chen and D. L. Mills, Phys. Rev. Lett. 58 (1987), 160–163.
12. A. B. Aceves and S. Wabnitz, Phys. Lett. A 141 (1989), 37–42.
13. D. N. Christodoulides and R. I. Joseph, Phys. Rev. Lett. 62 (1989), 1746–1749.
14. C. M. de Sterke and J. E. Sipe, Phys. Rev. A 38 (1988), 5149–516 and, Gap solitons, Progress in Optics 33 (1994), 203 - 260. T. G. Brown and B. J. Eggleton, Optics Express 3 (1998), no. 11. T. Opatrny G. Kurizki, A.E. Kozhekin and B. Malomed, Progress in Optics, to appear.
15. N. Akozbek and S. John, Phys. Rev. E. 57 (1998), 2287–2319.
16. B. J. Eggleton, C. M. de Sterke, and R. E. Slusher, J. Opt. Soc. Am. B. 14 (1997), no. 11, 2980–2992, J. Opt.Soc. Am. B. 16 (1999), no. 4, 587–599. B. J. Eggleton, R. E.
17. Goodman R. H., M. I. Weinstein, P. J. Holmes, J. of Nonlinear Science Reprint arXiv:nlin.PS/0012020 v3 5 Apr 2001.
18. J. Sánchez-Mondragón, J. Escobedo-Alatorre; M. Tecpoyotl-Torres; G. Martínez-Nikonoff and E. Alvarado Méndez. Chirping on a nonlinear finite stack**.** SPIE proceeding Vol. 5181, paper 25, September 2003.
19. W. Chen and D.L. Mills, Physical Review B, V36, p. 6269,1987
20. L. Matulic and J. H. Eberly, "Analytic study of pulse chirping in self-induced transparency," Phys. Rev. A 6, 822-836 (1972).
21. Christoper J. Herbert and Michelle S. Malcuit, Optics Letter, V18, pag. 1783, 1993.
22. McDonald and W. Firth, JOSA B, 1081-1089, (1993). N. B. Abraham and W. Firth, JOSA B7, 951, (1990).

2006

NOVEL OPTICAL MUX-DEMUX MODULE FOR FIBER-OPTIC COMMUNICATION APPLICATIONS

Romeo Selvas-Aguilar[1], Víctor Duran-Ramirez[2], Alejandro Martínez-Rios[3], Carlos Calles-Arriaga[1], and Arturo Castillo-Guzman[1]

[1]*Universidad Autónoma de Nuevo León, Facultad de Ciencias Físico Matemáticas*
66450, Nuevo Léon, México
Phone: +52 81-83294030, Fax: +52-81-83522954, e-mail: rselvas@fcfm.uanl.mx
[2]*Universidad de Guadalajara, Centro Universitario de los Lagos*
47460, Jalisco, México
Phone: +52 474-7423678, Fax: +52 477-4414209, e-mail: victor_duran@culagos.udg.mx
[3]*Centro de Investigaciones en Óptica A.C.*
Lomas del Bosque 115, Lomas del Campestre, 37150, León Guanajuato, México
Phone: +52 477-441 4200, Fax: +52 477-4414209, e-mail: amr6@cio.mx

Abstract-We demonstrated a novel design for a multi channel optical MUX/DEMUX module, which uses the principle of a Cassegrein-telescope. We carried out some optical simulations to show the feasibility to build up a multiplexer or de-multiplexer module for Dense Wavelength Division Multiplexing (4 channels). The set-up consists of a concave mirror that receives different beams which are then focused at the centre. For the case of a MUX-module, different radial positions enable injecting the system different wavelength inputs as the concave mirrors concentrates all the beams in one point (collector fibre). Moreover, for the case of a DEMUX-module, a bulk grating is positioned at one point between the concave mirror and the focal point of it, and when a stream of pulses with different wavelengths reaches this point, it automatically distributes the incoming signal in different radial positions (several collector fibers).
***Keywords*:** Cassegrein telecospe, DWDM system, optical communication.

I INTRODUCTION

Optical communication technology based on Dense Wavelength Division Multiplexing has allowed the exponential growth of the telecom industry. Where, every year, the increasing of information transported over a single fiber, demands a better carrier to do it. Without doubt the DWDM technology products represent the best option so far [1]. However it can only be possible with the appropriate integration of different components in the system. Major manufactures have obviously put all their resources into the development of the technology around DWDM to meet the rising demand from the carriers and the end users alike. Key components such multiplexors, de-multiplexors, circulators, isolators, etc are become part of the main research by these group of scientists [2].

In this letter, we proposed a simple and a novel multi channel MUX/DEMUX device. This device utilizes a concave mirror to couple light come from an arrangement of a number of fiber input connectors. Each input, individually, carries stream of pulses at different wavelengths. We ran ray traces of different field angles as well as different spot dimensions for the beams that are passed throughout our design. The simulations showed to be effectively a good approach for a MUX and DEMUX system.

1-4244-0628-5/06/$20.00©2006 IEEE.

II DESIGN ARCHITECT FOR THE NOVEL MUX-DEMUX DEVICE

The setup of the MUX-DEMUX device consists of several input port which are optically connected to the concave mirror. Each input port carries a signal sitting on a 50GHz-ITU wavelength grid, and those are simultaneously launched to the MUX-DEMUX system. The wavelengths selected in the simulations were 1550.12nm, 1550.92 nm, 1551.72 nm, and 1552.52 nm. which correspond to the C-band of the telecom windows [3]. To have an idea of how the system works, we are going to divide the explanation of the setup in two. For the case of a Multiplexer module, port 1, 2, …, 4 carry stream of beam pulses. Each beam is firstly collimated and then reaches the surface of the concave mirror which in a subsequent way the beam is concentrated at the focal point. At this point (collector telecom fiber), a fiber capture all the beams and transport all the information into the telecomm system. This principle enables successfully to combine coaxially using the concave mirror. Obviously there are some changes on the dimensions of the beams and some changes on the far field divergences of these beams and this will allow to effectively launch the beams in a standard telecom fiber (collector fiber, NA~0.17). To have a better appreciation, Figure 1 shows the MUX-DEMUX system in which only two ports as inputs were considered and the collector fiber.

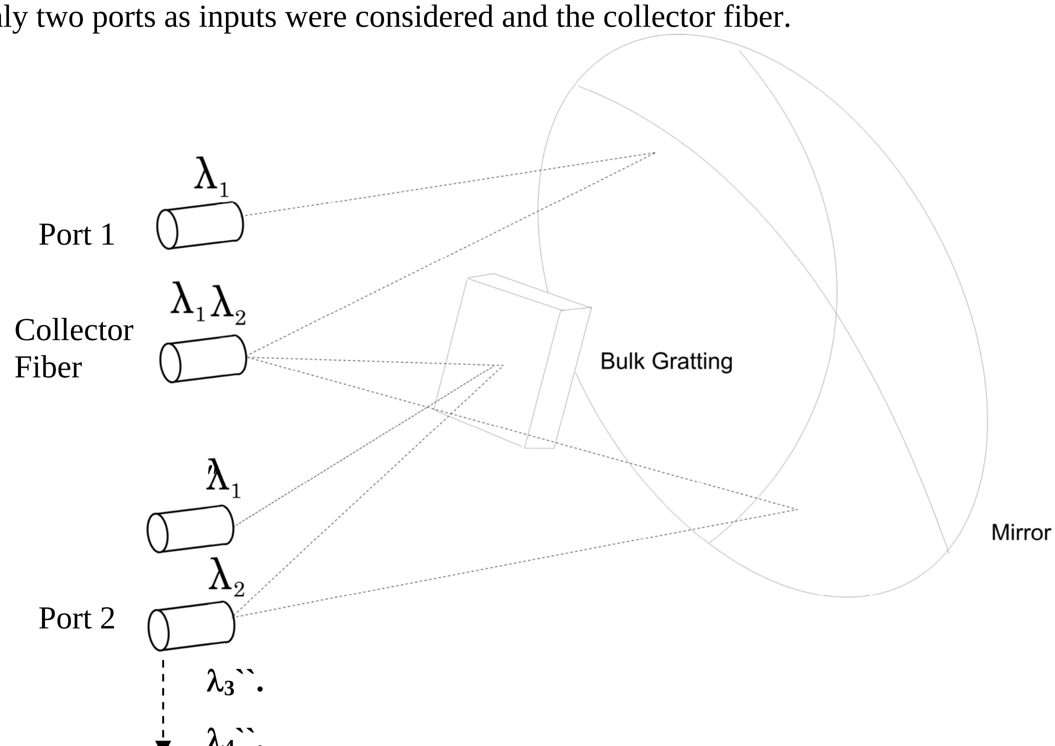

Figure 1 Lateral view of the spatial optical scheme proposed for a multi channel MUX-DEMUX module

For the case of a DEMUX-module, the central part of the system (collector telecom fiber) carried all the wavelengths into it. These signals are fedback to the surface of the concave mirror. However, at the path the beam will find a bulk grating which is placed with a calculated angle of ~110 degrees with respect to the optical axis and the *n*-orders diffraction beams are reflected at the port 1``, 2, ..,4``. Finally, each pulse is reconnected to a 4 different ports that are connected to the final telecomm network system. (See Figure 2)

III SIMULATIONS

The numerical model considered 3mm diameter lenses with 0.17 numerical aperture at the port 1, 2,.., n. The lenses are positioned in front of a 100 mm diameter concave mirror with a high reflectivity thin film and 0.3 numerical aperture, the details of the performance of this mirror are well explained in reference [4]. This mirror has an effective focal length of 10 cm. The collimated stream of pulses at port 1, 2, .., n are then reflected back at the focal point as the mirror concentrates all parallel incoming beams. Subsequently, all the wavelengths are launched in the collector fiber (see Fig. 2). In an opposite direction, the systems can also work as a de-multiplexer and for that there is a bulk grating of 600 lines/mm which is positioned at a calculated angle of 110 degrees wrt. optical axis of the path of the beams. The grating then diffracted the composed stream of pulses in different n-order of diffraction (zero order). This diffracted beams are sent back at the positions where the input beams of port 1``, 2, …, 4`` are localized.

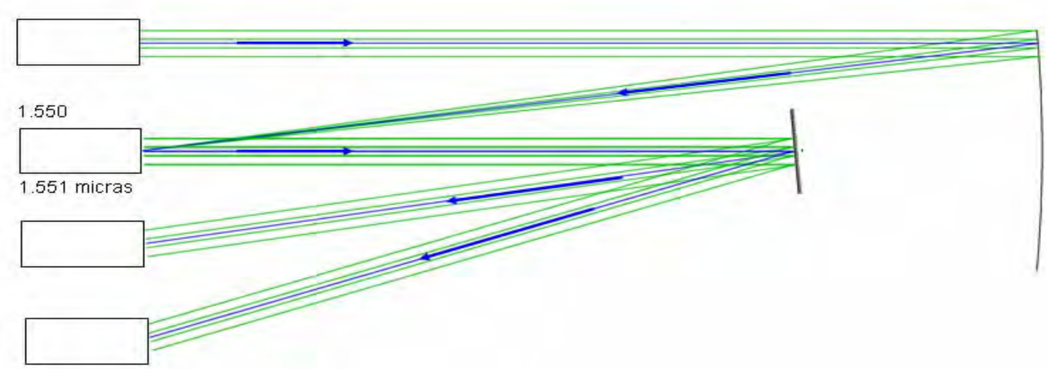

Figure 2 Simulation of the novel MUX-DEMUX system.

By using commercial software for optical design [5], we ran the ray traces of different field angles as well as different spot dimensions for the beams. This software computes the ray optics in which all rays that travel in different optical media are in accordance with a set of geometrical rules. The concave mirror is proposed to have a substrate glass composition and a polished metallic film deposition. Figure 3 shows the simulation for four different beams that are propagated throughout the system. The distribution of the fiber connector is also symmetrical so different set of n-beams will behave in the same way and can be added in the same way that this final scheme.

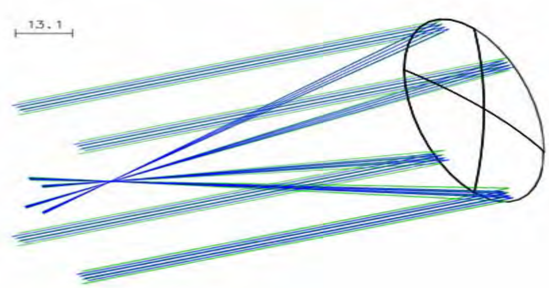

Figure 3 Simulation of the arrangement of the Multiplexor module only.

Figure 4 shows the spot diagram of the system. Different distance revealed a change on the spot size and also a chance on the angle of divergence. At the end, the final size (~30μm) is even less than the diameter of the collimator lens (2mm) located in front of the collector standard fiber, and the numerical aperture at the end is calculated to be less than 0.2 which also roughly corresponds to the numerical aperture of the collector fiber (0.17).

Figure 4 Spot beam diagram of the Fig. 3.

IV Discussion

The present design is considered as a good approach for a multi channel MUX-DEMUX module. With the simulation we can assume that the module of the four channels can be easily upgrade up to 8, 16, etc channels simultaneously. The most interesting results from the simulation are also that this special mirror transformed the collimating beams in concentrating beams with effective numerical aperture of less than 0.2 (matching the 0.17 NA of the collector fiber), and produces a reduction in the size of the beam (30 μm) which also match the physical dimension of the lens (2mm) in from of the collector fiber .

V Conclusion

In this paper, we proposed a novel and simple multi channel MUX-DEMUX module for spatially combination of several different wavelengths. We ran simulations for four beams that are propagating throughout the system. We also showed that the system has a good coupling efficiency and the final numerical aperture match the fiber NA of each output fiber.

Acknowledgements

Authors would like to thanks to the National Council of Science and Technology (CONACYT) for the support in the development of the present work as it was partially supported under Grant J4773-F.

References

1. Edited by Achyut K. Dutta, Niloy K. Dutta, *WDM Technologies Active Optical Components*, Academic Press, 2002, ch. 1& 2 and 13.

2. PC Becker, NA Olsson and JR Simpson, *Erbium-doped fiber amplifier, fundamentals and technology*, San Diego, CA: Academic Press, 1999, ch.1 & 2.

3. [WWW] Fiber Optics.info, Table for Standard ITU wavelengths for DWDM 50GHz and 100 GHz spacing
http://www.fiber-optics.info/DOCS/ITUgrid_dwdm.pdf#search=%2250%20GHz%20ITU%20wavelengths%22

4. R Selvas, A Martinez-Rios, and I Torres-Gomez, Power combiner for hih power diode lasers, *Fifth Symposium Optics, Proceeding of SPIE Vol. 6046*, 60462F, 2006.

5. OSLO Optics Reference, Lambda Research Corporation, Littleton, MA (2001).

MODELING AND OPTIMIZATION OF THE COUPLING EFFICIENCY FOR DOUBLE-CLAD FIBER

Carlos Calles[1], Romeo Selvas-Aguilar[1], Arturo Castillo-Guzmán[1], Jesús Escobedo Alatorre[2]

[1]Universidad Autónoma de Nuevo León, Facultad de Ciencias Físico-Matemáticas, 66450, Nuevo León, México.
Phone: +52(81) 8329 4030, Fax: +52(81) 8352 2954, e-mail: ccalles@fcfm.uanl.mx
[2]Centro de Investigaciones en Ingeniería y Ciencias Aplicadas, UAEM, 62210, Morelos, México.
Phone: +52(777) 329 70 72, Fax: +52(777) 329 70 72

Abstract− In this work, we simulate the efficiency of optical power transfer between a 915 nm diode laser, and a double-clad fiber optic. A lenses array allows collimating and focusing the pump energy to the fiber. This model was made using the optical design software OSLO. The result shows a high coupling efficiency of roughly 84%, which can increase the optical input power in fiber optics lasers.
Keywords: double-clad fiber, pump energy, coupling efficiency.

I. INTRODUCTION

Coupling efficiency plays key role in fiber optics lasers. A good coupling system assures that a high rate of optical pump power would be efficiently used. In designing fiber optic lasers, the most common element utilized for pumping is the laser diode. This optical element presents several advantages over molecular lasers of which are the compactness, low-cost, high optical radiance, etc. In consequence, these have been largely used as pumping devices. One disadvantage of this element is the poor beam quality factor. Diode lasers normally emit elliptic pattern beams, which make it difficult to coupling into a circular fiber optic. In order to solve this problem, some methods have been proposed. Sugiyama [1] designed a spot size converter that consisting of a light guide with a rectangular incident area (able to couple the diode laser irradiance), and a rectangular exit area which provides a circular spot size. In this device, at least one part of lateral side walls inclines from the slow axis direction. Thereby, it is able to regulate the divergence of the outgoing light, and to optically couple optical elements of different spot size with each other at a high-efficiency.

A practical method for coupling optical pumping power consists of lens arrays [2-4]. A typical coupling system consist of a collimator, a pair of prism to convert the spot from elliptical to circular cross section, an expander lens and a focus lens. These elements allow a good coupling efficiency. However, one important characteristic to be considered in a coupling system, besides its effectiveness, is the simplicity.

In this work, we propose a simple optical coupling array consisting of a laser diode, a collimator lens and a focused lens. Simulation of this design was performed with commercial optical design software. The main goals of this work were to achieve a high-coupling performance while maintaining a simple design. The spot size at the optimal focus length was found to be compatible with double-clad fiber.

The double-clad fiber allows higher output power than conventional ones. This special fiber consists of a core, an inner cladding and an outer cladding. Thus, pump energy is injected to the

1-4244-0628-5/06/$20.00©2006 IEEE.

inner cladding which has a larger diameter and larger NA than the core. Therefore they are suitable to work with high power laser diodes for fiber laser systems. In a already reported experiment with a double-clad fiber laser [5], in which the total pump energy was 15 W while the launched pump power was only 8 W, the authors feel appropriate to simulate pump coupling setup in order to increase the coupling efficiency and thus propose a method to improve the previous results. A first glance was that the rest of the energy was lost because of optical coupling problems. Then and with an appropriate coupling scheme, as the one proposed in this work, this kind of problem could be solved, setting aside a more efficient fiber laser.

The computation of the fiber coupling efficiency is based on the following: given an amplitude diffraction pattern *U(x',y')* and a fiber mode pattern $\psi(x',y')$, the coupling efficiency η is defined as the normalized overlap integral [6]

$$\eta = \frac{\iint U(x',y')\psi^*(x',y')dx'dy'}{\sqrt{\iint U(x',y')U^*(x',y')dx'dy'\iint \psi(x',y')\psi^*(x',y')dx'dy'}}, \tag{1}$$

where the asterisk denotes the complex conjugate. The power coupling efficiency *T* is given by

$$T = \eta\eta^* = |\eta|^2 \tag{2}$$

Since the evaluation of equation 1 requires that the diffracted amplitude to be known over a grid of points (*x',y'*) in the image plane, the program itself uses FFT diffraction calculations to compute U(x'y'). The form of the mode pattern $\psi(x',y')$ depends on the structure of the fiber. For a step index fiber, the fundamental mode is given by

$$\psi_{step-index}(r') = \begin{cases} \dfrac{J_0\left(\dfrac{ur'}{a}\right)}{J_0(u)}, & r' \leq a \\ \dfrac{K_0\left(\dfrac{wr'}{a}\right)}{K_0(w)}, & r' > a \end{cases} \tag{3}$$

where $r' = (x'^2+y'^2)^{1/2}$ and *u* and *w* are constants determined by the fiber construction parameters.

II. METHODOLOGY AND DATA

Simulation was performed with optical design software and it takes into account basically three different stages. Firstly, we have the optical pumping element i.e. the laser diode. Here, it is possible to vary as the wavelength as the numerical aperture of the object. Secondly, we have the optical array that is formed by a three lens collimator (L_1-L_3) with a numerical aperture NA of 0.5, followed by a lens that acts as a focusing element (L_4) with NA = 0.12. The characteristics of the elements forming this stage are showed in table 1. Thirdly, there is a fiber optic where we can change the core refraction index as well as the cladding refraction index. Besides of this, it is possible to adjust the fiber core radius.

Table 1 − Characteristics of the lens employed at the optical coupling array.

Element	Surface	Radius	Aperture Radius
L_1	In	0	2.5
	Out	0	
L_2	In	-6.949	3.5
	Out	-5.491	
L_3	In	-79.436	4.5
	Out	-9.788	
L_4	In	18.610	4.5
	Out	0	

As shown in Fig. 1, rays of light upcoming from laser diode are effectively collimated at the region between L_3 and L_4. This stage greatly contributes to the correction of the beam quality factor. In the next phase L_4, whose effective focal length is 36 mm, the laser pump beam is focused to a suitable spot size to be coupled into the double clad fiber optic.

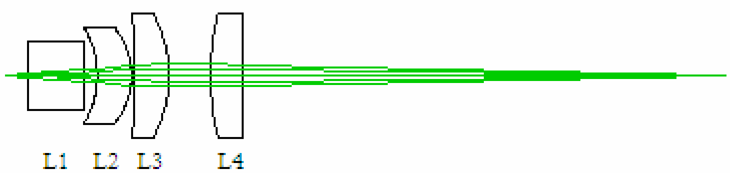

Fig. 1− Scheme of the optical coupling array.

III. RESULTS

One of the most important considerations in coupling light into a fiber optic is the spot size. In this simulation, the optical pumping source wavelength was 915 nm, and the spot size at the paraxial focus length was 15.69 µm as shown in Fig. 2. Therefore, this design is compatible with common Yb-doped double clad fiber.

We calculated the coupling efficiency based on the three main fiber characteristics: core refraction index, cladding refraction index and core radius. The best efficiency of 84% was performed by refraction index of 1.465 and 1.464 of core and cladding respectively, and a core radius of 12.5 µm.

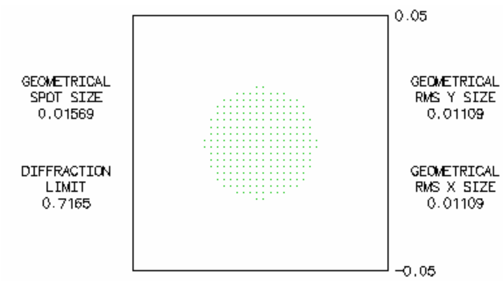

Fig. 2 − Geometrical spot size.

IV. Conclusions

We designed and simulated an optical pumping coupling system. The design consists of a collimator and a focusing lens. The results showed a spot size of 15 µm which can be coupled in a double clad fiber optic. The system provides a high optical coupling efficiency of 84 %. Since the wavelength that showed better results was 9150 nm, this model is suitable for Yb-doped double clad fiber optic lasers.

Acknowledgment

Authors would like to thanks to the National Council of Science and Technology for their support in the development of this paper under grant J4773-F.

References

1. T. Sugiyama, K. Kanagawa, "Spot size converter, semiconductor laser module and optical fiber laser device," U.S. Patent 6 834 071 B2, Dec. 21, 2004.
2. P. Smith, et al., "Switchable fiber coupling using variable-focal-length micro lenses," *Rev. Sci. Instrum.*, Vol. 72, No.7, July 2001.
3. Y. He, S. Mondal and F. Shi, "Design optimization of wedge-shaped lensed fibers for fiber-laser coupling: Fresnel reflection and Non-Gaussian mode effects," *J. of Lightwave Techno.*, Vol.21, No.10, October 2003.
4. T. Schmidt, P. Karlitschek, G. Marowsky, Y. Sano, "New simplified coupling scheme for the delivery of 20 MW Nd:YAG laser pulses by large core optical fibers," *Appl. Phys. B* 72, 183-186 (2001).
5. A Martinez-Rios, R Selvas, I Torres-Gomez, F Mendoza-Santoyo, H Po , AN Starodumov, and Y Wang, “Double-clad Yb-doped fiber lasers with non-circular cladding geometry”, *Optics Communications* (246): 385-392, February 2005.
6. OSLO Optics Reference, Lambda Research Corporation, Littleton, MA (2001)

High Power Er3+/Yb3+Doped Fiber Laser Suitable for Medical Applications

J. A. AlvarezChavez, A. MartínezRios, I. TorresGómez, R. Selvas Aguilar, J. A. Domínguez Lopez, and F. MartinezPiñon

Citation: AIP Conference Proceedings **854**, 84 (2006); doi: 10.1063/1.2356410
View online: http://dx.doi.org/10.1063/1.2356410
View Table of Contents: http://scitation.aip.org/content/aip/proceeding/aipcp/854?ver=pdfcov
Published by the AIP Publishing

High Power Er^{3+}/Yb^{3+}-Doped Fiber Laser Suitable for Medical Applications

J. A. Alvarez-Chavez, A. Martínez-Rios, I. Torres-Gómez, R. Selvas Aguilar, J. A. Domínguez-Lopez* and F. Martinez-Piñon**

Centro de Investigaciones en Óptica, Loma del Bosque 115, 37150 León, México
**Centro de Investigaciones en Matemáticas, Guanajuato, Mexico*
*** CIITEC – IPN, Sta. Catarina, D.F. México*
Email: jalvarez@cio.mx

Abstract. We present results on high-radiance quasi-single mode, high power, double clad, Er/Yb-doped fiber lasers with suitable output power for laser surgery in the 1550 nm wavelength region (central wavelength at 1545nm) and also suitable for optical coherence tomography (OCT), microsurgery, and skin resurfacing. We have demonstrated >5W from a co-doped fiber laser and a 5nm line-width.

Keywords: Lasers, Fiber, Medical.
PACS: 42.62.–b, 42.81.–I

INTRODUCTION

The use of Yb^{3+} as a sensitizer for co-doped high power fiber lasers has been widely used in the last few years[1]. There have been amazing record-breaking results with such co-doped sources [2]. In the present work, we discuss experiments carried out using the Er^{3+}/Yb^{3+} approach, which increases the choice of pump wavelengths for the erbium-doped fiber lasers.

Yb^{3+}-sensitized Er^{3+}-doped High-radiance Sources

Erbium-doped and Yb^{3+}-sensitized Er^{3+} glasses have been investigated for the last 30 years [3-4]. Er^{3+}/Yb^{3+}-doped fibers directly amplify signals within the third telecommunications window, at ~1550 nm. Some of the applications of Er^{3+}/Yb^{3+} –doped fiber amplifiers are found in the distribution of common antenna television (CATV), free-space communications,, super-fluorescent sources, and medical applications that benefit from the eye-safe nature of 1550 nm light[5]. Lower efficiency of EYDFs leads to lower available output powers, compared to those from Ytterbium-doped fiber lasers (YDF's). The Er^{3+}/Yb^{3+} co-doping technique allows pumping of Yb^{3+} ions using broad-stripe high-power pump sources to reach much higher output power levels. Yb^{3+} ions exhibit strong absorption over a wavelength range extending from 800-1100 nm. Yb^{3+} excited ions then transfer their energy to Er^{3+} ions. The $^2F_{7/2}$ level of the Yb^{3+}, exciting it into the $^2F_{5/2}$ level, absorbs pump photons. From there, a cooperative energy transfer process between the excited state Yb^{3+} and the ground state

CP854, *Medical Physics: Ninth Mexican Symposium on Medical Physics,*
edited by H. Mercado-Uribe, G. García-Torales, J. L. Flores-Núñez, and E. Castillo-Corona

Er^{3+} in the $^4I_{15/2}$ level excites the Er^{3+} to the $^4I_{11/2}$ level while dropping the Yb^{3+} back to its ground state [7].

Free-running Fiber Laser Results

The main objective for this work is to develop efficient cladding-pumped Er^{3+}/Yb^{3+} using a pump concentrator unit with the following optical characteristics: >25W, CW at 982nm. The initial work consisted on the optimization of the launching efficiency, fiber characterization, fiber laser set-up and finding the optimum device length for our purposes. We aimed at obtaining >5W at the "eye-safe" wavelength of 1550nm. For the experiment, we used fiber shown in Fig. 1a, with the set-up shown on the right. A good power level from this device can be obtained in the laboratory without too much careful alignment and only a good end-cleaving of the fiber is required for the 4% Fresnel reflection and cavity gain build-up. Figure 2 shows the output characteristics at 1545nm.

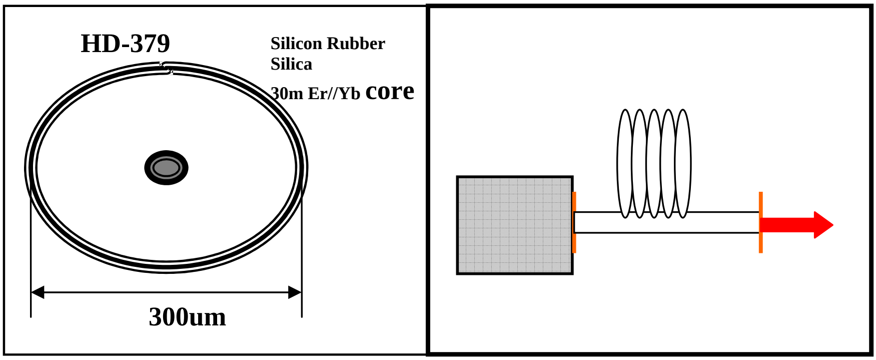

(a) (b)

FIGURE 1. Schematic of the energy transfer from Yb^{3+} to Er^{3+} ions and fiber laser configuration

The multimode beam obtained from this device is due to the 30-um core of the fiber. This relatively big size core was chosen to increase the launching efficiency and absorption. The slope efficiency is 30%. The maximum output power is 6.2W continuous wave at 1545nm.

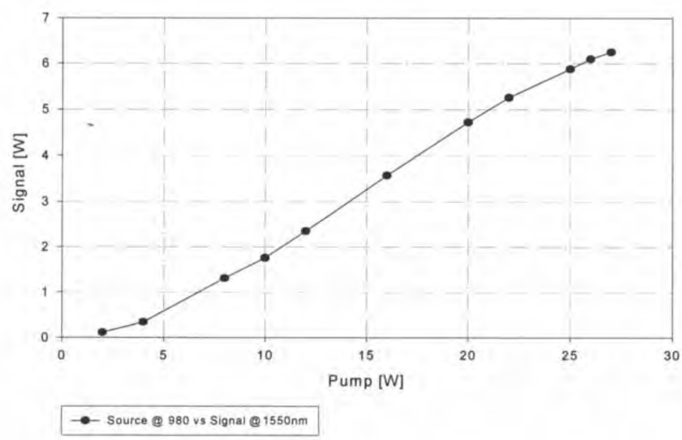

FIGURE 2. Output characteristics of the HD-379 Er^{3+}/Yb^{3+} high-power, fiber laser: Output power vs. launched power

CONCLUSIONS

We have demonstrated an efficient, high radiance, Er/Yb-doped fiber laser with a novel inner-clad structure, more then 5W output power at the eye-safe wavelength of 1545nm and with a simple, portable experimental set-up. We intend to explore more options of pump sources, dopants and fiber design to develop new high power sources with good beam quality and flexibility.

ACKNOWLEDGEMENTS

Authors would like to acknowledge the support from CIO, CIMAT and CIATEC, all from México.

REFERENCES

1. J.D. Minelly, W.L. Barnes, R.I. Laming, P.R. Morkel, J.E. Townsend, S.G. Grubb and D.N. Payne, *IEEE Phot. Tech. Lett.* **5**, (1993)
2. Y Jeong, J. Nilsson, J.K. Sahu, D.B.S. Soh, P Dupriez, C.A. Codemard, S. Baek, D.N. Payne, R. Horley, J.A. Alvarez-Chavez and P.W. Turner, *Opt. Lett.* **30**, 955-957, (2005)
3. E. Snitzer and R. Woodcock, *Appl. Phys. Lett*., **6**, 45-46, (1965)
4. V.P. Gapontsev, S.M. Malitsin, A.A. Isninev, V.B. Kravchenko, *Opt. Laser Tech*., **14**, 189-196, (1982)
5. V. Gapontsev et.al., *Adv. Solid State Lasers Topical Meeting*, Tech Digest, 258, Salt Lake City, 1998.

GAIN AND NUMERICAL MODELLING OF RARE-EARTH DOPED FIBER DEVICES

A Castillo-Guzmán[1], R Selvas[1], C Calles[1], M Basurto-Pensado[2]

[1]*Universidad Autónoma de Nuevo León, Facultad de Ciencias Físico-Matemáticas, 66450, Nuevo León, México.*
Phone: +52(81) 8329 4030, Fax: +52(81) 8352 2954, e-mail: acastillo@fcfm.uanl.mx
[2]*Centro de Investigaciones en Ingeniería y Ciencias Aplicadas, UAEM, 62210, Morelos, México.*
Phone: +52(777) 329 70 72, Fax: +52(777) 329 70 72

Abstract- We compute the evolution of a signal, pump, backward and forward ASE in a fibre laser in a model that takes into account the modal shape of the radiation fields, the spectral shape of cross sections and of forward and backward propagation ASE, pump power depletion, and saturations due to ASE and or signal. The model can be easily extended to different rare-earth fibre lasers configurations subject to some constrains, since the physics remains the same in many cases. Some spectroscopy data of important fibre fabrication companies and published papers are then used to calculate the amplification, and gain. Three different rare earth doped fibres (namely ytterbium, neodymium, and thulium) were objects of this analysis. Finally, the numerical calculations showed to be in good agreement with reported experimental results (slope efficiency, etc).
***Keywords*:** Rare earths; Fibre laser.

I. INTRODUCTION

Cladding-pumping has revolutionized fibre lasers over the last decade. The perspective of that a single-mode diodes are limited in power to a few hundred miliwatts changed with the breakthrough idea, referred to as cladding-pumping (using double-clad fibers), patented by James Kafka at Spectra Physics [1]. A double-clad fiber, indeed, enables a good match with the output beam from broad-stripe diode. These are multi-mode devices that can generate much higher powers than single-mode ones. Thus, with cladding-pumping, a double-clad fibre laser can produce much higher output power, in a beam that nevertheless can be diffraction-limited. Cladding-pumped fibre lasers are currently considered for many applications, where high laser powers are required.

Simplicity is a major attraction of active fibre devices. By simply incorporating a dopant (typically a rare earth) into the core of an optical fibre, a powerful gain-medium is realized. The first rare-earth doped fibre devices go back to the 1960’s when C.J. Koester and E.Snitzer [2,3] developed a flash-lamp-pumped neodymium-doped fibre amplifier.

Rare-earth doped fibers offer many advantages for example: they are lightweight and flexible and can be coiled so that compactly packaged and robust devices can be realized; they are well-controlled beam shape, owing to the confinement of light in the core of the fibre; the thermal management is simple thanks to the extended length, large surface area, and small transverse dimension of the fibre [4]. We can also find the rare-earth fibers good devices offering a high gain, and the use of a glass host leads to a wide bandwidth, which makes them suitable for amplifiers as well as for widely tunable lasers. Other attractive features of fibers lasers include narrow linewidth (with wavelength-selection), efficiency, stability, reliability, and temporal characteristics ranging from CW to femtosecond pulses. All these attractions make fibre lasers very useful in areas such as thermal printing, drilling, welding, cutting, material processing,

1-4244-0628-5/06/$20.00©2006 IEEE.

nonlinear frequency conversion, remote pumping of EDFAs, range finding, defense, aerospace, and medicine [5.6].

For those reasons, the rare-earth modeling is acquiring so much importance now in our days. This work is focus in the modeling of three different rare-earth doped fibers (Ytterbium, Neodymium and Thulium). These rare-earths are the most applied in investigation because of their high conversion efficiency compared with other rare-earths.

II. NUMERICAL MODEL

The equations do need to be solved numerically. Assume again that the pump and the signal light are co-propagating. The numerical solution proceeds as follows: First, the (discretised) forward-travelling ASE spectrum and the pump and signal powers are propagated forward according to Eqs. (1) – (6) with *S– ASE* = 0 in (5).

$$\frac{dP(z,v)}{dz} = g_m(z,v)P(z,v) \tag{1}$$

$$g_m(v) = \int_0^\infty \Psi(r,v)\left[N_2(r,z)\left(\sigma_e(v) - \sigma_{ESA}(v)\right) - N_1(r,z)\sigma_a(v)\right]2\pi r dr \tag{2}$$

$$\gamma_e(z,v) = \sigma_e(v)\int \Psi(r,v)N_2(r,z)2\pi r dr \tag{3}$$

$$\frac{dS^{+}ASE(z,v)}{d(\pm z)} = g_m(z,v)S^{\pm}ASE(z,v) + 2hv\gamma_e(z,v) \tag{4}$$

$$R(r,z) = \frac{P_p(z)\Psi(r,v_p)\sigma_a(v)}{hv_p} + \frac{P_p(z)\Psi(r,v_s)\sigma_a(v_s)}{hv_s}$$

$$+\int_0^\infty \Psi(r,v)\frac{S^{+}ASE(z,v) + S^{-}ASE(z,v)}{hv}\sigma_a(v)dv \tag{5}$$

$$n_2 = \frac{R}{(R+W+A)} \tag{6}$$

The equations are integrated numerically, e.g. with a Runge-Kutta method. At the same time, the population inversion throughout the fibre is calculated. The resulting forward-travelling light powers are then used in (5) when (4) is integrated backward to yield the backward-travelling ASE spectrum. In the process, the population inversion is recalculated. Appropriate boundary conditions (determined by the endreflectors) are used to couple forward and backward-propagating light fields to each other. Then, (1) and (4) are integrated forward again, now including the *S– ASE(z,v)* just found in (5). This process is repeated until convergence is reach. Other methods for solving (1 and 5) exist, too. In the case of a laser, no signal is injected. Instead, the lasing field builds up from spontaneous emission.

III. RESULT AND DISCUSSION

Ytterbium is an interesting dopant for several reasons. The energy level structure is extremely simple in compared with many other rare-earths, consisting of a split ground state $^2F_{7/2}$ and a split excited state $^2F_{5/2}$. The lack of other energy levels in the infrared and the visible ensures that ESA will not be a problem and hence the results presented below on efficiency and output power should be scalable to much higher values. Fig.1 shows the results in this rare earth.

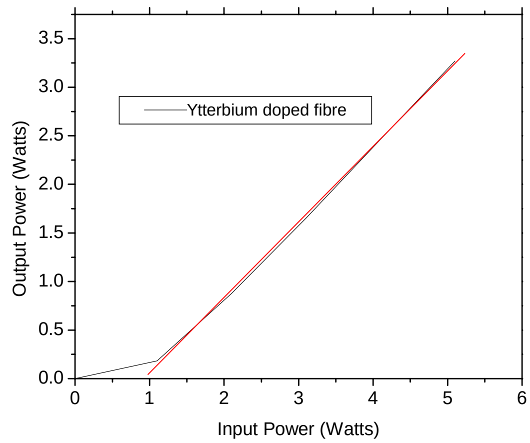

Fig.1 Ytterbium results, output power versus pump power.

The maximum output power at 980 nm was 3.27 watts for an absorbed pump power of 5.11 watts and the threshold absorbed power was 1.07 watts. The slope efficiency with respect to absorbed power was 77.20%. Other data of Ytterbium doped fibre modelling are: the total length of the fibre was 3.95 m and the dopant concentration was $25x10^{25}$ iones/cm^3.

Compared with Ytterbium, Thulium has a very much more complicated energy level structure. Laser action in a Tm-doped fiber can be achieved by pumping into one of several available absorption bands, each having its own advantages and disadvantages. Fig. 2 shows the results for the thulium doped fiber.

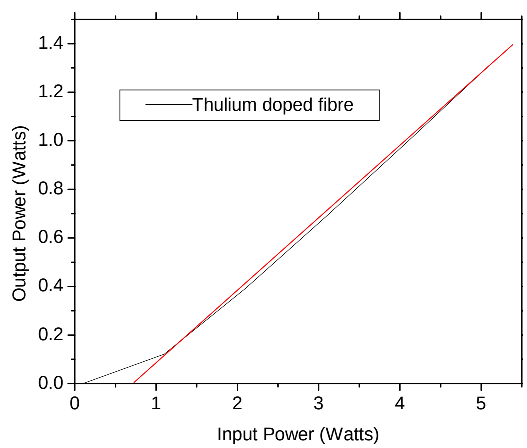

Fig.2 Thulium results, output power versus pump power.

Thulium doped fibre pumped at 780 nm achieved a total output power of 1.31 watts out of 5.11 watts with a threshold absorbed power of 1.10 watts. We obtained a slope efficiency of 30.88%. The dopant concentration was $110x10^{27}$ iones/cm^3 with a total fibre length of 0.5 m.

Neodymium is modelled with a three-level system. Fig. 3 shows what we obtained out of this modelling. It was pumped at 807 nm to amplify light at 1058 nm. The maximum output power was 2.56 watts with a threshold of 1.12 watts. We achieved a slope efficiency of around 56.01% with a dopant concentration of $12.90x10^{24}$ iones/cm^2 and a total fibre length of 120 m.

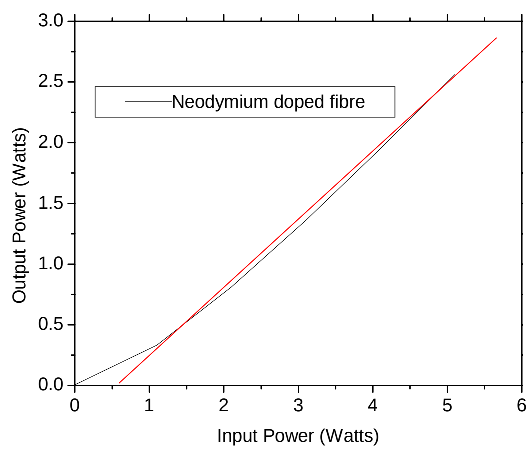

Fig.3 Neodymium results, output power versus pump power.

IV. Conclusion

The results obtained in this work, were compared with other rare-earth doped-fibre simulations and we realized that our work is reliable. We utilized some spectroscopy data of important fibre fabrication companies as a base like the diameters of the fiber, indexes of refraction, pump wavelength, etc; that guarantee even more our work.

The model utilized can be easily extended to other rare-earth fiber laser configuration, since the optics remains the same. On Ytterbium, Neodymium and Thulium, the model worked efficiently, with 77.20%, 56.01% and 30.88% of slope efficiencies respectively.

References

1. J. Kafka, "Laser diode pumped fiber laser with pump cavity", US Patent 4, 829, 529: 1989.
2. E.Snitzer, "Optical maser action of Nd^{3+} in a barium crown glass", *Phys. Rev. Lett.*, Vol. 7, pp. 444-446, 1961.
3. C.J Koester and E. Snitzer, "Amplification in a fiber laser", *Appl. Opt.*, Vol. 3, pp. 1182-1186, 1964.
4. K.I. Ueda, H. Sekiguchi, and H. Kan, "1 kW cw output from fiber embedded lasers", in Proc. *Conference on Lasers and Electro-Optics*, Long Beach, USA: CPDC4, 2002.

5. D. Anthon, J. fisher, M. Keur, K. Sweeney, D. Ott, P. Matton, and C. Emslie, “High power optical amplifiers for CATV applications”. *Optical Fiber Communication Conference*, Anaheim, USA, Vol. 2: paper, 2001.
6. S. D. Jackson and A. Lauto, “Diode-pumped fiber lasers: a new clinical tool”, *Lasers in surgery and Medicine*, Vol. 30, pp. 184-190, 2002.

Compact, simple tuneable mechanism for fibre lasers

A. Martínez-Ríos, R. Selvas-Aguilar[1], I. Torres-Gomez, D.A. May-Arrioja[2], G. Anzueto-Sanchez, J.J. Sánchez-Mondragon[2]

Centro de Investigaciones en Óptica, León, Gto., 37170, México

[1]Facultad de Ciencias Físico Matemáticas, UANL, Cd. Universitaria, N,L., 66450, México

[2]Instituto Nacional de Astrofísica, Óptica y Electrónica, Pue., Puebla, 72000, México

Abstract: A simple tuning-mechanism for an ytterbium-doped fibre laser is implemented. Based on the wavelength-dependence of the re-imaging distance that occurs in multimode-fibre, a fibre-gripper is fabricated to provide automatic-alignment of the multimode-fibre and a fibre-mirror.

OCIS Codes: (140.3600) Lasers, tuneable; (060.2310) Fibre optics

The broad spectral line-width of fibre lasers makes them attractive candidates for wavelength tuneable sources. Moreover, they have found important applications in several areas such as material processing, industry and medicine. However, the use of components to tune a wide gain medium is interpreted as a synonymous of complexity and voluminous. In this work, we present an enhanced design for wavelength tuning in a fibre laser. For this purpose, a novel tuneable fibre laser is demonstrated in which the wavelength selectivity is realized by adjusting the separation between a broadband mirror and the fibre facet of a 15 mm long, 105/125 um multimode fibre (MMF). The MMF is spliced to a single mode fibre which is spliced to the active ytterbium doped fibre. The fluorescence signal entering into the multimode fibre will be reproduced as single images at periodic intervals along the propagation direction of the fibre. The length of the fibre is chose to be slightly shorter than the first re-imaging point, such that the signal coming out from the MM fibre is obtained in free space. Since the position of the re-imaging point is wavelength dependent, different wavelengths will be imaged at different positions as mentioned in ref [1]. But, as a way to enhance the tuning in this fibre laser, a fibre gripper was then fabricated that automatically align the tuning mechanism module. The new setup consisted therefore, of a fibre gripper which is essentially a channel with negative slope walls. The gripper structure is designed such that when a fibre is inserted it will be held within the channel (Fig. 1a), moreover a double clad ytterbium doped fibre, DC YDF, is end-pumped by a fibre pigtailed laser diode with 1.5 W of fibre coupled output power at a wavelength of 915 nm. The end of the DC YDF used for pumping was perpendicularly cleaved to provide feedback for laser oscillation, and also to operate as the output coupler for the laser. The other end of the fibre was spliced to the tuning mechanism. The fibre mirrors used in the tuning mechanism were fabricated on standard single mode fibres by coating one of their facets with gold film using a standard thermal evaporator. As previously stated, wavelength tuning is achieved by varying the distance between the MMF and the fibre mirror. The tuning of the system was characterized by measuring the lasing wavelength as a function of the separation between the MMF and the fibre mirror. The results are shown in Fig. 1b. We demonstrated an enhanced tuning mechanism in a cladding pumped fibre laser and a tunability of 12 nm was measured with this new implementation.

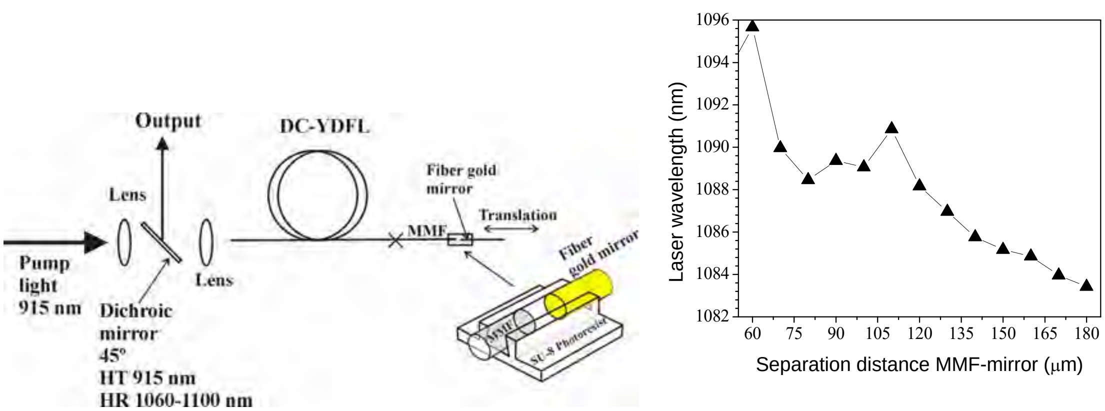

(a) (b)

Figure 1: a) Experimental tuneable setup, b) Experimental tuning results.

References:

[1] R Selvas, I Torres-Gomez, A Martinez-Rios, J Alvarez-Chavez, D May-Arrioja, P LiKamWa, A Mehta, and EG Johnson, 'Wavelength tuning of fiber lasers using multimode interference effects', Opt. Express, 2005, **13**, pp 9439-9445.

A simple, widely tunable band-rejection holey-fiber filter

D. E. Ceballos Herrera, I. Torres-Gómez, A. Martínez-Ríos, J. A. Alvarez-Chavez
Centro de Investigaciones en Óptica, León, Gto., 37170, México
danielc@cio.mx
R. Selvas-Aguilar,
Facultad de Ciencias Físico Matemáticas, UANL, Cd. Universitaria, N.L., 66450, México
J.J. Sánchez-Mondragon
Instituto Nacional de Astrofísica, Óptica y Electrónica, Pue., Puebla, 72000, México

Abstract

We report a widely tunable band-rejection filter made with holey fiber and based on microbending induced long period grating. The holey fiber filter shows a 200 nm tuning range and <0.5 dB out-of-band loss.

OCIS Codes: (060.2310) Fibre optics, (060.2340)

Introduction

Long period fiber gratings (LPFG) have been efficiently used in optical filtering operations. These components are used as non-reflecting band-rejection filters, band pass filters and tunable band-rejection filters. A non-reflecting band-rejection filter is used to block communication channels or remove Stokes orders in cascaded Raman amplifiers and Raman modulators [1]. A band pass filter allows the transmission of particular optical bands, while a tunable band-rejection filter enables broadly tunable filters for communications systems and laser applications. Recently, this last type of filter is under study because their potential applications in optical communications and other special applications.

Two ways to implement a tunable band-rejection fiber filter based in a LPG have been reported. The first case requires permanent recording of a long period grating in the fiber, in which strain, temperature or flexure is applied to obtain the tunable LPFG [2, 3]. The other way consist on applying mechanical stress in the fiber to induce the LPG in which the grating period can be easily modified to tune the wavelength center of the band-rejection filter [4]. In the latter case, the tuning range is at least three times wider than examples of the first methods reported, with similar modulation index and bandwidth. Additionally, in the mechanical induced deformation method the band-rejection filter can be erasable or reconfigurable in the fiber.

In this letter, we present a simple widely tunable band-rejection holey fiber filter based on microbending induced long period grating. The experimental results show a tuning range over 200 nm, with less than 0.5 dB loss out-of-band, modulation index of 10 dB and adjustable bandwidth from 20 to 40 nm. These characteristics and its simple implementation to operate in the near infrared region make it an attractive in widely tunable fiber filters.

Experiment and results

A periodical mechanical stress in an optical fiber induces an effective index modulation. This periodical perturbation couples energy from the fundamental mode (LP_{01}) in the fiber core to cladding forward modes (LP_{lm}). The coupling is highly efficient at a wavelength given by the phase matching condition $\lambda = (n_{Co} - n_{Cl})\Lambda$, where n_{Co} and n_{Cl} are the propagation constants of the core and cladding respectively and Λ is the induced perturbation period. The effective modulation index induced by mechanical stress is due microbending and press contributions via the photo-elastic effect. Because the long period (400-2000 μm) in LPG, corrugated plates and springs have been used to apply periodical mechanical stress on the optical fiber [5,6]. Additionally, experimental results show that ordinary optical communication fibers require higher pressure compare to holey fiber because the micro-structured air holes are more sensible to microbending [7]. For that reason, holey fibers could be a better option in the implementation of mechanically induced LPG as band-rejection fiber filters.

In this proposal the tunable band-rejection filter is obtained by pressing a semicircular section of a photonic crystal fiber on a corrugated grooved plate (CGP) with a flat plate as is shown in Figure 1a. The corrugated plate was fabricated with a radial step grooved pattern, in which each step groove has 600 μm of diameter and 900 μm depth. This CGP design permits to change the period (Λ) with the curvature radius R, according to the expression $\Lambda = \frac{\pi}{90} R$, here R is in mm. For this design Λ varies from 663 to 1047 μm. The dimensions of the CGP and the cover flat plate are 60 mm long and 30 mm wide and the semicircular grooved sector in the corrugated plate has internal and external radius of 19 mm and 35 mm respectively. The PCF used in the experiment is a single mode fiber operating in the infrared region with 10 μm core diameter and 125 μm cladding diameter.

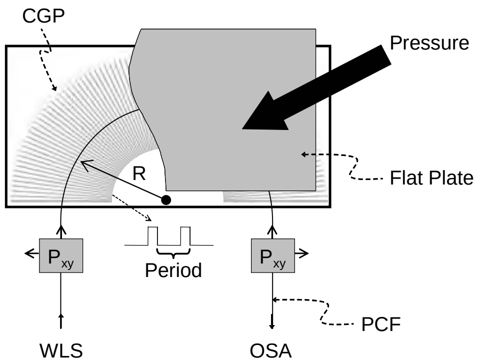

(a)

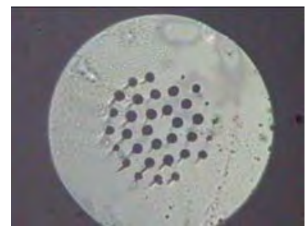

(b)

Figure 1. (a) Schematic of experimental set up, (b) Holey fiber.

In the spectral transmission characterization of band-rejection filter the signal from a white light source (WLS) was launched into one end of the PCF through a FC adapter, while the other end was coupled to the optical spectral analyzer (OSA). Then, the fiber was laid in semicircular form on the grooved plate employing two x-y translation stages (P_{XY}) and a simple manual press system was used to push the cover flat plate on the RPG. The spectral transmission of the tunable rejected filter for different values of curvature radius is shown in figure 2a, where we can observe a tunable range of at least of 200 nm and a maximum modulation index 15 dB at 1017 nm. In all cases the out-of-band loss was less than 0.7 dB, and as we increase the curvature radius the central wavelength experiments a linear red shift as shown in Figure 2b.

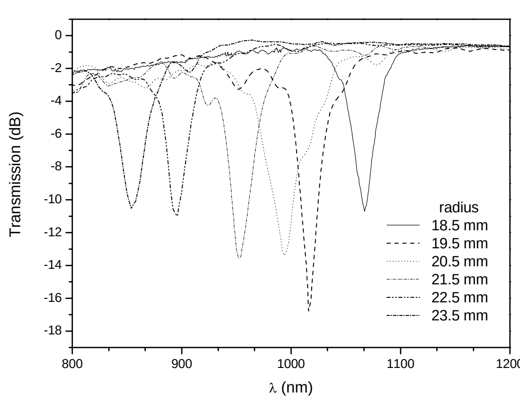

(a)

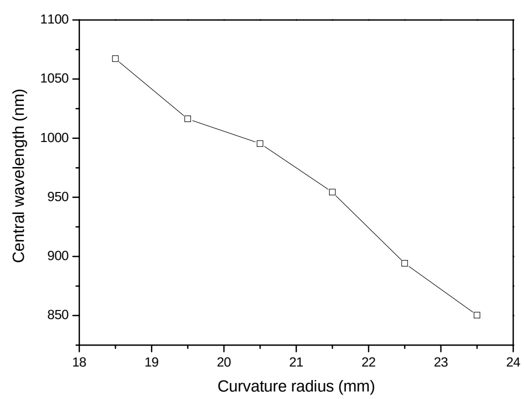

(b)

Figure 2. (a) Transmission spectra for different curvature radius, (b) Red shift central peak for curvature radius.

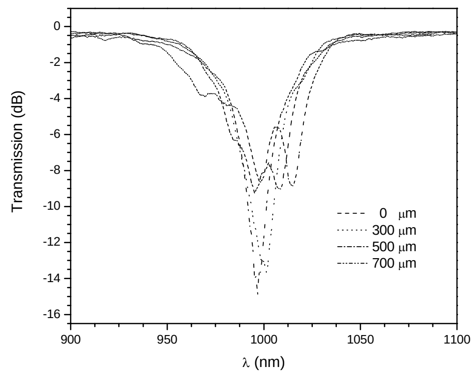

Figure 3. Bandwidth as function of the radial off set.

The bandwidth of the rejection filter can be detuned by introducing an offset in the semicircular position of the holey fiber in the corrugated plate. Figure 3 shows the bandwidth variation as a function of the offset of the semicircular trajectory. For small offsets the bandwidth is almost constant but for off sets more than 500 μm the bandwidth could increase from 15 to 30 nm, although the modulation index decrease till 8 dB. Finally, the set up was also proved with standard single mode fiber SMF28 but not notches were observed with the same conditions of the holey fiber case.

Conclusions

We propose a simple widely tunable rejected filter based in mechanical deformation that operates from visible to near infrared. The experimental results show a tuning range wider than 200 nm with insertion loss of less than 0.7 dB. Line-width could be detuned from 15 to 30 nm by adjusting the position of the fiber over the radial grooved plate. We found that the proposed set up requires low pressure (3.3 kg_f) in order to obtain deep, 15 dB modulation and the configuration is not sensitive to curvature diameters larger than 3 cm. Moreover, other reported mechanical deformation methods on tunable are limited to operate in PCF devices operating from the visible to near infrared region. This because FCF requires larger period to blue shift of the wavelength center as opposed ordinary fiber. The tunable band-rejection filter promise potential applications on photonic crystal fiber devices operating from visible to the first communication window.

Acknowledgments

Dr. Ismael Torres thanks to CONACYT for the financial support in the project **44308-Y**. Also we thanks to technicians from mechanical workshop from CIO for their valuable help.

References

[1] Anton Skorucak, “Novel fabrication technique for long period gratings in optical fibers and filter applications,” Master of Science (Physics), University of Southern California, 1999.
[2] A. A. Abromov, A. Hale. R. S. Windeler and T. A. Strasser, “Widely tunable long-period fibre gratings”, Electron. Lett., Vol. 35, No. 1, 1999.
[3] Gregory D. Van Wiggeren, Thomas K. Gaylord, Donald D. Davis, Mohammand I. Braiwish, Elias N. Glytsis, and Emmanuel Anemogiannis, “Tuning attenuating, and switching by controlled flexure of long-period fiber gratings”, Opt. Lett., Vol. 26, No. 2, 2001.
[4] S. Savin, M. J. F. Digonnet, G. S. Kino, and H. J. Shaw, “Tunable mechanically induced long-period fiber gratings”, Opt. Lett., Vol. 25, No. 10, 2000.
[5] Chien-Hung Lin, Qun Li, Amy A. Au, Yan Jiang, Enboa Wu, and Henry P. Lee, “Strain- induced Thermally tuned long-period fiber grating fabricated on a periodical corrugated substrate”, J. Lightwave Technol., Vol. 22, No. 7, 2004.
[6] Takashi yokouchi, Yoshifumi Suzaki, Kiyoshi Nakagawa, Makoto Yamauchi, Masanori Kimura, Yasuo Mizutani, Susumu Kimura and Seiki Ejima, “Thermal tuning of mechanically induced long-period fiber grating”, Appl. Opt. Vol. 44, No. 24, 2005
[7] Xia yu, Ping Shum, Songnian Fu, Xinyong Dong, and Hairong Liu, “Anomalous properties of cascaded photonic crystal fiber based long period gratings”, Proc. of SPIE Vol. 6019, 2005.

An approach to a tunable multi-wavelength fiber laser

A. Castillo-Guzman[a], Serge Doucet[b], Sophie LaRochelle[b], R. Selvas-Aguilar[a]
[a]School of Mathematical and Physical Sciences, Autonomous of Nuevo León University, Av. Universidad s/n, Cd. Universitaria, San Nicolás de los Garza 66451, Nuevo León, México.
[b]COPL, Department of Electrical and Computer Engineering, University of Laval, Quebec, Canada G1K 7P4

ABSTRACT

We show an approach to a tunable multi-wavelength fiber laser. The beam bending steel technique has been applied for our purpose. Variations on the relative distance between the fiber and the steel beam demonstrate alterations on important laser characteristics like, output power, wavelength shift and wavelength spacing.

Keywords: multi-wavelength fiber laser, optical fiber Bragg grating, beam bending steel

1. INTRODUCTION.

Optical fiber lasers with single frequency combs covering the different optical telecommunication bands find many applications in the communication and sensors areas. The requirements for these kinds of lasers have changed through recent time, even more; optical devices that cover a certain range of tunable wavelength are now needed.

Many techniques have been applied to Fiber Bragg Grating (FBG) in order to reach tunable ranges. The compression technique has demonstrated to be the one which offers not only a widely tunable range but low-cost and small insertion losses [1] also this technique gives to the FBG a much better resistance to breakage [2].

Recently we can find in the literature techniques based on compressing the FBG, such as the axial compression [3] and the beam bending technique which has proved to be a proper technique for a high tunable range, low insertion losses and small variation of the full width at half-maximum [4, 5]. Being this technique the chosen one to our work. In the other hand some of them need piezoelectric actuators which are associated with high voltage amplifiers [6, 7] making them bulky and costly.

An important implementation to the compression technique has been the addition of an embedding material [8]. This addition has improved some important characteristics as duplicate the tunable range and reducing the full width at half-maximum. The advantages for using high difference Young Modulus materials on tunable grating optical systems are well known [3, 5, 8] accomplishing low insertion losses with long wavelength shift. The material with a high Young Modulus normally used is a steel plate along with a low Young Modulus material as an embedded one. The polymer Surlyn 8940 from DuPont is a good example of an embedded material. Among other reasons for the usage of the Polymer Surlyn 8940, is that it adheres quite well to the metal and to the silica. This polymer comes in the form of small pellets with a diameter of 2mm approximately.

In this paper, we show a glance of our approach to a tunable multi-wavelength fiber laser. We have tested three different opto-mechanical devices: cylindrical shape, screw longitudinal shape and beam bending steel but in this paper we just show the most promising one. All compression devices were tested with passive fiber Bragg grating (FBG) with length

2nd Workshop on Specialty Optical Fibers and Their Applications (WSOF-2),
edited by Juan Hernández-Cordero, Ismael Torres-Gómez, Alexis Méndez, Proc. of SPIE
Vol. 7839, 783928 · © 2010 SPIE · CCC code: 0277-786X/10/$18 · doi: 10.1117/12.871825

of 25 mm which is more than 2 times the length of the experiment published in [3, 5, 8]. Previous work mainly observed the central wavelength deviation without observing the phase response stability.

2. EXPERIMENTATION

2.1 Beam bending (u-compression).

The beam bending technique consists in mounting the polymer and the grating on a metal plate (steel) in order to apply a compression force in both sides of the metal plate giving to it a U shape. The beam bending is shown as follows in Fig. 1.

A molding process is needed in order to set the optical fiber perfectly aligned, this process consists on setting different polymer layers on a metal plate delimitated by a Teflon mold. The final polymer shape has dimensions of 117mm, 10m, 7mm, long-wide-height approximately. The optical fiber grating final level was reached with 4 layers placed at 150˚C for 3 hours each one before laying down the optical fiber grating on the polymer. Then two more layers at 120˚C for 4 hours each one were set above.

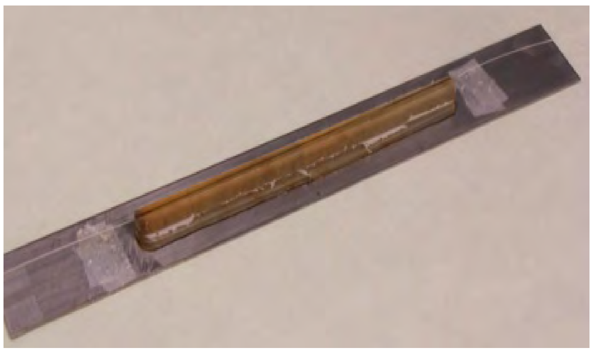

Figure 1. Polymer set on a metal plate after the molding.

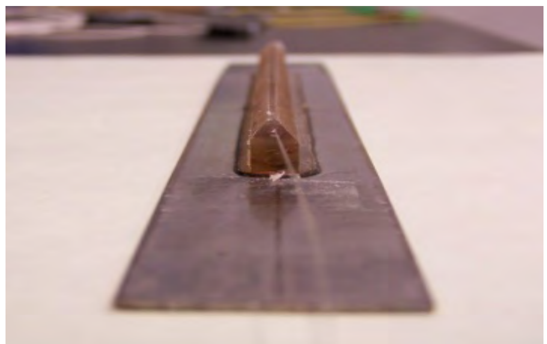

Figure 2. Frontal view of the mold with a pyramid shape.

At this point we were concerned about reducing the excess of polymer by a machining process so a pyramid shape was adopted. It was considered critical the fiber alignment so in this mold was a priority. Fig. 2 shows a front view of the final pyramid shape after the machining. The results showed a good correlation of the wavelength shift and wavelength spacing between long and short wavelengths as they are showed in Fig. 3 and Fig. 4.

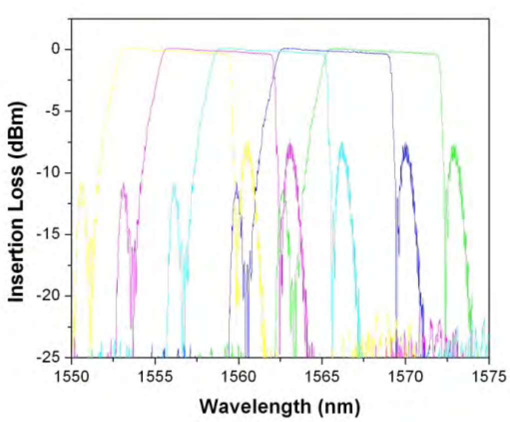

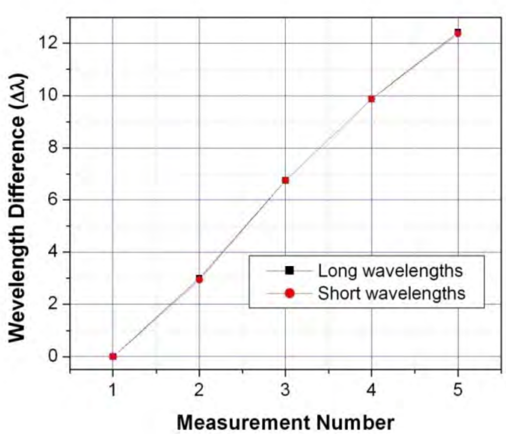

Figure 3. Wavelength shift of the U compression device with pyramid shape, machining process and grating aligned.
Figure 4. Wavelength difference of the U compression device with pyramidal shape, machining process and grating aligned.

A special analysis was done by a MATLAB program, to compare the spectral shape of all measurements by superimposing the wavelength shifted spectra. The program plots the applied spectral shifts and 3dB bandwidth for all measurements. Fig. 5 shows this comparation analysis.

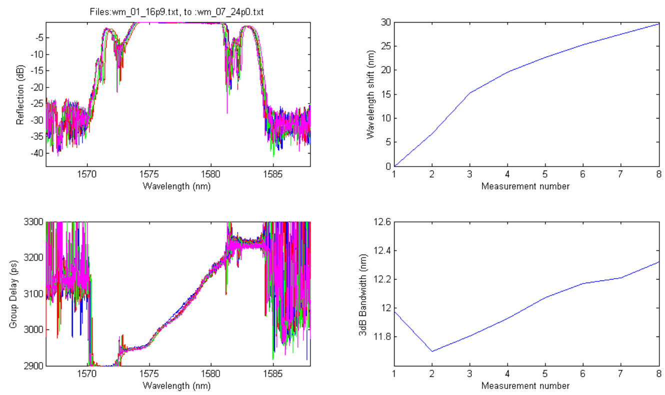

Figure 5. Matlab analysis.

U-compression system clearly demonstrates good performances as tuning system. Fig. 5 show small variations of the fiber Bragg grating group delay response and 3 dB bandwidth variation less than 5% (11.7nm/12.3nm).

2.2 Experiment of lasers with U-compression device.

The retained approach for the lasers experiment was the U-compression device because it clearly demonstrates less impact on the FBG phase response while compression was applied. The range of tuning is dependent of the relative distance between the fiber and the steel beam (L_{FB}). Three different values of L_{FB} were tested to see if some trade off exist between the tuning range and laser stability.

2.2.1 Experiment of U-compression with L_{FB}=6mm

Fig. 6 and Fig. 7 shows the polymer mold of the fiber laser with L_{FB} = 6 mm before the final machining process. Steel beam dimensions are 210 mm long, 25.4 mm width and 1 mm height. The fabricated mold has length of 117 mm and a width of 10 mm. The mold height depends on the tested distance between the fiber and steel beam.

Figure 6. Fabricated mold.

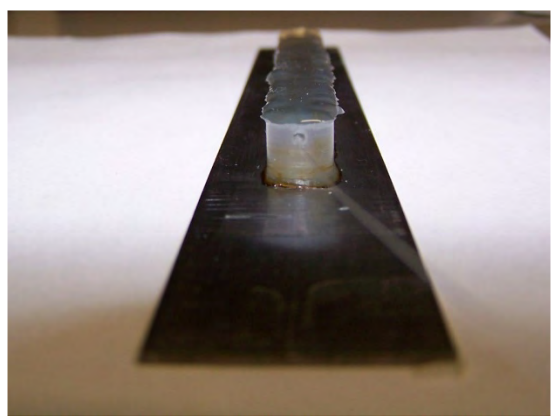

Figure 7. Frontal view of the fabricated mold.

Compression system is shown Fig. 8(a.i,b.i). It is shown a side view of the compression device for compression screw positions of 18 mm and 20.5 mm respectively. On each figure, two curves are superimposed on the picture to compare the beam bending to parabolic and circular functions. In a.ii and b.ii, each corresponding function is plotted and their difference is calculated in a.iii and b.iii. The Y axis units are in pixels of the related picture. These results clearly demonstrate that bending device allows to produces a bending shape very close to the desired circular one.

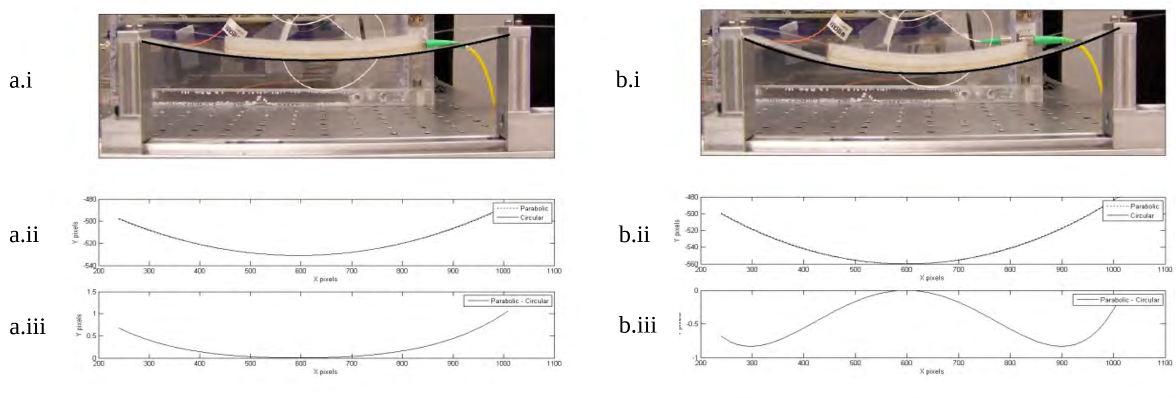

(a) (b)

Figure 8. (a,b). Beam bending shape analysis with a screw distance of 18mm and 20.1mm respectively.

Fig. 9 shows the spectrums for respective compression screw position. We can see that wavelengths were down shifted by ≈15 nm for relative displacement of 1.1% (2.4 mm / 210 mm). We also observe that output power was not especially affected by the down shifting process.

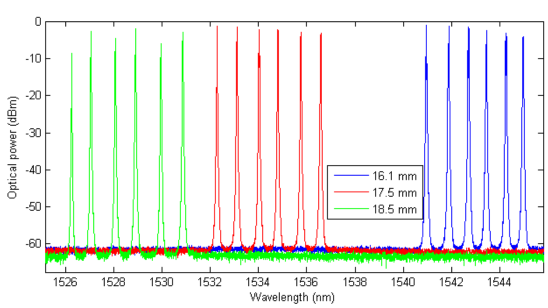

Figure 9. Wavelength shift spectrums at different screw position.

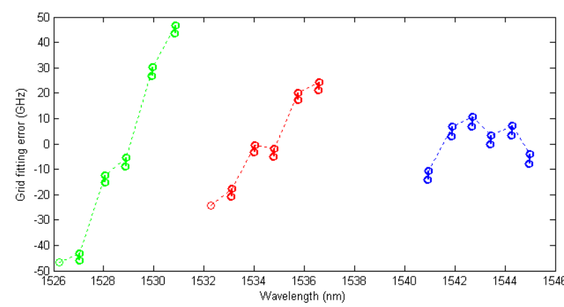

Figure 10. Grid error relative to 100 GHz.

Fig. 10 shows the evolution of the grid error relative to a 100 GHz grid. We can see that the application of the U-compression increases peak-to-peak grid error, which indicates that FBG chirp is slightly affected.

We also tested the option to make an expansion to create up shift of the wavelength. Some instability were observed during the extension application. It was previously observed that when we apply expansion on the mold, it requires longer time (compare to compression) to obtain the final expansion state. Then, while the OSA is sweeping, we can see simultaneously that laser wavelength is up shifting (same direction of the OSA sweep). That creates unusual spectral measurement like it is presented in Fig. 11 in red. This spectrum was taken for a screw position of 17.3 mm (bending forced in up direction). After this point, screw position of 17.6 mm, we saw a radical power decreasing. The observation of the noise floor reduction potentially indicates that we damaged the input splice between fiber HI1060 and EY302 in the mold.

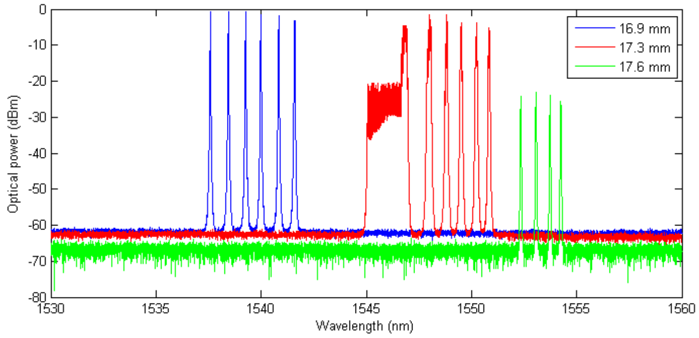

Figure 11. Strange spectral emission (red color).

After these measurements, we did the machining process to improve the symmetry and also create the pyramid shape of the mold. Fig. 12 and Fig. 13 show the sample after machining.

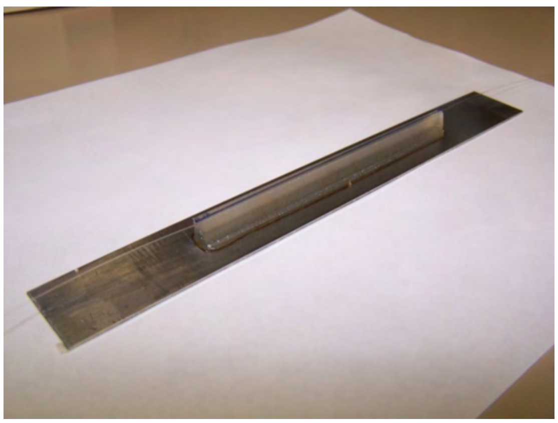

Figure 12. Machining process with pyramidal shape.

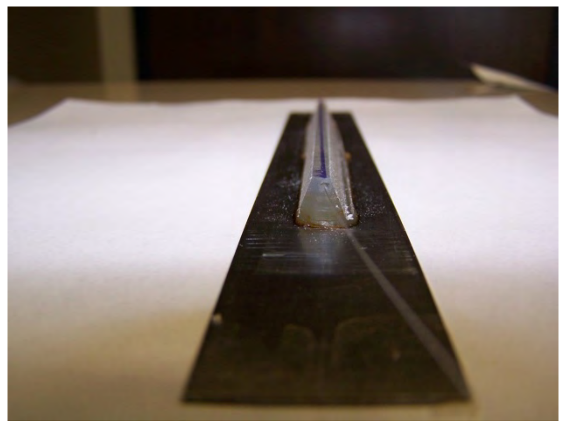

Figure 13. Front view of the mold with pyramidal shape.

Fig.14 shows different spectrums for respective compression screw position. We can see that wavelengths were down shifted by ≈16 nm. These measurements show lower output power relative to non-machined mold measurement. Like previously mentioned that was observed during the expansion experiment and it is potentially caused by splice break.

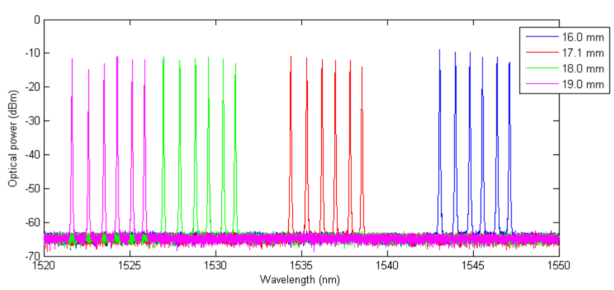

Figure 14. Wavelength shift spectrums at different screw positions.

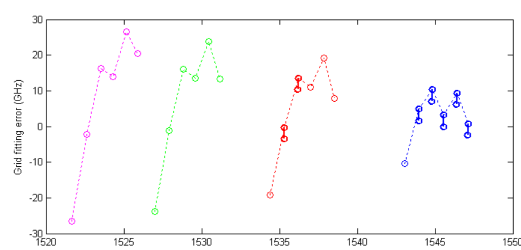

Figure 15. Grid error deviation.

Fig.15 shows the grid error evolution. We can see that chirp is quite affected but the peak to peak deviation.

These results were at first point of view very promising. However the things were not the case when we began to reduce the compression. Fig. 16 shows the output spectra while de screw distance was reduce to decrease the applied compression.

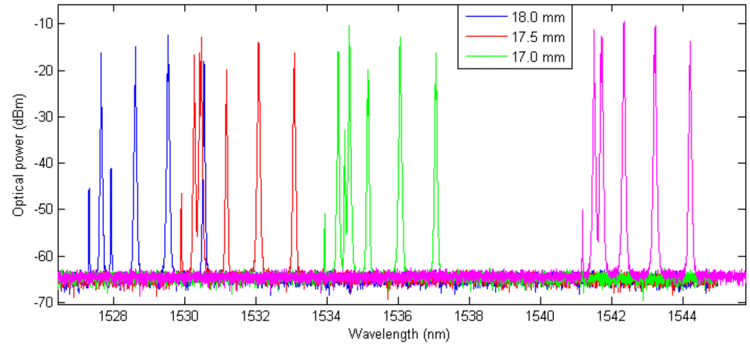

Figure 16. Spectral emission when the decreasing compression.

After few compression/release cycles, the output spectrum becomes different to the initial states observed at the beginning. At that moment, we were suspecting two potential problem sources. First, it was the accumulation of residual stress coming from the hysteresis of the polymer. Then after few cycles, the laser structure can potentially be affected by non-uniform stress along the grating. The second one was the potential temperature increase which can potentially makes polymer melting around the fiber and then let the fiber to adopt a non-well aligned position.

2.2.2 Experiment of U-compression with L_{FB}=2mm

Previous experiments showed problems coming from the use of a large distance between the fiber and the steel beam (L_{FB}). Then we tested another laser sample with smaller distance. Our expectations were that by reducing L_{FB}, the fiber would benefit of more thermal dissipation ability by more proximity of the steel beam. We also expect that putting the fiber more close to the steel beam will then ensure more stable deformation applied on the fiber.

Before taking the entire series of spectral measurement, we make an initial compression test by observing the laser performance. The evolution of the wavelength shift seemed very stable (output power) the instability disappeared at all, even in the first wavelength shift, a total range tuning of 20 nm were reached. 16 nm were for compression of the fabricated mold and 4 more nm were for extension. After the firsts observations (extension/compression) the instability appeared again.

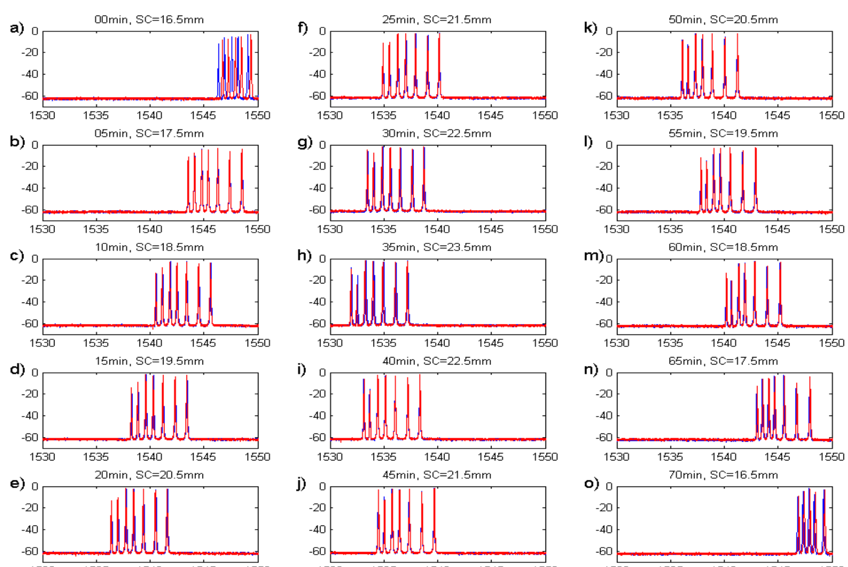

Figure 17. Measurement of spectral emissions at different times.

Even if the laser was affected by the first compression test, we got a series of spectral measurements while compression was applied. Fig. 17 shows several measurements for different time (relative to the pump activation). Each graph shows measurement just after compression application (blue) and 4 minutes after (red) for each screw position (SC). Graphs a) to h) show the spectral shift evolution while compression is gradually applied and i) to o) while it was release.

Graph c) and m) shows the laser degradation after on cycle. In m), the laser does not go back to its referred SC (c) and also presents output power alterations.

2.2.3 Experiment of U-compression with LFB=0mm

Experiment with L_{FB} = 2mm still presented some laser deterioration when we reach large wavelength shift. We then decided to test the performances of the minimal value of L_{FB} which is equal to 0. A laser sample was directly place inside a small groove made directly on the steel beam to keep in straight line the fiber during the molding process and compression experiment. A small layer of polymer was melted over the fiber laser to ensure its fixation. With this minimal L_{FB} distance, we expected to obtain a better cycling performance due to the direct contact between the fiber laser and the steel beam compressor which ensure better heating dissipation and fast response. Fig.18 shows the spectral shift evolution while the compression is increased (a to f) and released (f to i).

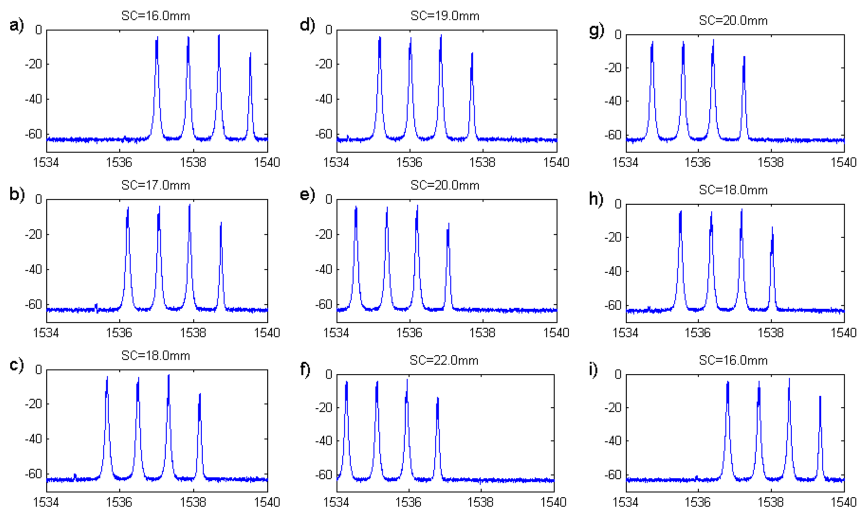

Figure 18. Spectral shift evolution during compression.

We clearly see that output power is not affected by the compression cycle for similar deformation as applied for L_{FB}=2 mm. We also observe very quick response of the tuning changes. Each time we rapidly modified the SC, the observed change was automatically saw on the next sweep on the OSA (fast sweep with low sensitivity).

CONCLUSION

Use of polymer mold as compression device requires lot of precaution during the melting process to ensure uniform distribution of the stress along the fiber. We observed some benefit on machining operation by making a pyramid cross section shape to improve stress uniformity by reducing the retention force of the upper part of the mold. U bending compression device is the only one design which gives the ability to uniformly distribute the stress along the fiber. We experiment wavelength shift of about 30 nm with small bandwidth variation less than 5%. If the desired application is more tolerant to FBG chirp variation, the only limit of the U bending will be the elastic limit of the used steel beam.

Multiwavelength laser tuning is a really more complex technique to develop. We observed relatively good tuning response when we began the measurement of specific laser. However, we observed deterioration of the lasers performances when compression/release cycle was performed with lasers in operation. We suspecting fiber heating (from high energy pump absorption) is the major issue in the system. We think that fiber temperature increase can reach value close to the melting point of the polymer and then deteriorate the fiber alignment inside the polymer mold. Only the experiment with direct contact of the fiber with the steel beam showed good performance at the expense of the tuning range.

From our point of view, tuning system for multiwavelength laser would be potentially be made by finding a specific metallic material which has high Young modulus and elastic limit. By fixing the fiber laser directly on this new beam, we will be able to reach larger tuning range. However, this approach can benefit from the tuning range extension coming from the distance L_{FB}. Another option is to find another material to replace the actually used polymer. It would be preferable to select a material with good adhesion to metal and silica but with higher melting temperature. It would be also preferable that this material will have good thermal conductivity. However, it looks to be difficult to find this kind of material.

REFERENCES

[1] Iocco, A.; Limberger, H.G.; Salathe, R.P.; , "Tension and compression tuned Bragg grating filter," *Optical Communication, 1998. 24th European Conference on*, vol.1, no., pp.229-230 vol.1, 20-24 Sep 1998 doi: 10.1109/ECOC.1998.732516.

[2] Set, S.Y.; Dabarsyah, B.; Goh, C.S.; Katoh, K.; Takushima, Y.; Kikuchi, K.; Okabe, Y.; Takeda, N.; , "A widely tunable fiber Bragg grating with a wavelength tunability over 40 nm," *Optical Fiber Communication Conference and Exhibit, 2001. OFC 2001*, vol.1, no., pp. MC4-1- MC4-3 vol.1, 2001 doi: 10.1109/OFC.2001.927833.

[3] E. Bélanger, M. Bernier, J. P. Bérubé, S. Gagnon, D. Côté, and R. Vallée, "Purely axial compression of fiber Bragg gratings embedded in a highly deformable polymer," Appl. Opt. **47**, 652-655 (2008).

[4] Alessandro Iocco, Hans Georg Limberger, Rene Paul Salathe, Lorna A. Everall, Karen E. Chisholm, John A. R. Williams, and Ian Bennion, "Bragg Grating Fast Tunable Filter for Wavelength Division Multiplexing," J. Lightwave Technol. **17**, 1217- (1999).

[5] C.S. Goh; M.R. Mokhtar; S.A. Butler; S.Y. Set; K. Kikuchi; M. Ibsen, "Wavelength tuning of fiber Bragg gratings over 90 nm using a simple tuning package," *Photonics Technology Letters, IEEE* , vol.15, no.4, pp.557-559, April 2003.

[6] Goh, C.S.; Set, S.Y.; Kikuchi, K.; , "Widely tunable optical filters based on fiber Bragg gratings," *Photonics Technology Letters, IEEE* , vol.14, no.9, pp. 1306- 1308, Sep 2002 doi: 10.1109/LPT.2002.801080.

[7] G. A. Ball and W. W. Morey, "Compression-tuned single-frequency Bragg grating fiber laser," Opt. Lett. **19**, 1979-1981 (1994).

[8] Erik Bélanger, Bernard Déry, Martin Bernier, Jean-Philippe Bérubé, and Réal Vallée, "Long-term stable device for tuning fiber Bragg gratings," Appl. Opt. **46**, 3189-3195 (2007).

Characterization of a Mechanically Induced Long-Period Fiber Grating on an Erbium Doped Fiber

H. De los Reyes[1], A. Castillo-Guzman[1], D. Ceballos-Herrera[1], R. Selvas-Aguilar[1].

[1]Universidad Autónoma de Nuevo León (UANL), Facultad de Ciencia Físico-Matemáticas (FCFM), Av. Universidad s/n, Cd. Universitaria, San Nicolás de los Garza, Nuevo León, México.

acastillog@gmail.com

Abstrtact: The characterization of a mechanically induced long-period fiber grating (MLPFG) on an Erbium doped fiber (EDF) is analyzed. A shift of 40 nm of the resonance peaks were observed varying MLPG´s fabricated with CO_2 laser.

OCIS codes: (050.0050) Diffraction and gratings; (050.2770) Grating

1. Introduction

MLPFG are transmission filter well used in optical fiber telecommunications and optical fiber sensing applications. These devices also work like band-pass filter [2], multiple wavelength filters [3], and strain measurements [4] just for mention some of them. MLPFG´s are temporally formed by refractive index perturbations in the core and in the cladding which allow the coupling of the light between the fundamental mode in the core and the co-propagating higher order modes in the cladding [1].

It is found in the literature several techniques to inscribe a MLPFG, for example using a coiled spring [5], or a silicon fixture [6]. Among these techniques, there is one which uses two metal grooved plates [1] which has demonstrated some advantages, like easy implementation, high repeatability etc. Inducing the two plate's technique made of acrylate by a CO_2 laser directly into an Erbium doped fiber (EDF), we obtained a spectral transmission characterization which has not been reported yet.

2. Experiments and Results

In this work, the MLPFG is obtained by pressing a single mode erbium doped fiber on a corrugated grooved plate by a flat plate. Three different corrugated plates with different periods (Λ) each, were used. These periods were 540, 570 and 600 nm. The three corrugated plates were fabricated of acrylate with a CO_2 laser. Each plate contains 62 step grooves with a diameter of 275 μm. Fig. 1 shows 3 step grooves of a corrugated grooved plate with a period of 570 μm.

Fig. 1 Corrugated grooved with a period (Λ) of 570 μm.

The spectral transmission characterization of the MLPFG´s was obtained by using the spectral fluorescence of the EDF. A 980 nm diode was fusion splice with a WDM which was also fusion spliced with one end of the EDF. The other end of the EDF was coupled to an optical spectral analyzer (OSA). The EDF was laid over each corrugated grooved plate (3) one at a time, being the flat plate, the cover using a simple manual press system. Fig. 2 shows the schematic experimental setup.

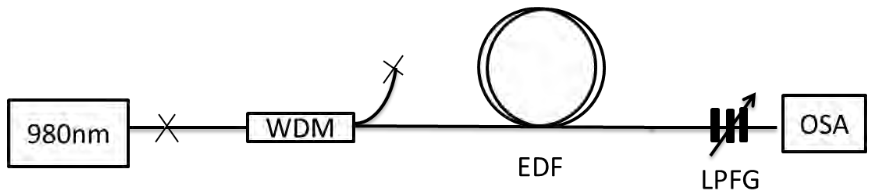

Fig.2 Schematic experimental MLPFG setup.

Once the 3 corrugated grooved plates were used, the spectral transmission was achieved as it is shown in Fig. 3. It is indicated with the numbers 1 to 3 the excited modes with the 3 different corrugated grooved plates. According to the results, there is a shift of 40 nm in the resonant dip wavelength. Maximum depth notches of 3.5 dB were achieved. It is important to remember that the tuning span was limited by the EDF fluorescence.

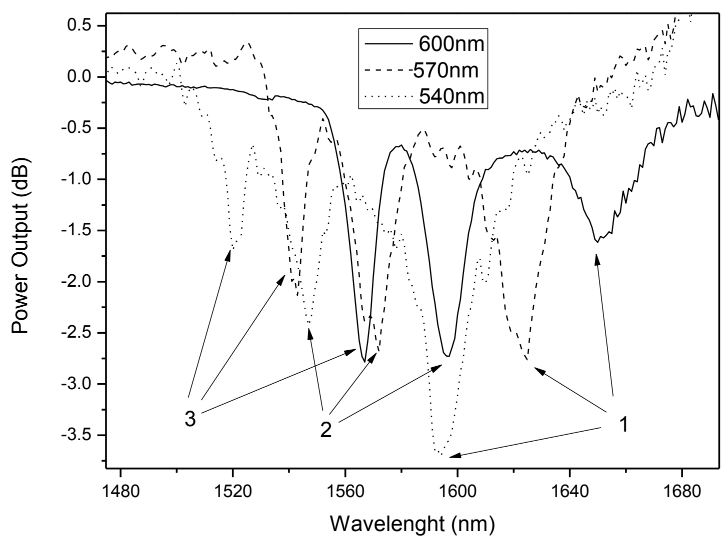

Fig. 3 Tuning span of 3 MLPFG on a EDF.

3. Conclusions

The spectral response of MLPFG´s made by pressing a grooved plate and a flat plate over a single-mode EDF was analyzed. Both the grooved plate and the flat plate were made of acrylate fabricating the MLPFG´s with a CO_2 laser. A maximum shift of 40 nm in the resonant dip wavelength was observed with a 3.5 dB depth notches as a maximum with less than 1 dB out of band losses.

4. References

[1] D.E Ceballos-Herrera, I. Torres-Gomez, A. Martinez-Rios, L. García-de-la-Rosa, J.J Sanchez-Mondragon. “Torsion sensing characteristics of mechanically induced long-period holey fiber gratings”. IEEE Sensors J. 2010, pp.1200–5.

[2] H. Sakata, K. Nishio, M. Ichikawa. “Tunable bandpass filter based on force- induced long-period fiber grating in a double cladding fiber”. Opt. Lett. **35,** 1061–3 (2010).

[3] X.W Wang, Z.L Li, Q.Q Sheng. “Optimization of mechanically induced long- period fibre grating transmission spectrum”. Chin. Phys. Lett. **24**, 741–3 (2007).

[4] S.W James, R.P Tatam. “Optical fibre long-period grating sensors: characteristics and application”. Meas. Sci. Technol. **14**, 49–61 (2003).

[5] T. Yokouchi, Y Suzaki, K. Nakagawa, M. Yamauch, M. Kimura, Y. Mizutani, S. Kimura, S. Ejima. “Thermal tuning of mechanically induced long-period fiber grating”. Appl. Opt.**44**, 5024–8 (2005).

[6]Y. Jiang, Q. Li, C.H Lin, E. Lyons, I. Tomov, H.P Lee. “A novel strain-induced thermally tuned long-period fiber grating fabricated on a periodic corrugated silicon fixture”. IEEE Photon Technol. Lett. **14**, 941–3 (2002).

Erbium-doped tunable fiber laser

A. Castillo-Guzmán[*a], G. Anzueto-Sánchez[b], R. Selvas-Aguilar[a], J. Estudillo-Ayala[c], R. Rojas-Laguna[c], D. A. May-Arrioja[d] and A. Martínez-Ríos[e]

[a]Facultad de Ciencias Físico Matemáticas, UANL, Cd. Universitaria, CP 66450, Nuevo León, México;
[b]Universidad Politécnica de Chiapas, Calle Eduardo Selvas S/N, CP 29082, Tuxtla Gutiérrez, Chiapas., México;
[c]FIMEE, Campus Salamanca, Universidad de Guanajuato, CP 36885, Salamanca, Gto., México;

[d]Photonics and Optical Physics Laboratory, Optics Dept., INAOE, Tonantzintla, Puebla 72000, México;
[e]Centro de Investigaciones en Óptica, Lomas del Bosque 115, CP 37170, León, Gto., México.

ABSTRACT

The Erbium doped fiber laser (EDFL) has demonstrated to be the ideal source for optical communications due to its operating wavelength at 1550 nm. Such wavelength matches with the low-loss region of silica optical fiber. This fact has caused that the EDFL has become very important in the telecomm industry. This is particularly important for Dense Wavelength Division Multiplexing (DWDM) which demands the use of single emission sources with different emission wavelengths. In the long run, this increases the capacity of transmission of information without the necessity to increase the infrastructure, which makes tunable laser sources an important component in DWDM applications. Many techniques for tuning have been demonstrated in the state of the art and we can mention, for example, the ones using birefringence plates, bulk gratings, polarization modified elements, fiber Bragg gratings, and very recently the use of multimode interference (MMI) effects. The MMI consists in the reproduction of single images at periodic intervals along the propagation direction of a multimode optical fiber, taking into account that these single images come from a single mode fiber optic.

Here, a compact, tunable, erbium-doped fiber laser is experimentally demonstrated. The mechanism for tuning is based on the multimode interference self-imagining effect, which results in a tunable range of 12 nm and optical powers of 1mW within the region of 1549.78-1561.79nm.

Keywords: Erbium doped fiber laser, multimode interference effect, fiber optics.

1. INTRODUCTION

Erbium doped fiber lasers (EDFLs) operating around 1550nm are the ideal emission source used in optical communications because it coincides with the low-loss region of silica optical fiber. Therefore, significant amount of research has lead to a variety of EDFLs which have played an important role in this industry [1]. Single emission sources are used as signal sources in the telecom industry, and typically different emission wavelengths are required for DWDM systems. As a result, the ability to have a single laser source that could be tuned between different wavelengths, in real time, has gained a place in the DWDM technology. For this reason, tunable laser sources have been widely investigated to supply the demand of DWDM technology. Many techniques for tuning have been demonstrated in the state of the art and we can mention, for example, the ones using birefringence plates, bulk gratings, polarization modified elements likes the one used by Shenping Li et al, where a single polarization fiber acts simultaneously as a polarizer and a tunable filter in a laser cavity [2]; fiber Bragg gratings likes the one used by Nathaniel L.C Libatique et al [3] where a tunable fiber Bragg grating and a line-width narrowing saturable absorption filter in conjunction with an intra-cavity etalon enable single-frequency emission, and very recently the use of multimode interference (MMI) effects. The latter method has

[*]acastillog@gmail.com; phone 52 81 83 29 40 30 ext. 6139

Laser Beam Shaping IX, edited by Andrew Forbes, Todd E. Lizotte, Proc. of SPIE Vol. 7062, 70620Y, (2008) · 0277-786X/08/$18 · doi: 10.1117/12.795136

allowed the demonstration of single-transverse sources with erbium-ytterbium-doped fiber, such as the one demonstrated by X Zhu et al [4] in which the splicing of a conventional passive single mode fiber onto a few cm-long active multimode fiber section enable to precisely control the diffraction laser output in a Er/Yb-co-doped fiber laser. However, in this paper, we set the configuration for a modified method using the MMI effect with a specialty erbium-doped fiber operating at around 1550 nm. The operation technique is well explained by Selvas et al. [5], in which the analytical analysis is referred to the operation window at 1060 nm. In a follow-up paper the same authors proposed a fancy change in the compact set-up for enhancing the tuning mechanism of the same Yb-doped fiber laser, in which the addition of a U-groove module increases the tunability range [6]. Similar MMI techniques have also allowed constructing very interesting devices [7], more advanced devices for planar waveguides [8] and some proposals for integrated sensors [9].

Here, a compact, tunable, erbium-doped fiber laser is experimentally demonstrated. The mechanism for tuning is based on the multimode interference self-imagining effect, which results in a tunable range of 12 nm and an optical power of 1mW within the region of 1549.78-1561.79nm.

2. EXPERIMENTAL SETUP.

The laser configuration consisted of a 9m long erbium-doped fiber (EDF) with a concentration of 200 ppm and 0.17 numerical aperture, a C-band optical fiber isolator, a 980/1550 WDM coupler, a 975 nm fiber pigtailed pumping diode laser with 90mW optical power, and the tuning mechanism, which involves a mirror with high reflectivity at the IR and a piece of multimode fiber (MMF) with a 105 µm core diameter. As can been seen in Figure 1, the pigtailed 975 nm pump source is fusion spliced to the optical isolator, which is then fusion spliced to a WDM (port 1). The port 3 of the WDM is then fusion spliced to the 9m long EDF, and the other end of the EDF fiber was used as the laser output to be monitored by the optical spectrum analyzer (OSA). The port 2 of the WDM is finally fusion spliced to a 10.31mm long MMF, and a mirror is placed in front of the MMF facet. The length of the MMF is calculated such that re-imaging around 1562 nm occurs right at the MMF output facet. Therefore, by simply changing the separation distance between the mirror and the short piece of MMF, the retro-reflected wavelength can be easily selected due to the wavelength dependence of the MMI re-imaging effect. The separation between the MMF output facet and the mirror was carefully controlled using a translation stage mechanism. This mechanism was able to change the separation in 8µm steps, and at each step the optical spectrum was acquired using the OSA. A typical V-groove was used to simplify the fiber´s alignment in order to manipulate the tuning, just by adjusting the separation distance between the mirror and the multimode facet fiber. The simplicity of the scheme enables us to construct a low cost and effective tunable device fibrerized.

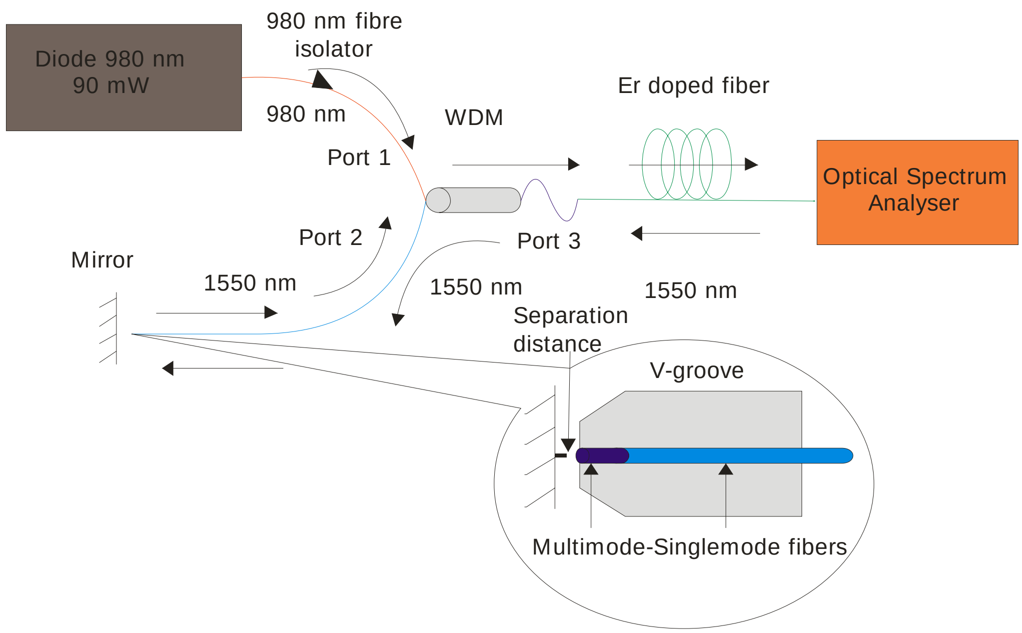

Fig. 1. Experimental setup for the tunable, fiber laser

3. DISCUSSION AND RESULTS

The Finite Difference Beam Propagation Method (FD-BPM) was used to numerically model the MMI effect that occurs in our MMF. The data considered for the simulations was that of a commercial MMF with a 105 µm core diameter, and numerical aperture of 0.22. As shown in Fig. 2, the first re-imaging point at a wavelength of 1562nm occurs at a distance of 10.31mm. The MMF is then experimentally cleaved at this distance such that when the mirror is in contact to the MMF facet, this particular wavelength will be reflected. According to MMI theory, shorter wavelengths will have appear at longer distances, and moving the mirror away form the MMF facet should tune to shorter wavelengths. The experimental length of the MMF was slightly shorter than the calculated length, which can be inferred from the experimental results.

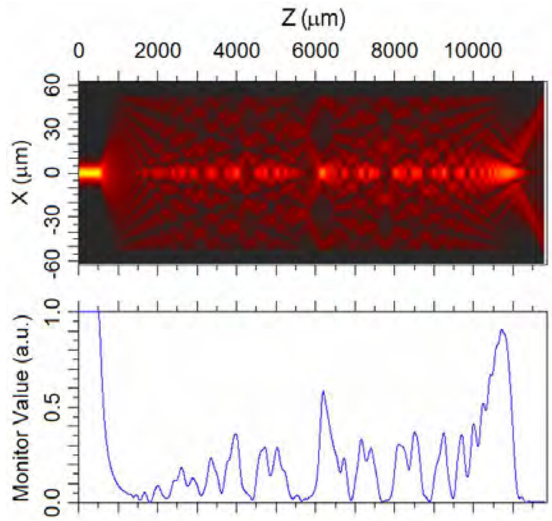

Fig. 2. Beam propagation characteristics of a 105 µm MMF for 1562nm

The laser wavelength can therefore be tuned by varying the distance between the MMF facet and the broadband mirror. Thereby, the tunable erbium fiber laser was experimentally demonstrated as shown in Fig. 3 and it revealed a tunability of 12 nm ranging from 1549.78nm to 1561.79nm with output powers of 1mW. The range tuned was within the C Band for Telecommunication, which is ideal for application related to DWDM technology. The tunability of the system was characterized measuring the lasing wavelength against the separation distance between the MMF and the mirror. The numerical simulations and experimental results are in a good agreement.

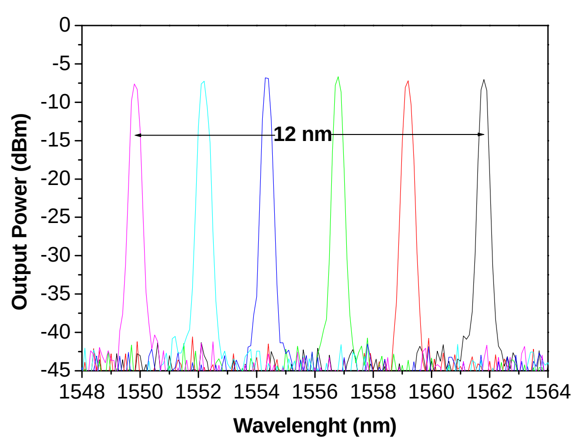

Fig. 3. Experimental tuning results.

Another important application will be related to high power lasers, since the design could be easily changed by using a double-clad structure fiber or used this lasing emission as input signal for a MOPA configuration. Thus, a cladding pumping technique with strongly saturated erbium-doped fiber should be the ideal option to explore a tunable laser with higher output power.

4. CONCLUSION

It was demonstrated for the first time an erbium-doped tunable fiber laser based on the MMI re-imaging effect. A tuning range of 1549.78nm through 1561.79nm was demonstrated with output optical power up to 1mW. It was obtained a tuning range which can be easily applied to the DWDM technology. The simplicity of the setup permitted to construct a low cost fiber tunable source with unique characteristics, being the stability and repeatability the best outstanding features of this system.

5. ACKNOWLEDGEMENT

Authors want to thank to Ismael Torres-Gomez for their grateful discussions and also thanks for the support of the National Council of Science and Technology under grants 61085 and also the supported by the program of Nuevos-.PTC-PROMEP from the Mexican Secretariat of Public Education SEP under grant 2523. Additionally D.A. May-Arrioja thanks the CONACYT program “Becas Post-doctorales” for its support.

6. REFERENCES

[1] Desurvire, E.,[Erbium-doped Fiber Amplifier], Wiley, New York, 1-100 (1994).

[2] Shenping, L. et al, "Wavelenght tunable stretched-pulse mode-locked all-fiber erbium ring laser with single polarization fiber," Optics Express 14(13), 6098-6102 (2006).

[3] Libatique, N., J., C., Wang L., and Jain R., K., "Single-longitudinal-mode tuanable WDM-channel-selectable fiber laser", Optics Express, 10 (25), 1503-1507 (2002).

[4] Zhu, X., et al. "Single-transverse-mode output from a fiber laser based on multimode interference", Optics Letters, 33 (9), 908-910 (2008).

[5] Selvas, R., et al, "Wavelength Tuning of Fiber Lasers Using Multimode Interference Effects," Optics Express 13(23),9439-45 (2005).

[6] Anzueto-Sanchez, G., et al, "Enhanced Tuning in a Fiber Laser Based on Multimode Interference Effect," Electronics Letter 42 (23),1337-1339 (2006).

[7] Soldano, L., B., and Pennings, E., C., M., "Optical multi-mode interference devices based on self-imaging:Principles and Applications," J. Lightwave Technol. 13,615-627 (1995).

[8] Bukkems, H., G., et al, "A tunable-MMI-coupler-based wavelength adjustable laser", IEEE J. of Quantum Electronics,43 (7),614-21 (2007).

[9] May-Arrioja, D., A., et al, "Reconfigurable MMI splitter for sensing applications", Measurement Science and Technology 18 (10),3241-3247 (2007).

Fiber-optic Mach-Zehnder Interferometric Temperature Sensor

Cortez-Gonzalez Luis[1], Toral-Acosta Daniel[1], Selvas-Aguilar Romeo[1], Martinez-Rios Alejandro[2], Castillo-Guzman Arturo[1], Ceballos-Herrera Daniel[1]

[1]*Universidad Autonoma de Nuevo Leon, Centro de Investigacion en Ciencias Fisico Matematicas, CICFIM, Av Universidad SN*

[2]*Centro de Investigaciones en Optica A.C., Loma del Bosque115, C.P. 37150, Leon, Guanajuato, Mexico*

lccg_fcfm@hotmail.com

Abstract: An interferometric temperature sensor based on a Mach-Zehnder all fiber configuration is proposed. The interferometer was fabricated by double tapering a single mode fiber and tested on surrounding liquid media whose temperature was varied showing a high sensitive performance of 0.035nm/°C.

OCIS codes: (060.2300) Fiber measurements; (060.2370) Fiber optics sensors; (120.3180) Interferometry; (120.6780) Temperature; (120.6810) Thermal effects.

1. Introduction

All-fiber Mach-Zehnder interferometers are of great interest due to its reliability, efficiency and easy fabrication process. They are useful for sensing applications and metrology of temperature, micro-bending, strain and refractive index in diverse areas from manufacturing to research laboratories. Several configurations and fabrication techniques have been demonstrated to construct MZ interferometers including Long Period Gratings (LPG) [1], fiber Bragg gratings (FBG) [2], singlemode-multimode-singlemode structures (SMS) [3], and fiber tapers [4, 5].

In this paper, we present a fiber optic temperature sensor based on a Mach-Zehnder Fiber Interferometer (MZFI). The MZFI was made by double tapering a single mode fiber allowing the core-cladding modal interference. Samples of glycerin/water solution at different concentrations were used to correct dispersion losses due to refractive index difference. Temperature of samples was varied from 25 - 100°C showing sensitivity of 0.035nm/°C.

2. The MZ fiber interferometer

A SMF is been used to make the interferometer. In the single mode fiber, a couple of tapers have been made with 10 mm of separation, each one of this with a 30 µm in diameter in order to conform a divisor and a coupler for the guided light in the core. The tapered structure is fabricated with a Vytran glass processing system GPX-3400. In the SMF core a LP_{01} mode is excited and it travels along the fiber; at the first taper the small diameter allows the evanescent field to incorporate certain power to the cladding, once a certain optical path is traveled through the cladding, the light incorporates again to interfere with the core mode at the second taper.

Fig. 1. MZFI made with a double taper configuration

Once the MZFI is conformed, it is put in a controlled heater with a container in which a small portion of sample liquid is deposited. In order to decrease dispersion loss, a glycerin/water solution with 95/5 % concentration is used. The refractive index of the solution was previously measured with an Abbe commercial refractometer to verify refractive index (RI) matches with the cladding value RI (1.47).

3. Experimental Setup

The experimental setup of the fiber optic MZ temperature sensor is shown in figure 2. The response of a MZFI was studied. In order to verify easier the small changes in wavelength, a 20cm long ytterbium (Yb) doped fiber was fusion spliced to the MZ interferometer. A laser source at 980 nm and a wavelength division multiplexing 980/1060 nm was added to the setup and with a perpendicular facet end fiber in the WDM a resonator cavity was conformed to stimulate Yb laser emission.

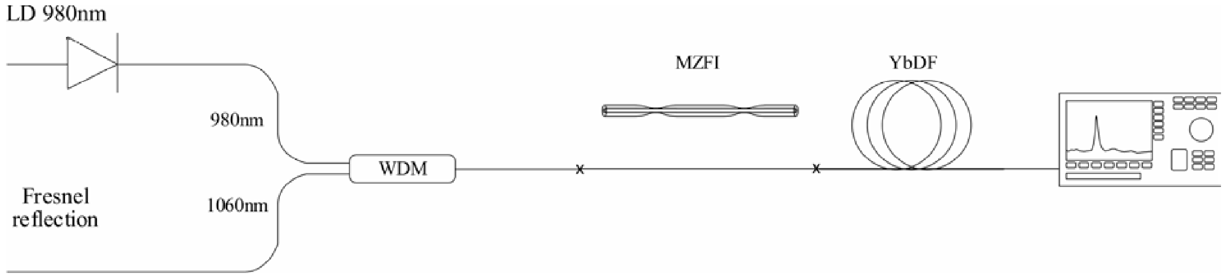

Fig. 2. Experimental setup of the MZFI temperature sensor

Additionally the MZFI was submerged in a container with the refractive index liquid solution which was also heated to verify the changes. Finally, small variations in an ytterbium emission signal at 1027 nm were measured in an optical spectrum analyzer.

4. Results and discussion

An experiment with a glycerin solution at 95/5 of concentration was carried out varying the temperature with an ± 1°C precision. Heating the solution from 25 to 100°C with steps of 5°C, and small changes in temperature were caused and let the system to stabilize in temperature every 5 minutes. The results are exposed in figure 3 showing a linear behavior in the operation range and a shift from 1027.5 nm to 1030.1 nm. This shifting wavelength was observed to be 2.6 nm in a temperature range from 25 to 100°C achieving a high sensitivity in temperature of 0.035 nm/°C.

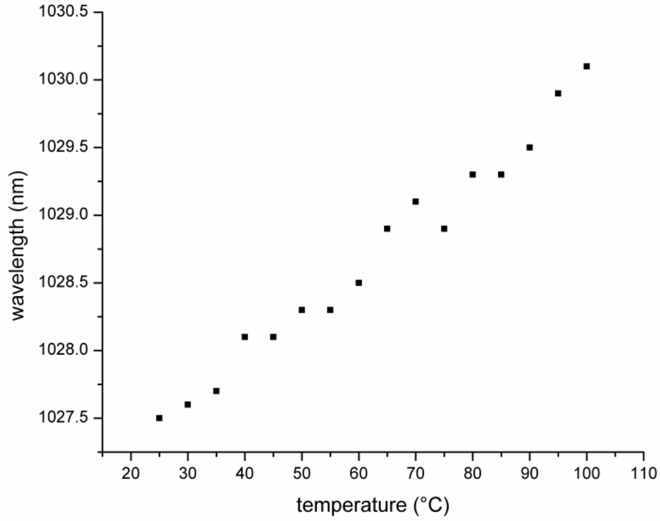

Fig. 3. Linear behavior of the MZFI sensor

5. Conclusions

In conclusion, we have demonstrated a linear all fiber Mach- Zehnder fiber optic sensor. The device is reliable and compact for use in lab tests. The sensor was proved to exhibit a modal core-cladding interference and a high sensitivity in temperature of 0.035 nm for an easy made structure.

6. References

[1] Y. Hou, T. Zhu, L. Shi, Q. Zhang, and K. S. Chiang, "Remote high temperature sensing with a reflective bandpass longperiod fiber grating and a fiber ring laser," Meas. Sci. and Technology 24(9), pp. 094023 (2013).

[2] C. Crunelle, C. Caucheteur, M. Wuilpart, and P. Megret. "Quasi-distributed temperature sensor combining Fibre Bragg Gratings and temporal reflectometry technique interrogation", Opt. and Las. in Engineering. 47(3-4),pp. 412-418, (2009).

[3] X. Lan, J. Huang, Q. Han, T. Wei, Z. Gao, H. Jiang, and H. Xiao. (2012, Jun.). “Fiber ring laser interrogated zeolite-coated singlemodemultimode-singlemode structure for trace chemical detection”. Opt. Lett. 37(11),pp. 1998-2000, (2012).

[4] Lecheng Li, Li Xia,* Zhenhai Xie, and Deming Liu, “All-fiber Mach-Zehnder interferometers for sensing applications”, Opt. Exp. 20(10), pp. 11109-11120, (2012).

[5] Youfu Geng, Xuejin Li, Xiaoling Tan, Yuanlong Deng, and Yongqin Yu, “High-Sensitivity Mach–Zehnder Interferometric Temperature Fiber Sensor Based on a Waist-Enlarged Fusion Bitaper”, IEEE Sensors, 11(11), (2010).

DESIGN AND OPTIMIZATION OF FIBER LENSES IN PLASTIC OPTICAL FIBERS FOR INDOOR ILLUMINATION

P. Viera-González[*1], G. Sánchez-Guerrero[1], G. Cárdenas-Ortiz[1], V. Guzmán-Ramos[1], A. Castillo-Guzmán[1], D. Peñalver-Vidal[2], D. E. Ceballos-Herrera[1] and R. Selvas-Aguilar[1]

[1]*Universidad Autónoma de Nuevo León (UANL), Facultad de Ciencia Físico-Matemáticas (FCFM), Centro de Investigaciones en Ciencias Físico-Matemáticas (CICFIM), Av. Universidad s/n, Cd. Universitaria, San Nicolás de los Garza, 66451, Nuevo León, México.*
[2]*Instituto Nacional de Astrofísica, Óptica y Electrónica, Luis Enrique Erro #1, Tonantzintla, 72000, Puebla, México*
**marlene.viera.gzz@gmail.com; phone +52 8183294030 ext. 7157*

ABSTRACT

We present a numerical analysis of different fiber termination shapes in order to study the maximum numerical aperture that can be obtained in end emitting plastic optical fibers with diameters around 10 mm. Our analysis includes the modeling of polished fibers with parabolic shape, conical lensed fibers, and wedged fibers with different lengths, angles and curvatures respectively. The optimization of these parameters allows us to obtain a maximum possible angle which the light can be emitted at the plastic fiber end. These results contribute to minimize the use of fiber components in luminaire systems which can be based in solar concentrators coupled to plastic optical fibers, and consequently it allows us to reduce their installation cost. We also analyze the light distribution of the emitted light and the optical tolerances of the parameters above mentioned to evaluate the performance of the optimized fiber lens. These results are of great interest for the improvement and design of compact luminaire systems based in optimized plastic fiber lens for indoor illumination.

Keywords: plastic fibers, fiber lenses, numeric aperture

INTRODUCTION

Since the beginning of the human race the indoor illumination has played a key role in everyday life and, at the same time, it has contributed with the waste of energy and the pollution of the planet according to the consumed electricity to produce this illumination. In 1997 the global lighting electricity production was 2016 TWh, this amount represents a $230-billion lighting energy bill and generates 1775 million tons of carbon dioxide (CO_2); a research made in 2002 estimated that this lighting electricity production will continue growing with the time[1,2]. Under this context, renewable lighting sources must be considered as an important issue when energy saving is pretended[1]. It is estimated that the implementation of measures for saving electrical energy for illumination with actions such as improving lighting systems may reflect a savings of $75-$115 billion/year and, besides direct savings, indirect energy savings can be found reached due of the reduction in heat production inside the edifications and the reduced energy consumption for air conditioner systems[2,3].

Furthermore, it is believed that most electrical light sources produce negative effects in humans, for example: problems with the degradation of bilirubin, low levels of vitamin D, alteration of the circadian rhythms and inadequate secretion of melatonin, which is related with the depression when it reaches low levels. By contrast, daylighting is compound by the full-spectrum and it is the type of light that the human eye is adapted by evolution. In the field of psychology, the natural illumination has been associated with higher productivity, lower absenteeism, positive attitudes, reduced fatigue, reduced eyestrain and satisfactory controls of the circadian rhythms[3].

One solution for energy saving is the use of illumination systems based on solar concentrators and plastic optical fibers (FOP). In this context, optical fibers play an important part in the fields of illumination and solar applications, such as solar lighting for indoor illumination, photo-bioreactors and hydrogen generation, safety lighting in explosive environments, among others[6-10]. Lighting systems based in plastic fibers collect the Sunlight and transport it using FOPs inside the edifications, resulting in saves of electrical energy and providing the occupants of the benefits of natural lighting[4]. These fiber optic daylighting systems need to be improved because their efficiency depends of advanced

Nonimaging Optics: Efficient Design for Illumination and Solar Concentration X,
edited by Roland Winston, Jeffrey Gordon, Proc. of SPIE Vol. 8834, 88340P

tracking solar systems, generating with this an expensive production cost. Looking other ways to improve these kind of systems the researchers are trying to increase the efficiency of the optical components and the coupling between them[5]. The light distribution by the plastic fiber is a key factor due to losses and the limited numerical aperture[9]. That represents a limiting when the light is delivered at the luminaire. As consequence, recent works have concentrated efforts on improving the light-propagating properties of larger core diameter fibers (around 10 mm of diameter) in order to introduce, transport, and emit in an efficient way the solar radiation propagating inside them.

In this paper aims to present an analysis of the numerical aperture of the plastic fibers when different types of fiber lenses are implemented at the fiber output and, at the same time, it seeks to compare the results obtained with similar patterned silica fibers[10]. With this analysis we are able to find the designing parameters and tolerances necessary to fabricate in an optimized way fiber output surfaces in order to improve the output angles of the emitted rays, and obtain a higher illuminated area.

2. THEORETICAL BACKGROUND

Plastic and silica glass are the two dominant materials used to fabricate optical fibers. For solar lighting applications, plastic fibers with larger core diameters provide more flexible solutions than silica fibers because they are less sensitive to bending induced by movements in solar tracking systems or the curved path followed during the fiber installation in the building structure. Nevertheless, plastic fibers have larger material attenuation (~0.1dB/m) compared to glass fibers (~0.1dB/km). This limitation makes the use of plastic fibers for lighting applications acceptable only in lengths lower than 30 meters; however, in the majority of cases, these distances are sufficient. Basically, plastic fibers are fabricated with a Polymethyl-methacrylate resin (PMMA) as core material with refractive index 1.492, and with Fluorinated polymer as cladding material with refractive index 1.418. The employment of these materials produces plastic fibers with high numerical apertures around 0.5. The control of this numerical aperture is of great importance to introduce or emit light from the fiber with high efficiency.

2.1 Definition of the Numerical Aperture

The capacity of a fiber to capture light depends on the angle of aperture of the acceptance cone. The acceptance cone contains all the possible light rays traveling in air with direction to the fiber input, and guided when they enter to the fiber. In Fig. 1, it is shown a step-index optical fiber constructed of two layers; the core with a refractive index n_1, where the light is guided. The core is surrounded by the cladding with a refractive index $n_2<n_1$. Light injected into the core with some incidence angle θ with respect to the fiber axis strikes the core-cladding interface. From Snell's law, when the angle of incidence is greater than the critical angle ϕ_c (Fig. 1), light is reflected and guided further along the core. The greatest possible angle at which light can be launched into the core and guided by the optical fiber is the acceptance angle θ_{max}. For a planar fiber end, we can obtain an analytical expression for the acceptance angle:

$$\sin\theta_{\max} = n_1\sqrt{1-\sin^2\phi_c}\ , \tag{1}$$

According to Snell's law, we have $\sin\theta = n_1 \sin\phi_t$ at the interface air-core, and $n_1 \sin\phi_c = n_2 \sin 90°$ at the interface core-cladding. The sine of the angle of acceptance is called numerical aperture (NA), and it is given by:

$$NA = \sqrt{n_1 - n_2}\ , \tag{2}$$

The numerical aperture is a very important parameter of an optical fiber because it indicates the fiber capacity for accepting and guiding light. Fibers with a higher numerical aperture can accept more light. As it was mentioned above, numerical aperture of plastic fibers is typically larger than in glass fibers and is often approximately 0.5, which facilitates easier the coupling of light into the fiber.

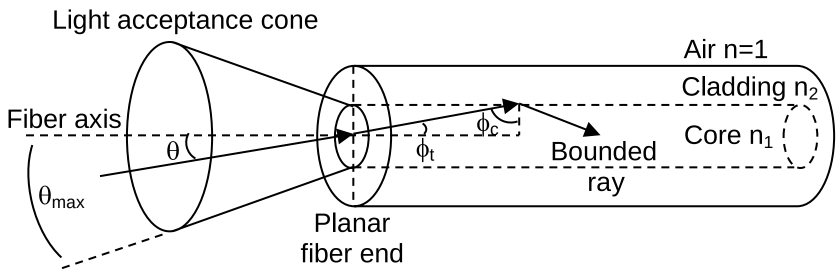

Figure 1. Numerical aperture of an optical fiber with planar cut end.

2.2 Considerations of the Numerical Aperture on non-planar surfaces

It is clear that each point of the surface at the fiber output will emit rays with the same acceptance angle (or numeric aperture) defined at the planar input. Nevertheless, this condition is not valid if the output face is modified with different shapes, for example conical lensed ends with different lengths, angles, and curvatures. In this case, an adequate shape of the conical end could increase the numerical aperture at the fiber output instead of use a planar end[10-13]. This increasing in NA is of great importance to minimize the use of fiber components in luminaire systems based in plastic optical fibers, due to the fact that a higher NA implies an increment of the acceptance angle and consequently a major illuminated area without necessity to use additional external lenses to expand the emitted light.

Then, according to Eq. 1, the output angle of the emitted rays depends not only on the refractive indexes of the core and cladding, but also on the curvature of the fiber surface, which can be defined using the coordinates of the emission point on the modified end with respect to the fiber axis (R, h, ϕ), as it can be observed in Fig. 2.

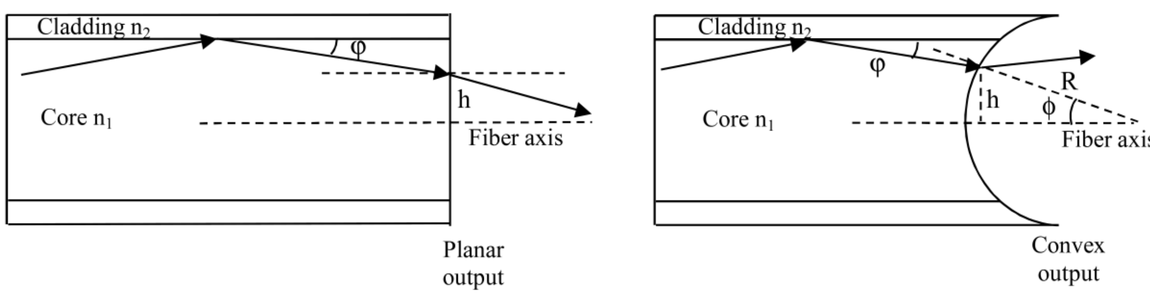

Figure 2. Output angles of the emitted rays for planar and convex outputs. Both configurations are drawn using the same angle φ for the ray traveling inside the fiber.

As it can be observed in Fig. 2, a same ray can be emitted with different ways modifying the surface output of the fiber. If we choose the correct surface, we can obtain a higher acceptance angle of the emitted rays, and to increase the numerical aperture of the system. In order to increase the NA at the output end we have to use conical shapes like parabolas or wedged ends, nevertheless their analytical description are more complex, although we can overcome this difficulty performing modeling based in ray tracing of the different output surfaces. In this case more parameters like curvature radius, curvature center position and shapes have to be considered. The optimization of these parameters allows us to obtain a maximum possible angle which the light can be emitted at the plastic fiber end. These results contribute to minimize the use of fiber components in luminaire systems which can be based in solar concentrators coupled to plastic optical fibers[13], and consequently it allows us to reduce their installation cost.

On the other hand, it is desirable to analyze the light distribution of the emitted light and the optical tolerances of the parameters above mentioned to evaluate the performance of the optimized fiber conical end. This numerical characterization is shown in later sections.

3. NUMERICAL EXPERIMENT AND RESULTS

Theoretically, the output of a FOP can be modified using different fiber lenses, like was mentioned in the previous section. A FOP with the characteristics shown in Table 1 and a 'white source point' of 1million of emitted rays with an aperture cone angle of 48˚ and a power of 50,000 lumens, which is composed by different wavelengths (0.4, 0.5, 0.6, 0.7 and 0.8 micrometers) were modeled using ZEMAX-EE optical design software. For this simulation the source point was put almost in the surface of the FOP with the objective of modeling the plastic fiber while is illuminated by the light concentrated in the focal point of a collector system.

Table 1. Physical characteristics of a Polymethyl-methacrylate FOP.

PMMA Optical Fiber	
Total diameter	10 mm
Core diameter	9 mm
Core refractive index	1.491
Cladding refractive index	1.418
Length	50 m

For this numerical experiment, four different forms of lenses were selected (Fig. 2): Concave surface with parabolic curvature, convex surface with parabolic curvature, conic surface, and tilted planar surfaces.

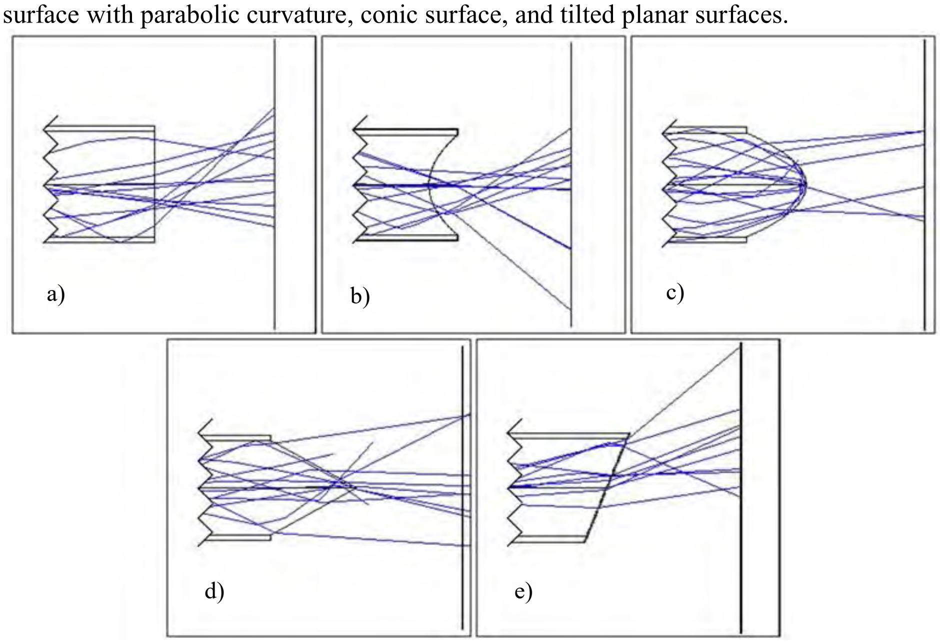

Figure 3. Comparative between the different types of fiber lenses modeled for the numerical experiment. Every image shows in an illustrative manner the physical appearance of each configuration. a) FOP with typical planar end. b) Plastic fiber with a parabolic concave surface. c) Fiber optic lens with a parabolic convex shape. d) Plastic fiber with conic termination. e) FOP with tilted termination.

In the simulation, the geometric parameters of each fiber lenses were varied, in the case of the concave and convex surfaces the curvature radius was modified from 1 to 20 mm (convex case) and from -20 to -1 mm (concave case); in this case, the minus sign indicates the curvature center position respect to the surface, positive at right, and negative at left. For the conic surface the aperture angle changed from 56.3˚ to 3.9˚; and, in the case of the tilted surfaces the slope varied from 1˚ to 45˚.

Two different detectors were utilized during the experiment. The first one was a detector volume with a size of 80x80x2 mm placed at a distance of 10 mm from the fiber where the incidence flux was measured. The size of the light spot and the light distribution on a transversal line are shown in Fig. 4, 5 and 6 for each termination shown in Fig. 3.

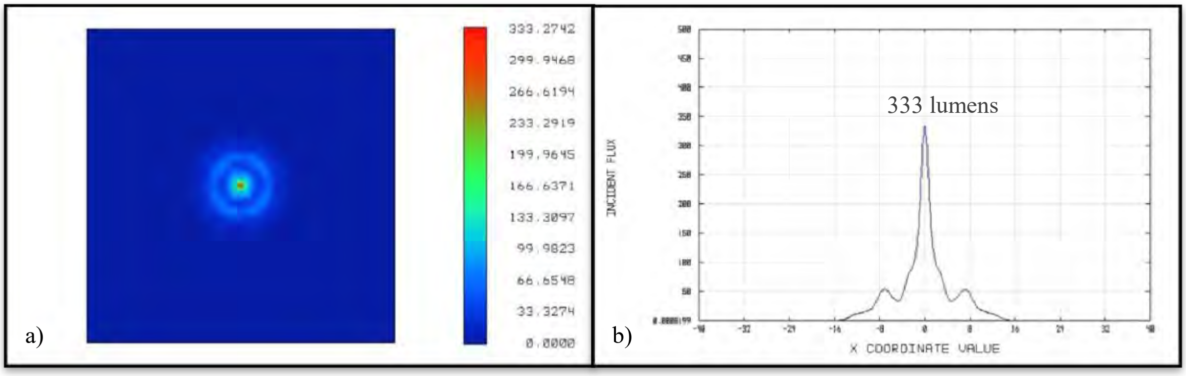

Figure 4. a) Incident flux (lumens) distributed on the detector and b) light distribution on a transversal line for a planar end. The spot is contained in an area with 15 mm of diameter and reach a peak intensity of 333 lumens.

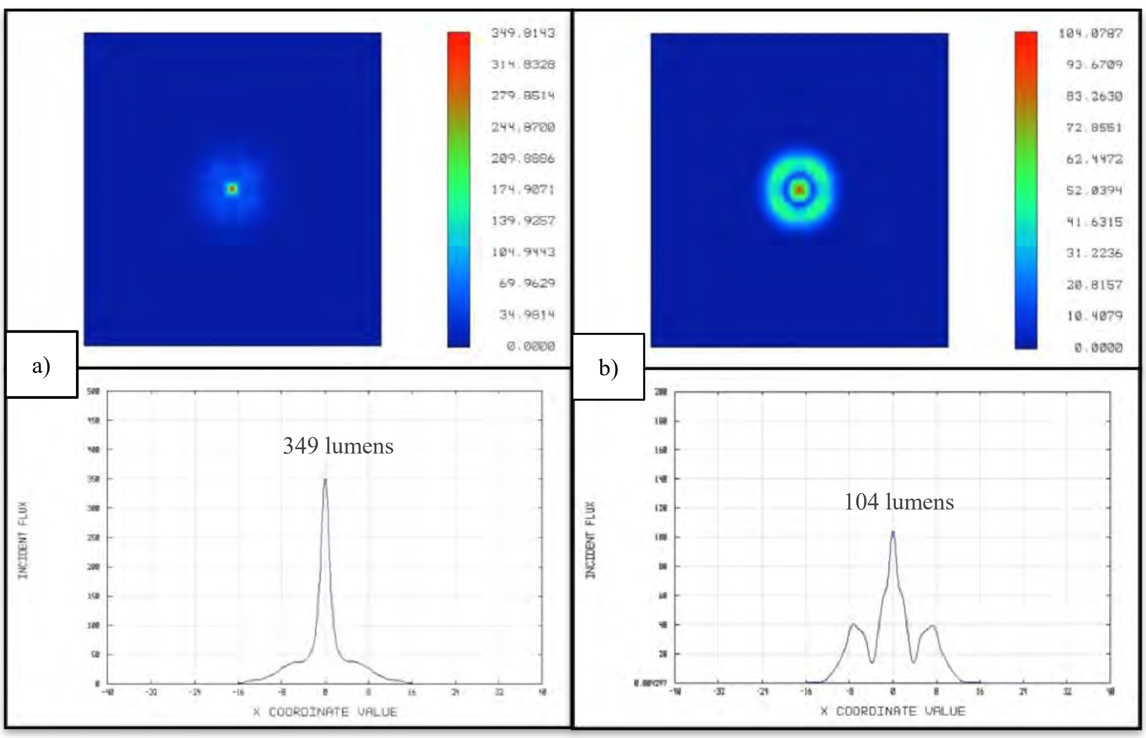

Figure 5. Incident flux (lumens) distributed on the detector and light distribution on a transversal line for: a) the parabolic concave lens, and b) the parabolic convex lens, with curvature radius of 10 mm and -10 mm, respectively. The x-axis shows the radius of the spot and the y-axis show the flux. Both show a spot with a radius of 16 mm but different peak intensities. The parabolic concave lens shows a peak intensity of 349 lumens, and the parabolic convex lens shows a peak intensity of 104 lumens.

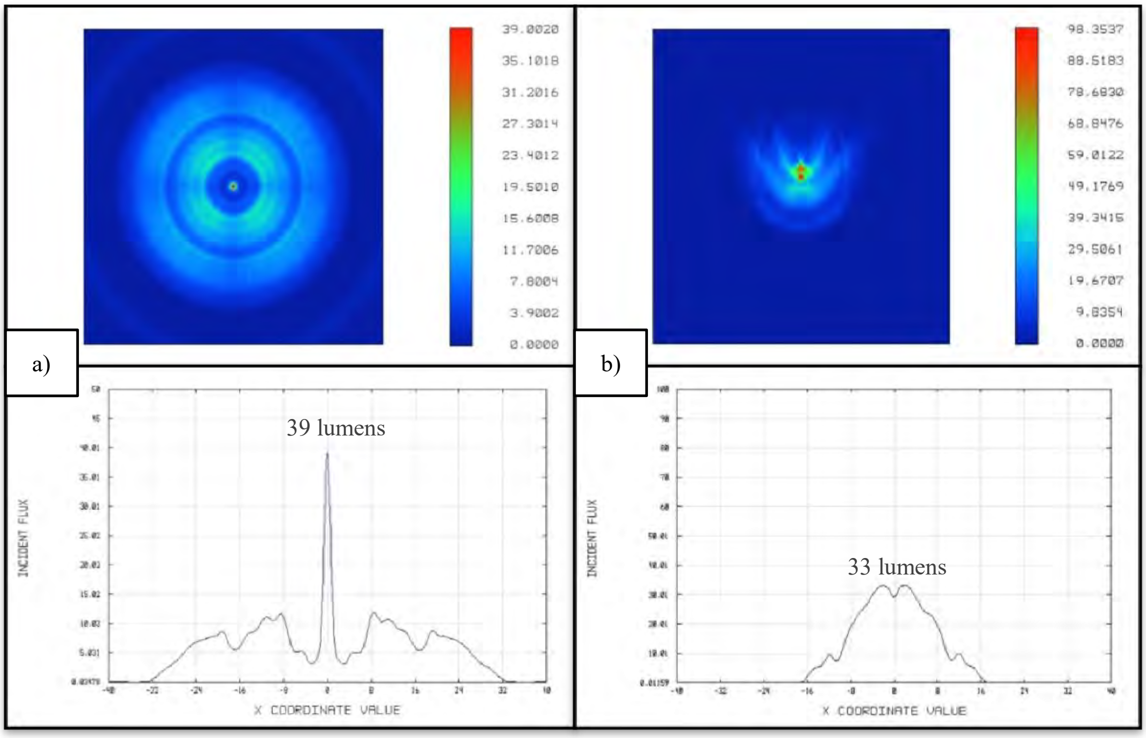

Figure 6. Incident flux (lumens) on the detector for: a) The fiber with conic termination with an semi-angle of 16.7˚, and b) the fiber end tilted an angle of 29˚. Different sizes and distributions of the light spot can be observed. For the conic termination there is a peak intensity of 39 lumens and a spot radius of 40 mm. For the end tilted fiber there is a peak intensity of 33 lumens and a spot radius of 17 mm.

The second one was a flat detector with a size of 50x50 mm. In this one, the luminous intensity was measured considering the incidence angle of the emitted rays on the detector. Fig. 7 shows the power concentrated by solid angle, showing the numerical aperture obtained in each case.

The concave lenses do not generated significant variations in the aperture angle but show a uniform distribution in the light spot; during the experiment the concave surfaces reached the best uniformity in the light spot in the cases when the curvature has a radius between 6 to 13 mm. By contrast, the parabolic convex lenses can increase the numerical aperture slightly (2˚ - 6˚), but cannot reach uniform outputs; the simulation showed a better uniformity in the output when the curvature radius were between -10 to -8 mm.

The plastic fibers with conic termination show the higher variation in the aperture angle, among 52˚ to 80˚, due of the variations in the conic semi-angle, but in general way the spot generated by the semi-angles higher than 10˚ show an increase in the aperture angle. Furthermore, the light output reaches an acceptable uniformity when the conic semi-angle was in the range of 14˚ - 20˚.

The FOP with tilted end was the only lens that does not have revolution symmetry and due to the tilt the total internal reflection was broken for some rays. The main characteristic of the output is that emitted rays are redirected toward the same direction as the inclination of the fiber end, besides it is observed that this surface breaks the total internal reflection of some rays propagating inside the fiber.

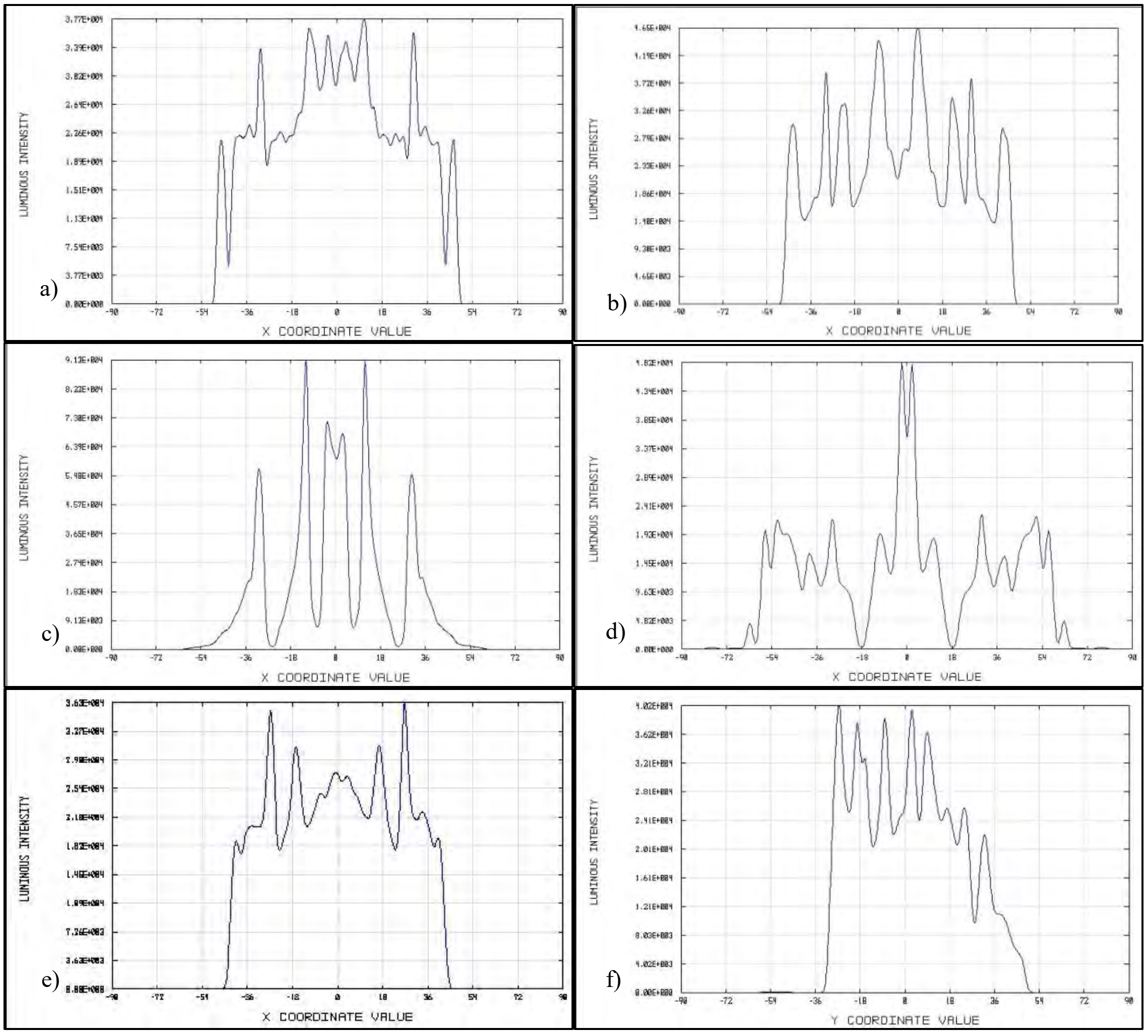

Figure 7. Every graph shows the luminous intensity measured by the flat detector. The x-axis shows incidence angle in degrees for the x-coordinate (with a y-coordinate equals to zero) and the y-axis represents the luminous intensity in lumens. a) FOP without lenses, the light spot has and aperture angle of 50˚ and total power of 45,883 lumens. b) Concave lens with a curvature radius of -10 mm, an aperture angle of 50˚ and total power of 46,227 lumens. c) Convex lens with a curvature radius of 10 mm, an aperture angle of 60˚ and total power of 40,090 lumens. d) FOP with conic end, the cone has a semi-angle of 16.7° and expand the light with an aperture angle of 80˚ and total power of 46,020 lumens. d) Fiber end tilted 29° with an aperture angle of 48˚ and total power of 33,507 lumens. e) This image represents the cross section for the y-axis using the fiber end tilted 29°.

4. CONCLUSION

We have reported a numerical analysis of different fiber termination shapes in order to study the maximum numerical aperture that can be obtained in end emitting plastic optical fibers with diameters around 10 mm. We modeled using ray tracing of the emitted rays from different surfaces outputs of the fiber using shapes like: concave, convex, conic and tilted planar lens. We observe that the suggested surface in order to increase the acceptance cone at the output end is a cone with semi-angle between 14˚ and 20˚. Other important result is the case of the parabolic concave lens where the output has uniformity, for a curvature radius among 6 to 13 mm, even better than the FOP without lenses. These results contribute with the improvement and design of compact luminaire systems based in optimized plastic fiber lens for indoor illumination.

REFERENCES

[1] Dubois, M. C. and Blomsterberg, A., “Energy saving potential and strategies for electric lighting in future North European, low energy office buildings: A literature review,” Elsevier Science SA. Energy and Buildings, 43(10), 2572-2582 (2011).

[2] Mills, E. and Orlando, E., “Why we’re here: the $230-billion global lighting energy bill,” Proc. Right Light 5 Conf., 369-385 (2002).

[3] Edwards, L. and Torcellini, P., “A literature review of the effects of natural light on building occupants,” U.S. Department of Energy (DOE) Information Bridge, July 2002, <http://www.osti.gov/bridge/basicsearch.jsp> (September 2012). http://www.nrel.gov/docs/fy02osti/30769.pdf

[4] Maxey, L. C., Lapsa, M. V., Boudreaux, P., Earl, D. D., Morris, J. and Bunch, T., “Hybrid Solar lighting: Final technical report and results of the field trial program”, U.S. Department of Energy (DOE) Information Bridge, 2008, <http://www.osti.gov/bridge> (February 2013). http://www.nrel.gov/docs/fy02osti/30769.pdf

[5] MUHS, J. “Design and analysis of hybrid solar lighting and full-spectrum solar energy systems. En: Solar 2000 Conference, 2000, Madison, Wisconsin. 2000.

[6] Grisé, W. and Patrick, C., “Passive solar lighting using fiber optics,” Journal of Industrial Technology, Vol. 19, No. 1, (2003).

[7] Jaramillo, O. A., del Río, J. A. and Huelz, G., “A thermal study of optical fibers transmitting concentrated solar energy,” J. Phys. D: Appl. Phys., Vol. 32, 1000-1005, (1999).

[8] Kandilli, C. and Ulgen, K., “Review and modeling the systems of transmission concentrated solar energy via optical fibres,” Renewable and Sustainable Energy Reviews, Vol. 13, No. 1, 67-84, (2009).

[9] Kandilli, C, Turkoglu, A. K. and Ulgen, K., “Transmission performance of fibre-optic bundle for solar lighting,” International Journal of Energy Research, Vol. 33, 194-204 (2009).

[10] Bescherer, K., Munzke, D., Reich, O. and Loock, H.-P., "Fabrication and modeling of multimode fiber lenses," Applied Optics, Vol. 52, No. 4, (2013).

[11] Kovacevic, M. S., Djordjevich, A. and Nikezic, D., “Effects of end face tilt angle on numerical aperture for straight and bent plastic optical fibers,” Fiber and Integrated Optics, Vol. 26, 111-122, (2007).

[12] Hokkanen, A. and Tammela, S., “Hemisphererically ended optical fiber lenses,” Physica Scripta, Vol. T69, 159-172, (1997).

[13] Ullah, I. and Shin, S., “Development of optical fiber-based day lighting system with uniform illumination,” Journal of the Optical Society of Korea, Vol. 16, No. 3, 247-255, 2012.

Effect of Gain and Temperature in all-fiber Multimode Interference Filters based in double-clad Yb-doped fibers

Daniel E. Ceballos-Herrera, Valentín Guzmán-Ramos, Romeo Selvas-Aguilar, Arturo Castillo-Guzmán, Daniel Toral-Acosta, Luis Cortez-González,
Universidad Autónoma de Nuevo León, Facultad de Ciencias Físico Matemáticas FCFM, Av. Universidad S/N, Cd. Universitaria, San Nicolás de los Garza, C.P. 66450, Nuevo León, México
de.ceballos.herrera@gmail.com

Abstract: We show a tunable multimode-interference filter based on a Yb-doped fiber. The filter is tuned up to 3.2 nm modifying the gain of the Yb-doped fiber, and has a temperature sensitivity of 0.22nm/°C.
OCIS codes: (060.0060) Fiber Optics and Optical Communications; (060.2370) Fiber Optics Sensors

1. Introduction

Recently, the multimode interference (MMI) in optical fibers has been extensively studied due to their interesting applications in optical fiber sensors, fiber tunable lasers, photonic switches, all-fiber optical tunable filters, etc. [1-8]. The MMI is produced when an electromagnetic field is coupled into a multimode waveguide; then, a specific set of eigen-modes of the MM waveguide is excited and each of them propagates along the waveguide independently with its own propagation constant. During their propagation can occurs a superposition of these excited modes generating a complicated field distribution due to multiple interferences; however a self-imaging of the input field can be obtained at certain positions. Due to their origin, the self-imaging position depends specifically on wavelength, refractive index and length of the MM waveguide. In order to modify the self-imaging position we can change the ambient conditions of the MM waveguide using curvatures, temperature, and strain, modifying in this way the refractive index and length of the MM fiber. In this work we present a novel option to change the self-image position using active MM fibers. Our proposal consists in to use a double-clad Yb-doped fiber as a MM waveguide, and by changing the pump power level of the Yb-doped fiber, we modify its emission gain, which can affect the refractive index of the doped core, and consequently to change the spectral characteristics of the MMI-filter. Our results show evidence of this effect, and additionally we characterize the temperature dependence of the active MMI filter.

2. Experiment and results

The experimental setup is shown in Fig. 1. A white light source and a laser diode with emission at 980nm were used. To form the MMI filter we use a 5.2 cm length of double clad Yb doped fiber (YB1200-10/125) with 10μm of core diameter, and we spliced in both sides two single mode fibers (SMF28) with 8 μm of core diameter respectively.

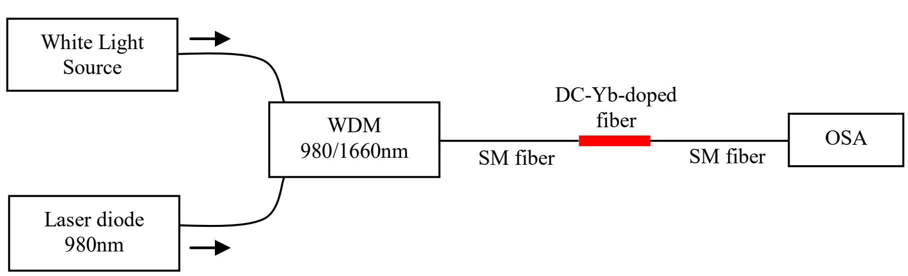

Fig. 1. Experimental Setup.

However the difference in core diameters between the SMF fibers and the Yb-doped fiber is not large, we can obtain multimode interference as it is observed in Fig. 2a due to the fact that in the 1300-1650nm wavelength region the Yb-doped fiber shows a multimode behavior.

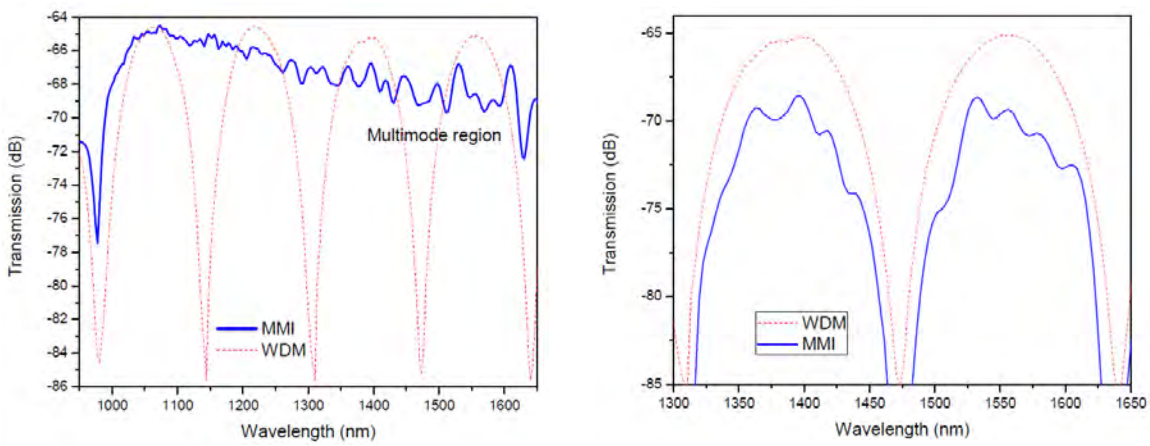

a) b)

Fig. 2. a) Spectral transmission of the MMI filter using a white light source, in this case, the MMI filter is not spliced to the WDM. Also, in this incise is shown in red the spectral transmission of the WDM used in setup. b) Spectral transmission of the MMI filter spliced to the WDM in blue.

If we use the setup shown in Fig. 1 only with the white light source as input, we obtain the spectral transmission observed in Fig. 2b. Then, our interest is to modify the spectral transmission of the MMI filter changing the pump power of the diode laser at 980nm. To proceed to measure this, we use at the same time the white light source and the laser diode in the setup, obtaining the results shown in Fig. 3.

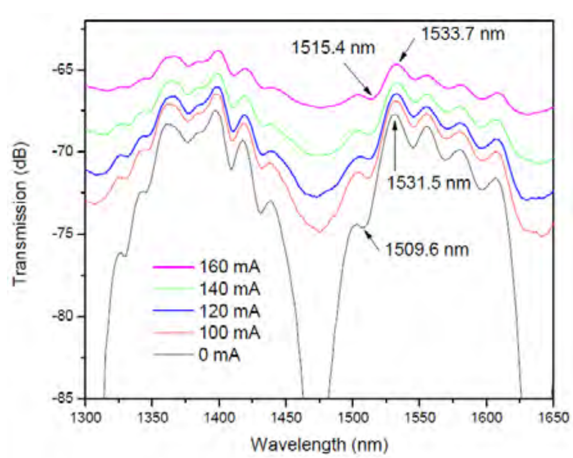

Fig. 3. Spectral transmission of the MMI filter for different current of the laser diode at 980nm

According to Fig. 3, the spectral characteristics of the MMI filter are modified as the pump power level of the laser diode is increased. One of the principal characteristics is the tuning of the peaks in the spectrum of the MMI filter, which can shift up to 3.2 nm. This result is of great interest for power tunable devices, and suggests novel properties of MMI devices that have to be studied in detail in future works.

Additionally, we show the temperature response of the active MMI filter as it is shown in Fig. 4. In This case, we use only the white light source as input.

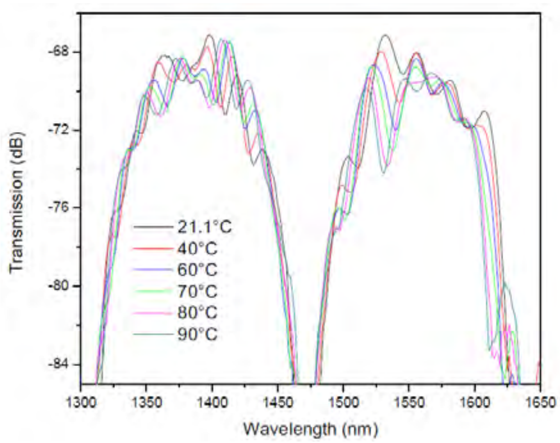

a)

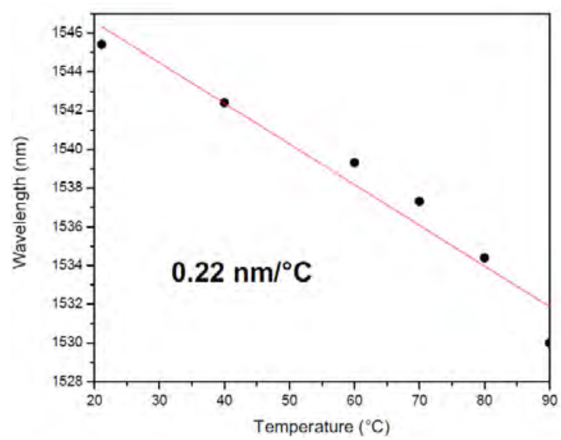

b)

Fig. 4. a) Temperature response of the MMI filter spliced to the WDM and using only a white light source. b) Sensitivity on temperature.

According to Fig. 4, the sensitivity of the MMI filter measured for the peak located at 1530nm is 0.22 nm/°C respectively; however it is possible to obtain higher sensitivities to temperature in other wavelength ranges.

3. Conclusions

We have reported the tuning of an active MMI filter modifying the pump power level of the doped fiber and changing its temperature. In both cases, we obtain a wavelength shift of the peak located at 1530nm. For tuning based in power level, the peak shifts to longer wavelengths up to 3.2 nm, while, for tuning using temperature the peak shift to shorter wavelengths with a sensitivity of 0.22 nm/°C. These results are reproducible and are of great interest for the design and development of power tunable filters and sensors based in multimode interference devices.

4. References

[1] L. B. Soldano, E. C. M. Penning, “Optical multi-mode interference devices based on self-imaging: principles and applications,” J. Lightwave Technol. **13**, 615-627 (1995).

[2] A. Mehta, W. S. Mohammed, and E. G. Johnson, “Multimode interference-based fiber-optic displacement sensor,” IEEE Photon. Technol. Lett. **15**, 1129-1131, (2003).

[3] R. Selvas-Aguilar, I. Torres-Gomez, A. Martinez-Rios, J. A. Alvarez-Chavez, D. A May-Arrioja, P. Likamwa, A. Mehta, E. G. Johnson, “Wavelength tuning of fiber lasers using multimode interference effects,” Opt. Express **13**, 9439-9445, (2005).

[4] J. E. Antonio-Lopez, A. Castillo-Guzman, D. A. May-Arrioja, R. Selvas-Aguilar, and P. LiKamWa, “Tunable multimode-interference bandpass fiber filter,” Opt. Lett. 35, 324-326 (2010).

[5] J. E. Antonio-Lopez, J. J. Sanchez-Mondragon, P. LiKamWa, D. A. May-Arrioja, “ Fiber-optic sensor for liquid level measurement,” Opt. Lett. 36, 3425-3427 (2011).

[6] L. Ma, Y. Qi, Z. Kang, Y. Bai, S. Jian, “Tunable fiber laser based on the refractive index characteristic of MMI effects,” Opt. and Laser Technol. 57, 96-99 (2014).

[7] S. Silva, E. G. P. Pachon, M. A. R. Franco, J. G. Hayashi, F. X. Malcata, O. Frazao, P. Jorge, C. M. B. Cordeiro, “Ultra high-sensitivity temperature fiber sensor based on multimode interference,” Appl. Opt. 51, 3236-3242 (2012).

[8] Y. Gong, T. Zhao, Y. J. Rao, Y. Wu, “All-fiber curvature sensor based on multimode interference,” IEEE Photon. Technol. Lett. **23**, 679-681 (2011).

Enhancing of thermal effects in ultra-fattening Yb-doped fiber lasers

G. Sánchez-Guerrero*[a], D. Toral[a], A. Castillo-Guzmán[a], V. Guzmán-Ramos[a],
D. E. Ceballos-Herrera[a], R. Selvas-Aguilar[a]
[a]Universidad Autónoma de Nuevo León, Facultad de Ciencias Físico-Matemáticas, Av. Universidad S/N, Cd. Universitaria, San Nicolás de los Garza, C.P. 66451, Nuevo León, México

ABSTRACT

The thermal effect of an Yb-doped fiber laser with fattening is numerically investigated. We have identified two principal sources of thermal sensitivity: The temperature dependence of the cross-section of the pump and signal radiations, and modifications of the numerical aperture (NA) due to changes in temperature. We have found that the first factor affects principally the thermal response of the fiber laser with fattening and this sensitivity can be modulated according to the fattening ratio. Additionally this thermal response is higher than that found in doped fibers without fattening. Our results are reproducible and contribute with new information for the development of novel temperature fiber laser sensors.

Keywords: Thermal effects, fattening, doped fibers

1. INTRODUCTION

Yb-doped fiber lasers have become a key piece of many powerful applications; we can mention for example the delivery of high power lasers and fiber laser sensors. In the first case, many efforts have been made to improve the performance of high power fiber lasers. Nevertheless, a special attention has to be taken in account when temperature effects in Yb-doped fibers are considered. In this sense, temperature perturbations generate instabilities caused by thermal modifications of the doped core. At this respect, many works have reported changes of the cross-sections of the doped fiber due to thermal effects; these changes have a great influence on the performance of fiber lasers, being these magnified at low pump powers [1-9]. These temperature effects have been studied in cylindrical doped fibers; however have not been analyzed in tapered doped fibers and doped fibers with fattening.

Additionally, many efforts have been made to develop temperature and strain fiber sensors for environmental measurements where immunity to electromagnetic interferences and personal safety are required. A large number of fiber optic temperature sensors based on different principles and structures have been developed; between them, we can distinguish two principal groups which are based in doped [10-17] and un-doped fibers [18-24]. In the first group, we can mention sensors based in the temperature dependence of the fluorescence lifetime of rare-earth doped fibers, and techniques based in the fluorescence intensity ratio, or by using the linear variation with temperature of the amplified spontaneous emission in doped fiber amplifiers [10-17]. In these sensors, the key point is the temperature dependence of the pump and signal cross-sections of the doped fiber. On the other hand, for the second group of temperature sensors based in un-doped fibers, these have been developed using modal interference techniques, such as fiber Fabry–Perot interferometers, fiber Bragg gratings, long period gratings, optical fiber couplers, tapered fibers or fibers with fattening [18-24]. In these sensors, the principal key is the temperature dependence of the dielectric material that modifies the modal behavior of the propagating radiation in the waveguide which generates a power variation at the end of the fiber. In fact, several works have been done to improve the performance of these temperature sensors employing a combination of these sensing techniques in doped and un-doped fibers with the goal to discern between simultaneous strain and temperature measurements [10-13]. This continuous progress to develop improved temperature sensors requires the necessity to explore novel configuration based on the sensing techniques described above. In this sense, we propose the use of a fiber with fattening, inscribed simultaneously in a doped fiber amplifier, which poses an additional temperature sensitivity caused by its temperature-dependence cross-sections. In fact, the efficiency of pump absorption in doped fiber lasers with fattening has to be studied [5-6], and a detail analysis of its temperature response has to be performed. For this reason, in this work we present an analysis of the temperature sensing characteristics of a Yb-doped fiber laser with fattening and we explore its feasibility to be used as a sensing component in temperature fiber sensors. In this analysis, we study the thermal response of the doped fiber with fattening using a parabolic longitudinal shape and a co-propagating pump scheme.

Laser Beam Shaping XIII, edited by Andrew Forbes, Todd E. Lizotte, Proc. of SPIE Vol. 8490, 84900N

· doi: 10.1117/12.929852

2. NUMERICAL EXPERIMENTS, RESULTS AND DISCUSSION

To study thermal effects in the Yb-doped fiber fattening, we can distinguish two types of perturbations:

1. Changes in the refractive index of the cladding and "active core" by temperature.
2. Changes of the absorption and emission cross-sections of the "active core" by temperature.

It is worth to mention that variations in temperature cause thermal expansion of the fiber in both transverse and longitudinal directions. As a result, a modification of the section shape with fattening can be expected. In this sense, the ratio of fattening for a fixed propagation length can be reduced or increased depending on the coefficient of thermal expansion (CTE) of the fiber. This expansion modifies the modal behavior of the propagating light according to the progressive changes by temperature of the cladding and core along the fiber with fattening. Here we suppose that the fiber is uniformly heated along the section with fattening and the thermal expansion of the transversal direction has radial symmetry. In this way, we can expect that the section with fattening can be modified uniformly along the fiber. Nevertheless, we are focusing only on thermal effects of fiber lasers with fattening due to changes of the refractive index of the cladding and active core, and changes of the cross sections of the doped fiber. The study performed in this work contributes to understand the sensitivity of fiber lasers with fattening at different temperatures. In this case, the temperature values considered in this work do not reach 2000°C, which correspond to the molding temperature necessary to modify strongly the fiber material. The temperature range considered in the analysis is 20-120°C. However we have to keep in mind that a more detail analysis of temperature in these lasers have to involve a study of thermal expansion effects in doped fibers with fattening.

We start our analysis of the temperature effect in active fiber with fattening by considering the first point mentioned above, i.e. changes in the refractive index of the core and cladding. Modes traveling in fibers with fattening depend strongly on the refractive index of core and cladding. In other words, the fraction of the fundamental mode propagating along the core will change as temperature is modified. Then, a similar behavior can be expected in active fibers with fattening. In a general case, the core fraction of the fundamental mode in cylindrical fibers is reduced as temperature is increased, and consequently, this behavior is repeated naturally in short sections of a fiber with fattening.

So, we have to analyze how the mode fraction within the core with fattening is modified by temperature. Without loss of generality, we can consider a Gaussian shape of the pump and signal fundamental mode traveling in a fiber with fattening. As it is mentioned above, a fiber with fattening can be fabricated in single and multimode fibers, and according to the fattening shape and pump conditions the fundamental mode can be selectively excited. In our case, we consider a single mode doped fiber, in this way, the pump and signal radiation exists only as fundamental mode in the doped fiber with fattening, then we can write the transverse intensity pattern using a Gaussian envelope approximation as follow [25]:

$$f_{p.s}(r) = \frac{1}{\pi\Omega^2} e^{-r^2/\Omega^2} \tag{1}$$

Where subscripts *p* and *s* refer to pump and signal radiations, and Ω is determined by the characteristic of the fiber like the refractive indexes and radius of the core and cladding respectively. The multiplying factor in Eq. 1 is chosen to normalize *f(r)* as follows: $2\pi\int f_{p,s}(r)dr = 1$.

For a step index fiber, Ω is approximately given by:

$$\Omega = aJ_0(U)\frac{V}{U}\frac{K_1(W)}{K_0(W)} \tag{2}$$

Where a is the core radius, $U = a\sqrt{k^2 n_1{}^2 - \beta^2}$, $W = a\sqrt{\beta^2 - k^2 n_2{}^2}$, $V = ka\sqrt{n_1^2 - n_2^2}$, $k = 2\pi/\lambda$, n_1 and n_2 are the refractive indices of the "active core" and cladding respectively, and β is the propagation constant of the pump or signal mode. For a given V, the value of W can be obtained using the empirical relationship $W = 1.1428V - 0.996$ valid only for step index fibers. In this way, according to the pump and signal wavelengths, one can obtain the respective values of

U, W, and V using the Numerical Aperture (NA) of the fiber $\left(NA = \sqrt{n_1^2 - n_2^2} \right)$, and subsequently the parameter Ω. This procedure is accurate for $1.5 < V < 2.5$.

Previous works on cylindrical doped fibers report a reduction of the slope efficiency in the signal generation as temperature is increased [26-28]. This behavior is directly related to modifications in the absorption and emission cross-sections and also by modifications of the numerical aperture *NA* of the active fiber. Due to the different glass composition, concentration of dopants and co-dopants, and the degree of structural disorder on the glass network used in different active fibers, the change rate of *NA* with respect to temperature can not be determined easily for each doped fiber. To overcome this complication, we consider an average behavior of NA considering the refractive indices changes by temperature reported in Ref. [8], where values of *NA* between 0.18-0.19 with temperature increments of 20°C to 120°C can be calculated. This approximation allows us to analyze how the fundamental mode of the pump and signal radiations is confined in the doped core. Once determined the variation range of NA with temperature, we consider an active fiber with fattening.

We can now analyze the effect of temperature in an active fiber with fattening and with an initial core radius of 1.5μm and a final core radius of 2μm which corresponds to a fattening ratio of T=0.75. If we take the value of NA=0.18 for 20°C and NA=0.19 for 120°C,the calculation of Ω gives the following results for the Gaussian envelope of the fundamental mode at both ends of the fiber with fattening.

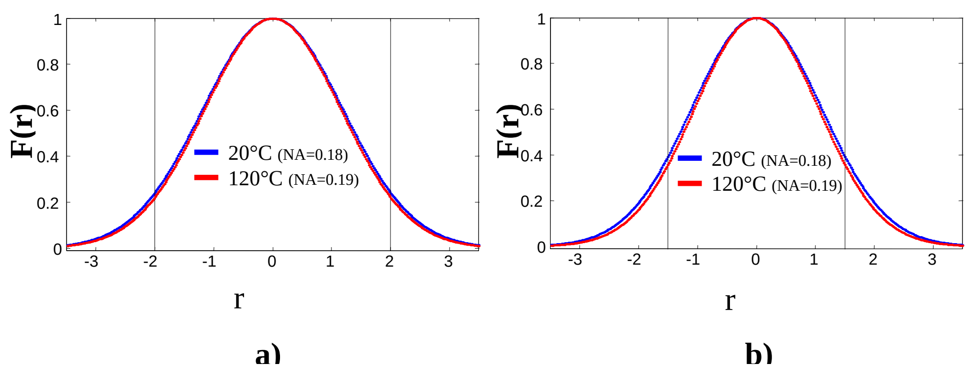

Figure 1. Temperature behavior of transversal profiles at both ends of the fiber with fattening: a) Final end with core radius r=2μm, b) Initial end with core radius r=1.5μm.

As it can be observed in Fig. 1, the transversal profiles of the fundamental mode at 1064 nm are modified slightly at both ends of the fiber with fattening for different values of numeric aperture NA. However, we can distinguish that the end with a lower core radius is more sensitive to variations of NA. If one considers that the changes of NA are attributed to variations of the refractive indices of the cladding and core by temperature, Then, Fig. 1 suggests that the end with lower core radius is slightly more sensitive to thermal variations. This result can be inferred if we consider Ω in Eq. (2) which indicates the width of the Gaussian profile. According to Eq. (2), Ω can be strongly modified as the arguments of the Bessel functions are near the origin and a higher dependence on the parameter Ω with temperature is expected.

Now, we analyze the thermal effects of doped fibers with fattening considering absorption and emission cross-section modifications due to changes in temperature. Previous works in cylindrical fibers have reported changes in population of the energy levels in Yb-doped glasses, and broadening of the homogeneous line-width as temperature is increased [1-6]. It results in modifications of the absorption and emission cross-sections for the signal and pump radiations. In this case, it is worth to mention that these effects may vary for each individual doped fiber. Independently of the different changes of cross-sections reported in recent works, we focusing in the effect of these changes in doped fibers with fattening. Without loss of generality, we use the changes of absorption and emission cross-sections by temperature reported in Ref. [1], which is representative of several Yb-doped fibers. These changes are expressed in the following equations:

$$\sigma(T) = \sigma(20°C) + \frac{d\sigma}{dT}\Delta T \quad (3)$$

$$\frac{d\sigma_{abs}^{1064nm}}{dT} = 7.78\times10^{-29}\, m^2 / °K \quad (4)$$

$$\frac{d\sigma_{em}^{1064nm}}{dT} = -2.44\times10^{-28}\, m^2 / °K \quad (5)$$

$$\frac{d\sigma_{abs}^{976nm}}{dT} = \frac{d\sigma_{em}^{976nm}}{dT} = -1.63\times10^{-27}\, m^2 / °K \quad (6)$$

Where, σ_{abs}^{1064nm}, and σ_{em}^{1064nm} are the absorption and emission cross-sections for the signal wavelength and, σ_{abs}^{976nm}, and σ_{abs}^{976nm} are the absorption and emission cross-sections for the pump wavelength, respectively.
In order to model a temperature dependent Yb-doped fiber laser with fattening, we numerically analyze the following coupled equations:

$$\frac{dI_p(r,z)}{dz} = \left(\sigma_{em}^p(T)\times n_2(T) - \sigma_{abs}^p(T)\times n_1(T)\right) N_{tot} I_p(r,z) \quad (7)$$

$$\frac{dI_s(r,z)}{dz} = \left(\sigma_{em}^s(T)\times n_2(T) - \sigma_{abs}^s(T)\times n_1(T)\right) N_{tot} I_s(r,z) \quad (8)$$

where, $I_p(r,z)$ and $I_s(r,z)$ are the pump and signal intensities, N_{tot} is the total Ytterbium population, σ_{abs}^p, σ_{em}^p, σ_{abs}^s, σ_{em}^s are the temperature dependent absorption and emission cross-sections of the pump and signal at 976nm and 1064nm respectively, and $n_1(T)$, $n_2(T)$ are the temperature-dependent upper and lower-state populations of Yb, which are given at a steady state by the following equations:

$$n_2 = \frac{R_{abs} + W_{abs}}{R_{abs} + R_{em} + W_{abs} + W_{em} + A_{esp}} \quad (9)$$

$$n_1 = 1 - n_2 \quad (10)$$

Where, $R_{abs} = \sigma_{abs}^p I_p h\nu_p$, $R_{em} = \sigma_{em}^p I_p h\nu_p$, $W_{abs} = \sigma_{abs}^s I_s h\nu_s$, and $W_{em} = \sigma_{em}^s I_p h\nu_s$.
In these equations, the ASE generation is not considered and only effects of the fattening and temperature modifications are investigated.

In order to consider the taper effects and the overlap of the pump and signal fundamental mode with the active core, we can use [25]:

$$I_{p,s}(r,z) = P_{p,s}(z) f_{p,s}(r) \quad (11)$$

Where subscripts *p* and *s* refer to pump and signal radiations, $P_{p.s}(z)$ are the z-dependent powers at the pump and signal wavelengths, and $f(r)$ is given by Eq. 1. It is clear at this point that the effect of the fattening and temperature in parameter Ω defined in Eq. 2 directly modifies the evolution of pump and signal intensities described in Eq. 7 and 8.

If we consider the pump power at any value of z, we have,

$$P_{p,s}(z) = \int_0^{\infty}\int_0^{2\pi} I_{p,s}(r,z) r dr d\varphi = 2\pi \int_0^{\infty} I_{p,s}(r,z) r dr \tag{12}$$

Then,

$$\frac{dP_{p,s}(z)}{dz} = 2\pi \int_0^{\infty} \frac{dI_{p,s}(r,z)}{dz} r dr \tag{13}$$

Using Eq. 11 and 13, we can rewrite Eq. 7 and 8 as follows:

$$\frac{dP_p(z)}{dz} = 2\pi \int_0^{a(z)} \left(\sigma_{em}^p(T)\times n_2(T) - \sigma_{abs}^p(T)\times n_1(T)\right) N_{tot} P_p(z) f_p(r) r dr \tag{14}$$

$$\frac{dP_s(z)}{dz} = 2\pi \int_0^{a(z)} \left(\sigma_{em}^s(T)\times n_2(T) - \sigma_{abs}^s(T)\times n_1(T)\right) N_{tot} P_s(z) f_s(r) r dr \tag{15}$$

On these equations, we assume that the fiber is doped with uniform Yb-concentration up to the core radius "*a*" which depends on *z*. Besides, it is worth to note that $n_1(T)$ and $n_2(T)$ depend on $f_{p.s}(r)$ due to their relation with I_p and I_s intensities.

Once the temperature dependent coupled equations are defined, we proceed to model a Yb-doped fiber amplifier with a linear fattening shape, which allows us to obtain a representative temperature behavior of a Yb-doped fiber laser. This model is performed in CW regime using the following scheme:

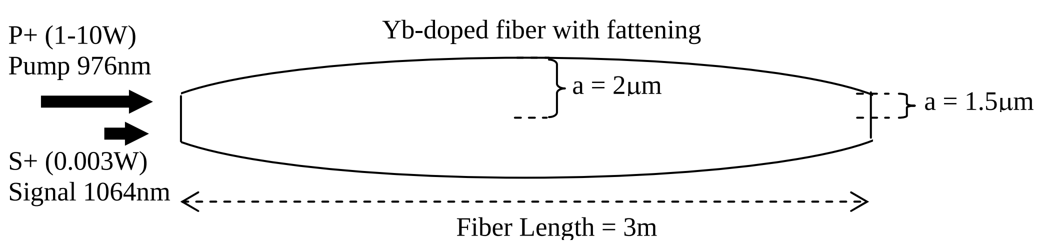

Figure 2. Temperature dependent modeling using a parabolic shape of the fattening in the Yb-doped fiber amplifier with co-propagating single pump.

Firstly, we analyze the radiation conversion along the fiber between the pump and signal radiations at a fixed temperature of 20°C. At this temperature, the absorption and emission cross-sections of pump and signal radiations are: $\sigma_{abs}^p = 1.488x10^{-24} m^2$, $\sigma_{em}^p = 1.829x10^{-24} m^2$, $\sigma_{abs}^s = 6x10^{-27} m^2$, and $\sigma_{em}^s = 3.58x10^{-25} m^2$, for $976nm$ and $1064nm$ pump and signal wavelengths respectively. As it can be observed, the longitudinal shape of the fiber with fattening is considered parabolic, and the temperature is changed from 20°C to 120°C. In this first numerical experiment the numerical aperture NA=0.18 is considered constant along the fiber and it has no modifications by temperature. This suggestion is supported considering the negligible changes of NA shown in Fig. 1 for both temperatures 20 and 120°C respectively. Then, we analyze only the effects of temperature dependent cross-sections on the fiber amplifier with and without fattening. The corresponding results of the signal conversion for the fiber with and without fattening at two different temperatures are shown in Fig. 3.

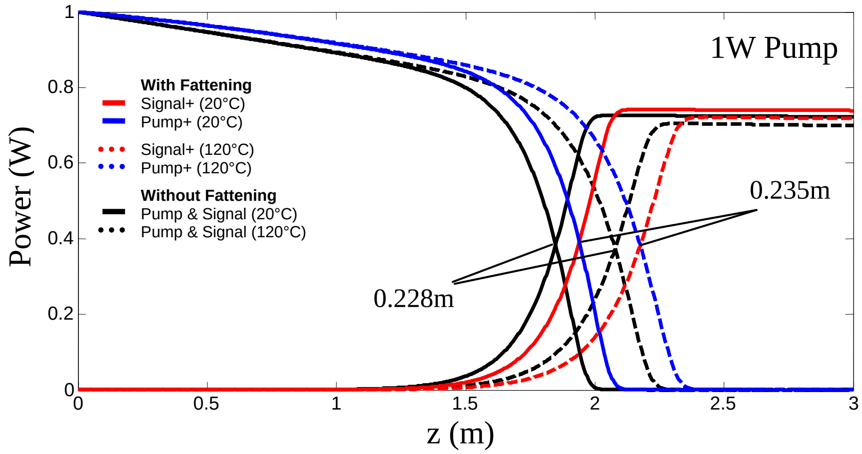

Figure 3. Modeling of a Yb-doped fiber amplifier with and without fattening. Evolution of the Pump and Signal radiations at two different temperatures for 1W of pump power.

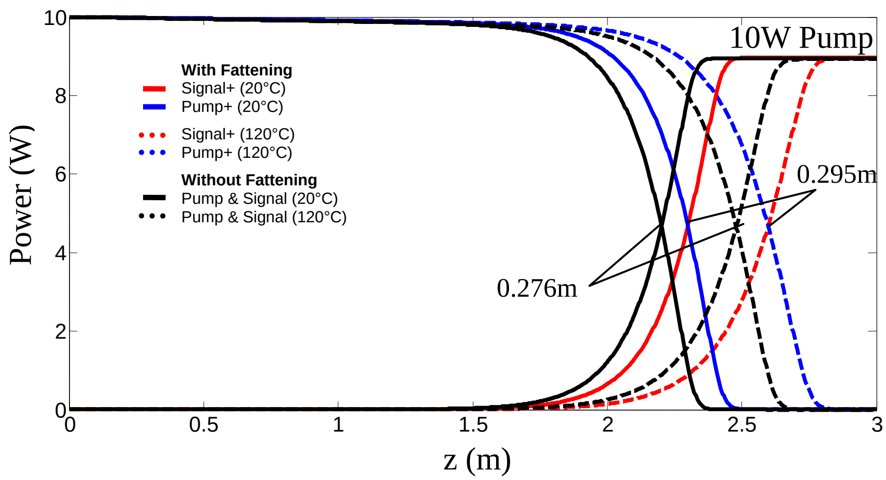

Figure 4. Modeling of a Yb-doped fiber amplifier with and without fattening. Evolution of the Pump and Signal radiations at two different temperatures for 10W of pump power.

It is important to note the behavior of the cross point of the signal and pump radiations shown in Figs. 3 and 4, due to the fact that this cross-point shift is an indicative of how temperature can affect the performance of the Yb-doped amplifier. According to this consideration, we can observe that signal conversion is more sensitive to changes in the temperature dependent cross-sections when a fiber with fattening is used. Also, according to Figs. 3 and 4 the temperature sensitivity of the signal radiation in the fiber amplifier for the co-propagating case grows as the temperature is increased and it is higher for low values of the pump power as it can be observed in the output power of the signal. This is an important result to consider in the design of fiber lasers and temperature fiber sensors. Additionally, this sensitivity can vary according to the length of the fiber used. For example, these calculations were made with 3m of fiber length; however, more sensitivity changes can be obtained at 2-2.5m where the cross-point of the signal and pump radiations are located as is shown in Fig. 3. Additionally, further analysis has to be performed to optimize the temperature sensitivity using different fattening ratios and the longitudinal shape of the doped-fiber with fattening.

3. CONCLUSION

We have reported a numerical analysis of the temperature effects in Yb-doped fibers with fattening; our results can be extrapolated to other doped fibers and are of great interest for the improvement of high power tapered lasers, and the development of temperature fiber laser sensors. Power field distribution changes with changes in refractive index have been calculated, which in turn are temperature dependent. The range of temperature studied was from 20 to 120 ^{o}C. The effect is enhanced because of the change of the mode field distribution along the fiber with fattening. We also predicted, as a consequence, that the evolution of the pump and signal absorption as a function of distance also changes with temperature. The shifting of the curves is significant from fibers with and without fattening at different temperatures. It was determined that the temperature sensitivity is higher for lower pump power levels in a co-propagating case. We believe that these results are useful for the prediction of temperature behavior of an Yb-doped fiber laser, for the possibility of temperature sensing and even it could constitute a form to modulate or tune the fiber laser response via adjustment of its operating temperature.

REFERENCES

[1] Henry, L. J., Shay, T. M., Hult, W. D., and Rowland, K. B., “Thermal effects in narrow linewidth single and two tone fiber lasers,” Opt. Express 19, 6164-6176 (2011).

[2] Henry, L. J., Shay, T. M., Hult, W. D., and Rowland, K. B., “Enhancement of output power from narrow linewidth amplifiers via two-tone effect--high power experimental results,” Opt. Express 18, 23939-23947 (2010).

[3] Vazquez-Zuñiga, L. A., Chung, S., and Jeong, Y., "Thermal characteristics of an ytterbium-doped fiber amplifier operating at 1060 and 1080 nm," Jpn. J. Appl. Phys. 49(2), (2010).

[4] Grukh, D. A., Kurkov, A. S., Paramonov, V. M., and Dianov, E. M., “Effect of heating on the optical properties of Yb3+-doped fibres and fibre lasers,” Quantum Electron. 34(6), 579–582 (2004).

[5] Brilliant, N. A., and Lagonik, K., “Thermal effects in a dual-clad ytterbium fiber laser,” Opt. Lett. 26(21), 1669–1671 (2001).

[6] Peng, X., and Dong, L., “Temperature dependence of ytterbium-doped fiber amplifiers,” J. Opt. Soc. Am. B 25(1), 126–130 (2008).

[7] Newell, T. C., Peterson, P., Gavrielides, A., and Sharma, M. P., “Temperature effects on the emission properties of Yb-doped optical fibers,” Opt. Commun. 273(1), 256–259 (2007).

[8] Saito, K., Yamamoto, R., Kamiya, N., Sekiya, E. H., and Barua, P., “Fictive temperature dependence of optical properties in Yb-doped silica”, Proc SPIE 6998, 69981J–1 to 69981J–8, (2008).

[9] Canat, G., Mollier, J. C., Jaouën, Y., and Dussardier, B., , "Evidence of thermal effects in a high-power Er3+-Yb3+ fiber laser," Opt. Lett. 30, 3030-3032 (2005).

[10] Wade, S. A., Baxter, G. W., Collins, S. F., Grattan, K. T. V., and Sun, T., “Simultaneous strain-temperature measurement using fluorescence from Yb-doped silica fiber,” Rev. Sci. Instrum., 71, 2267 (2000).

[11] Liu, T., Fernando, G. F., Zhang, Z. Y., and Grattan, K. T. V., “Simultaneous strain and temperature measurements in composites using extrinsic Fabry-Perot interferometric and intrinsic rare-earth doped fiber sensors”, Sensors and Actuators 80, 208-215 (2000).

[12] Trpovski, S., Wade, S. A., Collins, S. F., and Baxter, G. W., “Er^{3+}:Yb^{3+} doped fibre with embedded FBG for simultaneous measurement of temperature and longitudinal strain”, Meas. Sci. Technol. 16, 488-496, (2005).
[13] Jung, J., Nam, H., Lee, J. H., Park, N., and Lee, B., “Simultaneous measurement of strain and temperature by use of a single-fiber Bragg grating and an erbium-doped amplifier,” App. Opt. 38, (1999).
[14] Wade, S. A., Collins, S. F., and Baxter, G. W., “Fluorescence intensity ratio technique for optical point temperature sensing,” App. Phys. Lett. 94(8), (2003).
[15] Paez, G., Strojnik, M., “Experimental results of ratio-based erbium-doped-silica temperature sensor,” Opt. Eng. 42, 1805, (2003).
[16] Maurice, E., Monnom, G., Dussardier, B., Saïssy, A., Ostrowsky, D. B., and Baxter, G. W., “Erbium-doped silica fibers for intrinsic fiber-optic temperature sensors,” Appl. Opt. 34, 8019-8025, (1995).
[17] Castrellon-Uribe, J., and García-Torales, G., “Remote temperature sensor based on the up-conversion fluorescence power ratio of an erbium-doped silica fiber pumped at 975 nm,” Fiber and Integrated Optics 29, 272-283, (2010).
[18] Zhu, S., Jie-wen, X., Fu-Fei, P., and Ting-Yun, W., “Temperature sensor based on a single-mode tapered optical fiber," Journal of Shanghai University 15, (2011).
[19] Kwang-Taek, K., and Kiu-Ha, P., “Fiber-optic temperature sensor based on single mode fused fiber coupler," J. Opt. Soc. Korea 12, 152-156 (2008).
[20] Prerana, P., Ravendra, K. V., Bishru, P., and Bezwada, N., “High sensitivite fiber optic temperature sensor based on a side-polished single-mode fiber coupled to a tapered multimode overlay waveguide," J. Opt. Soc. Korea 14, 337-341 (2010).
[21] Díaz-Herrera, N., Navarrete, M. C., Esteban, O., and Gonzalez-Cano, A., “A fibre-optic temperature sensor based on the deposition of a thermochromic material on an adiabatic taper," Meas. Sci. Technol. 15, (2004).
[22] Villatoro, J., Monzon-Hernandez, D., and Mejía, E., “Fabrication and modeling of uniform-waist single-mode tapered optical fiber sensors," Appl. Opt. 42(13), 2278-2283 (2003).
[23] Zhu, S., Jie-wen, X., Fu-Fei, P., and Ting-Yun, W., “Single-mode tapered optical fiber for temperature sensor based on multimode interference," Proc. of SPIE 8311, 83112B (2011).
[24] Monzon-Hernandez, D., Mora, J., Perez-Millan, P., Díez, A., Cruz, J. L., and Andres, M. V., "Temperature Sensor Based on the Power Reflected by a Bragg Grating in a Tapered Fiber," Appl. Opt. 43, 2393-2396 (2004).
[25] Ghatak, A., Thyagarajan, K., “Introduction to fiber optics,” Chapter 14-Optical fiber amplifiers”, Cambridge, University Press, Pags. 296-297.
[26] Ustimchik, V., Nikitov, S., and Chamorovskii, Y., “Studying the properties of double-clad active cone optic fibers,” Journal of Communications Technology and Electronics, 56(10), 1249–1255 (2011).
[27] Filippov, V., Chamorovskii, Y., Kerttula, J., Golant, K., Pessa, M., and Okhotnikov, O. G., “Double clad tapered fiber for high power applications,” Opt. Express 16(3), 1929–1944 (2008).
[28] Filippov, V., Chamorovskii, Y., Kerttula, J., Kholodkov, A., and Okhotnikov, O. G., “Single-mode 212 W tapered fiber laser pumped by a low-brightness source,” Opt. Lett. 33(13), 1416–1418 (2008).

Design of a solar collector system formed by a Fresnel lens and a CEC coupled to plastic fibers

Perla M. Viera-González*, Guillermo E. Sánchez-Guerrero, Daniel E. Ceballos-Herrera, Romeo Selvas-Aguilar
Centro de Investigación en Ciencias Físico Matemáticas, Av. Universidad, San Nicolás de los Garza, N.L., México 66455

ABSTRACT

Among the main challenges for systems based in solar concentrators and plastic optical fibers (POF) the accuracy needed for the solar tracking is founded. One approach to overcome these requirements is increasing acceptance angle of the components, usually by secondary optical elements (SOE), however this technique is effective for photovoltaic applications but it has not been analyzed for systems coupled to POFs for indoor illumination. On this subject, it is presented a numerical analysis of a solar collector assembled by a Fresnel lens as primary optical element (POE) combined with a compound elliptical concentrator (CEC) coupled to POF in order to compare its performance under incidence angle direction and also to show a trade-off analysis for two different Fresnel lens shapes, imaging and nonimaging, used in the collector system. The description of the Fresnel lenses and its designs are included, in addition to the focal areas with space and angular distribution profiles considering the optimal alignment with the source and maximum permissible incident angle for each case. For both systems the coupling between the optical components is analyzed and the total performance is calculated, having as result its comparison for indoor illumination. In both cases, the systems have better performance increasing the final output power, but the angular tolerance only was improved for the system with nonimaging concentrator that had an efficiency over 80% with acceptance angles $\theta_i \leq 2°$ and, the system integrated by the imaging lens, presented an efficiency ratio over 75% for acceptance angles $\theta_i \leq 0.7°$.

Keywords: Nonimaging Optics, Fresnel lens, Compound elliptic concentrators, plastic optical fiber, illumination, solar collection.

1. INTRODUCTION

Since the XIX century, Fresnel lenses have been used with different purposes as lighthouses, imaging systems, hydrogen generation, solar-pumped lasers and light concentration. Moreover, in contrast with other concentrators, Fresnel lenses offer flexibility in optical design thanks to its high manufacture error tolerance, light-weight, small volume and low cost. Indoor illumination by sunlight concentration with Fresnel lenses is one of the uses of imaging Fresnel lenses which has grown its implementation due to the importance of reduce the energy consumption in modern societies[1–3].

For improve the final performance, this work proposes and analyzes a system that includes, in addition to the primary optical element (POE), a secondary optical element (SOE), looking to reduce the losses due to change in incidence angle and optical decoupling with the Plastic Optical Fiber (POF). The compound elliptic concentrator (CEC) represents a viable solution due to its easy manufacture process and its capacity of obtain high concentration ratios[1,4–8].

On this subject, a numerical analysis of two different systems is presented, one with imaging concentrator and the other with nonimaging concentrator, integrated by a Fresnel lens combined with a CEC, as SOE, coupled to POF in order to compare its performance under changes of incidence angle and also to show a trade-off analysis for different Fresnel lens shapes used in the collector system.

For both systems, the Fresnel lenses were designed using the edge-ray method proposed by Leutz[1,2,9] and the CEC is designed, according to the absorber area of the nonimaging Fresnel lens, using the string method[8]. Every system, integrated by the Fresnel lens, the CEC and the POF, was simulated using Radiant Zemax® in a series of iterations varying the incidence angle of the source-rays over the collector.

Since some of the losses are inevitable, such as absorption loss and reflection loss[10], the present work pursuits obtain a proposal for indoor illumination with Fresnel lenses and POF that employs a less sophisticated tracking system with an increase in the acceptance angle of the collector without significant reductions of the final performance.

1.1 Theoretical background

Work in solar energy collection implies the use of solar concentrators which can be analyzed depending of the optical principles applied for light transmission: refraction or reflection; and the kind of concentration they provide: imaging and nonimaging. The nonimaging concentrators can be ideal concentrators, that means the concentrator geometry's design may approach the thermodynamic limit of concentration, besides imaging optics usually do not reach ideal levels of concentration. In contrast, imaging concentrators approach to focal points instead of the focal areas that result of nonimaging collection[1,2,4,10]

As mentioned above, imaging Fresnel lenses in solar collection require high tracking precision, moreover, nonimaging Fresnel lenses are based in the edge ray principle and offer an acceptance angle, leading to less tracking precision as proposed in this work; although, both are essentially chains for prisms designed following the main concepts of Geometrical Optics, particularly the Snell's Law.

The imaging Fresnel lens can be designed with grooves facing inwards (toward the focal point) or facing outwards (toward the source), for the first case the prisms have smaller angles compared with the prisms of the second case, this leads in the fact that imaging lenses facing outward are less prone to focal errors but, furthermore, these lenses are difficult to clean and are prone to shadowing losses.

Nonimaging Fresnel lenses generally have grooves facing inwards, which generate a smooth outer surface, and should reduce focal aberrations, these advantages allow that nonimaging Fresnel lenses could be used as solar concentrators, collimators and for lighting applications[2,11].

As in the case of PV systems, solar illumination systems require efficiency and reliability, but the limitations of each kind of Fresnel lens may difficult to obtain high efficiency systems. The objectives of secondary optics elements are create a determinate irradiance distribution and increase the tolerance of alignment and tracking by catching refracted light that otherwise would miss the receiver[12,13], these two objectives can be adapted for systems using POF. In the case of the SOE design, it is necessary set, as initial conditions, the area and acceptance angle of the receiver (the FOP). A graphic description of the problem addressed in this paper is shown in Figure 1.

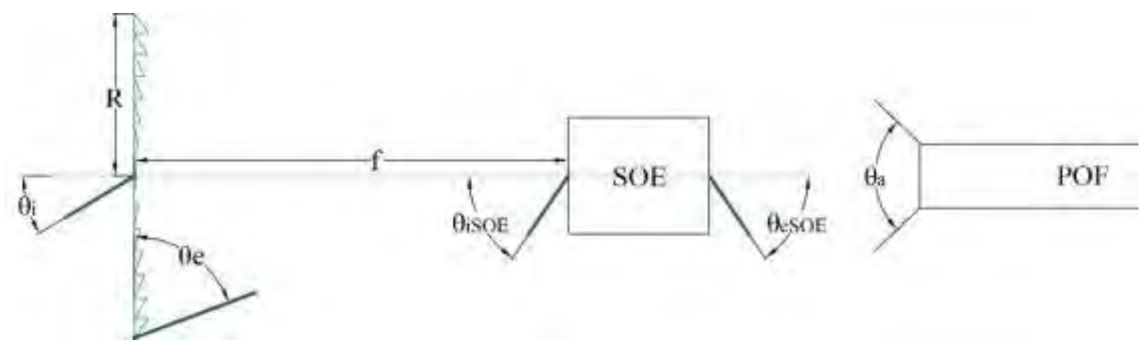

Figure 1: The SOE has to match the POF incidence angle and the Fresnel lens exit. The SOE can reduce the hot spot produced by the Fresnel lens.

Similar to POEs, the SOEs may accomplish three roles: refraction, reflection or a combination of both, but, for the case of systems implementing POF, must take in advance the focal aberrations produced by the angular misalignment between the source and the Fresnel lens and the acceptance cone of the fiber. The literature had reported different geometries for SOEs and its effects for CPV and solar concentration in general, not only using Fresnel lenses as POE but also with other solar concentrators; between the options listed, the compound parabolic concentrator (CPC) is one of the most often choices due to its efficiency and easy-manufacturing design because, although it combination cannot achieve the thermodynamic limit, it has been viewed as one of the best possible combinations[12–17].

The generalization of the CPC for finite sources lead to the compound elliptical collector in 2D, this nonimaging design, in principle collect all the rays from a source, but as in the case of the CPC, a rotational symmetry will cause losses due to skewness. The Figure 2 shows the CEC in 2D and explains the construction process for this nonimaging element[8].

Figure 2: String method applied for CEC design. Rays from B land on D and rays from P in any point between the absorber [DC]. The rays exit angle on the CEC is increased, but considered to fit the FOP.

When a waveguide, as the POF, is used for transmit the light collected it is important take in advance the greatest possible acceptance angle θ_{max}. From Snell's law, when the angle of incidence is greater than the critical angle ϕ_c (Figure 3), light is reflected and guided further along the core. The maximum acceptance angle at which light can be launched into the core and guided by the optical fiber is the acceptance angle θ_{max} we can be obtain by the analytical expression:

$$\sin\theta_{max} = n_1\sqrt{1-\sin^2\phi_c} = \sqrt{n_1^2 - n_2^2} \quad (1)$$

where each one of the variables are defined in Figure 3.

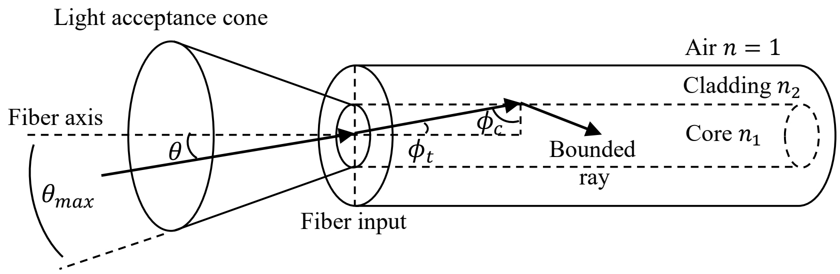

Figure 3: Numerical aperture of an optical fiber.

2. NUMERICAL EXPERIMENTS

This section describes the process of design of two systems for solar collection with Fresnel lenses and FOP as final absorber and describes the numeric analysis performed for its performance comparison. Due to the fiber, both systems must concentrate the light collected over the area of the fiber core and considering the acceptance angle of the fiber.

2.1 Solar Collector design

As it was mentioned before, the Fresnel lens design consists in calculate, using iterative methods, each one of its prisms; for this work the prisms selected for create the Fresnel lenses were conventional refractive prisms[10] according with the theory proposed by Leutz et al. based on Geometrical and Nonimaging Optics[1,2]; for the case of the imaging lens, it was considered as a specific case of a nonimaging lens, where the acceptance half-angle was $\pm\theta = 0°$ and having, each prism, a constant width.

The material used for design both lenses was Polymethyl Methacrylate (PMMA) that has a refractive index $n = 1.4921$ considering a wavelength $\lambda = 555$nm[12] and, in the two cases, the lenses were designed as revolution symmetry surfaces.

The imaging Fresnel lens was designed considering a f-number ($f^{\#} = f/2R$, being f the focal length and R the lens radius) equals to 1.0[5], this characteristics allows a half-output angle $\theta_o \approx 26.56°$ that corresponds with the half-acceptance angle of the POF as will be seen in next section. The complete list of design parameters is presented in **¡Error! No se encuentra el origen de la referencia.**. The Figure 4.A shows the resulting lens that have prisms facing inward.

Table 1. Design parameters for the imaging and the nonimaging Fresnel lenses.

	Imaging Fresnel lens	**Nonimaging Fresnel lens**
Radius	99.0 mm	83.1 mm
Arc half-length	-	94.5 mm
F-number ($f^{\#}$)	1.0	1.19
Focal length (f)	198.0 mm	
Number of prisms	90	90
Aperture segment angle (ω)	Variable	0.3°
Prism width (Δx)	1.1 mm	Variable
Acceptance half angle (θ_i)	0°	5°
Output half angle (θ_o)	26.5°	27°

In the case of the nonimaging Fresnel lens, the focal length was the same as the used for the imaging lens and, looking an output angle that corresponds with acceptance angle of the fiber, the maximum output half angle was set on 27° and, the segment angle of each prism, on 0.3°. The aperture radius and half-length resulting are shown on The imaging Fresnel lens was designed considering a f-number ($f^{\#} = f/2R$, being f the focal length and R the lens radius) equals to 1.0[5], this characteristics allows a half-output angle $\theta_o \approx 26.56°$ that corresponds with the half-acceptance angle of the POF as will be seen in next section. The complete list of design parameters is presented in **¡Error! No se encuentra el origen de la referencia.**. The Figure 4.A shows the resulting lens that have prisms facing inward.

Table 1. Design parameters for the imaging and the nonimaging Fresnel lenses. This lens was designed for an acceptance angle of ±5°, the Figure 4.B illustrates the final design.

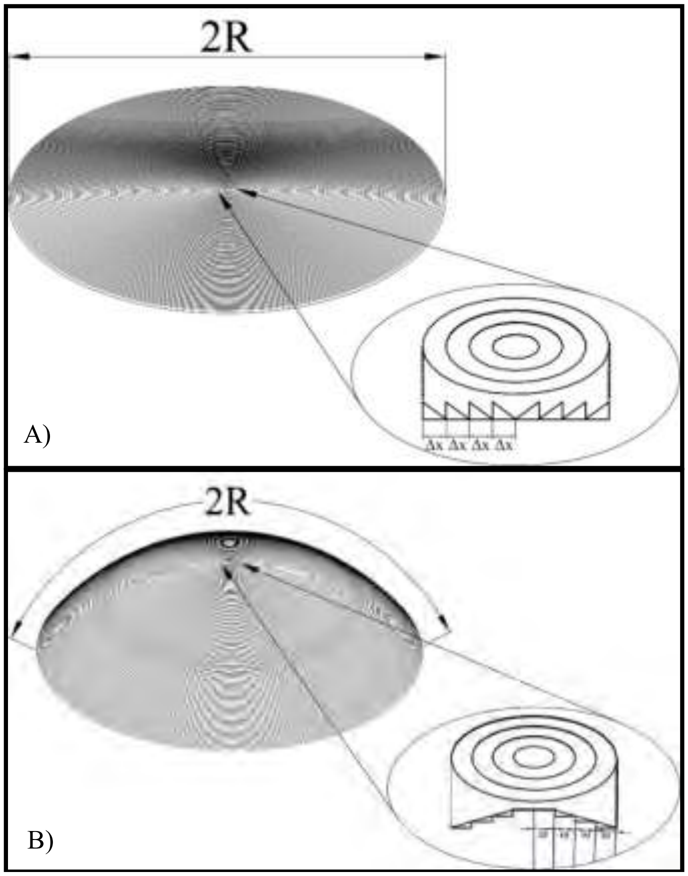

Figure 4. Fresnel lenses designed. A) Imaging Fresnel lens composed by 90 prisms with constant width (Δx) facing inward. B) Nonimaging Fresnel lens with 90 prisms with constant segment angle (ω). For the nonimaging lens it was considered that the arc half-length were approximately equals to the imaging lens aperture radius.

For the design method presented by Leutz et al. [1,2], the acceptance half angle of the nonimaging Fresnel lens is related with the focal length and the half width of the absorber by:

$$f = \frac{d}{\tan \theta_i} \tag{2}$$

Where d represents the half width of the absorber. This limits the focal area to have a radius of 17.3 mm that will be considered for the CEC design.

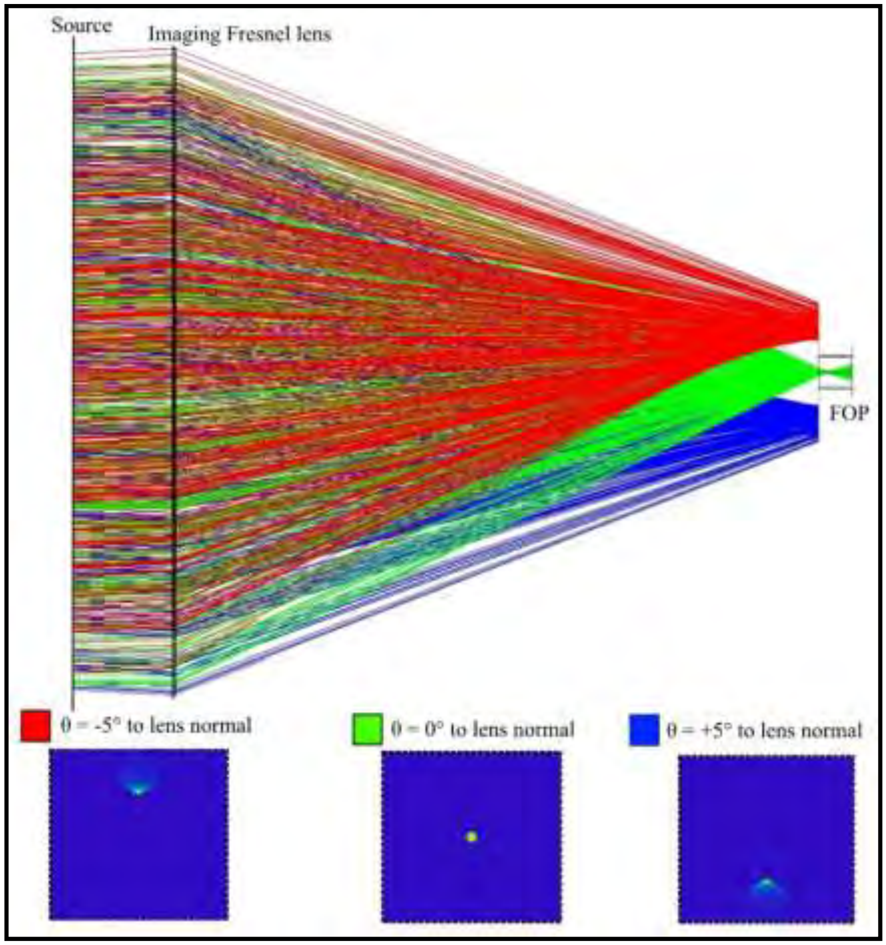

Figure 5. Imaging Fresnel lens focusing a collimated white light source (D65) with $\theta = 0°$ (green) as ideal incident angle and $\theta = \pm 5°$ (red and blue) as maximum incident angles. The radiance in position space is shown for each case.

For every Fresnel lens designed, a series of simulation was performed for analyze the angular and special distribution captured in a radiometric detector placed at a distance equals to the focal length. In each case, the incidence angle of the source was changed in steps of 0.1° from 0° to 5°. The Figure 5 shows the imaging Fresnel lens systems with its spatial distributions for the cases of -5°, 0° and 5° and the Figure 6 shows the same setup for the nonimaging Fresnel lens. In both systems, the FOP was placed at the focal length and it could be observe that the extreme cases ($\theta_{i-} = -5°$ and $\theta_{i+} = 5°$) do not allow the light enter into the FOP. A more detailed description of these simulations can be found in the Results section.

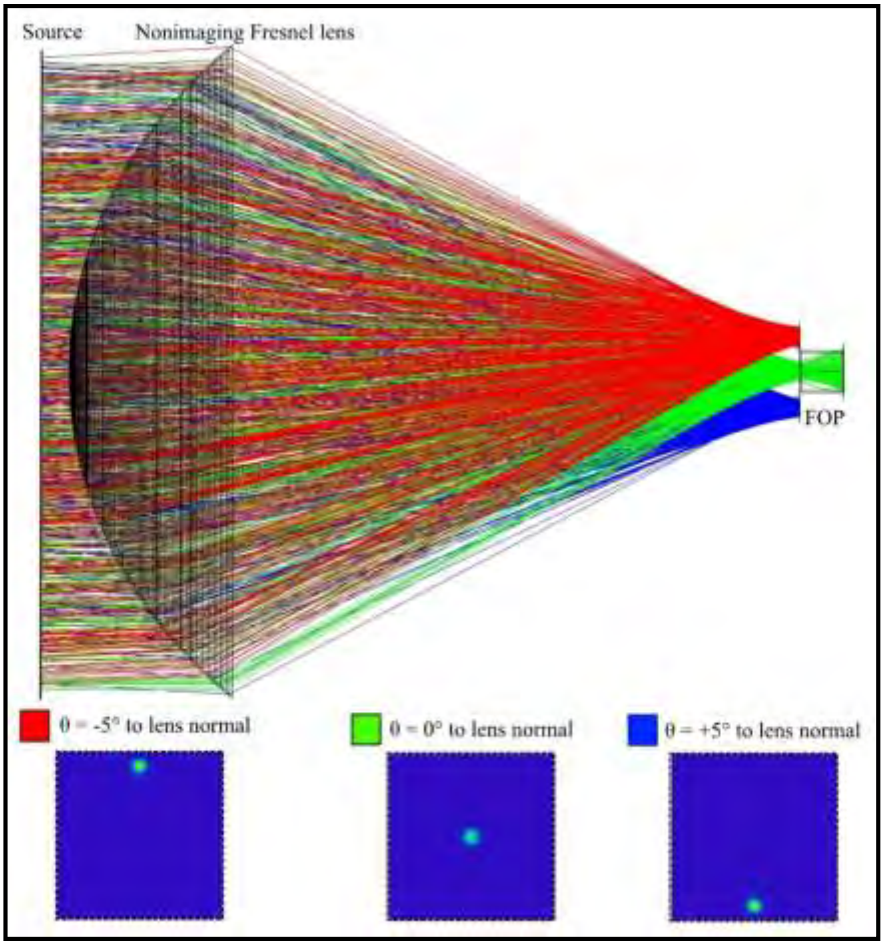

Figure 6. Nonimaging Fresnel lens focusing a collimated light source D65 with $\theta = 0°$ (green) as ideal incident angle and $\theta = \pm 5°$ (red and blue) as maximum incident angle. The radiance in position space is shown for each case.

2.2 Secondary optics element (SOE) design

The CEC designed for the systems has the role of redirect the light collected towards the POF in a very small area with the objective of avoid the losses generated by focal area aberrations due to angular misalignment with the source. The design process of the SOE is illustrated in the Figure 7. The resulting CEC takes the nonimaging Fresnel lens absorber area as the input area diameter [AB] of 34.6 mm and the input area for the POF core as its output area that has a diameter [CD] of 9 mm.

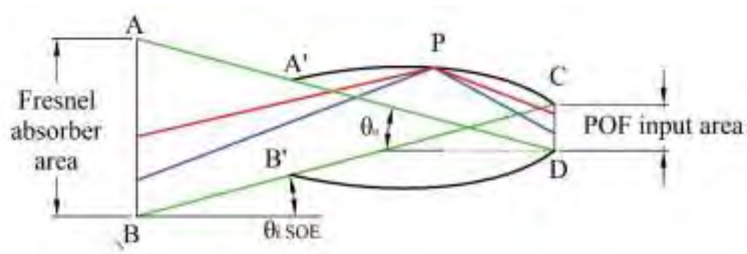

Figure 7. CEC design based on the Fresnel lens and POF output and input power profiles.

The CEC generated has as entrance area diameter [A'B'] of 18.5 mm, that limits the entrance of the light collected for all the acceptance angles, but represents the option for reduce the output area to 9 mm.

2.3 Illumination system design

The general designs consists of a Fresnel lens (Imaging or Nonimaging) as a Primary Optical Element (POE), a Compound Elliptic Concentrator as a Secondary optical Element (SOE) and a Plastic Optical Fiber with PMMA (n = 1.4921),which has a solid core with radius of 4.5 mm, and fluorinated polymer (n = 1.418) cladding as final receiver. The difference between the 2 systems presented is the use of an Imaging or Nonimaging Fresnel lens and it is show in Figure 8.

As it was mentioned before, the acceptance angle of the fiber was taken into account for the design of the other optical elements, this acceptance angle was calculated using Eq. 1 and has the value of $\theta_a \approx 27.66°$.

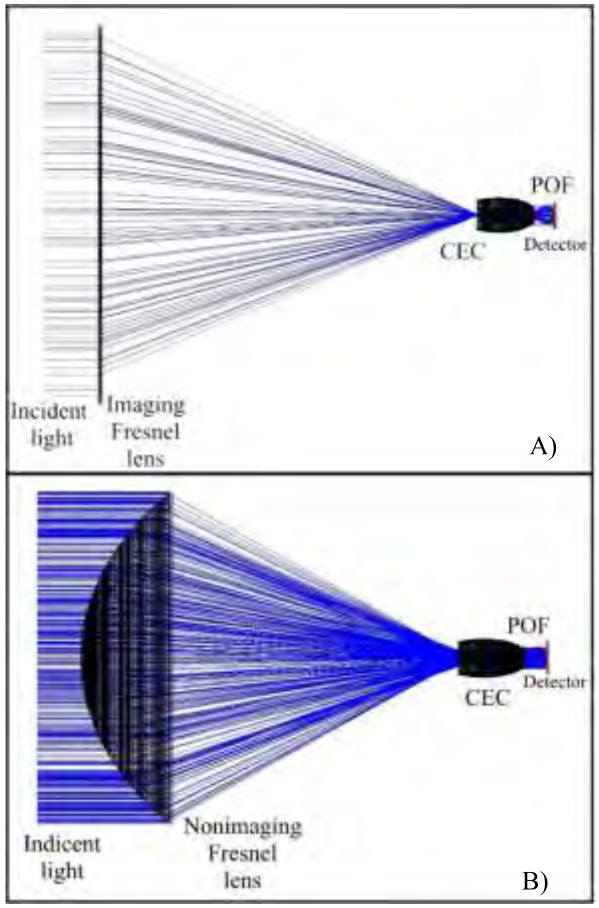

Figure 8. The upper design shows the Imaging System and the lower one the Nonimaging System. Both system are designed with the same SOE element and considering as final collection area de input of the POF. The ray trace shown represents the ideal case of normal incidence.

Every system must combine the functions of concentration and angular correction using the SOE for decreasing the losses in the coupling with the POF[16].

2.4 Methodology

The source implemented for the system was a collimated with the spectral distribution of a D65 source. For the optical fiber, only a segment of 10mm was used because the losses related with the fiber propagation do not be considered for the present work. The exact placement of the CEC was selected for each case looking for the smaller area of concentration at the entrance of the CEC; for the imaging Fresnel lens it was 5 mm nearest the lens and for the nonimaging 20 mm.

For the numerical experiments, the systems shown in Figure 8 were simulated but, for obtain better results, additional detectors were placed among the system, one just before the POE and other one just after. For the case of the nonimaging Fresnel lens, the detector placed before it has an aspheric surface similar to the Fresnel surface. An extra detector was placed for verify the output angle of the SOE and, finally, a third detector was placed after de POF for measure the final power output of the system.

The results presented in the next section will be in terms of ratio instead of watts because the final performance for every simulation was compute considering the light entering the concentrator and the losses due to material absorption and other aberrations of the Fresnel lenses.

3. RESULTS

3.1 Focal area profiles

Each one of the displayed areas in

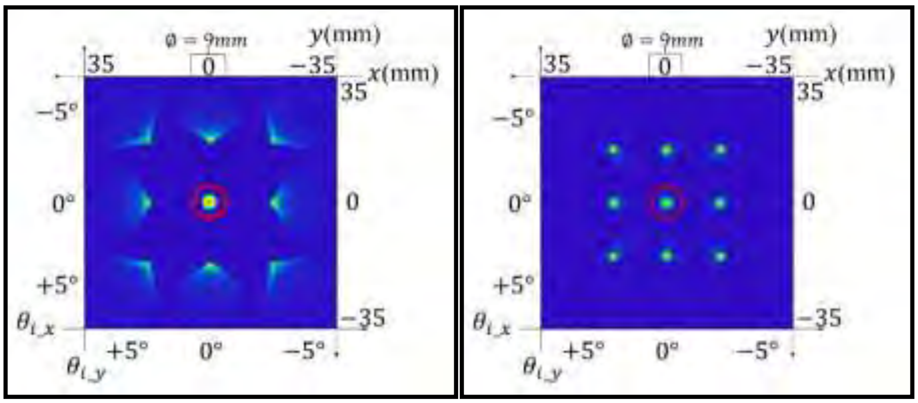

Figure 9 corresponds to a square radiometric detector of 70 mm length that shows the space distributions for different incident angles of the source over the POE; the left side detector contains the output profiles of the imaging lens and the right side the nonimaging outputs. The red circumference represents the POF and, as can be seen: to higher incidence angle, higher displacement outside the fiber area. In addition, for the case of the imaging Fresnel lens, the output profile presents aberrations, in contrast, the nonimaging lens maintain a well-defined spot.

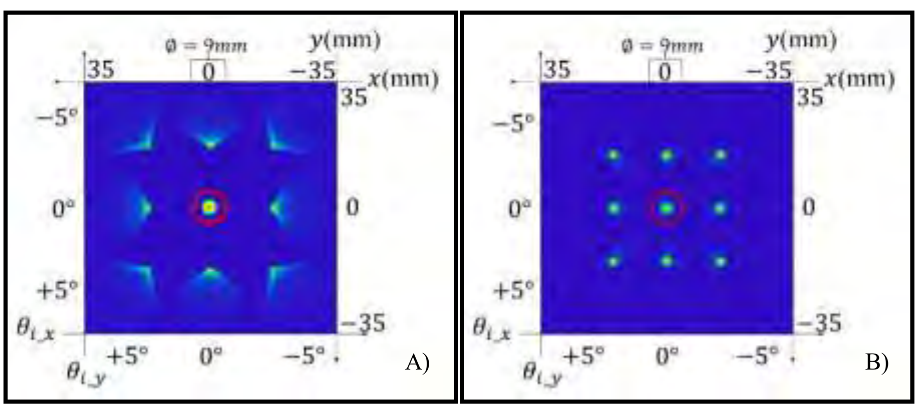

Figure 9. Focal area profiles, for different incident angles ($\theta_{i\_x} \approx -5°, 0°, +5°$ and $\theta_{i\_y} \approx -5°, 0°, +5°$). For both detectors the red circle indicates the input of the POF. A) Imaging Fresnel lens. B) Nonimaging Fresnel lens.

For the angular distribution of the lens profiles, the Figure 10 shows that when the incidence angle of the source over the lens change, the output will increase the half angle, resulting in losses due to angular decoupling between the lens and the fiber. The losses presented in the system without SOE are related with both factors, the angular and space distributions that cannot be coupled into the fiber.

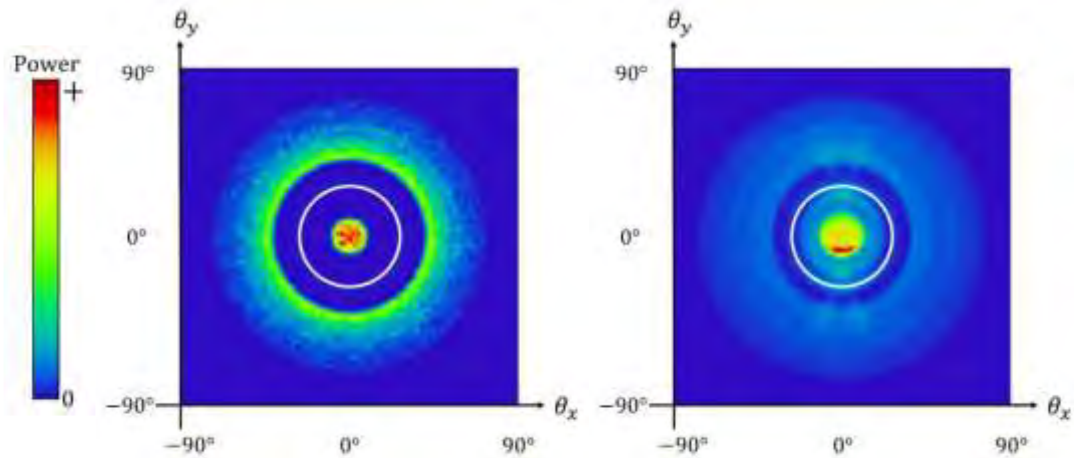

Figure 10. Radiant intensity profiles. The angular distribution shown in each case is the accumulative output for different incident angles ($\theta_{i\_x} \approx -5°, -2.5°, 0°, +2,5°, +5°$ and $\theta_{i\_y} \approx -5°, -2.5°, 0°, +2,5°, +5°$). The white circle represents the angular acceptance of the POF $\theta_a \approx 27.66°$. The left side detector shows the system with the imaging Fresnel lens and the right size the system with the nonimaging collector.

3.2 System performance without SOE

The systems were probed without SOE (Figure 11) and the final results shown that the imaging Fresnel lens has a tolerance around $\theta_i = 1°$ due to the aberrations presented in the focal point that affects the angular output. For the nonimaging lens, the system only allows incidence source with $\theta_i < 0.3°$ because the displacement of the focal area is higher than the input area of the POF.

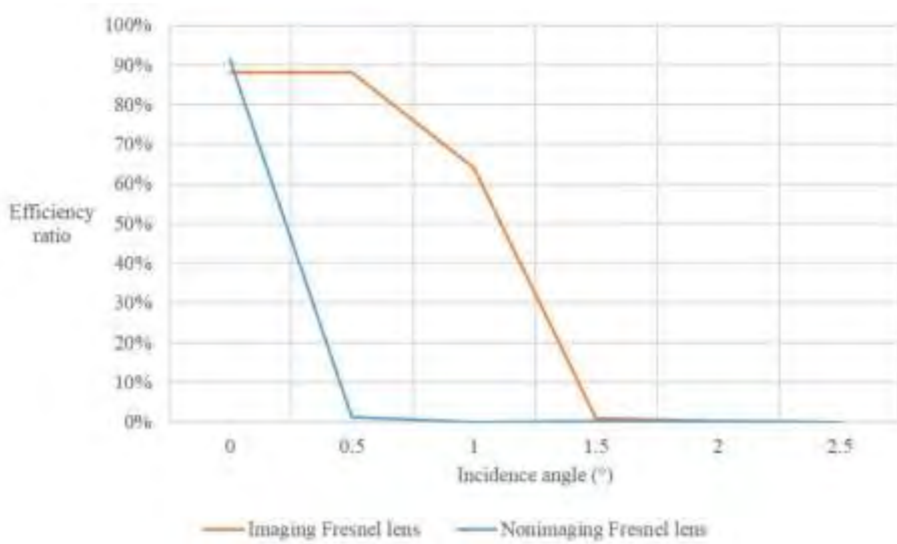

Figure 11. Efficiency ratio of the systems without SOE.

As the CEC was designed considering the output angles of the Fresnel lenses the output of the CEC must be analyzed for assure the angular acceptance of the fiber; the Figure 12 shows the radiance in angle space measured at the output of the SOE, just in the place where the POF is placed for the complete system. This results probes that the light collected will be transmitted, for most of the cases, inside the fiber, the spots that are located outside the angular acceptance of the fiber corresponds with its space misalignment. The angular distribution for the system with the imaging lens shows almost the same angular distribution before and after de CEC.

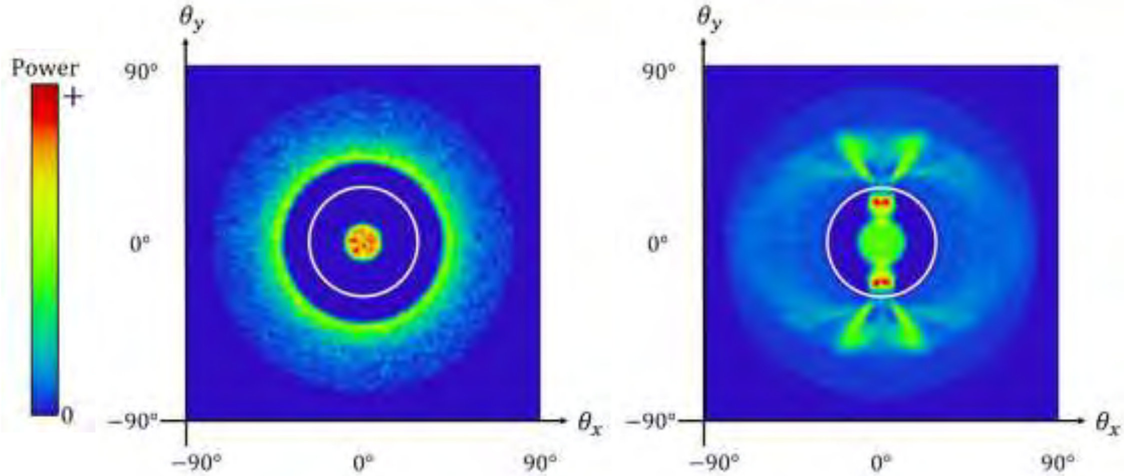

Figure 12. Angular distribution of the CEC output. The white circle represents the acceptance of the POF $\theta_a \approx 27.66°$. The left side detector shows the system with the imaging Fresnel lens and the right size the system with the nonimaging collector.

3.3 Total performance

The total performance, which represents the output power measured in system integrated by the Fresnel lens with the CEC coupled with the POF without considering the losses produced by the collector, of both systems was increased, as is show in Figure 13; for the nonimaging Fresnel lens the total performance remains constant over 80% with an acceptance angle of incidence of $\theta_i = 2°$, in addition, the incidence angle of $\theta_i = 2.5°$ represents a system with an efficiency over 50%. The imaging collector have a performance over 75% with angular tolerance of $\theta_i = 1°$, that corresponds with the typical tolerance of the imaging Fresnel lenses but, in this system, with higher performance.

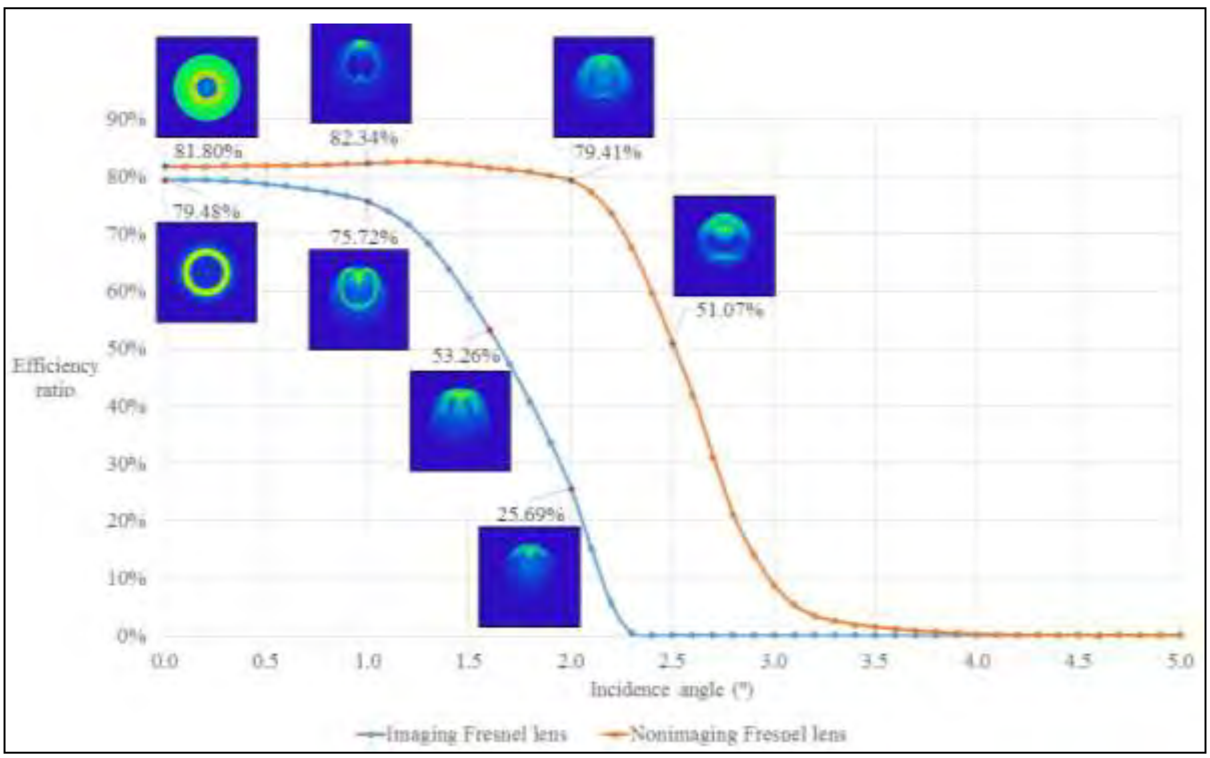

Figure 13. Efficiency ratios of both systems. The insets placed along the graph for both systems represents the space distribution at the fiber output. The system with the nonimaging collector shows a better performance with angular tolerances

over $\theta_i = 2°$, in contrast, the system with the imaging Fresnel lens increase its performance around a 10% but has, in general, a lower angular tolerance than the nonimaging lens.

As was mentioned in the methodology, two detectors were placed before and after de POE for exclude the losses related with the material absorption and aberrations of the lenses that are computed by Zemax when the construction material is founded in its glass catalogue. The losses presented were ~3% for the nonimaging and ~10% for the imaging lens; in the case of the imaging lens was detected that the prisms presents reflection of part of the rays arriving.

4. CONCLUSIONS

The imaging Fresnel lens performance was affected for the incidence angle of the source just as is reported in the literature[1], but the introduction of the SOE allows an increment in the final performance of the system and improve the space distribution of the lens.

The nonimaging Fresnel lens can be designed with different acceptance angles, but this tolerance affects directly the size of the output spot, limiting the coupling with the fiber; this can be shown in the Figure 11 where the final performance of the system with nonimaging collector is lower than the performance of the system with the imaging POE although the nonimaging lens shows a better performance. The introduction of the CEC in this system results in higher tolerance for the incidence angle of the source and allows, for the tolerance angles, maintain the performance over 80%.

Although the nonimaging Fresnel lens was designed for an acceptance angle of $\theta_i = 5°$, the final angular tolerances were lower due to the displacement and size of the focal area. For future works, a similar analysis will be performed for nonimaging Fresnel lenses optimized with acceptance half-angle decoupled to the absorber area and considering other types of prisms[5,6]. In addition, it is necessary look for other SOEs that can be coupled easily into the system.

At the end, the introduction of the SOE in each system, represents the possibility of implement a solar tracking system less sophisticated that improve the system, which was the main objective of the present work. It is possible conclude that, for the case where the CEC is not implemented, the imaging Fresnel lens is a better option, unless the waveguide that will be use have a greater acceptance angle or area; if the CEC will be included in the system, the nonimaging collector is a better option and, in general, this system complies the requirements for indoor solar illumination.

ACKNOWLEDGMENTS

This research was supported by CONACYT (Consejo Nacional de Ciencia y Tecnologia) with the scholarship 387533. The presentation of the present work during the Optics and Photonics Meeting 2015 was supported by the AMO (Academia Mexicana de Optica), the SPIE, Newport Corporation the Facultad de Ciencias Fisico Matematicas of the Universidad Autonoma de Nuevo Leon.

REFERENCES

[1] Leutz, R., Suzuki, A., Nonimaging Fresnel Lenses, Springer, Berlin, Heidelberg (2001).
[2] Leutz, R., Suzuki, A., Akisawa, A.., Kashiwagi, T., "Shaped nonimaging Fresnel lenses," J. Opt. A Pure Appl. Opt. **2**(2), 112–116 (2000).
[3] Xie, W. T., Dai, Y. J., Wang, R. Z., Sumathy, K., "Concentrated solar energy applications using Fresnel lenses: A review," Renew. Sustain. Energy Rev. **15**(6), 2588–2606 (2011).
[4] Leutz, R., Suzuki, A., Akisawa, A., Kashiwagi, T., Toksoy, J., "Developments and designs of solar engineering Fresnel lenses," Proc. Symp. Energy Eng., 759–765, DTIC Document (2000).
[5] Pan, J. W., Huang, J. Y., Wang, C. M., Hong, H. F., Liang, Y. P., "High concentration and homogenized Fresnel lens without secondary optics element," Opt. Commun. **284**(19), 4283–4288, Elsevier B.V. (2011).
[6] Akisawa, A., Hiramatsu, M., Ozaki, K., "Design of dome-shaped non-imaging Fresnel lenses taking chromatic aberration into account," Sol. Energy **86**(3), 877–885, Elsevier Ltd (2012).
[7] Benítez, P., Miñano, J. C., Zamora, P., Mohedano, R., Cvetkovic, A., Buljan, M., Chaves, J.., Hernández, M., "High performance Fresnel-based photovoltaic concentrator," Opt. Express **18**(9), A25–A40 (2010).
[8] Chaves, J., Introduction to nonimaging optics, CRC Press (2008).

[9] Leutz, R., Suzuki, A., Akisawa, A., Kashiwagi, T., "Design of a Nonimaging Fresnel Lens for Solar Concentrators," Sol. Energy **65**(6), 379–387 (1999).
[10] Zhuang, Z., Yu, F., "Optimization design of hybrid Fresnel-based concentrator for generating uniformity irradiance with the broad solar spectrum," Opt. Laser Technol. **60**, 27–33, Elsevier (2014).
[11] Leutz, R., Susuki, a., Akisawa, a., Kashiwagi, T., "Nonimaging Fresnel lens concentrators for photovoltaic applications," [ISES Solar World Congress] (1999).
[12] Fu, L., Leutz, R., Annen, H. P., "Evaluation and comparison of different designs and materials for Fresnel lens-based solar concentrators," 8 September 2011, 81240E – 81240E – 6.
[13] Fu, L., Leutz, R., Annen, H. P., "Secondary optics for Fresnel lens solar concentrators," 19 August 2010, 778509–778509 – 6.
[14] Winston, R.., Welford, W. T., "Design Of nonimaging concentrators as second stages in tandem with image-forming first-Stage concentrators," Appl. Opt. **19**(3), 347–351 (1980).
[15] Kritchman, E. M., "Nonimaging second-stage elements: a brief comparison," Appl. Opt. **20**(22), 3824–3825 (1981).
[16] Buljan, M., Miñano, J. C., Benítez, P., Mohedano, R., Chaves, J., "Improving performances of Fresnel CPV systems: Fresnel-RXI Köhler concentrator," Opt. Express **22**(S2), A205 (2014).
[17] Gordon, J. M., Ries, H., "Tailored edge-ray concentrators as ideal second stages for Fresnel reflectors," Appl. Opt. **32**(13), 2243 (1993).

Intracavity absorption gas sensor in the near-infrared region by using a tunable erbium-doped fiber laser based on a Hi-Bi FOLM

R. I. Álvarez-Tamayo, M. Durán-Sánchez, A. Barcelata-Pinzón, P. Prieto-Cortés, A. F. Rodríguez-Berlanga, et al.

R. I. Álvarez-Tamayo, M. Durán-Sánchez, A. Barcelata-Pinzón, P. Prieto-Cortés, A. F. Rodríguez-Berlanga, A. A. Castillo-Guzmán, G. Salceda-Delgado, R. Selvas-Aguilar, "Intracavity absorption gas sensor in the near-infrared region by using a tunable erbium-doped fiber laser based on a Hi-Bi FOLM," Proc. SPIE 10654, Fiber Optic Sensors and Applications XV, 1065413 (14 May 2018); doi: 10.1117/12.2305033

Event: SPIE Commercial + Scientific Sensing and Imaging, 2018, Orlando, Florida, United States

Intracavity absorption gas sensor in the near-infrared region by using a tunable erbium-doped fiber laser based on a Hi-Bi FOLM

R. I. Álvarez-Tamayo*[a], M. Durán-Sánchez[b], A. Barcelata-Pinzón[c], P. Prieto-Cortés[d], A. F. Rodríguez-Berlanga[d], A. A. Castillo-Guzmán[d], G. Salceda-Delgado[d], R. Selvas-Aguilar[d]
[a]CONACyT – Universidad Autónoma de Nuevo León, Av. Universidad S/N, San Nicolás de los Garza, Nuevo León, Mexico 66451; [b]CONACyT - Instituto Nacional de Astrofísica, Óptica y Electrónica, Optics Department, L. E. Erro 1, Puebla, México, 72824; [c]Universidad Tecnológica de Puebla, Antiguo Camino a la Resurrección 1002-A, Puebla, México, 72300; [d]Universidad Autónoma de Nuevo León, Av. Universidad S/N, San Nicolás de los Garza, Nuevo León, México, 66451
* alvarez.tamayo@hotmail.com

ABSTRACT

We report an experimental study erbium-doped fiber laser for gas pressure detection in the L-band wavelength region by laser intracavity absorption spectroscopy. By using a high-birefringence fiber optical loop mirror as spectral filter within the ring cavity laser, the wavelength of the generated laser line is finely selected and tuned in a range of ~10 nm in order to select the wavelength where the gas absorption line is exhibited. Experimental results for detection of CO_2 pressure with absorption at 1573.2 nm are shown and discussed. The proposed fiber laser sensor exhibits reliability and stability for gas detection with absorption in the L-band such as CO_2, CO, and H_2S.

Keywords: Tunable fiber lasers; laser absorption spectroscopy; remote gas detection; EDF fiber lasers; wavelength filtering devices.

1. INTRODUCTION

In the last decades, the atmospheric environment concern has motivated many efforts in different research fields for detection and monitoring of pollutant gases. Compared with electrical sensors, optical sensors exhibit advantages such as compactness, fast response, immunity to electromagnetic interference, high-sensitivity, and possibility of remote sensing. These advantages make them attractive for continuous monitoring of gas presence. Particularly, optical fiber sensors have been of persistent interest for gas detection by absorption spectroscopy. However, most of these sensors uses broadband light source frequently in the visible spectrum, far-infrared or UV wavelength ranges where absorption wavelength bands are exhibited in most of gases of interest. Rare-earth doped fibers used as gain medium exhibit broad bandwidth amplification in which the absorption lines of different target gases are covered. In case of erbium-doped fibers (EDF), commonly the gain spectrum usually spans over 40 nm in the C-band. This feature make EDF-based systems attractive for detection of pollutant gases with strong absorption lines in this near-infrared (NIR) waveband such as acetylene (C_2H_2), methane (CH_4), hydrogen iodide (HI), and ammonia (NH_3) [1]. However, the optical response is obtained from a wide straight transmission/reflection spectrum limits the selectivity of the detected gas. In order to increase the selectivity of the measured gas, erbium-doped fiber lasers (EDFL) have been studied for its application in laser absorption spectroscopy operating in the 1.55 µm NIR waveband. The use of a spectral filter included in EDFL for selection of the generated laser line improves the sensing selectivity [2]. In addition, where the spectral filter is wavelength tunable it offers the possibility of multi-gas sensing with the same laser configuration. In this consideration, different EDFL gas sensors have been reported based on the use of spectral filters such as fiber Bragg gratings (FBG) [2,3], Fabry-Perot filters [4,5], and fiber interferometers [6]. In this sense, the fiber optical loop mirror (FOLM) with high birefringence (Hi-Bi) fiber in the loop has been proved its reliability as spectral filter for wavelength selection and tuning of stable generated laser lines in fiber lasers operating in the 1.55 and 2 µm wavelength ranges [7,8]. Nevertheless, compared with the fundamental lines observed in the mid-infrared wavelength range, the gases detected in the NIR wavelength range exhibit weak absorption overtones lines, which lead to a low gas absorption sensitivity of the sensor [9]. In this consideration, intra-cavity laser absorption spectroscopy (ICLAS) stands for a reliable gas detection technique to increase the absorption sensitivity in NIR wavelength regions with weak absorption lines. In conventional absorption spectroscopy techniques the gas container acts as short absorption cell when interacts with light, on the other hand, in ICLAS technique the gas cell is inserted within a laser cavity, then, the numerous passes of light through the

Fiber Optic Sensors and Applications XV, edited by Alexis Mendez, Christopher S. Baldwin, Henry H. Du, Proc. of SPIE Vol. 10654, 1065413 · © 2018 SPIE · CCC code: 0277-786X/18/$18 · doi: 10.1117/12.2305033

absorber allows to convert the short absorption cell into a high-efficiency multi-pass optical system improving the detection sensitivity [2]. In ICLAS gas sensors based on conventional EDF lasers operating in the C-band, acetylene is the commonly detected gas because exhibits the strongest line strength (at 1532.83 nm) from the available gases in the supported wavelength range. The use of an L-band EDF as a gain medium in EDFL design allows the obtaining of generated laser lines in a wavelength range from 1560 to 1620 nm. In this wavelength range the most important gases of interest are carbon dioxide (CO_2), carbon monoxide (CO), and hydrogen sulphide (H_2S). Different L-band EDFL operating in the L-band for their potential application as ICLAS gas sensors have been reported [10-12].

In this work, we present a tunable ring cavity EDFL based on the use of a Hi-Bi FOLM as spectral filter for laser emission in the L-band wavelength range. The laser wavelength is finely tuned by temperature variations on the Hi-Bi fiber of the FOLM. A generated laser line is wavelength tuned at 1573.2 nm in which CO_2 exhibit an absorption line. Results of stability of the generated laser wavelength are discussed. In order to probe the performance of the proposed laser configuration for intra-cavity laser absorption spectroscopy, preliminary results of CO_2 gas pressure detection are obtained. The reliability of the proposed ring cavity EDFL based on a Hi-Bi FOLM for detection of gases with absorption lines in the L-band wavelength range is experimentally demonstrated.

2. EXPERIMENTAL SETUP

The experimental setup of the proposed L-band EDFL is shown in Figure 1. The ring cavity uses an L-band EDF (NA of 0.25 and concentration of 3000 ppm) as gain medium. The EDF is pumped through a 980/1550 nm wavelength division multiplexer (WDM) by a 250 mW laser diode at 980 nm. An optical isolator (ISO) ensures unidirectional propagation of light. The Hi-Bi FOLM used as spectral filter is connected to an optical circulator (OC). A polarization controller (PC) used to stabilize the generated laser line and a 90/10 coupler which provides the output port completes the cavity. In order to perform intra-cavity laser absorption spectroscopy, a gas cell was inserted within the cavity between the PC and the 90/10 coupler. The pass of light through the gas cell was optimized by using two fiber collimators (Thorlabs F260FC-1550).

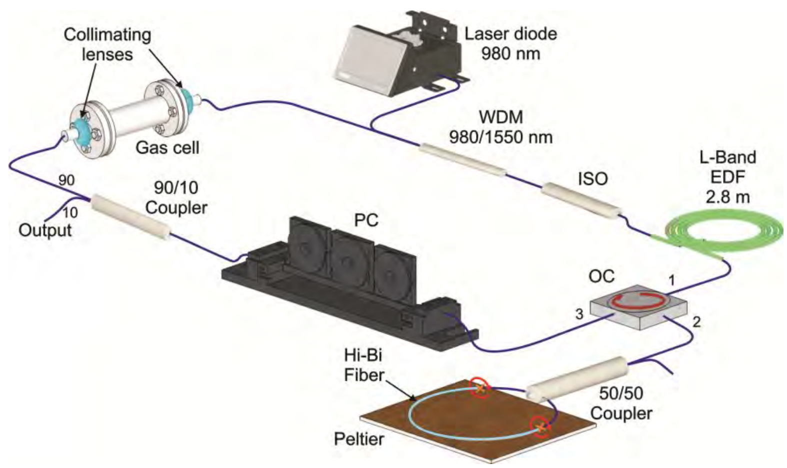

Figure 1. Experimental setup of the L-band EDF laser.

3. RESULTS AND DISCUSSION

The Hi-Bi FOLM is formed by a 50/50 coupler with output ports interconnected by a Hi-Bi fiber segment with length of 40-cm and birefringence of 5.25×10^{-4}. The reflection/transmission spectrum of the Hi-Bi FOLM exhibits a periodical modulation of the input signal whose period can be calculated by [13]:

$$\Delta\lambda = \frac{\lambda^2}{B \cdot L}, \tag{1}$$

where λ is the wavelength of the input light. B and L are the birefringence and the length of the fiber loop, respectively. By using the Eq. (1), with the parameters of the Hi-Bi fiber used the calculated wavelength period of the Hi-Bi FOLM operating around 1570 nm is of 11.72 nm. The Hi-Bi FOLM modulation period can be wavelength displaced by temperature changes on the Hi-Bi fiber. In addition, the fringe contrast of the modulated reflection/transmission spectrum can be adjusted by twisting of the fiber splices between the 50/50 output ports and the Hi-Bi fiber. For a Hi-Bi FOLM constructed with a 50/50 coupler at temperature t and input wavelength λ, the reflection can be described as follows [14]:

$$R = \frac{\gamma}{2}\left(1 + A\cos\left(\frac{2\pi}{\Lambda}(\lambda - \lambda_0) + \frac{2\pi}{T}(t - t_0)\right)\right), \tag{2}$$

where Λ and T are the measured wavelength and the estimated temperature periods, respectively. λ_0 and t_0 are the respective wavelength and temperature values where the Hi-Bi FOLM exhibits maximal reflection. The coefficient γ represents the insertion losses of the Hi-Bi FOLM and the constant A is the fringe contrast between the maximum and minimum reflection. The Hi-Bi FOLM reflected spectrum for Hi-Bi fiber temperatures controlled to 17 and 20°C was measured with a pump power under the lasing threshold of 38 mW at the output with an optical spectrum analyzer (OSA). The measurements were performed with the cavity opened by blocking the input collimation lens at the gas cell position. The input signal of the Hi-Bi FOLM is the amplified spontaneous emission (ASE) of the EDF, then, the reflected output spectrum of the Hi-Bi FOLM is a periodical modulation of the EDF ASE. Figure 2(a) shows the Hi-Bi FOLM reflection which was estimated as the measured Hi-Bi FOLM output signal divided by the previously measured EDF ASE observed in the inset of Figure 2(b). Additionally in Figure 2(a) is presented the simulated Hi-Bi FOLM reflection for the fiber loop temperatures of 17 and 20°C, by using Eq. (2). The following parameters were used: t_0=25.1°C is the room temperature and λ_0=1570.54 nm is the wavelength of a maximal reflection peak at room temperature (as it can be observed from Figure 2(b)). λ of 1572 and 1574.5 nm are the wavelength at a maximum reflection peak for each Hi-Bi fiber loop temperatures of 17°C and 20°C, respectively. A=1 since the rotation stages were set to obtain the maximum fringe contrast. γ was estimated in 0.446 by the insertion losses obtained from the estimated reflection of the Hi-Bi FOLM. Λ=11.8 nm and T=24.8°C are the measured wavelength and temperature periods. As it can be observed, the simulation parameters are quite fitted with the estimated reflection of the Hi-Bi FOLM. With the increase of the Hi-Bi fiber loop temperature, the modulated spectrum of the Hi-Bi FOLM shifts toward shorter wavelengths. Figure 2(b) shows the sensitivity of the wavelength shift of the Hi-Bi FOLM spectrum to temperature variations on the Hi-Bi fiber loop. As it can be observed, from the room temperature at 25.1°C, a maximum reflection peak of the Hi-Bi FOLM is wavelength displaced toward longer wavelengths from 1570.54 to 1574.92 nm when th Hi-Bi FOLM temperature is decreased to a minimum of 16°C. The wavelength displacement of the Hi-Bi FOLM modulation spectrum as a function of the Hi-Bi fiber loop temperature can be linearly fit to a slope of -0.476 nm/°C.

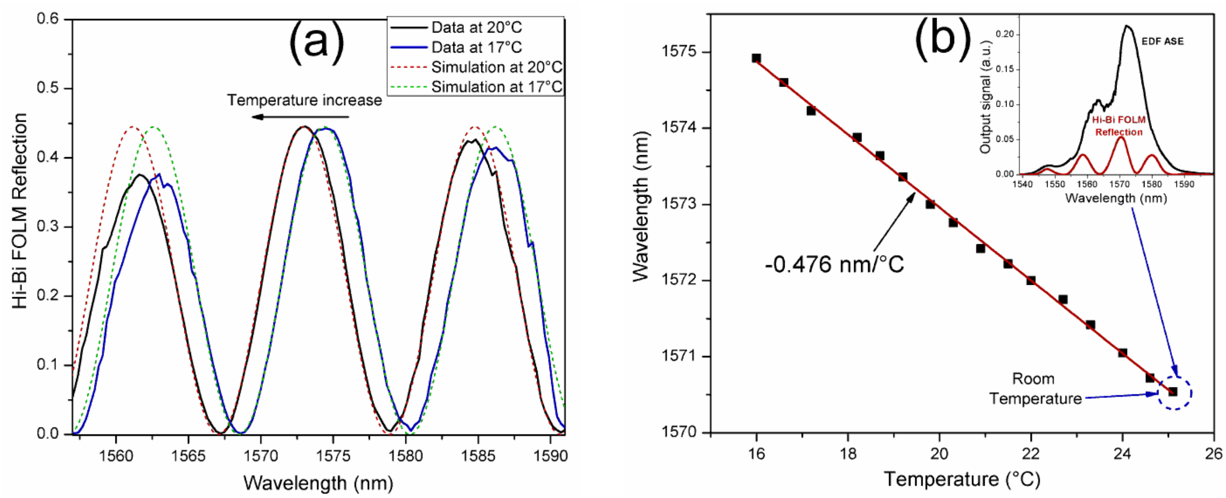

Figure 2. Characterization of the Hi-Bi FOLM, (a) the measured and the simulated reflected spectrum at Hi-Bi fiber loop temperature of 17ºC and 20ºC, (b) the wavelength displacement of a maximum peak by Hi-Bi fiber loop temperature variations. Inset: The ASE of the EDF and the reflected Hi-Bi FOLM spectrum at room temperature.

Figure 3 shows the output spectrum of the laser line measured at the output with the OSA. In order to obtain laser emission, the cavity was closed by the careful adjustment of the collimation lenses without the gas cell inserted within the cavity. Then, by setting the temperature of FOLM Hi-Bi fiber loop to 17°C, the laser wavelength was tuned near to

1573 nm in which the absorption of the CO_2 is expected [12]. The results were obtained with pump power of 125 mW in which the maximum amplitude of laser emission was achieved. The solid black and the blue curves show the output signal of the EDF laser emission without and with the gas cell inserted within the laser cavity, respectively. As it can be observed a single laser line at the central wavelength of 1573.2 nm is generated. Attenuation in the laser line amplitude of ~30% is observed when the gas cell is inserted. The full width at the half maximum (FWHM) for the laser line with the gas cell is of ~215 pm. The dotted red curve shows the Hi-Bi FOLM reflected spectrum. As it can be observed, the laser line is generated in the immediacy of a maximal reflection peak of the Hi-Bi FOLM.

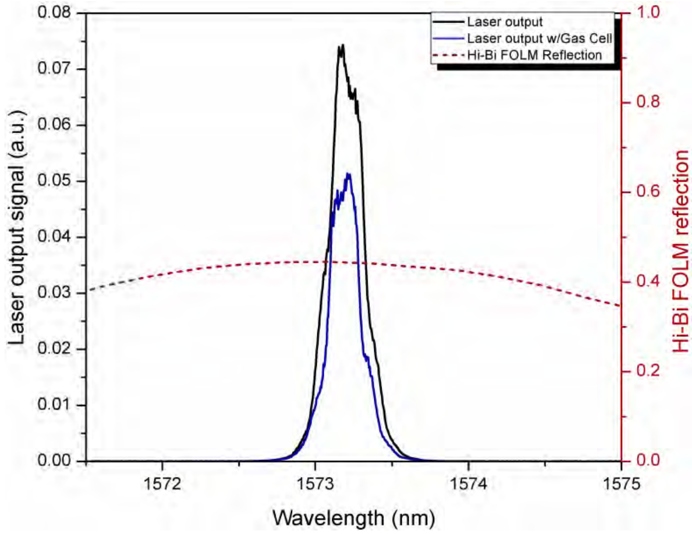

Figure 3. The EDF laser output spectrum with and without the gas cell insertion by using the Hi-Bi FOLM as spectral filter.

The long-term stability of the laser is shown in Figure 4. A set of 20 measurements with a time interval of 5 minutes between each measurement were obtained with the OSA. The EDF laser line was tuned at 1573.2 nm by controlling the Hi-Bi fiber loop to 20°C. Then, the PC was used to control the stability of the generated laser line. When the Hi-Bi fiber loop temperature and the PC adjustments allow observing a stable generated laser line, the measurements were obtained. As it can be observed the generated laser line exhibits good stability over a scanning time of 120 minutes. The stability results show that the proposed EDF laser experimental setup can be used as source for gas detection by direct laser absorption spectroscopy techniques.

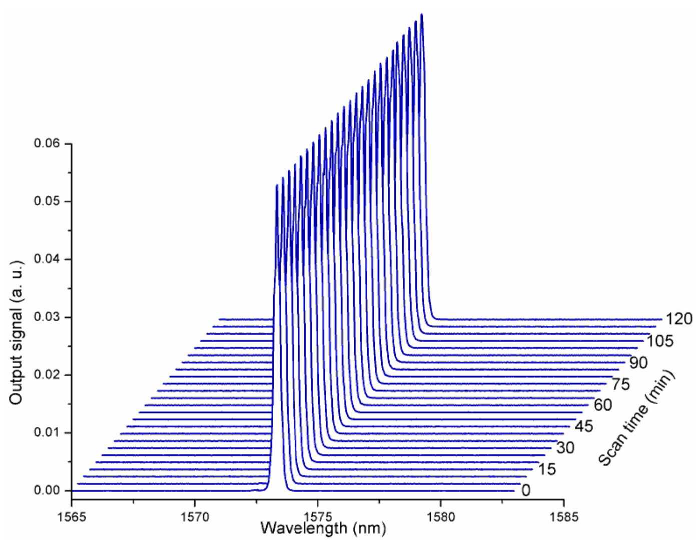

Figure 4. Stability of the EDF laser wavelength tuned at 1573.2 nm.

Figure 5 shows the response of the laser line as a function of the CO_2 gas pressure. For this purpose, the gas cell was filled with 100% of CO_2 concentration to a maximum gas pressure of 1.5 kg/cm^2. The CO_2 exhibits different absorption bands near to the 1570 nm wavelength range. In order to adjust the laser to a maximum detection with the gas cell at the maximum gas pressure, the laser line was finely tuned in wavelength by temperature changes on the Hi-Bi FOLM fiber loop. By monitoring the decrease of the laser line peak power, the maximum response was achieved at ~1573.2 nm. From the maximum absorption settings, the gas was removed from the gas cell at controlled pressures of 1.1, 0.8, and 0 kg/cm^2. The absorption bands of the CO_2 at the 1570 nm wavelength range are overtones with weak peak absorption coefficient of ~1.5×10-7 [ppm-m]$^{-1}$ with is around three magnitude order less than other gases detected in the NIR region such as acetylene. Then, although from the experimental results it can be observed low sensitivity of the EDF laser line to CO_2 pressure, the gas is detected.

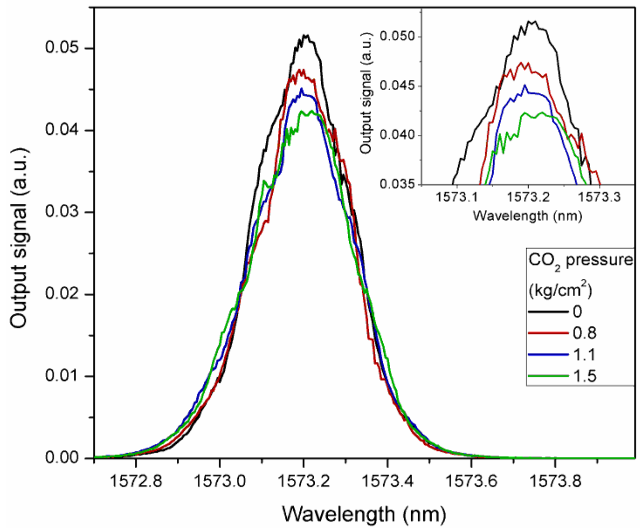

Figure 5. The EDF laser output spectrum as a function of the pressure of CO_2 within the gas cell.

Figure 6 shows the normalized peak power of the EDF laser line as a function of the CO_2 gas pressure of the results obtained in Figure 5. The laser line exhibits maximal peak power variation sensitivity of ~18% to variations of the CO_2 gas pressure from the gas cell filled with 100% concentration to empty. Since the laser peak power exhibits low sensitivity to CO_2 pressure, the results were obtained for only four gas pressures. However, the sensitivity of the laser line can be linear fitted to a peak power variation of -11.87% for each kg/cm^2 of CO_2 gas pressure.

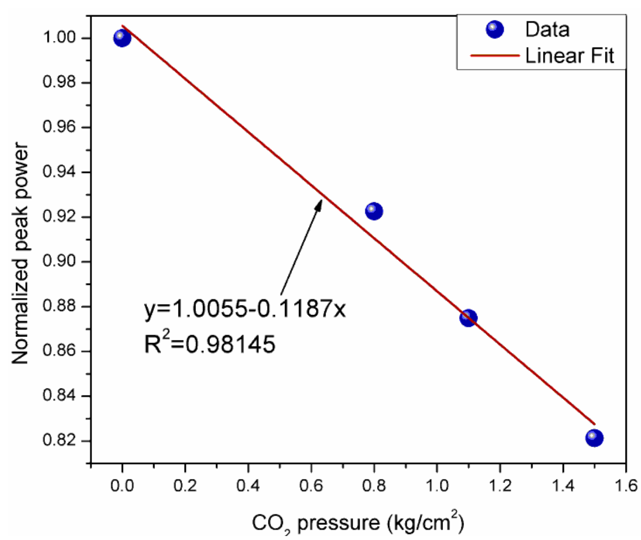

Figure 6. The normalized peak power of the EDF laser line as a function of the CO_2 gas pressure.

The detection of CO_2 by using the proposed L-band all-fiber EDF laser is experimentally demonstrated. However, in order to enhance the stabilization and the sensitivity of the system, the implementation of the laser should be combined with different techniques reported [2-5]. The use of a Hi-Bi FOLM as spectral filter for fine tuning of the generated laser line is demonstrated as a straightforward method for development of all-fiber lasers for its application as sensors of different gas characteristics. The proposed all-fiber EDF laser represents a reliable alternative as light source for detection of gases in the L-band wavelength region. The fine wavelength tuning and the stability of the generated laser line make it suitable for detection of CO and CO_2, among other gases with absorption bands in the L-band.

4. CONCLUSION

In this paper, we experimentally demonstrated an L-band tunable ring cavity EDFL based on the use of a Hi-Bi FOLM as spectral filter. By temperature variations on the FOLM Hi-Bi fiber, the wavelength of the generated laser line was finely tuned at 1573.2 nm where the maximal absorption of CO_2 was achieved. The laser line exhibits good stability, required for gas detection by laser absorption spectroscopy techniques. The performance of the laser configuration was applied for intra-cavity laser absorption spectroscopy of CO_2 pressure. Although the expected low sensitivity of the laser line to CO_2 absorption is expected, detection of the gas is observed in a laser peak power variation of ~18%. The reliability of the EDFL based on a Hi-Bi FOLM was demonstrated for detection of gases with absorption lines in the L-band waveband.

ACKNOWLEDGEMENTS

This work was funding by CONACyT grant 256401 and supported in part by SEP-PROMEP grants 103.5/15/11043 and DSA/103.5/16/10510. R. I. Alvarez-Tamayo and M. Durán-Sánchez want to thanks to Cátedras CONACyT program.

REFERENCES

[1] He, Qixin., Zheng, C., Liu, H., Wang, Y., Tittel, F. K., "A near-infrared gas sensor system based on tunable laser absorption spectroscopy and its application to CH4/C2H2 detection," Proc. SPIE 10111, 1011135 (2017). DOI: 10.1117/12.2250965

[2] Zhang, Y., Zhang, M., Jin, W., Ho, H. L., Demokan, M. S., Culshaw, B., Stewart, G., "Investigation of erbium-doped fiber laser intra-cavity absorption sensor for gas detection," Opt. Commun. 232, 295-301 (2004). DOI: 10.1016/j.optcom.2004.01.013

[3] Zhang, Y., Zhang, M., Jin, W., "Sensitivity enhancement in erbium-doped fiber laser intra-cavity absorption sensor," Sens. Actuators A 104, 653-658 (2003). DOI:10.1016/S0924-4247(03)00058-X

[4] Li, M., Yang, F., Luo, Y., Peng, G., "An intra-cavity absorption fiber gas sensor based on performance enhanced techniques," J. Teraheartz Sci. Electron. Information Technol. 13(4), 16674-16686 (2015). DOI: 10.11805/TKYDA20150427.653

[5] Mizuno, K., Mugino, A., Sekigami, Y., Yoshii, Y., Kuze, H., Takeuchi, N., "Enhanced Detection of Gas Absorption Using an Erbium-Doped Fiber Ring Laser," Jpn. J. Appl. Phys. 41(8), 5458-5462 (2002). DOI: 10.1143/JJAP.41.5458

[6] Shi, J., Wang, Y., Xu, D., He, Y., Jiang, J., Xu, W., Zhang, H., Su, G., Yan, C., Yan, D., Yao, J., "Remote Gas Pressure Sensor Based on Fiber Ring Laser Embedded With Fabry–Pérot Interferometer and Sagnac Loop," IEEE Photon. J. 8(5), 6804408 (2016). DOI: 10.1109/JPHOT.2016.2605460

[7] Álvarez-Tamayo, R. I., Durán-Sánchez, M., Pottiez, O., Ibarra-Escamilla, B., Bello-Jiménez, M., Kuzin, E. A., "Self-Q-switched Er–Yb double clad fiber laser with dual wavelength or tunable single wavelength operation by a Sagnac interferometer," Laser Phys. 25(7), 075102 (2015). DOI: 10.1088/1054-660X/25/7/075102

[8] Posada-Ramírez, B., Durán-Sánchez, M., Álvarez-Tamayo, R. I., Ibarra-Escamilla, B., Bravo-Huerta, E., Kuzin E. A., "Study of a Hi-Bi FOLM for tunable and dual-wavelength operation of a thulium-doped fiber laser," Opt. Express 25(3), 2560-2568 (2014). DOI:10.1364/OE.25.002560

[9] Stewart, G., Atherton, K., Yu, H., Culshaw, B., "An investigation of an optical fibre amplifier loop for intra-cavity and ring-down cavity loss measurements," Meas. Sci. Technol. 12(7), 843-849 (2001).

[10] Zhou, K. J., Zheng, W., "L-band Erbium-Doped Fiber Laser with Polarization Maintaining Ring Cavity," Laser Phys. 20(7), 1632-1635 (2010). DOI: 10.1134/S1054660X10130244

[11] Perez-Herrera, R. A., Ullan, A., Leandro, D., Fernandez-Vallejo, M., Quintela, M. A., Loayssa, A., Lopez-Higuera, J. M., Lopez.Amo, M., "L-Band Multiwavelength Single-Longitudinal Mode Fiber Laser for Sensing Applications," IEEE J. Lightw. Technol. 30(8), 1173-1177 (2012). DOI: 10.1109/JLT.2011.2174138
[12] Marshall, J., Stewart, G., Whitenett, G., "Design of a tunable L-band multi-wavelength laser system for application to gas spectroscopy," Meas. Sci. Technol. 17(5), 1023-1031 (2006). DOI:10.1088/0957-0233/17/5/S15
[13] Álvarez-Tamayo, R. I., Durán-Sánchez, M., Pottiez, O., Kuzin, E. A., Ibarra-Escamilla, B., Flores-Rosas A., "Theoretical and experimental analysis of tunable Sagnac high-birefringence loop filter for dual-wavelength laser application," Appl. Opt. 50(3), 253-260 (2011). DOI: 10.1364/AO.50.000253
[14] Álvarez-Tamayo, R. I., Durán-Sánchez, M., Pottiez, O., Ibarra-Escamilla, B., Cruz, J. L., Andrés, M. V., Kuzin, E. A., "A dual-wavelength tunable laser with superimposed fiber Bragg gratings," Laser Phys. 23(5), 055104 (2013). DOI:10.1088/1054-660X/23/5/055104

In-fiber modal interferometer based on multimode and double cladding fiber segments for tunable fiber laser applications

P. Prieto-Cortés, R. I. Álvarez-Tamayo, M. Durán-Sánchez, A. Castillo-Guzmán, G. Salceda-Delgado, et al.

P. Prieto-Cortés, R. I. Álvarez-Tamayo, M. Durán-Sánchez, A. Castillo-Guzmán, G. Salceda-Delgado, B. Ibarra-Escamilla, E. A. Kuzin, A. Barcelata-Pinzón, R. Selvas-Aguilar, "In-fiber modal interferometer based on multimode and double cladding fiber segments for tunable fiber laser applications," Proc. SPIE 10512, Fiber Lasers XV: Technology and Systems, 105122R (26 February 2018); doi: 10.1117/12.2288460

Event: SPIE LASE, 2018, San Francisco, California, United States

In-fiber modal interferometer based on multimode and double cladding fiber segments for tunable fiber laser applications

P. Prieto-Cortés[a], R.I. Álvarez-Tamayo[b,*], M. Durán-Sánchez[c], A. Castillo-Guzmán[a], G. Salceda-Delgado[a], B. Ibarra-Escamilla[d], E. A. Kuzin[d], A. Barcelata-Pinzón[e], R. Selvas-Aguilar[a]
[a]Universidad Autónoma de Nuevo León, Av. Universidad S/N, San Nicolás de los Garza, Nuevo León, México, 66451
[b]CONACyT – Universidad Autónoma de Nuevo León, Av. Universidad S/N, San Nicolás de los Garza, Nuevo León, México, 66451
[c]CONACyT - Instituto Nacional de Astrofísica, Óptica y Electrónica, Optics Department, L. E. Erro 1, Puebla, México, 72824
[d]Instituto Nacional de Astrofísica, Óptica y Electrónica, Optics Department, L. E. Erro 1, Puebla, México, 72824
[e]Universidad Tecnológica de Puebla, Antiguo Camino a la Resurrección 1002-A, Puebla, México, 72300

ABSTRACT

We report an in-fiber structure based on the use of a multimode fiber segment and a double cladding fiber segment, and its application as spectral filter in an erbium-doped fiber laser for selection and tuning of the laser line wavelength. The output transmission of the proposed device exhibit spectrum modulation of the input signal with free spectral range of ~21 nm and maximum visibility enhanced to more than ~20 dB. The output spectrum of the in-fiber filter is wavelength displaced by bending application which allows a wavelength tuning of the generated laser line in a range of ~12 nm. The use of the proposed in-fiber structure is demonstrated as a reliable, simple, and low-cost wavelength filter for tunable fiber lasers design and optical instrumentation applications.

Keywords: Tunable fiber lasers, erbium-doped fiber, in-fiber interferometer, modal interference, wavelength filtering devices.

1. INTRODUCTION

Tunable fiber lasers based on erbium-doped fiber (EDF) operating on the wavelength region of 1.55 µm have been of persistent interest for applications in different research areas such as optical communications because of the low transmission losses at the operation waveband and for pumping laser sources design for thulium-doped fiber lasers development. For the wavelength selection and tuning of the generated laser wavelength, different fiber interferometers and filters used as spectral filters have been investigated [1-3]. In particular, in-fiber modal interferometers have been demonstrated as reliable optical spectral filters because of their many advantages such as all-fiber compatibility, low insertion losses, ease of fabrication and low cost. In-fiber structures are constructed by fusion splicing of different fiber segments. The modal interference is produced by a fiber element used to recombine the excited coupled modes from cladding with the core modes which cause modulated transmission of the input signal. Different techniques have been reported to produce modal interference by in-fiber structures including the use of tapered fibers [4,5,6], multimode interference effect [7-9], micro-structured fibers [10-12], splices between fibers with different core mode areas [13], and core-offset splices [2, 14], among others. Moreover, in-fiber structures based on double cladding fibers (DCF) have been reported as reliable modal interferometers for their application in the design of straight transmission fiber sensors and multi-wavelength fiber lasers with advantages such as robustness, repeatability and ease of construction, and long-term operation [15-17]. However, reported DCF-based in-fiber interferometers exhibit low fringe contrast and irregular modulation profiles at the 1.55 µm wavelength range which make them no suitable for their use as spectral filters for

Fiber Lasers XV: Technology and Systems, edited by Ingmar Hartl, Adrian L. Carter, Proc. of SPIE
Vol. 10512, 105122R · © 2018 SPIE · CCC code: 0277-786X/18/$18 · doi: 10.1117/12.2288460

wavelength selection and tuning of the generated laser wavelength in tunable EDF lasers which requires spectral filters with long wavelength periods and high fringe visibility.

In this work, we present a novel an in-fiber DCF-based modal interferometer by including a multimode fiber segment to the in-fiber structure which allows increasing the fringes visibility of its transmission spectrum. In addition with the increase of the fringe visibility, the in-fiber interferometer was designed with a long wavelength transmission period of ~21 nm in order to use it as spectral filter in a tunable EDF laser. By bending application on the in-fiber interferometer, the wavelength of the EDF laser generated laser is tuned in a total range of ~12 nm. The laser line exhibits narrow bandwidth of ~0.25 nm and high optical noise-to-signal ratio (ONSR) of ~44 dB. The proposed in-fiber modal interferometer is demonstrated as a reliable wavelength filter for tunable fiber lasers design.

2. OPERATION PRINCIPLE OF THE IN-FIBER MODAL INTERFEROMETER

As it is shown in the schematic diagram of Figure 1, the in-fiber structure is based on segments of a multi-mode fiber (MMI, Thorlabs AFS105/125Y) with length L_1=1.17 cm and a DCF segment with inserted between single-mode fiber (SMF) segments. The DCF segment with length L_2=2.5 cm is a home-made refractive index (RI) W-profile fiber with core, inner cladding and outer cladding refractive indices of 1.459, 1.454 and 1.457, respectively, and core diameter of 7 µm, inner cladding diameter of 47 µm and outer cladding diameter of 125 µm. The modal interferometer was constructed by fusion splicing of the aforementioned fiber segments in a SMF-MMF-DCF-SMF (SMDS) structure. The structure is based on a conventional SMF-DCF-SMF with the addition of a MMF inserted to increase the light intensity coupled to the DCF cladding in order to enhance the fringe contrast of the modal interferometer transmission spectrum. In addition with the increase of the portion of light coupled to the inner cladding of the DCF from the MMF, when light from the input SMF is coupled to the MMF, the core mode is distributed in different modes along the MMF length. The phase difference between the different modes propagated in the MMF leads to multimode interference (MMI) effect which produces resonant dips of the input signal spectrum where constructive interference is maximal, which involve an unwanted effect. However, strong resonant dips can be avoided for the operation wavelength range by choosing a proper MMF length L_1 [18].The light is propagated along the MMF reaching the MMF-DCF splice in which part of the light is coupled to the core of the DCF converted to the core mode and a significant portion of the light is coupled to the inner cladding of the DCF. Because of the W-profile of the DCF, the cladding modes are not restricted to the inner cladding. Then, cladding modes from inner and outer cladding are returned to the core-cladding region and propagated along the DCF. In order to reduce the high order modes interference which produce irregular oscillations, the SMDS structure was painted with black ink, then, the light coupled from the MMF to the outer cladding of the DCF is dissipated through partial energy transfer to high-order modes on the surface interface. The most significant intensity of the input light is propagated along the core and inner cladding along DCF with length L_2. The DCF acts as a modal Mach-Zehnder interferometer where modal interference is produced by the optical path difference between the propagated core and cladding modes (which represent the arms of the interferometer) because of the RI difference. Then, when the propagated modes along the DCF reach the output SMF, a significant part of the light power from the core and cladding modes of the DCF is coupled to the output SMF core in which interfere producing a periodical modulated output transmission of the input signal.

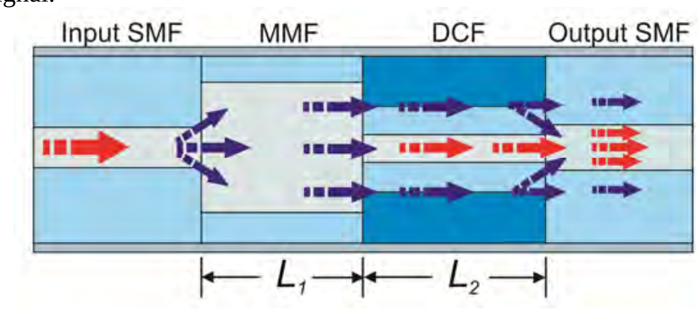

Figure 1. Schematic diagram of the in-fiber modal interferometer and light propagation.

Figure 2 shows the three-dimensional propagation of the light modes along the SMDS modal interferometer was simulated by beam propagation method (BPM) as it is shown in Figure 2. The input light is a normalized core mode input from the input SMF at the wavelength of 1550 nm in which the intensity is maximal. The painted surface was simulated with an arbitrary refractive index of 1.5. As it can be observed, the energy from the input SMF core mode is distributed in different modes along the MMF segment producing a multimode interference at the lead-in facet of the DCF. A main part of the light energy from the MMF is coupled into the core and first cladding of the DCF, where more intensity is observed along the core. However, dominant cladding modes are strongly excited. As a result, modal Mach-Zehnder interference is produced in the core of the output SMF. The light power from the core mode and the excited cladding modes from the DCF is mostly distributed in the SMF core rather than in the cladding.

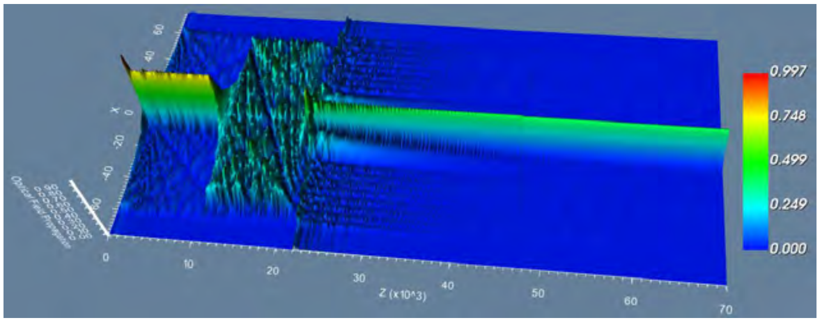

Figure 2. Three-dimensional BPM simulation of the SMDS modal interferometer.

3. EXPERIMENTAL SETUP

Figure 3 shows the experimental setup of the all-fiber ring cavity tunable EDF laser. An L-band EDF with length of 2.8 m, concentration of 3000 ppm and NA of 0.25 is used as the gain medium. The EDF is pumped at 980 nm by a 250 mW laser diode (LD) through a 980/1550 nm wavelength division multiplexer (WDM). The ring cavity is completed with an optical isolator (ISO) used to ensure unidirectional light propagation, a polarization controller (PC) used to adjust and stabilizes the generated laser line, and a 90/10 optical coupler used as the laser output. The laser output spectrum is measured with an optical spectrum analyzer (OSA) at the 10% output port of the 90/10 coupler. The SMDS structure acts as spectral filter to select the wavelength in which the wavelength of the generated laser line is determined by the maximum gain peak. The in-fiber SMDS structure was mounted on a flexible metal sheet whose ends were placed on a pair of mounts over stages to ensure its position. One of the stages remains fixed while the other is a micrometric translation stage. By linear displacements on the translation stage, the generated laser line is wavelength tuned by bending application on the in-fiber modal interferometer.

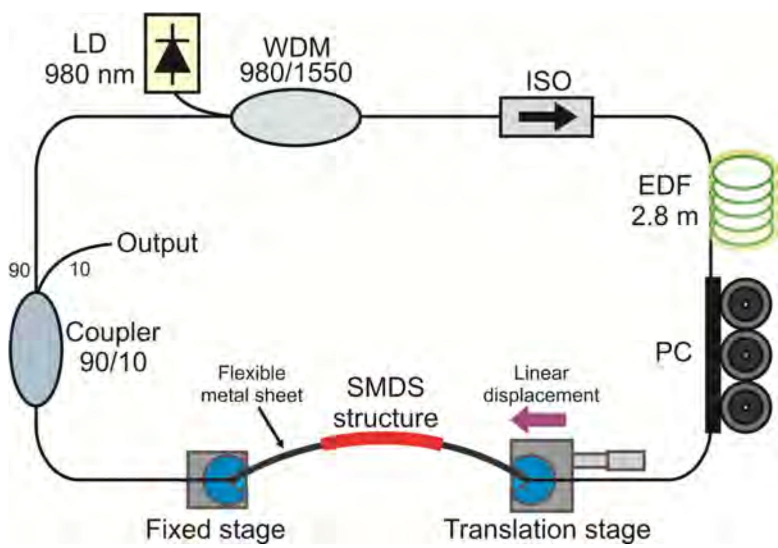

Figure 3. Experimental setup of the ring cavity tunable EDF laser.

4. RESULTS AND DISCUSSION

The in-fiber SMDS modal interferometer exhibits a periodical modulation of the input signal which depends on phase difference between the light propagated along the core and cladding of the DCF. Because both portions of light distributed in the core mode and the dominant cladding modes travel the same physical length L_2, the optical path difference depends on the effective refraction indices difference between the core and cladding (Δn_{eff}). Operating in a wavelength (λ), the wavelength period of the SMDS interferometer modulated transmission spectrum ($\Delta\lambda$) can be approximated to [17]:

$$\Delta\lambda = \frac{\lambda^2}{\Delta n_{eff} \cdot L_2}, \quad (1)$$

In addition, in-fiber structures based on DCF are sensitive to bending. As bending is applied to the SMDS structure its physical length and the mode refractive index varies. As a result, the optical path of the cladding modes is modified while the core mode remains immune to bending. The variation of the refractive index experienced by the interfered modes is approximately the same leading to an optical path difference mainly affected by the physical length. Then, the effect produced by bending of the DCF is a wavelength displacement of the SMDS interferometer transmission spectrum toward shorter wavelengths as the bending is increased, making DCF-based in-fiber structures useful spectral filters for tunable fiber lasers design. However, typically for conventional SMD-DCF-SMF (SDS) structures reported, the fringe contrast is rather low in the 1.55 µm wavelength range (less than 2 dB) because of the low portion of light intensity coupled from the input SMF core to the DCF inner cladding [15-17]. Thus, SDS modal interferometers have been reported for their application as spectral filters for straight transmission curvature and refractive index fiber sensors and for multi-wavelength fiber lasers approaches. In our proposed SMDS modal interferometer, the insertion of a MMF in order to couple more light intensity to the DCF inner cladding results in a significantly fringe contrast increase of the in-fiber interferometer transmission spectrum which make it attractive for its application as tunable spectral filter for tunable fiber lasers design. In order to characterize the transmission spectrum of the proposed tunable spectral filter, the laser cavity shown in Figure 3 was opened at the splice between the 90% port of the 90/10 coupler and the WDM input signal port. Then, the amplified spontaneous emission (ASE) of the EDF is the input signal to the SMDS modal interferometer. Figure 4 shows the transmitted output spectrum of the SMDS structure to the EDF ASE input signal by bending variations. By linear displacement on the translation stage, bending on the SMDS structure was applied from straight position to 2000 µm each 200 µm of linear displacement. The measurements were obtained in the output port by the OSA with the maximum pump power application of 250 mW. As it can be observed, the transmitted output signal of the SMDS interferometer is a periodical modulation of the input signal with wavelength period of ~21 nm. At straight position, a main modulation period with fringe contrast of ~23 dB and maximum peak at the wavelength of ~1573.5 nm is observed. The laser line is expected to be generated at the wavelength in which the maximum gain transmission peak is shown. While bending on the SMDS structure is increased the modulated output spectrum exhibits a wavelength displacement toward shorter wavelengths.

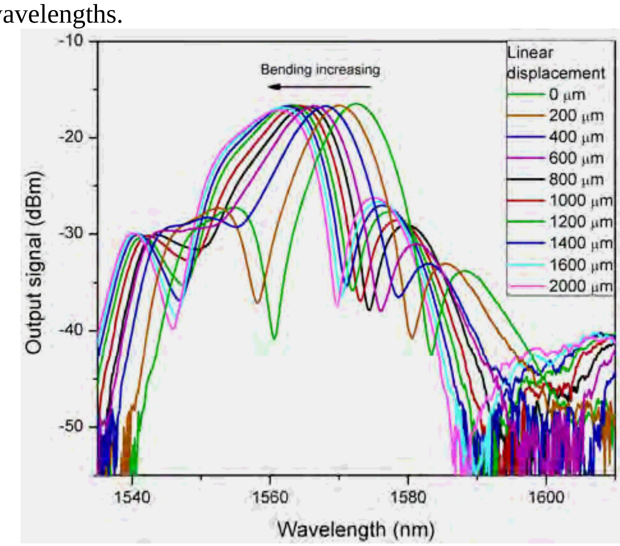

Figure 4. The spectral response of the SMDS modal interferometer by bending variations.

Figure 5 shows the spectrum of the generated laser line. The transmitted output spectrum of the SMDS is also shown. The experimental result was obtained with the OSA at the output port with a pump power of 250 mW. The laser emission was obtained without bending application on the SMDS structure. As it can be observed, single laser emission with wavelength centered at 1573.7 nm which coincides with the maximum gain peak of the in-fiber interferometer transmission modulation. The laser wavelength exhibits a narrow 3-dB linewidth of 95.3 pm and an optical signal-to-noise ratio (OSNR) of 49.6 dB.

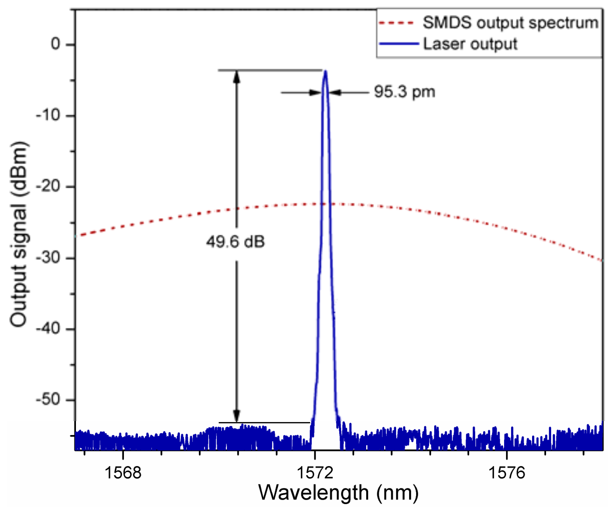

Figure 5. The generated laser wavelength without bending application at the SMDS output transmission spectrum.

Figure 6 shows the operation of the EDF laser under wavelength tuning of the generated laser line. Single wavelength laser emission is observed in a wavelength tuning range of ~12 nm. A set of 9 measurements of the EDF laser line spectrum tuned as a function of the bending applied on the SMDS structure were obtained at the output port with an OSA and a launched pump power of 250 mW. The bending of the in-fiber modal interferometer was varied by linear displacements of the translation stage in an interval of 200 µm from straight position to 1600 µm. As it can be observed, the laser line is displaced toward shorter wavelength as the bending of the SMDS structure is increased. It is worth to note that although there is not a linear of wavelength tuning of the laser line as a function of the linear displacement; the relation is approximately linear with respect to the amount of bending applied in the range shown. With the increase of the linear displacement over 1600 µm, the SMDS structure is less sensitive to bending variations. As a result, the wavelength displacement of the generated laser line is less perceptible.

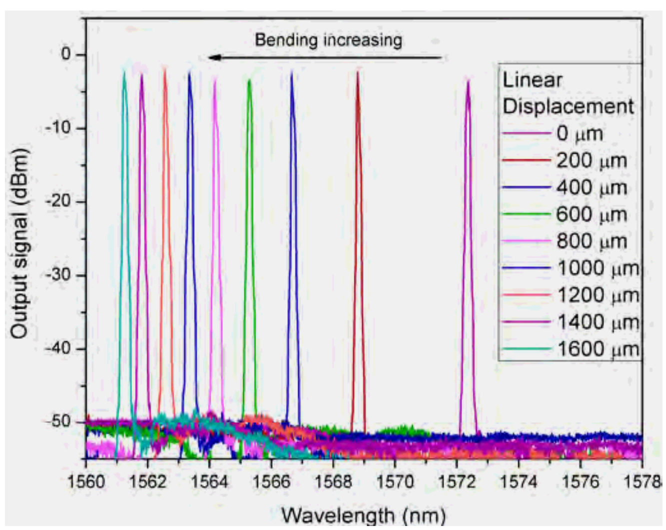

Figure 6. The wavelength tuning of the EDF laser line by bending variations on the SMDS structure..

5. CONCLUSIONS

In this paper, a novel in-fiber modal interferometer based on MMF and DCF segments and its application for the spectral selection and tuning of the laser line of a ring cavity EDF laser were experimentally demonstrated. By including a MMF in a DCF-based in-fiber modal interferometer, the fringe contrast of the modulated transmission spectrum was increased from ~ 2 dB to more than 20 dB in comparison with a conventional SMF-DCF-SMF structure. The increase of the fringe contrast of the proposed SMDS structure makes it suitable for its application as spectral filter for tunable fiber lasers design. The all-fiber EDF laser exhibits wavelength tuning range of ~12 nm, narrow laser line 3-dB spectral linewidth of ~95 pm and ONSR of 49.6 dB. The reliability of the proposed SMDS in-fiber structure as simple, repeatable, low-cost and easy fabrication wavelength filter for tunable EDF fiber lasers design operating in the 1.55 μm wavelength band was experimentally demonstrated.

ACKNOWLEDGEMENTS

This work was funding by CONACyT grant 256401 and supported in part by SEP-PROMEP grants 103.5/15/11043 and DSA/103.5/16/10510. R. I. Alvarez-Tamayo and M. Durán-Sánchez want to thanks to Cátedras CONACyT program.

REFERENCES

[1] Silva S. and Frazão O., “Multimode interference-based fiber sensor in a cavity ring-down system for refractive index measurement,” Opt. & Las. Technol. 91, 112–115 (2017).
[2] Mao L., Lu P., Lao Z., Liu D. and Zhang J., “Highly sensitive curvature sensor based on single-mode fiber using core-offset splicing,” Opt. & Las. Technol. 57, 39–43 (2014).
[3] Liu J., Wang M., Liang X., Dong Y., Xiao H. and Jian S., “Erbium-doped fiber ring laser based on few-mode-single-mode-few-mode fiber structure for refractive index measurement,” Opt. & Las. Technol. 93, 74–78 (2017).
[4] Niu L., Zhao C-L., Gong H., Li Y. and Jin S., “Curvature sensor based on two cascading abrupt-tapers modal interferometer in single mode fiber,” Opt. Commun. 333, 11–15 (2014).
[5] Raji Y. M., Lin H. S., Ibrahim S. A., Mokhtar M. R. and Yusoff Z., “Intensity-modulated abrupt tapered fiber Mach-Zehnder interferometer for the simultaneous sensing of temperature and curvature,” Opt. & Las. Technol. 86, 8–13 (2016).
[6] Miao Y., Zhang K., Liu B., Lin W. and Yao J., “Characteristics of bend sensor based on two-notch Mach-Zehnder fiber interferometer,” Opt. Fiber Technol. 18(6), 509–512 (2012).
[7] Gong Y., Zhao T., Rao Y-J., and Wu Y., “All-fiber curvature sensor based on multimode interference,” IEEE Photon. Technol. Lett. 23(11), 679–681 (2011).
[8] Sun C., Wang M., Liu J., Ye S., Liang L. and Jian S., “Fiber ring cavity laser based on modal interference for curvature sensing,” IEEE Photon. Technol. Lett. 28(8), 923–926 (2016).
[9] Mehta A., Mohammed W. and Johnson E. G., “Multimode interference based fiber-optic displacement sensor,” IEEE Photon. Technol. Lett. 15(8), 1129–1131 (2003).
[10] Bai X., Fan D., Wang S., Pu S. and Zeng X., “Strain sensor based on fiber ring cavity laser with photonic crystal fiber in-line Mach–Zehnder interferometer,” IEEE Photon. J. 6(4), 6801608 (2014).
[11] Li C., Ning T., Li J., Zhang C., Zhang C., Lin H. and Pei L., “Fiber-optic laser sensor based on all-fiber multipath Mach–Zehnder interferometer,” IEEE Photon. Technol. Lett. 28(18), 1908–1911 (2016).
[12] Sierra-Hernandez J. M., Rojas-Laguna R., Vargas-Rodriguez E., Estudillo-Ayala J. M., Mata-Chavez R. I., Jauregui-Vazquez D., Hernandez-Garcia J. C., Andrade-Lucio J. A. and Gutierrez-Gutierrez J. C., “A tunable multi-wavelength laser based on a Mach–Zehnder interferometer with photonic crystal fiber,” Laser Phys. 23(5), 055105 (2013).
[13] Nguyen L. V., Hwang D., Moon S., Moon D. S. and Chung Y., “High temperature fiber sensor with high sensitivity based on core diameter mismatch,” Opt. Express 16(15), 11369–11375 (2008).
[14] Huerta-Mascotte E., Sierra-Hernandez J.M., Mata-Chavez R.I., Jauregui-Vazquez D., Castillo-Guzman A., Estudillo-Ayala J.M., Guzman-Chavez A.D. and Rojas-Laguna R., “A core-offset Mach Zehnder interferometer based on a non-zero dispersion-shifted fiber and its torsion sensing application,” Sensors 16(6), 856 (2016).

[15] Pang F., Liu H., Guo H., Liu Y., Zeng X., Chen N., Chen Z. and Wang T., "In-fiber Mach–Zehnder interferometer based on double cladding fibers for refractive index sensor," IEEE Sensors J. 11(10), 2395–2400 (2011).
[16] Zlodeev I.V. and Ivanov O.V., "Transmission spectra of a double-clad fibre structure under bending," Quant. Electron. 43(6), 535–541 (2013).
[17] Castillo-Guzmán A.A., Alvarez-Tamayo R.I., Sierra-Hernández J.M., Salceda-Delgado G., Selvas-Aguilar R., Durán-Sánchez M. and Ibarra-Escamilla B., "In-fiber Mach-Zehnder interferometer based on a Nd-doped double-clad fiber for switchable single and dual-wavelength EDF laser operation," Laser Phys. 27(5), 055102 (2017).
[18] Álvarez-Tamayo R. I., Durán-Sánchez M., Prieto-Cortés P., Salceda-Delgado G., Castillo-Guzmán A. A., Selvas-Aguilar R., Ibarra-Escamilla B. and Kuzin E. A., "All-fiber laser curvature sensor using an in-fiber modal interferometer based on a double clad fiber and a multimode fiber structure," Sensors 17(12), 2744 (2017).

Multifunctional cube-like system for biomedical applications featuring 3D printing by dual deposition, scanner, and UV engraving

J. V. Guzmán-González, M. I. Saldaña-Martínez, O. G. Barajas-González, V. Guzmán-Ramos, A. K. García-Garza, et al.

J. V. Guzmán-González, M. I. Saldaña-Martínez, O. G. Barajas-González, V. Guzmán-Ramos, A. K. García-Garza, M. G. Franco-Herrada, R. J. Selvas Aguilar, M. A. García-Ramírez, "Multifunctional cube-like system for biomedical applications featuring 3D printing by dual deposition, scanner, and UV engraving," Proc. SPIE 10095, Laser 3D Manufacturing IV, 1009511 (24 February 2017); doi: 10.1117/12.2251588

Event: SPIE LASE, 2017, San Francisco, California, United States

Multifunctional cube-like system for biomedical applications featuring 3D printing by dual deposition, scanner and UV engraving

J.V. Guzmán-González[*,a], Saldaña-Martínez M. I.[a], Barajas-González O. G.[b], Guzman-Ramos V.[c], García-Garza A. K.[a], Franco-Herrada M. G.[a] , R.J. Selvas Aguilar[c] and García-Ramírez M. A.[d]

[a]Mechanical and Electrical Engineering Faculty, Autonumous University of Nuevo Leon, Av. Universidad S/N, 66451, San Nicolás de los Garza, Nuevo León, México; [b]Physics Department, Goethe University Frankurt, Max-von-Laue-Str. 9, 60439, Frankfurt, Germany; [c]Physics and Math Research Center, Autonumous University of Nuevo Leon, Av. Universidad S/N, 66451, San Nicolás de los Garza, Nuevo León, México; [d]Electronics an Computer Sciencies Faculty, University Center for Sciences and Engineering, Universidad de Guadalajara, Blvd. M. García Barragán 1421, Ciudad Universitaria, 44430, Guadalajara, Jalisco, México

ABSTRACT

In this paper, a cubic-like structure is proposed to scan and print tools used as medical equipment at low cost for developing countries. The structure features a 3-axis frame plane that uses high-precision step motors. An actuator drives the “x and y” axis through serrated bands with 2 mm pitch. Those give an accuracy of 2.5 microns tops. The z-axe is driven by and inductive sensor that allows us to keep the focus to the printing bed as well as to search for non-smooth areas to correct it and deliver an homogeneous impression. The 3D scanner as well as the entire gears are placed underneath in order to save space. As extrude tip, we are using a 445 nm UV laser with 2000 mW of power. The laser system is able to perform several functions such as crystallizing, engraving or cut though a set of mirror arrays. Crystallization occurs when the laser is guided towards the base. This process allows us to direct it towards the polymer injector and as a result, it crystalizes on the spot. Another feature that this system is the engraving process that occurs while the base moves. The movement allows the beam to pass freely towards the base and perform the engraving process.

Keywords: 3D scanning, 3D printer

1. INTRODUCTION

3D scanning is a process that converts real-world objects into three-dimensional digital files through an optic-based data acquisition system. Many different technologies can be used to create 3D renderings and each technology have advantages and disadvantages in terms on resolution. The best option for this technology depends on the type of object that you want to scan. In this 3D-printer, the scanner uses a laser line and a sensor that collects data from the object shape. To obtain the shape of the object, a base rotates and acquires the necessary data to generate the render.

The 3D Printing technology is an additive manufacturing process that fabricates a physical object from a digital design. The traditional production methods are subtractive, generating forms by removing of excess material. There are several 3D printing technologies as well as materials [1]. Every 3D print starts as a 3D digital model. The design file is sliced into thin layers that are sent to the 3D printer.

Printing process varies according to the technology in use. It started from basic desktop printers that as a principle melt a polymer material and lay it down to a base plate in which it is deposited, to large industrial machines that use a laser to selectively melt metal powder at high temperatures [1]. The printing process can take hours to complete according to the model size and other physical characteristics.

Chuck Hull invented the first 3D printing process called ‘stereolithography’ in 1983 [2]. He defined stereolithography as ‘a method and apparatus to fabricate solid objects by successively “printing” thin layers of the ultraviolet curable material one on top of the other’, he soon realized that his technique was not limited to only liquids, expanding the definition to ‘any material capable of solidification or capable of altering its physical state’.

Laser 3D Manufacturing IV, edited by Bo Gu, Henry Helvajian, Alberto Piqué, Corey M. Dunsky, Jian Liu, Proceedings of SPIE Vol. 10095, 1009511 · © 2017 SPIE
CCC code: 0277-786X/17/$18 · doi: 10.1117/12.2251588

All 3D printing technologies create physical objects from digital designs through deposition of layer by layer by using each one its own proprietary method. The most common technology in use is the Fused Deposition Modeling (FDM) printing process that starts with a solid material string called filament. The material can be extruded on a specific and fixed path created by a computer software. The advantage to this fabrication process is focused on the fast and low-cost prototyping as well as it can be used for a wide variety of applications.

Other process is the Stereolithography (SLA). This process uses a laser to solidifying the material and the digital light processing (DLP) employs a projector. To fabricate a 3D printed object, a platform is submerged into a translucent tank filled with an aqueous resin. This process is repeated layer by layer until the desired object is completed. This process is widely used for high-detail prototyping.

2. DEVELOPMENT

The machine was designed thinking in the market technologies for 3D printing and taking in to count the most commercial materials of printing such as SLA & FDM. It is also introducing a 3D mechanism for scanning. Below of the mechanism of the printer has a gear system for a plate that is used as a platform to take objects in different angles as shown in Fig. 1.

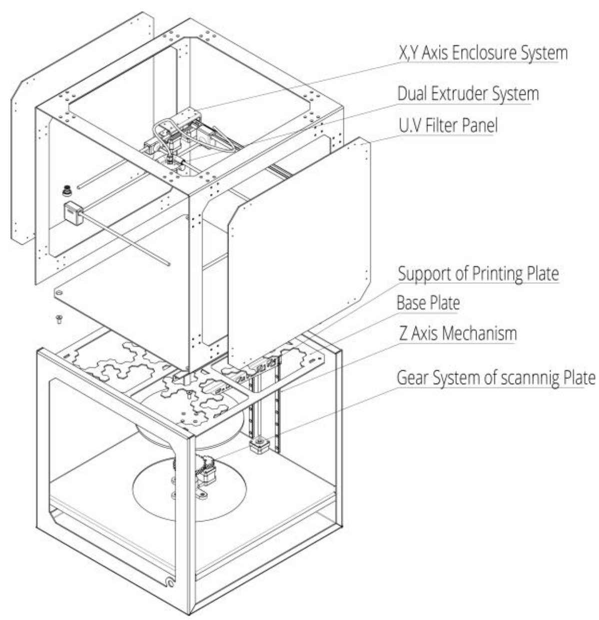

Figure 1. Schematic diagram of the 3D scan, 3D printer and engraving system

The dual extruder System is compounded by 2 kinds of nozzles (A & B) as shown in Fig. 2. The Nozzle A features a hot-end that provides heat to fuse the filament. The nozzle B have an optical array that proves a dual function as extruder & engraver. It is possible due to the dual position of the laser beam. The first position focuses the beam to the nozzle, this is to crystalize the SLA, by repeating this path layer by layer, it is able to create physical objects as shown in Fig. 2B. The second position release the laser beam to the plate, in this way it is possible to exploit as an engraver (Fig. 2C). The laser engraving is a non-contact process between the engraving object and the laser. The laser beam generates a wear effect on the part or material to engrave it. The level of wear that has the laser, is of a power of 2000 mW. The laser will have an input angle of 90º but a single side of the dual extruder nozzle that allows an angle to impact the liquid material and solidify it by making a manual shift of a laser engraving, as Fig. 2 shows.

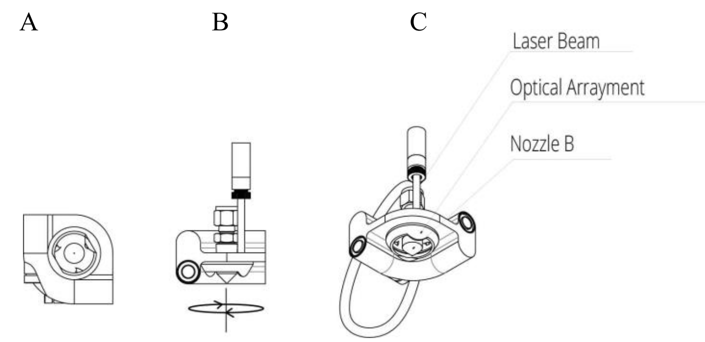

Figure 2. View of the nozzle and the laser

The next figure shows the performance on the printing mechanism. The movement on the axis “x” and “y”, shown in Fig. 3, depicts the movement enclosure system for the axes X&Y by using Nema 17 motors with 16 tooth pulley and 32 micro steep drivers that allows a resolution over 5 μm in booth axes.

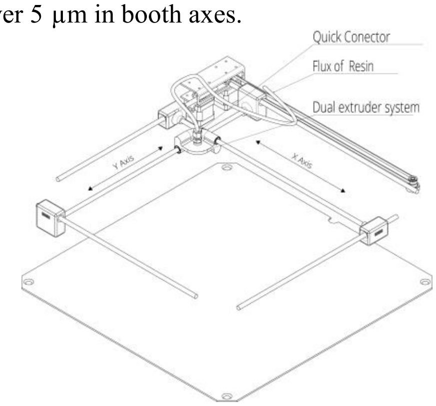

Figure 3. Isometric View of axes.

It is planned to add a camera, which will take the images from each angle while the base of the object will rotate on its axis. The 3D scanner uses two helicoidally gear system, the first with 30 and the second with 15 tooth as shown in Fig. 4. The system has a moving relation of 1:2, this is why, a Nema 17 stepper motor is used. The Nema 17 works with 1/32 micro steps. To calculate for one loop in the gear it is needed 12,800 pulses. According to the iterations, the maximum resolution is 0.02815° degrees.

$$360°\ degrees = (200\ steeps)(32\ micro\ steeps)(2\ revolutions) = 12{,}800\ pulses$$

1° degree = 35.5555 pulses

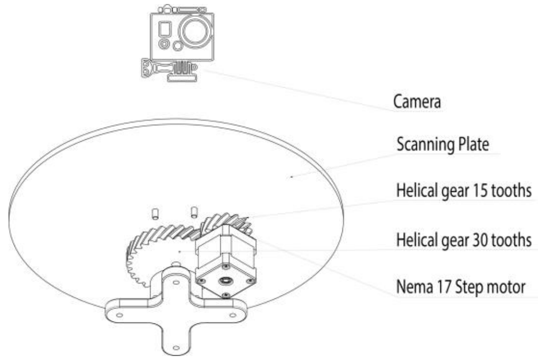

Figure 4. Explode view of scanning plate

3. RESULTS

The final design proves a maximum resolution of 5 μm and layers of 25 μm with a 40x40x40 cm of print volume. Also, with the dual extruder system, it allows us to print with different kind of materials and multipurpose impressions such as biomedical, didactic and industrial tools. In addition, the laser can make small cuts or engraving soft materials as raft wood, paper and cardboard. The machine opens an opportunity window to replicate physical objects

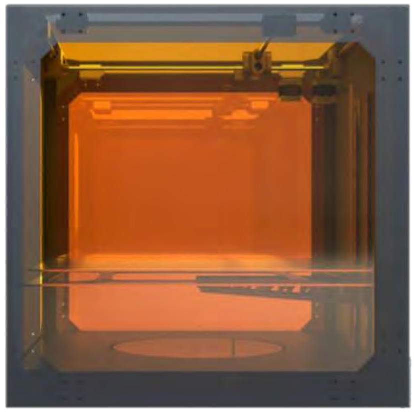

Figure 5. Schematic diagram of the entire system

4. CONCLUSIONS

A cubic-like structure to scan and print tools used as medical equipment at low cost is proposed. The structure features a 3-axis frame plane that uses high-precision step motors. An actuator drives the “x and y” axis through serrated bands with 2 mm pitch. Those give an accuracy of 2.5 microns tops. An UV laser at 445 nm with 2000 mW of power is used. The laser system is able to perform several functions such as crystallizing, engraving or cut though a set of mirror arrays. Crystallization occurs when the laser is guided towards the base. This process allows us to direct it towards the polymer injector and as a result, it crystalizes on the spot. Several materials such as FDM and SLA can be used. By having a 40X40X40 cm volume, it is possible to print large tools for several fields focused on tools used in bio applications at low cost.

5. REFERENCES

[1] What is the 3D printing, https://www.3dhubs.com
[2] decollage design Chuck Hull Short Bio, http://www.decollagedesign.com/chuck-hull/
[3] Saldana Martinez M.I., Guzman Gonzalez J.V., Barajas Gonzalez O. G., and other: 3D splint prototype system for applications in muscular transcutaneous electrical nerve stimulation (TENS), (2017)

Noise Suppression ASE of Erbium Doper Fiber Laser by Means of a Filter Optical Fiber Fattening

J.M. Estudillo-Ayala, R. I. Mata-Chavez, R. Rojas-Laguna, E. Vargas-Rodriguez, A. Martinez-Ríos, E. Alvarado-Méndez, M. Trejo-Duran and R. Selvas-Aguilar.
Universidad de Guanajuato, FIMEE, Campus Salamanca, Comunidad de Palo Blanco, Salamanca, Gto. México, C.P. 36730.
Tel: +524646479940, Fax: +524646472400.
Email:evr@salamanca.ugto.mx

Abstract: In this work we present the results obtained to couple a filter Optical fiber to Erbium doper fiber laser, with this setup we eliminate noise ASE.

OCIS codes: (060.0060) Fiber optics, (230.2285) Fiber devices and optical amplifiers

1. Introduction

Band-rejection fiber filters are required for the elimination of unwanted wavelengths in optical fiber systems, In optical fibers, wavelength dependent loss can be induced though the inscription of long period gratings (LPG's) A convenient way to fabricate LPG's in optical fibers is through the periodical application of an electric arc from a fusion splicer [1-3]. In this work we used fiber filters based on the fattening, a method for the fabrication of band rejection fiber filters based on the fattening of the optical fiber diameter by using a commercial fusion splicer, this method is describe in the reference[4].

2 Experimental Description

In this experiment, we used 9 meters of Erbium dope fiber (ER20-4/125) we couple to the fiber a WDM, and we used a laser pump diode of 980nm. In the cavity we splice the fiber filter fattening to the Erbium dope fiber and out the laser we see with a OSA the effect the put filter. We fabricate a LPG's to wavelength central of the 1560 nm, band loss of the filter varies in a range between 0.5-5 dB. In the results we see the out spectrum the laser is more narrow than the laser before we put the LPGs, this is because exist one attenuation due to LPGs. This result we need for to unite another amplifier without what the first amplifier is saturate and we have a good response. We do an analysis of the result the splice the LPG's with the Erbium doped fiber laser and compare with another LPG's filters.

3. References

[1] S. G. Kosinski and A. M. Vengsarkar, "Splicer-based long-period fiber gratings," in *Optical Fiber Communication Conference*, Vol. 2 of 1998 OSA Technical Digest Series (Optical Society of America, 1998), paper ThG3.

[2] G. Rego, P.V.S. Marques, J.L. Santos, H,M, Salgado, "Arc-Induced Long-Period Gratings," Fiber and Integrated Optics, **24** (3-4), pp. 245-259 (2005).

[3] G. Rego, R. Falate, J. L. Santos, H. M. Salgado, J. L. Fabris, S. L. Semjonov, and E. M. Dianov, "Arc-induced long-period gratings in aluminosilicate glass fibers," Opt. Lett. **30** (16), pp. 2065-2067 (2005).

[4] Mata-Chávez, R. I.; Martinez-Rios, A.; Torres-Gomez, I.; Alvarez-Chavez, J. A.; Selvas-Aguilar, R.; Estudillo-Ayala, J. "Wavelength bad-rejection filters based on optical fiber fattening by fusion splicing" Optics and Laser Technology, v. 40, iss. 4, p. 671-675.

Acknowledgments
CONACYT Project J51264 & J61085, Projects CONCYTEG 0716k662-061-A09

Novel optical refraction index sensor

Helena S. de los Reyes-Cruz[a], Edgar S. Arroyo-Rivera[a], Arturo Castillo-Guzman[a], Mario S. Lopez-Cueva[a], Romeo Selvas[a]
[a] Physical and Mathematical Science Research Center FCFM-UANL, Av. Universidad s/n, Cd. Universitaria, San Nicolás de los Garza, NL, México 66451
acastillog@gmail.com

ABSTRACT

This works describes a novel optical refraction index sensor which is based on the analysis of double reflection lecture detection. This process initially identifies the thickness of a semitransparent solid o liquid material by the retro-reflection of a laser diode at 633nm as a function of distance along the device under test with a Z-axis scanner to find the focusing point. This feedback signal brings how far traveled the beam path which is indirectly related with the refractive index at different materials, the data of the thickness at each layer is treating with a geometrical analysis of the beam velocity.
Keywords: fiber sensor, refractive index, double reflection lecture.

1. INTRODUCTION

Currently, the manufacturing industry has demand precision measurement at almost any point of its process. Traditionally, contact CMMs (coordinate measuring machines) represent the standard precision measurements, unfortunately, these include elements of physical contacts which are not desired in some important measurements. The new trends of precision measurement are therefore the noncontact systems. Mainly, it new kind of system represents more than 60% of the market for sensing and is widely used in the automobile, aerospace, and electronics industries [1].

An important feature in noncontact measuring for the thickness is the speed to process the information. This speed during the process means better control in the quality of parameters and suggested a lower manufacturing cost. There is no doubt about that the repeatability and the accurately are also very important features during production. The portability of the system also enables to set and adjust the tool or sensor to take data in real time.

This work describes a novel optical refraction index sensor which is based on the analysis of double reflection lecture detection. This process initially identifies the thickness of a semitransparent solid or liquid material by the retro-reflection of a laser diode at 633nm as a function of distance along the device under test. For the index detection, a lens is attached in a Z-axis-scanner to find the focusing point. This feedback signal brings how depth is penetrated the beam and also how far traveled the beam path. As we know, the refractive index is indirectly related to the traveled beam path at different materials, the data of the thickness at each layer is treating with a geometrical analysis of the beam velocity and all data can provides us of the refractive index at each material. The system is compact, robust and reliable.

2. OPTICAL REFLECTOMETRY

Nondestructive measurement of the optical properties of some samples as a function of distance along the device under test generally requires the methods of reflectometry. Diagnostics for concatenated components or long optical fiber transmission line are usually conducted with some variation of optical time domain reflectometry (OTDR) [2]. This method had proved to be of immense value in the metrology of optical transmission systems. Reported measurements include determination of fiber attenuation, break location, diameter fluctuations, spliced-quality, mode conversion at joints, defect identification, and micro-bending loss. Most of the applications are associated with testing long-distance optical communication systems.

In addition to the OTDR method there are different kinds of refractometers that have been used so far. Naming some of them, we could find examples of Pulfrich refractometer [3], Abbe refractometer [4] and refractometers which use a

Optomechanics 2011: Innovations and Solutions, edited by Alson E. Hatheway,
Proc. of SPIE Vol. 8125, 81250M · © 2011 SPIE · CCC code: 0277-786X/11/$18
doi: 10.1117/12.894563

minimal deviation angle for their measurements [5-7]. All these methods required geometrical configurations and Snell´s refraction laws as well. These refractometers have employed lasers as the light source. This implementation allows more precise measurements due to its spatial and temporal coherence.

In an interesting review article, Healey [8] described in some details the various types of single-mode reflectometer developed up to date. These include devices based on coherent detection and optical frequency-domain instruments. Here, we only mention the basic operating principles of the simple one, a conventional pulsed-echo OTDR. A schematic diagram of a typical device is given in Fig. 1. With this instrument, a pulsed beam is launched into the tested fiber through a directional coupler. A single port launches the pulse into the test fiber and recovers the returned signals. These signals may be classified as reflections from discrete discontinuities and a very weak distributed Rayleigh scattering. The signals are detected in a fast optical detector, processed and displayed as a function of time (or distance) over some kind of graphics display. The recorded response is often referred to as a signature, and represents a unique characteristic of the system under test.

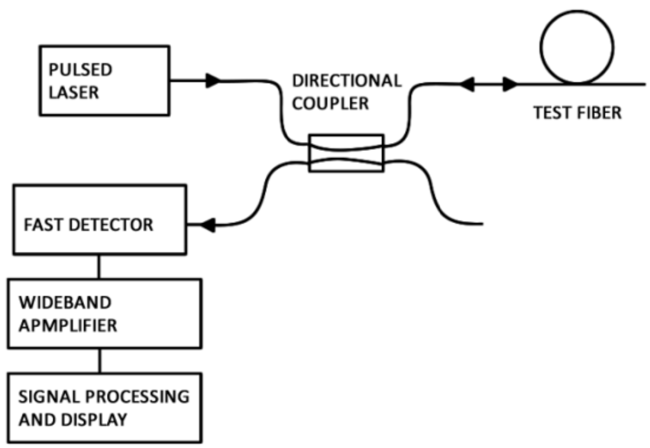

Fig. 1. Basic schematic diagram of a OTDR.

This simple idea to collect light from the backward direction of a fiber optics is an excellent feature that is widely used to develop sensor instruments. Typically, a fused coupler or a WDM are the optical passive elements used in this kind of setup. It basically works by the injecting of an optical signal in a fiber optics and in its forward direction this signal beam is put in contact with an external material, and then the response of its optical property of this material, such as the reflection, is used to get some information back to the system. Such a signal is retro-reflected into the fiber optics and collected in the optical passive element and delivered to an electronic system that interpreted it and give a measurant.

3. FOCUS & MEASURING PROCESS

Auto-focus system is widely used in photographic cameras and helps in the localization for the best position of a recollected light back from an exterior scenario and therefore to get a nice contrast and view of a picture. The focal length of a lens, in one hand, is the distance from the center of the lens to the principal focal point and technically in a convex lens, the light beam is concentrated with a maximum collected optical power. However, if the focus of the lens is misadjusted, the optical power drastically drops and thus the quality of an image is getting poor. As it can be seen in Fig. 2, the position d0, d1, d2 or d3 shows the power densities or diameter beam spots which varied against the distance, meaning that for the position d0, the power position has a highly concentrated beam and thus a maximum optical density power (or a maximum voltage 5V as is indicated in the illustrated example).

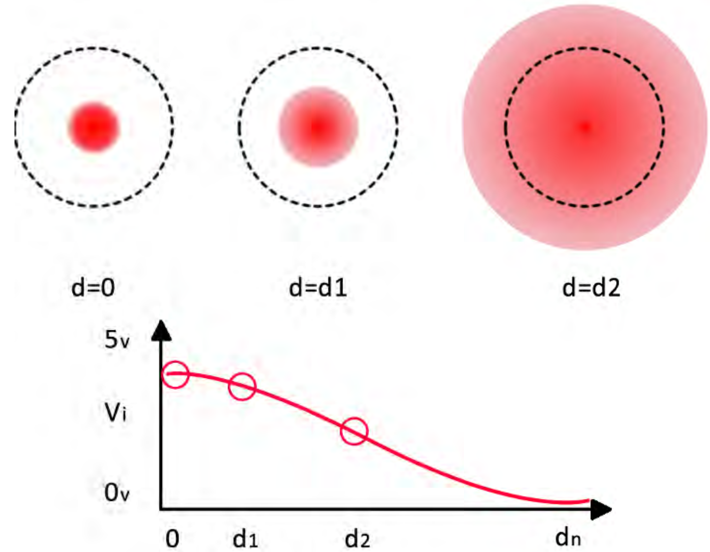

Figure 2: Power densities vs displacement as function of its focal point (focal point at d0).

Figure 3 shows the layout of a lens and its focus position and is described as a follow: the position of a moving platform relative to a fixed base (lens holder) is controlled by an external linear actuator motorized, which incorporate a lead screw passing through a lead nut in this platform. The rotation of such a lead screw is controlled by a stepper motor. This allows the system to control its position in a very accurate resolution of some micrometers. Relaying on this resolution, we scan the surface from an initial position up to a final position and recorded this displaced position and treated by a signal processing board to generate a data which corresponds to a thickness from a sample. In other words, these positions in distance are the focal point of the laser beam for these two positions. In this way, we can measure distance relative to the surface. In Fig. 3 also schematically shows two different focal points for two different spot diagrams.

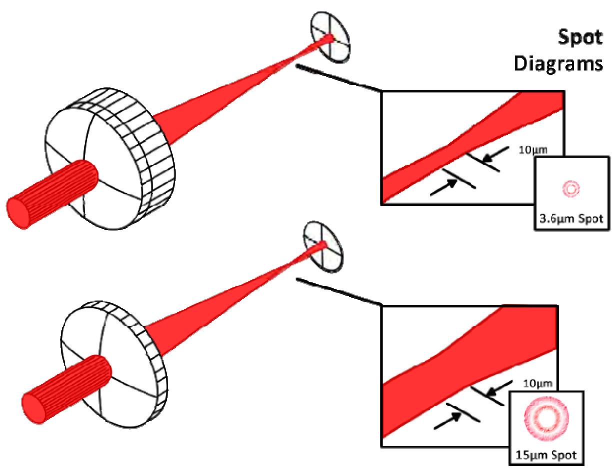

Figure 3: Layout decribing the focal point with spot diagrams for two different lenses

In the layout of Fig. 3, it is also describe experiments we carry out with two focused lenses and the selected lens corresponds when the beam at the focal point had a diameter of about 3.6 micrometer of diameter.

In addition to search the lens focal distance, another important point was the measuring process. The measuring process consists on obtaining the relative difference between the track travel by the light without a sample and the same track with a sample included. In order to obtain this ratio it is necessary to make 3 measurements. The first one is the relative height of our reference. For all the samples it was used a cooper plate due to its high reflectivity. All the samples were set on this plate. The second measurement is the relative surface height of each sample as it is shows in Fig. 4. The third one is the relative height of the bottom of the sample; this measurement is also showed in Fig. 4. Once the measurements are done, the next three formulas are applied,

$$Dif = D_{\max} - D_{\min} \tag{1}$$

where D_{max} is the third measurement, the bottom distance of the sample, D_{min} is the second measurement, the sample surface distance.

$$Dif_{ref} = D_{ref} - D_{\min} \tag{2}$$

where D_{ref} is the first measurement, the distance of the reference.

$$R.I = \frac{Dif_{ref}}{Dif} \tag{3}$$

where $R.I$ is the refractive index of the sample.

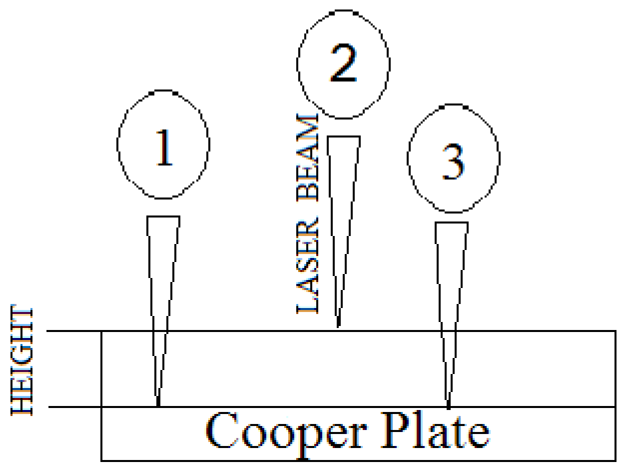

Figure 4. Measurmements required for obtaining the refractive index.

4. OPTICAL FIBER SENSOR

The optical fiber sensor set up is showed in Fig. 5. This set up consists in a diode of 630nm as the light source. This diode is fusion spliced with a WDM which sends the light to the sample through the mechanical arrangement. The light which is retro-reflected is collected by the same fiber and send it to a photodetector. Finally, an electronic system interprets the measurement.

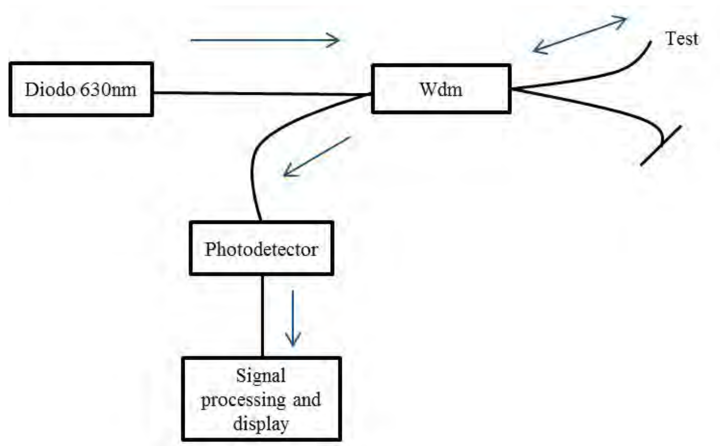

Fig. 5 Optical set up.

The Fig. 6 is a schematic diagram of the mechanical device which was design in order to scan certain distance range searching for the laser focal point.

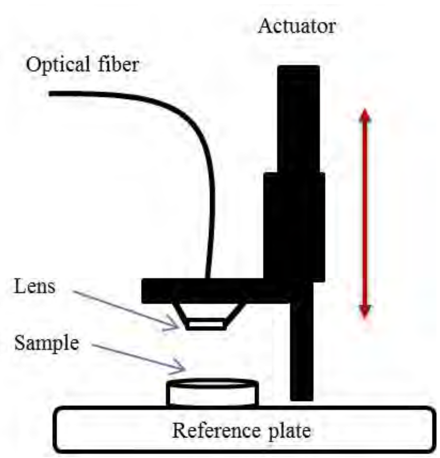

Fig. 6 Schematic diagram of the mechanical device.

The mechanical device consists on a actuator (Thorlabs Z812B) with a maximum travel distance of 12mm and a lens (Thorlabs C330TME-B). The program done to this application can manipulate some actuator parameters like its velocity; its acceleration and the distance of each step while the scanning. The parameters chosen for the experiments were: 2 mm/sec for acceleration, 2 mm/sec for velocity and 50μm per step.

Once established the actuator parameters, the actuator start moving towards the sample, each step done by the actuator was recorded on the computer in order to have a better resolution on the graph and therefore a more precise results after applying the math.

5. EXPERIMENTAL RESULTS

Fig. 7 and 8 show the results obtained. Fig. 7 represents the liquids and Fig 8 the solids semitransparent used in this work.

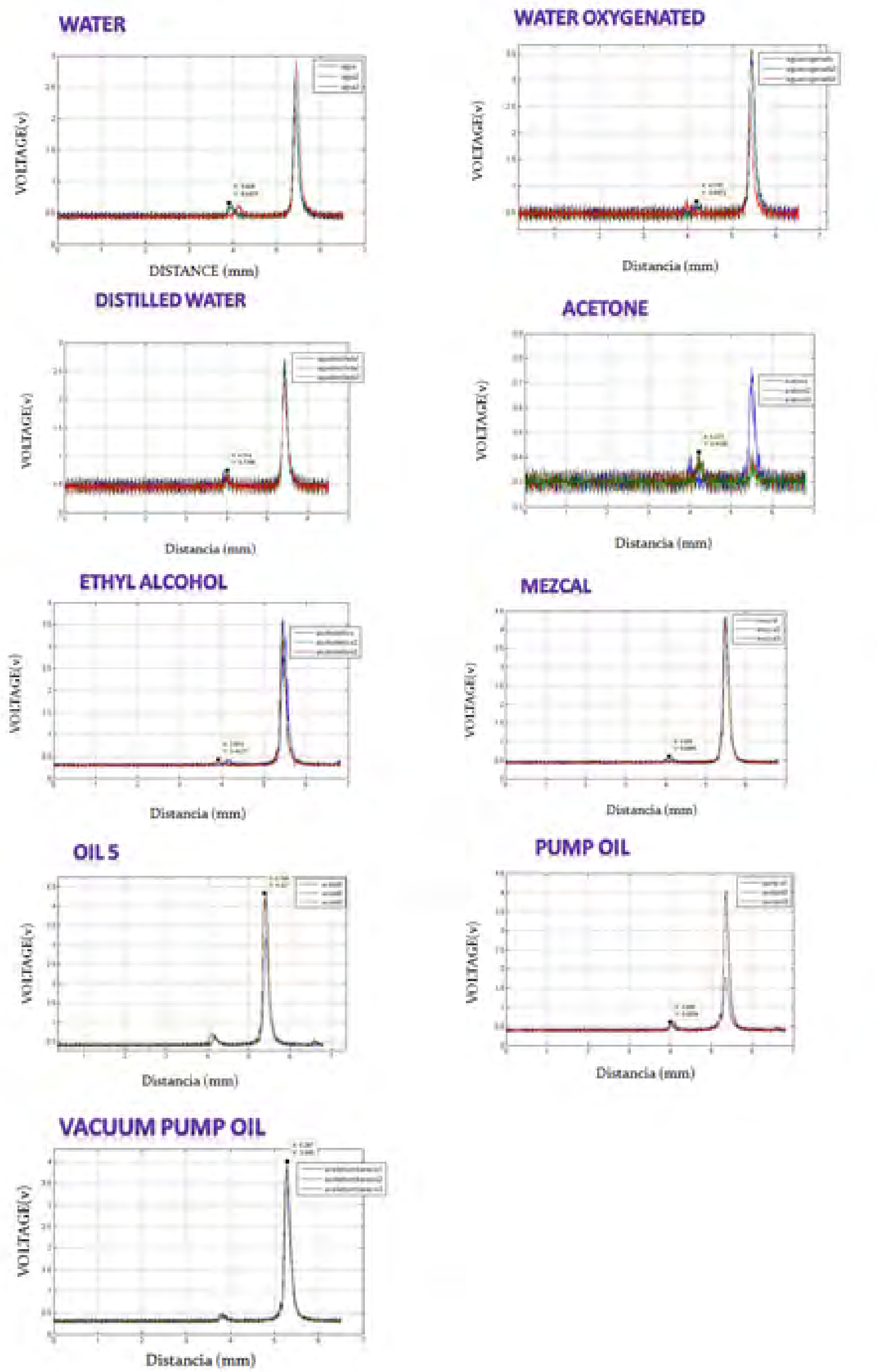

Fig. 7. Liquids double lecture experimental results.

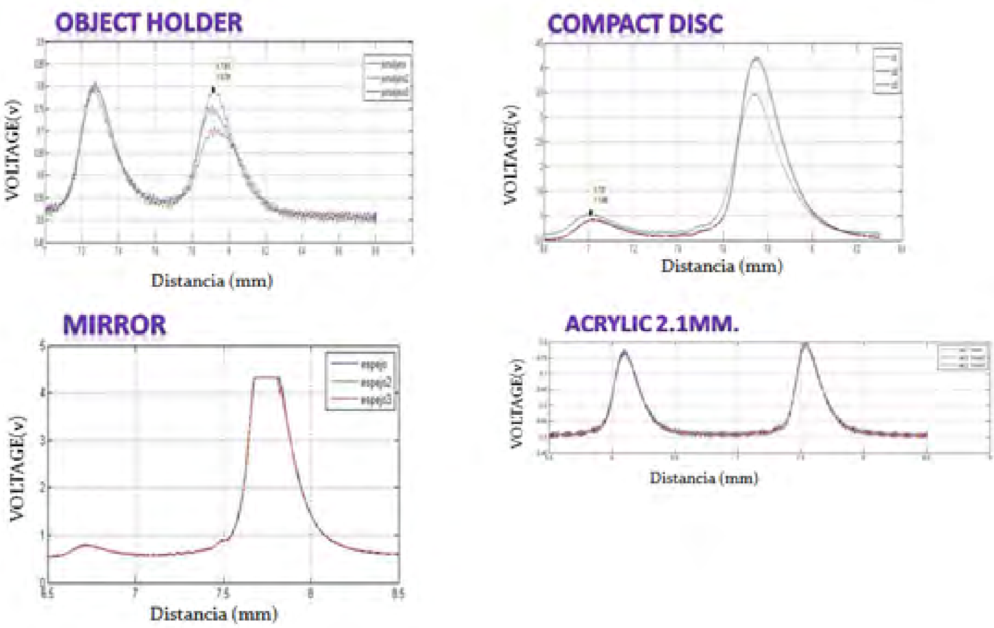

Fig. 8. Solids double lecture experimental results.

Each graph is a representation between the distance travel by the actuator and the light intensity (voltage) reflected by each sample. As it can be notice, each sample was tested three times, showing good agreements among them.

Now, applying Eq. 1-3, refractive indexes were obtained. Table 1 shows these results. Each result was compared with the refraction index reported for the literature showing to be in a good agreement. The error achieved is no greater than a 5%.

Table 1. Experimental results.

Sample	Refraction index
Water	1.320
Oxygen water	1.345
Distilled water	1.305
Ethyl alcohol	1.301
Mezcal	1.262
Acetone	1.272
Oil 5	1.369
Pump oil	1.402
Vacuum pump oil	1.405
Mirror	1.548
Compact disk	1.634
Object holder	1.445
Acrylic 2.1mm	1.487

6. CONCLUSIONS

It was concluded that the measuring of the refractive indexes of liquids and semitransparent solids are possible. The operation principle is based on the search of the lens focal point considering the maximum intensity of the laser beam which is reflected by each sample. Additionally, the instrument developed was found to be used for a large variety of sensing applications (eg. proximity sensing, deep analysis for gasoline contaminants, etc.). It is also considered the implementation of different wavelength lasers as light sources.

7. ACKNOWLEDGMENTS

This work was supported by the Mexican Council of Science and Technology (CONACYT) under grant 61085 and by the Mexican Ministry of Education (SEP) under grand 2523.

REFERENCES

[1] Shuzhue Yio, P. B. Ruffin, and F. T. S. Yu, [Fiber Optic Sensors], CRC Press, Ch. 1, 2& 3, (2008).

[2] OTDR, http://www.wisegeek.com/what-is-an-otdr.htm

[3] E. Moreels, C. de Greef, and R. Finsy, "Laser light refractometer", *Appl. Opt.* 23:3010 (1984).

[4] K. Kuhler, E.L. Dereniak, and M. Buchanan, "Measurement of the index of refraction of the plastic Phenxy PKFE", *Appl. Opt.* , 30:1711 (1911).

[5] B. W. Grange, W. H. Stevenson, and R. Viskanta, "Refractive index of liquid solutions at low temperatures: an accurate measurement", *Appl. Opt.* , 15:858 (1976),

[6] S. Nemoto, "Measurment of refractive index of liquid using laser beam displacement", *Appl. Opt*., 31:6690 (1992).

[7] F. docchio, S Corini, M. Perini, and R. S. Kasana, "A simple and reliable system for measuring the refractive index of liquids using a position-sensitive detector", *IEEE Trans. Instr. Meas.* 44:68 (1995).

[8] P. Healey, "Review of long wavelength single mode optical fiber reflectometry techniques", *IEEE/OSA J. Lightwave Technol.* LT-3, 876 (1985).

Noncontact fiber optic micrometer

F. Betancourt Ibarra[a*], Candelario Guajardo-Gonzalez[a], Arturo Castillo-Guzman[a], Valentin Guzman-Ramos[a], Romeo Selvas[a,b]

[a] School of Mathematical and Physical Sciences, UANL, San Nicolás de los Garza, 66451, NL, México

[b] Center for Innovation, Research and Development in Engineering and Technology, UANL, Monterrey, 66450, NL., México

*franciscobetancourt@live.com

ABSTRACT

A sensor instrument able to measuring the thickness of different semitransparent objects with a resolution of one micron is described. This is based on a fiber optic reflectometer and a laser autofocus system and permit to measuring the thickness of thin surfaces such as semiconductor films, plastic materials and semitransparent objects. The response time for the measuring was roughly 2 sec and the thickness results were compared with a digital mechanical micrometer and both are in good agreement.

Keywords: optomechatronics, fiber sensor

1. INTRODUCTION

Currently, the manufacturing industry has demand precision measurement at almost any point of its process. Traditionally, contact CMMs (coordinate measuring machines) represent the standard precision measurements, unfortunately, these include elements of physical contacts which are not desired in some important measurements. The new trends of precision measurement are therefore the noncontact systems. Mainly, it new kind of system represents more than 60% of the market for sensing and is widely used in the automobile, aerospace, and electronics industries [1].

An important feature in noncontact measuring for the thickness is the speed to process the information. This speed during the process means better control in the quality of parameters and suggested a lower manufacturing cost. There is no doubt about that the repeatability and the accurately are also very important features during production. The portability of the system also enables to set and adjust the tool or sensor to take data in real time. For these reasons, we developed an optomechatronic arrangement consisted in an optical fiber sensor, a computer interface and one axis positioning actuator which measures the thickness of different samples. Such instrument has a resolution of 1μm and measure time of only 2 sec.

2. OPTICAL REFLECTOMETRY

2.1 Fiber optic reflectometer

Nondestructive measurement of the optical properties of some samples as a function of distance along the device under test generally requires the methods of reflectometry. Diagnostics for concatenated components or long optical fiber transmission line are usually conducted with some variation of optical time domain reflectometry (OTDR) [2]. This method had proved to be of immense value in the metrology of optical transmission systems. Reported measurements include determination of fiber attenuation, break location, diameter fluctuations, spliced-quality, mode conversion at joints, defect identification, and micro-bending loss. Most of the applications are associated with testing long-distance optical communication systems.

In an interesting review article, Healey [3] described in some details the various types of single-mode reflectometer developed up to date. These include devices based on coherent detection and optical frequency-domain instruments.

2nd Workshop on Specialty Optical Fibers and Their Applications (WSOF-2),
edited by Juan Hernández-Cordero, Ismael Torres-Gómez, Alexis Méndez, Proc. of SPIE
Vol. 7839, 783927 · © 2010 SPIE · CCC code: 0277-786X/10/$18 · doi: 10.1117/12.869392

Here, we only mention the basic operating principles of the simple one, a conventional pulsed-echo OTDR. A schematic diagram of a typical device is given in Fig. 1. With this instrument, a pulsed beam is launched into the tested fiber through a directional coupler. A single port launches the pulse into the test fiber and recovers the returned signals. These signals may be classified as reflections from discrete discontinuities and a very weak distributed Rayleigh scattering. The signals are detected in a fast optical detector, processed and displayed as a function of time (or distance) over some kind of graphics display. The recorded response is often referred to as a signature, and represents a unique characteristic of the system under test.

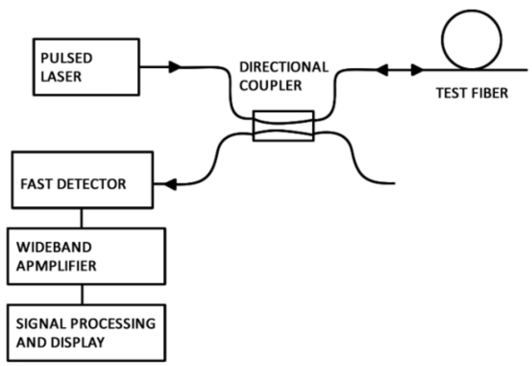

Fig. 1 OTRD system layout.

This simple idea to collect light from the backward direction of a fiber optics is a excellent feature that is widely used to develop sensor instruments. Typically, a fused coupler or a WDM are the optical passive elements used in this kind of setup. It basically works by the injecting of an optical signal in a fiber optics and in its forward direction this signal beam is put in contact with an external material, and then the response of its optical property of this material, such as the reflection, is used to get some information back to the system. Such a signal is retro-reflected into the fiber optics and collected in the optical passive element and delivered to an electronic system that interpreted it and give a measurant.

3. AUTOFOCUS SYSTEM

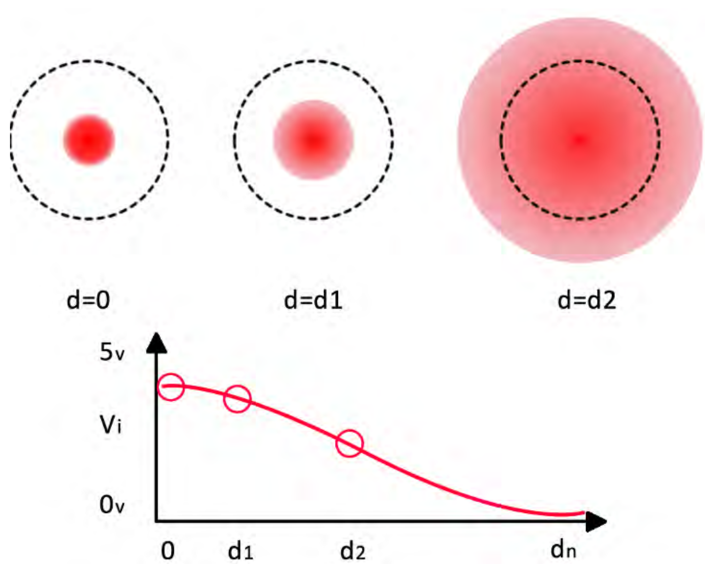

Figure 2: Power densities vs displacement as function of its focal point (focal point at d0).

Auto-focus system is widely used in photographic cameras and helps in the localization for the best position of a recollected light back from an exterior scenario and therefore to get a nice contrast and view of a picture. The focal length of a lens, in one hand, is the distance from the center of the lens to the principal focal point and technically in a convex lens, the light beam is concentrated with a maximum collected optical power. However, if the focus of the lens is misadjusted, the optical power drastically drops and thus the quality of an image is getting poor. As it can be seen in Fig. 2, the position d0, d1, d2 or d3 shows the power densities or diameter beam spots which varied against the distance, meaning that for the position d0, the power position has a highly concentrated beam and thus a maximum optical density power (or a maximum voltage 5V as is indicated in the illustrated example).

Figure 3 shows the layout of a lens and its focus position and is described as a follow: the position of a moving platform relative to a fixed base (lens holder) is controlled by a external linear actuator motorized, which incorporate a lead screw passing through a lead nut in this platform. The rotation of such a lead screw is controlled by a stepper motor. This allows the system to control its position in a very accurate resolution of some micrometers. Relaying on this resolution, we scan the surface from an initial position up to a final position and recorded this displaced position and treated by a signal processing board to generate a data which corresponds to a thickness from a sample. In other words, these positions in distance are the focal point of the laser beam for these two positions. In this way, we can measure distance relative to the surface. In Fig. 3 also schematically shows two different focal points for two different spot diagrams.

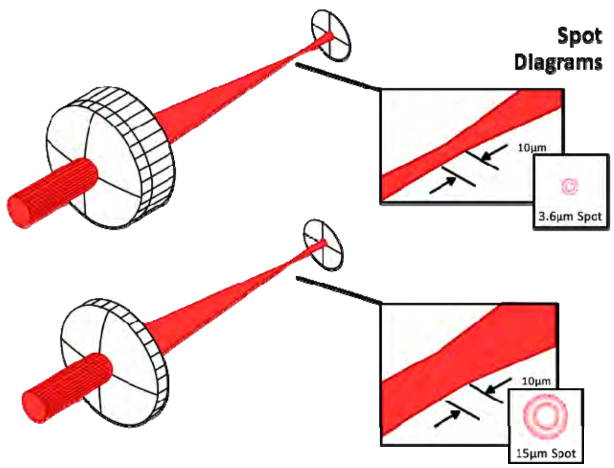

Figure 3: Layout decribing the focal point with spot diagrams for two different lenses

In the layout of Fig. 3, it is also describe experiments we carry out with two focused lenses and the selected lens corresponds when the beam at the focal point had a diameter of about 3.6 micrometer of diameter. Additionally, this spot size would allow to detecting the depth of small holes or material defects with diameter smaller than 4 micrometers, but the purpose of this work was only to determine the focal distance of plane surface rather than works for the depths of some special samples.

4. OPTICAL FIBER SENSOR

The optical fiber sensor consists in a directional 3dB coupler which divides the laser beam into two beams, one beam goes to ground, and the another transmit the light to the test surface and the reflecting light is send back to the coupler and photo detector to be then processed by a signal processing electronic board.

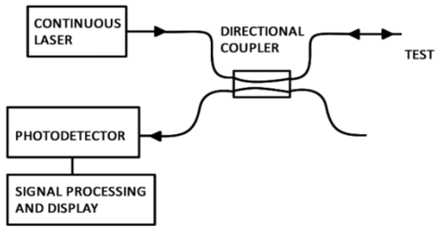

Fig. 4 Experimental Setup.

6. EXPERIMENTAL RESULTS

The results of the thickness on the plastic sample shown a relative error of +/- 2 micrometers, and did not require a correction factor because it only depends in its focal point instead of the reflectance coefficient of surface area. The system also uses a webcam which allow seeing the sensing point before making a measure, and it has to be calibrated and positioned in the *x-y* coordinate. In order to confirm the correct position between the camera viewer and the real position of the laser beam, a calibrated movement in its *x-y* position were implemented in the software, meaning that once it was get an image, the laser beam of our sensor moves automatically to this position and start a measurement.

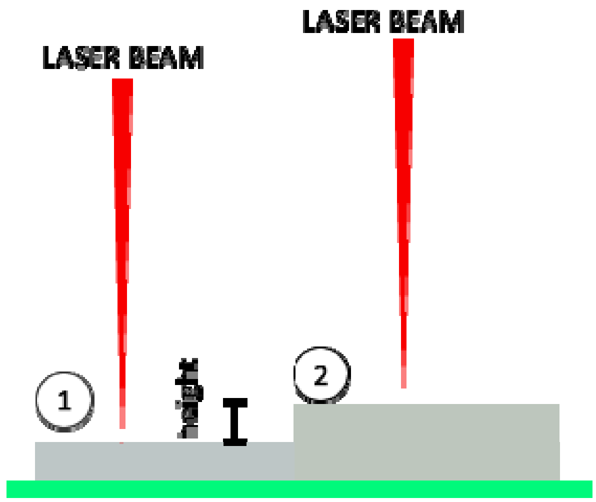

Figure 5: Explanation for a relative distance of a material which corresponds to the thickness

As showed in figure 5, we make measurements of the height relative to the surface by taking two points over the surface. The tests were made to prove the precision of the instrument which consisted in measuring different materials such as the width of a Compact Disk (opaque object), the width of a microscope slide (transparent objet) and a polymeric rectangular base. These measurements were compared with a Vernier Caliper instrument and the agreement between both measurements is fairly good as shown in Table 1.

Figure 6: Photos of the three different tested materials

Table 1: Experimental results

	Measurement with the Vernier Caliper	Measurement with the Noncontact fiber optic micrometer
Compact Disk	1.4487 mm	1.4657 mm
Microscope Slide	0.0496 mm	1.02 mm
Polymeric film sample	1.1mm	1.11mm

The table 1 shows that the instrument work well for opaque and semitransparent objects, but it doesn't work properly for a transparent like surfaces.

CONCLUSIONS

It was concluded that the measuring of the surface thickness using the focal point considering the maximum intensity of the laser beam over the surface is possible only for opaque or semitransparent objects, and it was found to be a cheaper way of detecting the thickness of some samples. Additionally, the instrument developed was found to be used for a large variety of sensing applications (eg. proximity sensing, index of reflection measurements, etc.).

ACKNOWLEDGMENTS

F. Betancourt and V. Guzman wish to thank the support provided by PROMEP and CONACYT through student grants, respectively. This work was supported by the Mexican Ministry of Education (SEP) under grant 2523 and by PAICYT-2009 under grant 133.

REFERENCES

[1] Shuzhue Yio, P. B. Ruffin, and F. T. S. Yu, [Fiber Optic Sensors], CRC Press, Ch. 1, 2& 3, (2008).
[2] OTDR, http://www.wisegeek.com/what-is-an-otdr.htm
[3] P. Healey, "Review of long wavelength single mode optical fiber reflectometry techniques," IEEE/OSA J. Lightwave Technol. LT-3, 876 (1985).

Novel 3-Axis Optical Fiber Alignment System

S. Salinas-Almaguer[a*], Candelario Guajardo-Gonzalez[a], Francisco Betancourt-Ibarra[a], Carlos Martinez-Hernandez, Romeo Selvas[a,b]

[a] School of Mathematical and Physical Sciences, UANL, San Nicolás de los Garza, 66451, NL, México

[b]Center for Innovation, Research and Development in Engineering and Technology, CIIDIT-UANL, Monterrey, 66450, NL., México

* xor_deus_deus@hotmail.com

ABSTRACT

This paper presents a 3-Axis enhanced alignment system for optical fiber. The arrangement uses in one of its axis a vision recognition system which employs Canny edge detector and Phase correlation. The other two-axis are aligned by controlling a couple stepper motors through displacement algorithms. The setup uses a commercial multimodal transmitter and receiver, multimode fiber, a digital microscope, three stepping motors and software. This automatic system takes an alignment time of 20 seconds and up to 70% of coupling power efficiency.

Keywords: Optomechatronics, Automatic Alignment, Fiber Optics, Image Processing.

1. INTRODUCTION

The main laboratory problem when working with fiber optics and lasers is to launch efficiently the light into these fibers. The alignment process needs considerable time and effort even for a skilled personal and due to this problem, the automatic alignment is becoming an important step to setup a whole experiment [1-3]. Today, there are some commercial solutions to this problem, but due to the high prices, this stage continues to be a manual process in many labs. The main goal of this research work is to develop a system which could be customized to fit with any manual alignment equipment of a laboratory and to have a resolution quite enough to cover the fiber optics applications need. As from our previous work [4], we start improving some crucial process like pre-alignment of the fiber and at that time, the used of a hexagonal shape arrangement of SMF´s fiber generates a map location of the spot light and throughout an USB based PC interface was possible to automate the alignment process. The drawback of this previous system was that the coupling efficiency was less than 60% and it previously required of a manual pre-alignment step in one of its axis. For this new version, it was added a third axis to the whole system which consists of a vision recognition system. It was then found in the literature that to reduce the pre-alignment time, some commercial systems use expensive machine vision systems and software to pre-align the fibers, instead of that, our third axis was proposed with a less expensive solution using a digital microscope and software based on the OpenCV library. This new feature in our system allows us to have a totally automatic alignment system and get a coupling efficiency of roughly 70% in only 20 sec.

2. THE ALIGNMENT PROCESS

The proposed alignment method begins with the automation process for every manual process. Firstly, we need to bring near enough to both fiber facets in order to launch a small power signal. This process is not as simple as it looks like, and sometimes required some support from a manual alignment process. Once it detects some signal, the automatic process starts with a digital microscope with a resolution quite enough to locate both fibers. By using software made in home, we propose the uses of the Canny edge detector to get a clear vision of both fibers, and the phase-correlation algorithm to make a relation between the image pixels and the motor steps which allow also calculate the motor steps required to align both fibers in the *z*-axis. Our computer screen is divided into two parts and each half displays one fiber image (the transmitter fiber and the receiver fiber). The next step is to maximize the signal, and this could be done in several ways depending of the step resolution of the alignment system, we therefore use a simple 3D scanning routine, very similar to our previous work [4] in which was possible to use a fiber array to map the light's spot beam and in this way get a maximum power by relocated the *x*-*y* axis. As a final step, the system could try to search for the best signal, and seeking

2nd Workshop on Specialty Optical Fibers and Their Applications (WSOF-2),
edited by Juan Hernández-Cordero, Ismael Torres-Gómez, Alexis Méndez, Proc. of SPIE
Vol. 7839, 783926 · © 2010 SPIE · CCC code: 0277-786X/10/$18 · doi: 10.1117/12.869390

automatically the place x,y,z, where the best signal is obtained. In figure 1, it is illustrated a flowchart in which is indicated the best way to work with the alignment process.

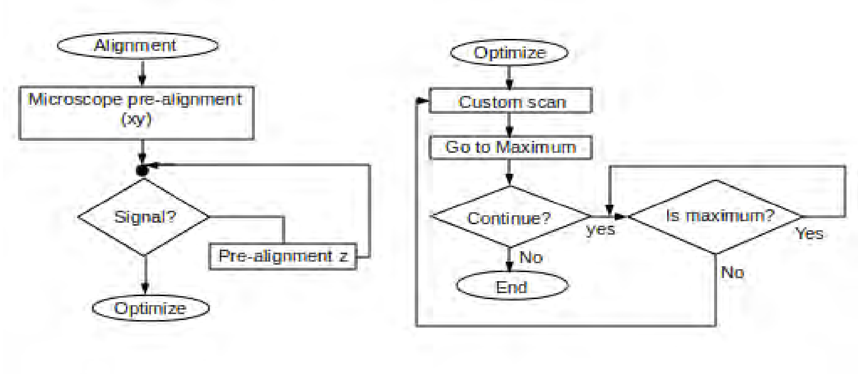

Fig 1. Flowchart of the alignment process.

2.1 The Alignment System

The system consists of a 3-axis manual translate stage mount, 3 stepper motors (1.8º per step) with motor drives, a 840 nm LED transmitter (OPF1412), a ST multi-modal fiber receiver (OPF2412), an USB data acquisition/control interface, a digital microscope, and software, see fig. 2.

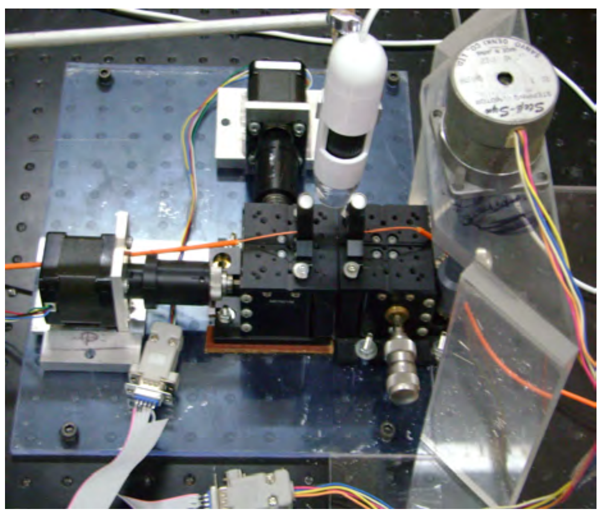

Fig 2. 3-axis alignment-mount with a digital microscope.

3-Axis Micro-block Flexure stage

The 3-axis stage translation mounts required to attach 3 stepper motors and be a device easy of controlling each movement, but most of the manual flexure stage mounts designs do not permit to adapt a third axis in a simple way. To avoid the problem, we suggest to using a separate translation mount to control this axis.

The software

The software was developed to run in the Linux operating system, using Qt and the OpenCV Library to perform the Canny edge detector and Phase Correlation algorithm and thus process a digital microscope image to determine the locations of these fiber facets. The Program also plots the real time signal intensity, and allowed calculating the current percentage of coupling which is based of the incoming voltage and the current from the LED transmitter and receiver, all data is acquired by the USB data acquisition/control interface.

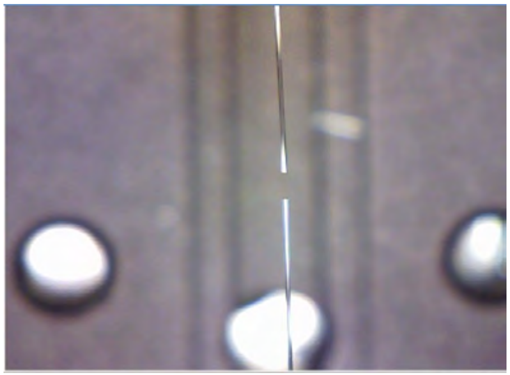

Fig 3. Microscope image of both fibers.

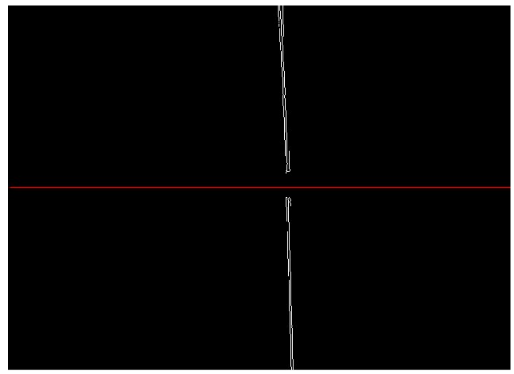

Fig.4 Processed image, the red line show each region to be processed with phase correlation algorithm.

3. EXPERIMENTAL SET UP AND RESULTS

Fig. 5 shows the experimental set up which consists of a 840 nm LED Transmitter (OPF1412) used as a pump, a multi-modal fiber (62.5/125µm) with ST connector, a 840 nm multi-modal receiver (OPF2412), 3-axis translate stage mount, 3 stepper motors (1.8º) and an USB control interface based on the PIC18F4550.

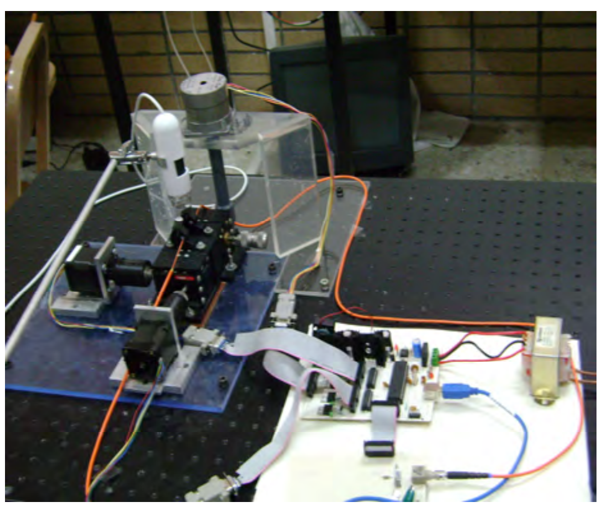

Fig 5. Experimental set up.

3.1 Procedure and Results

We automatically aligned the fibers using our system based on the maximum detected voltage from the incoming signal of the 840 nm receiver(OPF2412), and was also compare the results using a Thorlabs optical power meter. The achieved results are show in table 1 and are in good agreement.

Power Meter	Coupling Percentage	Average Time (Sec)
OPF2412	69.67	20

Table 1. Coupling efficiency and percentage alignment time.

CONCLUSIONS

As we have shown, it is possible to automate a 3-axis alignment system based on manual translate flexure stage mounts with a resolution good enough to start align multimodal or single mode fiber at a reasonable time. The system performance was fairly good and has a time processing of 20 Sec for the best coupling efficiency between two multimode fibers that corresponds a value of 70%. The system was totally automatic and it could be slightly modified for a better result.

There are several ways to improve this system, for example by substituting the actual stepper motors with one which has a 0.9º stepper resolution. Moreover, it could be possible to align multi-modal rare-earth-doped fibers based on its shining core by using line detection algorithms like the Hough transform, and aligning the fibers based on the fiber core position instead of the fiber outer cover cladding. By this way, it would be possible to get a time reduction at the optimizing process.

ACKNOWLEDGMENTS

Samuel Salinas wishes to thank the support provided by the SEP through a student grant. The authors thank to the F&L Group from the School of Mathematical and Physical Science at the UANL. This work was supported by the Mexican Ministry of Education (SEP) under grant 2523 and by PAICYT-2009 under grant 133.

REFERENCES

[1] Tan Kok Kiong, Lee Tong Heng, Dou Huifang and Huang Sunan, “Precision motion control, design and implementation”, Springer-Verlag, Chap. 1, 2001.

[2] James B. Taylor, Andres L. Carrano, Yahya Fathi, “Parametric design and optimization for a nonlinear precision x-y microstrage”, Journal of Manufacturing Systems, 2000.

[3] Thorlabs Catalog: Motion controlling electronics/ Autoalignment controller

[4] S Salinas-Almaguer, V Guzman-Ramos, C Calles-Arriaga, L Cortez-Gonzalez, R Selvas, “Novel Automatic Alignment of Specialty Optical Fibers”, in Proc. SPIE 7499, Seventh Symposium Optics in Industry, 2009.

Novel Automatic Alignment of Specialty Optical Fibers

S. Salinas-Almaguer[a], V. Guzman-Ramos[a], C. Calles-Arriaga[a], L. Cortez-Gonzalez[a], R. Selvas[a,b]
[a] School of Physical and Mathematical Sciences, UANL, Av. Universidad S/N, Cd. Universitaria, San Nicolás de los Garza, 66451, NL, México
[b] Center for Innovation, Research and Development in Engineering and Technology, UANL, Monterrey, 66450, NL., México

ABSTRACT

This paper presents the development of an automatic alignment system for specialty optical fibers. Based on a XY coordinates system, the alignment is achieved by the control of stepping motors through displacement algorithms. A hexagonal shape arrangement of SMF´s fibers generates a map location of the spot light. This photo-detection system enables to analyze the launching of the beam into the fiber. Through an USB based PC interface and software to automate the alignment process the device's performance has been improved in time and in optical coupling efficiency. The results obtained are 2 or 3 seconds in the alignment process and roughly 80% coupling efficiency.

Keywords: Optomechatronics, automatic alignment, fiber optics.

1. INTRODUCTION

Automatic alignment systems play an important role in various areas of technology development. In the field of research and development, mainly in the field of optics, high precision mounts are required for alignment of experimental arrangements with micrometric displacements or even nanometric [1,4]. The process of alignment of optical systems require a considerable time even for skilled personnel. Moreover, the implementation of these systems is useful for applications in diverse areas such as laser materials processing [2,3], industry, military, medical operations for high precision optical recording systems, etc. Automatic alignment systems require, in one hand, sensors that detect the signal and a system that process it, in order to align at the right position [5]. In our system, the sensing is replaced by reading signals through an arrangement of single mode fibers to locate the spot and optimize the performance of our whole device. This automation system brings a fast, economic and flexible way to improve the alignment process than commercial solution based systems.

2. THE ALIGNMENT

The alignment system comes from the need of optimization in the process of launching of a laser beam into an optical fiber. It is considered the alignment of a laser beam into a specialty optical fiber. The process starts by a 2-axis-dimension scanning of a system of fiber based photo-detection which search and find signal intensity in at least one of the fibers and through a location analysis, it will align the fiber to the right beam axis.

2.1 The Alignment System

The system consists of a CPU that through one computer software sent commands to an electronic control device via USB link as is seen in Fig. 1. The control device handles two stepping motors assembled to a XY positioning mechanical commercial system over which is mounted a hexagonal shape arrangement of fibers to photo-detect the light. The USB interface after reading the signal can control the translate mechanism by computing the reading data. Subsequently, the system was tested to align an incident laser beam.

Seventh Symposium Optics in Industry, edited by Guillermo García Torales, Jorge L. Flores Núñez, Gilberto Gómez Rosas, Eric Rosas, Proc. of SPIE Vol. 7499, 74990M · © 2009 SPIE · CCC code: 0277-786X/09/$18 · doi: 10.1117/12.849187

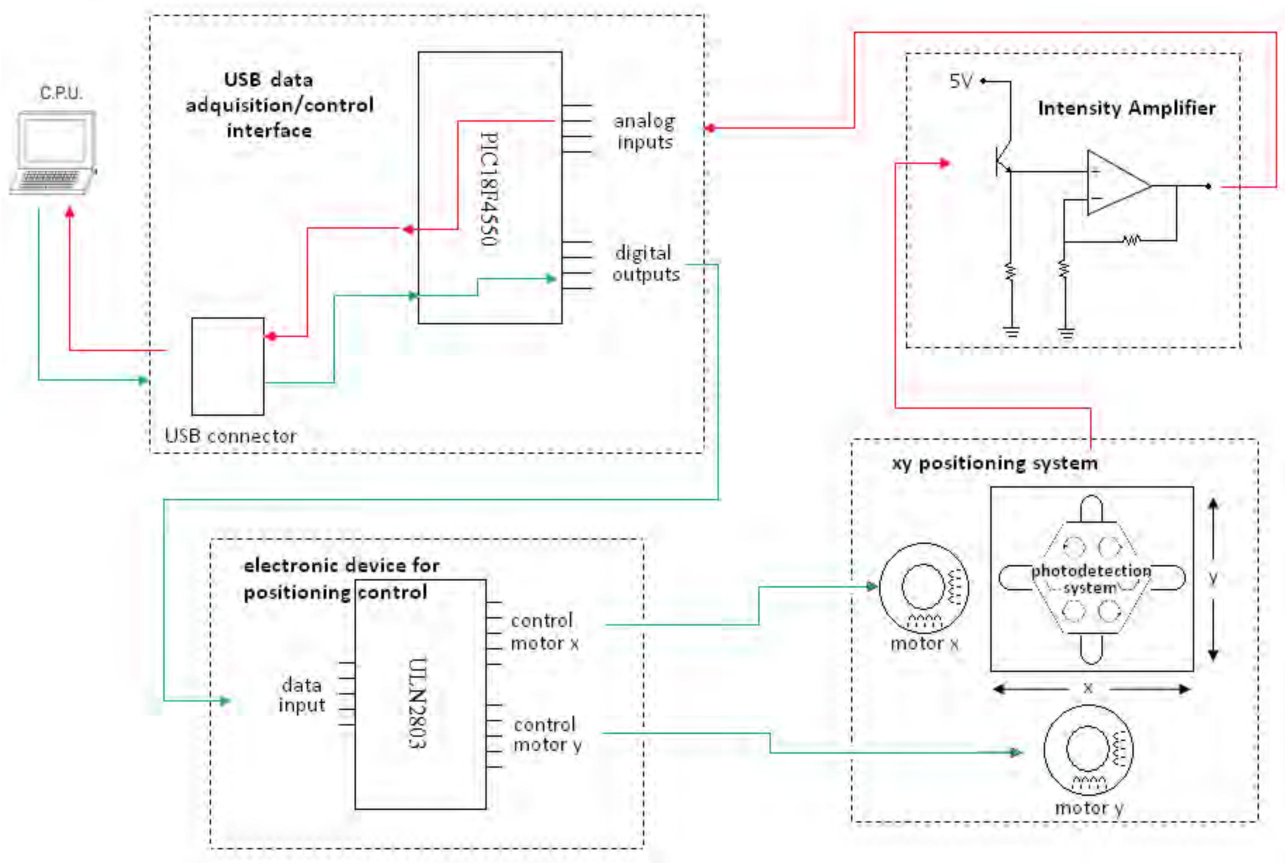

Fig 1. Description of alignment system's device.

Photodetection system

The system is based on a hexagonal geometric shape arrangement of SMF´s fibers as illustrated in Fig. 2. As it can be seen, the target fiber is located at the center. The hexagonal arrangement allows a bigger area for the light detection and a more precise location of the axis of the spot.

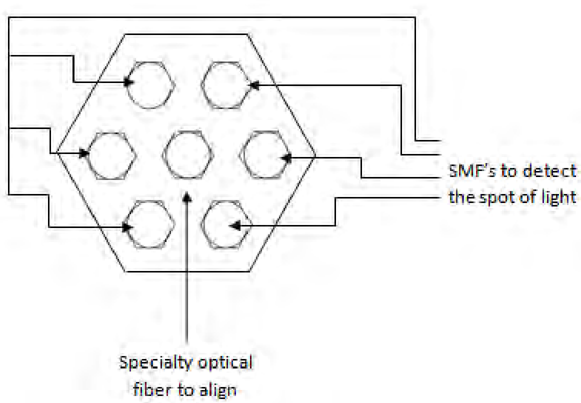

Fig 2. The fiber based photo-detection system

The fiber arrangement is connected to the measuring device that read the power intensities of each fiber. When a signal is detected in any fiber, the intensity information is sent to the CPU together with the coordinates of the receiving fiber. This information enables to micro-stepping movements to realign the whole fiber system and to get the maximum power intensity in this desired fiber. Table 1 illustrates the mapping in power of a laser beam.

Fiber No	coordinates	intensity
A	(x_A,y_A)	I_A
B	(x_B,y_B)	I_B
C	(x_C,y_C)	I_C

Table 1. Expected response of each fiber

The measurement of intensity in the arrays of fibers allows better localization of the axis of the light's beam through the hypothesis of a Gaussian distribution profile as it is well know that for a Gaussian beam has a maximum localized.

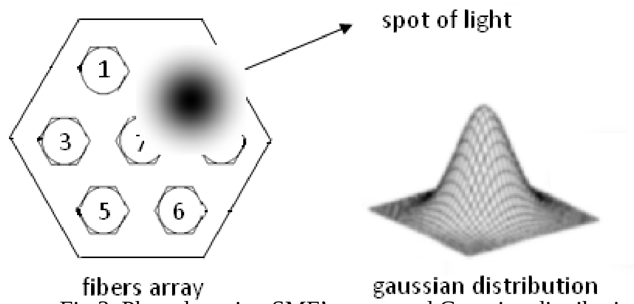

Fig 3. Photodetection SMF's array and Gaussian distribution

Intensity amplifier

Together with the photo-detection system, this feedback device is used to measure the intensity from each fiber and sends the data to the acquisition/control card. This device works through 2 internal stages: in the first stage, it takes measurements of intensities from each fiber using an array of photo-transistors. The second stage consists in the signal processing. Here, the signal is amplified from the photo-transistors and adjusted to be processed with the acquisition/control interface.

The software

The software was built to run Linux operating system, additional this program brings the user a manual control of the alignment process through a mouse scroll wheel interface, where every single wheel click moves the fiber array platform. This software program generates plots of the measured intensity of each fiber and decides how many steps the micro-motor must do. It brings a more precise control on maximizing the insertion of light in an optimum time.

3. EXPERIMENTAL SET UP AND RESULTS

Fig. 4 shows the experimental set up which consists of a 630 nm He-Ne laser used as pump, a fiber array, a specialty optical fiber, two stepping motors, and one interface.

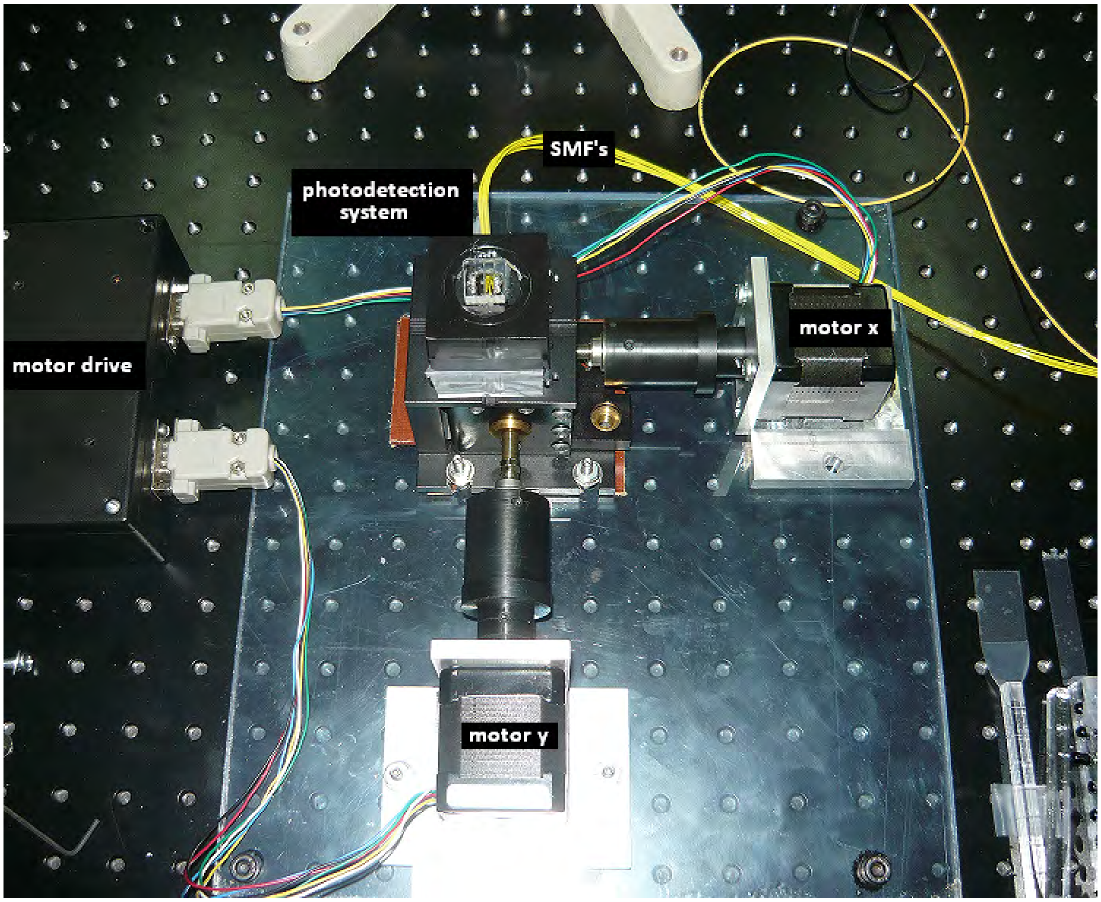

Fig 4. Experimental set up.

3.1 Procedure and results

We align manually the axes of the laser light and the fiber in order to maximize the percentage of light coupled. Afterwards, the system was tested in automatic mode by measuring the achieved alignment and its working time. These results of automatic alignment were compared with manual mode. Although the coupling efficiency in the manual mode is slightly higher, the average time for the process is significantly short. The target fibers can be any of type, such as, double clad fibers, multimode fibers, polarized fiber, highly nonlinear fibers, etc. Comparing with commercial devices for automatically aligned, it was found that the materials used in our proposed are considerably low. The system results to be robust, replicate and reliable. By including extra axes in our system, it will allow us expanding its functions to 3 or more axes.

Operating mode	**Average intensity (V)**	**Relative alignment (I_n/I_{max})**	**Average time (s)**
Manual	I_{max}	0.95	560
Automatic	I_1	0.8	2

Table 2. Experimental Results (coupling efficiency and time of alignment)

3.2 Conclusions

It was proved the efficiency of our system by the alignment process and enable us times that runs from 2 to 3 seconds for an optical power coupling efficiency of 80%. The cost for the whole systems is low when compare with a conventional automatic alignment system. The reliability of our system permits to accelerate the process of our research, focusing all the efforts only in the analysis of the phenomena to study. It is intended to optimize our system and expand its functions to 3 axis alignment.

ACKNOWLEDGMENTS

Samuel Salinas wishes to thank the support provided by the SEP through a student grant. The authors thank to the F&L group from school of physical and mathematical sciences (FCFM) at the autonomous university of Nuevo Leon (UANL) and also to thank to Monterrey Photonics S.A. de C.V. by the collaboration in the project

REFERENCES

[1] Tan Kok Kiong, Lee Tong Heng, Dou Huifang and Huang Sunan, “Precision motion control, design and implementation”, Springer-Verlag, Chap. 1, 2001.

[2] R. Dworkowsky and P. Wojcik, “Computer control for a high speed, precision laser cutting system”, Electrical and Computer Engineering, Vol. 1, pp. 187-189, September 1995

[3] James B. Taylor, Andres L. Carrano, Yahya Fathi, “Parametric design and optimization for a nonlinear precision x-y microstrage”, Journal of Manufacturing Systems, 2000.

[4] Thorlabs Catalog: Motion controlling electronics/ Autoalignment controller

[5] C. Calles-Arriaga, A. Castillo-Guzmán, R. Selvas-Aguilar, y D. Castañeda-Rodríguez, “Desarrollo de un sistema para alineación automática de arreglos ópticos”